

*The Quaternary climate in loess sediments:
Evidence from rock and mineral magnetic and
geochemical analysis*

Maurizio Sartori

**The Quaternary climate in loess sediments: Evidence
from rock and mineral magnetic and geochemical
analysis**

A Dissertation submitted to the
SWISS FEDERAL INSTITUTE OF TECHNOLOGY ZÜRICH
for the degree of
Doctor of Natural Sciences

Presented by

MAURIZIO SARTORI
Dipl. Natw., ETH-Zurich
Born: 12.6.1968
Locarno TI

accepted on the recommendation of

Prof. Dr. F. Heller,	examiner
Prof. Dr. W. Lowrie,	co-examiner
Prof. Dr. M. E. Evans,	co-examiner
Dr. J. Beer,	co-examiner

Contents

Abstract	1
Sommario	4
Publications	8

PART I

INTRODUCTION

Objectives	10
------------------	----

CHAPTER 1: Loess Deposits and Paleoclimate 13 |

1.1 Loess, a wind blown sediment 14 |

1.1.1 Grain size and mineral composition	14
1.1.2 Carbonate content	15
1.1.3 Lithological and structural properties of loess	15
1.1.4 Soils and paleosols	16
1.1.4.1 Climatic significance of soils and paleosols	18

1.2 Worldwide loess distribution 19 |

1.2.1 Introduction	19
1.2.2 Loess deposits in Europe	20
1.2.3 The Chinese Loess Plateau	22
1.2.3.1 Introduction	22
1.2.3.2 Regional distribution of loess	23
1.2.3.3 Lithostratigraphy	24
1.2.3.4 Magnetostratigraphy and the age of loess sedimentation	25
1.2.3.5 Climate evolution and the age of loess sedimentation	28
1.2.4 Loess deposits in Central Asia	29
1.2.5 Loess deposits on the American continents and in New Zealand	29
1.2.6 Matuyama-Brunhes boundary in loess deposits	30

1.3 Climatic significance of loess/paleosol deposits 32 |

1.3.1 Paleosols and susceptibility enhancement	32
1.3.2 Susceptibility enhancement and Milankovitch's theory	34

THEORETICAL BACKGROUND AND METHODOLOGY

CHAPTER 2: Magnetism 37 |

2.1 Atomic basis of magnetism 38 |

2.2 Fundamental parameters in magnetism 39 |

2.3 Magnetic behaviour in solid matters	39
2.3.1 Diamagnetism	39
2.3.2 Paramagnetism	40
2.3.3 Ferromagnetism	41
2.3.4 Ferromagnetic susceptibility	43
2.4 Processes of magnetization	43
2.4.1 Energies in a ferromagnetic grain	43
2.4.2 Magnetic domains	45
2.4.3 Magnetic relaxation and superparamagnetism	47
2.4.4 Magnetic hysteresis	48
2.5 Magnetic minerals	49
2.5.1 Hematite (α -Fe ₂ O ₃)	49
2.5.2 Magnetite (Fe ₃ O ₄)	51
2.5.3 Maghemite (γ -Fe ₂ O ₃)	52
2.5.4 Goethite (α -FeOOH)	53
2.6 Magnetic measurements	53
2.6.1 Room temperature	53
2.6.2 Low temperature measurements	57
<u>CHAPTER 3: Grain size analysis</u>	59
3.1 Introduction	60
3.2 Stoke's Law	60
3.3 Sedimentation and centrifugation	60
3.3.1 Sedimentation	60
3.3.2 Centrifugation	62
3.4 Mastersizer	63
<u>CHAPTER 4: Beryllium-10</u>	65
4.1 Cosmogenic Isotopes	66
4.1.1 Cosmic Rays	66
4.1.2 Primary particles	66
4.1.3 Interaction of cosmic rays with the atmosphere	67
4.1.4 Production of isotopes in the atmosphere	68
4.2 Beryllium - 10 (¹⁰Be)	70
4.2.1 ¹⁰ Be production rate	70
4.2.2 ¹⁰ Be in the atmosphere and transportation processes	71
4.2.3 ¹⁰ Be in soils	71
4.2.4 ¹⁰ Be, magnetic susceptibility and paleoprecipitation	73
4.2.5 Chemical extraction of ¹⁰ Be from loess sediments	75
4.2.6 Accelerator mass spectrometer (AMS)	78

PART II

RESULTS

CHAPTER 1: Determination of the Matuyama/Brunhes boundary (M/B) and magnetic properties of loess grain size fraction from the section at Paks (Hungary)	81
1.1 Introduction	82
1.2 Lithology	84
1.2.1 Young Loess	85
1.2.2 Old Loess	86
1.3 Experimental results	89
1.3.1 Natural remanent magnetization (NRM)	89
1.3.2 Low field susceptibility (χ) as a function of grain size	93
1.3.3 Hysteresis parameters as a function of grain size	95
1.3.4 Low temperature TRM	97
1.3.5 Zero Field Cooling	98
1.4 Discussion	99
1.4.1 Magnetostratigraphy	99
1.4.2 Room temperature measurements	100
1.4.3 Low temperature measurements	102
1.5 Conclusions	105
CHAPTER 2: Magnetic properties and chronology of the loess/paleosol sequence at Roxolany (Ukraine)	107
2.1 Introduction	108
2.2 The Roxolany loess-soil sequence	109
2.2.1 Unit I	109
2.2.2 Unit II	109
2.2.3 Unit III	111
2.2.4 Unit IV	112
2.2.5 Unit V and VI	112
2.3 Determination of the Matuyama-Brunhes boundary	114
2.4 Hysteresis and ARM	118
2.4.1 Hysteresis parameters	118
2.4.2 Anhysteretic remanent magnetization (ARM)	121
2.4.3 Loess/paleosol discrimination	124
2.4.4 Magnetic profiles	126

2.5 Discussion	132
2.6 Conclusions	139
<i>CHAPTER 3: Magnetic properties of two loess/paleosol sections from the western (Xiagaoyuan, Gansu province) and the central (Houzhuang, Shaanxi province) Chinese loess plateau</i>	143
3.1 Introduction	144
3.2 Lithological description	147
3.3 Rock magnetic results	152
3.3.1 Magnetic susceptibility	152
3.3.2 Hysteresis measurements	157
3.3.3 Temperature dependence of magnetic properties	161
3.4 Discussion	168
3.4.1 Chronology	168
3.4.2 Magnetic profiles	171
3.5 Conclusions	179
<i>CHAPTER 4: Climate changes during the last glacial/interglacial cycle: link between susceptibility, grain size and ¹⁰Be in the western (Xiagaoyuan, Gansu province) and the central (Houzhuang, Shaanxi province) Chinese loess plateau</i>	183
4.1 Introduction	184
4.2 Results	185
4.2.1 ¹⁰ Be, susceptibility and median grain size variation during the last interglacial cycle	185
4.2.2 Relationship between ¹⁰ Be concentration, susceptibility and grain size	189
4.2.3 ¹⁰ Be and susceptibility fluxes	193
4.2.4 The role of grain size	197
4.3 Conclusions	203
<i>CHAPTER 5: Conclusions</i>	205
References	212
Curriculum Vitae	230
Acknowledgements	231

ABSTRACT

Continuous accumulation of dust during the Quaternary has formed thick loess deposits on the northern continents, mainly in China, Europe and Central Asia. The magnetic properties of these aeolian sediments have recorded the paleoclimatic fluctuations in a detailed and complete way.

In the loess/paleosol sequence at Paks (Hungary), susceptibility was measured through a 49-meter profile of about 49 m depth: About 620 oriented samples were collected for rock magnetic and paleomagnetic investigations. The section covers a time span of about 850 ka, including the Brunhes and the youngest part of the Matuyama polarity chron (M/B boundary at 44.1 depth). Two loess and two paleosol samples were investigated magnetically in detail. They were split into 10 grain size fractions (ranging from 15 nm to 50 μm) using consecutive sedimentation and centrifugation steps. A strong grain size dependence of the magnetic susceptibility and other hysteresis parameters was observed. High susceptibility values measured in the paleosol samples, especially in the finest fractions, originate from neoformation of fine-grained iron oxides. Low temperature measurements identify magnetite and maghemite as the main carriers of the magnetic signal, and offer the possibility of separating the paramagnetic and ferri-magnetic contributions from the total magnetic signal.

In the Ukraine, about 900 closely spaced oriented samples were collected from the 48 m thick loess/paleosol section at Roxolany to establish an absolute time frame for the loess sequence and to compare and correlate the magnetic properties with the lithologic data in the light of their paleoclimatic significance. The upper part of the investigated section is of normal polarity, with the M/B boundary found at ~ 35 m depth. By extrapolation beyond the M/B boundary an age of 1 Ma was assigned to the entire section. A timescale was obtained by matching the susceptibility variations in the profile with the variations of the astronomically-tuned oxygen isotopes in marine sediments. The susceptibility record dated in this way allowed correlation of the loess sequence at Roxolany with other loess sequences in Europe and China, confirming its evolution as a result of global paleoclimatic variations during the Early Pleistocene. Paleoclimatic reconstruction inferred from lithological observations gives evidence of important differences between the upper ~ 23 m and the lower part of the section: in the latter the paleosols are of braunlehm type, a Mediterranean humid and warm climate type soil, while in the younger part, the paleosols are chernosems formed in a less humid and slightly colder

environment. Magnetic measurements confirmed the significant differences derived from the lithological observations, but lead to the conclusion that simple linear relationships cannot be established between ferromagnetic enhancement, soil evolution and paleoclimatic development.

About 1'100 oriented loess and paleosol samples were collected at 5 to 10 cm intervals from two loess sequences in China (Xiagaoyuan, Gansu Province, western loess plateau and Houzhuang, Shaanxi Province, central loess plateau). The differences in magnetic properties between these two localities, where loess formed under different paleoclimatic conditions, were studied and the impact of global long- and short-term climate changes on the Chinese loess plateau was determined. Xiagaoyuan is situated in a very dry, semi-desertic region (mean annual precipitation of ~300 mm); the section has a depth of 23 m, and is mainly composed of pristine unaltered loess: only two paleosols and the Holocene soil were identified. The climate at Houzhuang is warmer and more humid (mean annual precipitation of ~600 mm). The section, which has been sampled to a depth of 20 m, has been subject to much stronger pedogenesis, and consists mainly of paleosols (three pedocomplexes formed during interglacials and three paleosols formed during interstadial periods) and weathered loesses. A chronostratigraphic subdivision was obtained by matching the magnetic susceptibility variations with the astronomically-tuned oxygen isotope record. A maximum age of ~130 ka for the section at Xiagaoyuan and of ~250 ka for the section at Houzhuang was established. The Blake geomagnetic polarity event could not be discovered at either site. The ferromagnetic mineral constituents are similar in both sections, with magnetite/maghemite as the main minerals responsible for the magnetic enhancement. Important differences, however, are expressed by the magnitude of the magnetic signals. The generally higher ferromagnetic concentration in the loess layers at Houzhuang than in the loesses at Xiagaoyuan formed in the same time interval, indicates that significant pedogenesis affected the loesses at Houzhuang not only during interglacials, but also during glacial periods. Grain size fractionated samples from Xiagaoyuan and Houzhuang give clear evidence of the regional climate differences. A progressive increase of the very fine-grained superparamagnetic ferromagnetic component was observed with increasing pedogenesis. This is due to *in situ* production of magnetic minerals rather than changes in ferromagnetic concentration of the source material. Another important difference between the two studied sections, also related to the different paleoclimate evolution in these regions, is given by the higher sedimentation

rate observed at Xiagaoyuan: the horizon corresponding to the boundary between oxygen isotope stage 5 and 6 was found at 23 m depth at Xiagaoyuan (corresponding to a mean sedimentation rate of 17.7 cm/ka) and at 7.5 m depth at Houzhuang (corresponding to a mean sedimentation rate of 5.8 cm/ka). The high resolution at Xiagaoyuan permits detailed correlation between the magnetic and sedimentologic record and the marine and ice core oxygen isotope variations for the last ~130 ka. The oxygen substages 5a-e can be correlated with the susceptibility signal from the pedocomplex S_1 (S_1S_1 , S_1L_1 , S_1S_2 , S_1L_2 and S_1S_3). This was not possible at Houzhuang because of the strong pedogenesis that characterizes the whole of the last interglacial there. High-frequency climate changes (Bond cycles, Heinrich events) as observed in the GRIP core seem to correlate with the fluctuations of the frequency dependent susceptibility measured in incipient pedogenic layers of loess layer L_1 at Xiagaoyuan.

The ^{10}Be concentration was measured using 64 bulk samples and 36 grain size fractions obtained from four samples (one loess and one paleosol sample for each section). The samples originate from the pedocomplexes S_1 which represent the last interglacial (age between ~70 and ~130 ka). An inverse relationship between grain size and ^{10}Be concentration was found. The measurements did not give evidence of a linear relationship between ^{10}Be concentration and susceptibility. ^{10}Be concentrations in Xiagaoyuan reflect median grain size changes rather than susceptibility variations. Grain size spectra analysis revealed that the median grain size alone is not a good parameter for describing a specific grain size distribution and may not represent the median grain size of the original loess forming dust. A future model for paleoprecipitation reconstruction using ^{10}Be and susceptibility fluxes should consider the variations of the atmospheric ^{10}Be flux which are controlled by the intensity changes of the Earth's magnetic field.

SOMMARIO

Durante il Quaternario, il costante accumulo di polveri ha dato origine in Cina, Europa ed Asia centrale ad importanti depositi di loess. Le proprietà magnetiche di questi sedimenti hanno premesso di ricostruire le fluttuazioni paleoclimatiche in modo dettagliato e completo.

Presso Paks (Ungheria), la suscettività magnetica è stata misurata lungo un profilo di loess spesso circa 49 m. Circa 620 campioni orientati sono stati raccolti per essere sottoposti ad una serie di misure magnetiche e paleomagnetiche. Il profilo ha un'età complessiva di ca. 850'000 anni, e comprende la polarità magnetica di Brunhes e l'intervallo più recente a polarità inversa di Matuyama (la transizione M/B è stata individuata ad una profondità di 44.1 m). Due campioni di loess e due provenienti da un paleosuolo sono stati sottoposti ad analisi magnetiche dettagliate. Ogni campione è stato sottoposto a processi di risedimentazione e centrifugazione in modo da ottenere 10 frazioni granulometriche. Si è osservata una forte correlazione tra suscettività magnetica, parametri d'isteresi e granulometria. Gli alti valori di suscettività nei paleosuoli, misurati soprattutto nelle frazioni più fini, sono causati dalla formazione di minerali di ossidi di ferro della dimensione dell'ordine dei nanometri. Misure magnetiche a bassa temperatura permettono di identificare magnetite e maghemite come i principali responsabili del segnale magnetico, e permettono di separare la componente paramagnetica della suscettività da quella ferromagnetica.

In Ucraina circa 900 campioni orientati sono stati raccolti presso Roxolany, lungo un profilo di loess spesso 48 m. Lo scopo era quello di ricostruire una scala temporale assoluta e correlare le variazioni delle proprietà magnetiche con i dati litologici interpretati da un punto di vista paleoclimatico. La parte superiore del profilo considerato ha polarità normale, e la transizione M/B si situa a 35 m di profondità. Un'età di 1 milione d'anni per l'intera sezione è stata determinata per estrapolazione in base al tasso di sedimentazione medio. Si è ottenuta una scala temporale correlando le variazioni di suscettività lungo il profilo con le variazioni dell'isotopo di ossigeno, calibrate su base astronomica, misurate in sedimenti marini. Il profilo di suscettività (con valori di punta caratteristici nei paleosuoli) datato in questo modo permette di correlare la sezione di Roxolany con altri profili in Europa ed in China, confermando come l'evoluzione dei depositi di loess nel tempo è il risultato dei cambiamenti a livello globale occorsi durante il Pleistocene tardo. Importanti differenze tra i primi 23 m del profilo e la parte sot-

tostante sono state messe in evidenza da ricostruzioni paleoclimatiche basate su osservazioni litologiche: nella parte inferiore i paleosuoli sono di tipo *braunlehm*, un suolo originato da un clima caldo ed umido di tipo mediterraneo, mentre nella parte superiore i paleosuoli sono di tipo *chernosem*, originati da un clima meno umido e più freddo. Le misure magnetiche confermano l'importante differenza individuata dalle osservazioni litologiche, sottolineando inoltre come non sia possibile stabilire una relazione di tipo lineare tra l'aumento del segnale ferromagnetico, l'evoluzione del suolo e lo sviluppo del paleoclima.

Circa 1'100 campioni orientati di loess e paleosuolo provenienti da due profili in Cina (Xiagaoyuan, provincia del Gansu, nel plateau di loess occidentale, e Houzhuang, provincia dello Shaanxi, plateau di loess centrale), sono stati raccolti ad intervalli di 5 - 10 cm. Lo scopo era determinare la differenza tra le proprietà magnetiche in questi due profili di loess, formati sotto l'influenza di condizioni paleoclimatiche differenti, e determinare l'impatto delle variazioni globali del clima, a lungo e corto termine, nel plateau di loess cinese. Xiagaoyuan è situato in una regione molto secca, semi desertica, con precipitazioni annuali medie attorno ai 300 mm; la sezione presa in considerazione raggiunge una profondità di 23 m ed è composta generalmente da loess inalterato: si è potuto identificare solo due paleosuoli, oltre al suolo olocenico. Il clima a Houzhuang è più caldo ed umido con precipitazioni annuali medie attorno ai 600 mm. Questa sezione, campionata fino ad una profondità di 20 m, è stata soggetta a processi pedogenetici molto pronunciati ed è composta da paleosuoli e loess disgregati. I paleosuoli comprendono tre complessi pedogenetici formati durante periodi interglaciali e tre paleosuoli formati durante periodi interstadiali. Si è ottenuta una suddivisione cronostratigrafica correlando le variazioni di suscettività con le variazioni dell'isotopo di ossigeno calibrate su base astronomica. Si è stabilita un'età massima di circa 130'000 anni a Xiagaoyuan e di circa 250'000 anni a Houzhuang. A Xiagaoyuan l'evento geomagnetico di Blake non è stato individuato, probabilmente a causa del basso tasso di sedimentazione. La componente ferromagnetica è simile in entrambi i profili e il segnale magnetico è causato dalla presenza di magnetite e magemite. Importanti differenze tra i due profili sono espresse dalla differenza di intensità del loro segnale magnetico. L'intensità generalmente più elevata del segnale magnetico nelle coltri di loess di Houzhuang rispetto agli strati formati durante lo stesso periodo a Xiagaoyuan è indicativo della maggiore attività pedogenetica a Houzhuang, non solo durante periodi interglaciali, ma anche durante i periodi glaciali.

Le differenze regionali tra questi due profili sono enfatizzate dai risultati ottenuti dai campioni frazionati. Una crescita dell'attività pedogenetica è accompagnata da un aumento della componente ferromagnetica più fine. Questo è il risultato della produzione *in situ* di nuovi minerali magnetici e non è dovuto ad una variazione della componente ferromagnetica nel materiale originario dal quale il loess si è formato. Un'ulteriore differenza tra i due profili, legata alle differenti condizioni paleoclimatiche in queste due regioni, si esprime attraverso un tasso di sedimentazione molto più elevato a Xiagaoyuan rispetto a Houzhuang. Infatti l'orizzonte corrispondente alla transizione tra lo stadio isotopico 5 dell'ossigeno e lo stadio 6 si trova ad una profondità di 23 m a Xiagaoyuan (tasso di sedimentazione medio: 17.7 cm/ka) e di 7.5 m a Houzhuang (tasso di sedimentazione medio: 5.8 cm/ka). L'elevata risoluzione a Xiagaoyuan permette di correlare in modo dettagliato i dati magnetici e sedimentologici con le variazioni dell'isotopo dell'ossigeno ottenute da carote di sedimenti marini e da carote di ghiaccio durante gli ultimi ~130'000 anni. I substadi 5a-e dell'isotopo dell'ossigeno possono essere correlati con la suscettività del complesso pedogenico S_1 (S_1S_1 , S_1L_1 , S_1S_2 , S_1L_2 e S_1S_3). Questa operazione non è possibile a Houzhuang a causa dell'elevato grado di pedogenesi che caratterizzò l'intero ultimo stadio interglaciale. Le variazioni climatiche ad alta frequenza (cicli di Bond, eventi di Heinrich), osservate nella carota di ghiaccio del programma GRIP, possono essere correlate con le variazioni della suscettività in funzione della frequenza nei livelli con pedogenesi incipiente compresi nello strato L_1 a Xiagaoyuan.

La concentrazione di ^{10}Be è stata misurata in 64 campioni di roccia totale e 36 frazioni ottenute da quattro campioni di roccia totale (un campione di loess e uno di paleosuolo per entrambe le sezioni cinesi). I campioni provengono dai complessi pedogenici S_1 , e rappresentano l'intervallo di tempo corrispondente all'ultimo interglaciale compreso tra 130'000 e 70'000 anni. Si è stabilita una correlazione inversa tra granulometria e concentrazione di ^{10}Be . Le misure non evidenziano una correlazione lineare tra la suscettività e la concentrazione di ^{10}Be . A Xiagaoyuan la concentrazione di ^{10}Be riflette maggiormente le variazioni granulometriche piuttosto che quelle di suscettività. Le analisi granulometriche hanno rilevato che il valore della granulometria media (*median grain size*) non sia sufficientemente indicativo del tipo di distribuzione. Oltre a ciò, questo valore potrebbe non corrispondere al valore della granulometria media del materiale originale dal quale il loess si è formato. In futuro, un modello per le paleoprecipitazioni

basato sui flussi di ^{10}Be e di suscettività dovrà essere sviluppato determinando innanzitutto le variazioni del flusso atmosferico di ^{10}Be . Quest'ultimo parametro dipende dalle variazioni di intensità del campo magnetico terrestre.

PUBLICATIONS

PART II, Chapter 1

Sartori, M., Forster, T., Heller, F., Borkovec, M. and Hammann, J., Magnetic properties of different grain size fractions in loess sediments from Paks (Hungary), *Geol. Carpatica*, 47, 177-178, 1996.

Sartori, M., Heller, F., Forster, T., Borkovec, M., Hammann, J. and Vincent, E., Magnetic properties of loess grain size fractions from the section at Paks (Hungary), *Phys. Earth Planet. Inter.*, 116, 53-64, 1999.

PART II, Chapter 2

Heller, F., **Sartori, M.**, Hus, J., Geeraerts, R., Hailwood, E., Montgomery, P., Gendler, T., Bagin, V., Virina, E. and Tsatskin, A., Paleoenvironmental change documented by magnetic investigations at Roxolany, A loess type section near Odessa (Ukraine), *Geol. Carpatica*, 47, 208-209, 1996.

Tsatskin, A., Heller, F., Hailwood, E. A., Gendler, T. S., Hus, J., Montgomery, P., **Sartori, M.** and Virina, E. I., Pedosedimentary division, rock magnetism and chronology of the loess/paleosol sequence at Roxolany (Ukraine), *Palaeogeogr. Palaeoclim. Palaeoec.*, 143, 111-133, 1998.

PART I

INTRODUCTION

OBJECTIVES

Reconstruction of the Quaternary climate is an important constraint for the development of climate models that lead to a better understanding of past and present and prediction of future, climate development. In the last decade climate change has become a globally-discussed matter, and was the central theme of several international conferences (Rio, 1992; Kyoto, 1997; Buenos Aires, 1998; Bonn, 1999). The analysis of the marine and ice paleoclimatic records has demonstrated that in addition to the control by the Earth's orbital variations, the climatic system went rapid variations during the last glacial and interglacial periods (Dansgaard et al., 1993, Taylor et al., 1993).

Compared with the climate information preserved in marine sediments and in the polar ice caps, the continental paleoclimatic record is much more fragmentary. Terrestrial high-resolution paleoclimate archives of long duration, however, have been found in the Quaternary loess sediments which cover wide continental areas especially on the northern hemisphere. The loess deposits typically consist of alternating loess beds, which formed by dust deposition under cold-arid climate conditions, and paleosol layers, which developed during warm-humid periods. The evidence for these climate changes comes from paleontological studies which observe changing mollusc assemblages (Lozek, 1964; Rousseau and Puisségur, 1990), from calcium carbonate depletion and $\text{Fe}_2\text{O}_3/\text{FeO}$ increase in paleosols (Liu et al., 1985), from clay mineral enrichment by weathering processes in paleosols and investigations of micromorphological structures of the paleosols (Kukla, 1977; Bronger and Heinkele, 1989, 1989a; Fedoroff and Courty, 1987, 1989) and from rock magnetic investigation (Heller and Liu, 1984, 1986; Kukla et al., 1988; Zhou et al., 1990; Maher and Thompson, 1992; Evans and Heller, 1994; Chen et al., 1997; Fang et al., 1999).

At first, paleomagnetic investigations were used only for dating the loess sediments. They established that the oldest of these windblown sediments started to accumulate some 2.6 Ma ago close to the Gauss/Matuyama chron boundary (Heller and Liu, 1982). It was also demonstrated that the susceptibility time series obtained from localities in Alaska, China and Central Asia correlate remarkably well with the oxygen isotope signal, and yield spectral power estimates in agreement with those predicted by the astronomical (Milankovitch) theory of ice ages (Heller and Liu, 1986; Begét and Hawkins, 1989; Wang et al., 1990; Forster et al., 1994). The susceptibility variations now serve as a dating tool on a high resolution timescale in long, continuous loess sections.

The potential of rock magnetic characteristics of loess as paleoclimatic proxies, combined with sedimentological and geochemical data, is attracting more and more attention in the Earth sciences (Heller et al., 1993; Beer et al., 1993; Maher et al., 1994; Liu et al., 1995; Chen et al., 1997). In peridesertic midlatitude regions, low field susceptibility and other magnetic parameters are enhanced in paleosols and weathered loess beds, most probably due to *in situ* formation of new very fine grained (superparamagnetic) ferrimagnetic minerals (Zhou et al., 1990; Maher and Thompson, 1991; Liu et al., 1995). Composition and grain size distribution of these minerals and their modes of formation (organic by bacterial activity or inorganic by direct precipitation from mobilized iron complexes) are being investigated with the goal of quantitatively correlating loess properties and paleoclimatic factors such as rainfall and temperature.

This work aims at improving our understanding of the magnetism-paleoclimate relations in loess materials and presents results from four different loess/paleosol sequences sampled in Europe (Hungary, Ukraine) and in China (western and central loess plateau). Magnetic, sedimentologic and geochemical properties have been measured in order:

- To provide a time frame for the deposition history using paleomagnetic polarity stratigraphy and magnetic susceptibility correlative to the marine oxygen isotopic timescale.
- To establish a relationship between the climatic significance of the lithologic characteristics and the loess/paleosol magnetic properties.
- To develop reliable techniques for detection and isolation of the magnetic minerals responsible for the enhancement observed in paleosols and weathered loesses.
- To establish a link between geochemical and magnetic properties in order to identify their potential for quantitative climate reconstruction.
- To correlate the loess paleoclimatic time series with records of abrupt and short-lived climatic changes from the North Atlantic region and elsewhere, with the intention of contributing to assessing the impact of global climatic changes.

Chapter 1
***LOESS DEPOSITS AND
PALEOCLIMATE***

1.1 Loess, a wind blown sediment

Loess is a German word derived probably from the word “losch” which was first introduced into the scientific literature by the German tax inspector and amateur geologist Karl Caesar von Leonard to indicate loose and unconsolidated sedimentary deposits along the Rhine Valley near Heidelberg (Kirchenheimer, 1969). The term has become common in earth sciences since the middle of the 19th century to indicate wind-blown Quaternary silt deposits (Lyell, 1847; Virlet d’ Aoust, 1857; von Richthofen, 1882; Russell, 1944).

Loess and loess-like deposits cover ~10% of the land surface of the earth. Semi-arid and temperate climates are the ideal conditions for loess deposits to form on plains (Pampean Plain, Russian Plain), on plateaus (Chinese loess plateau) and along river basins (Danubian Basin, middle Rhine Basin, Mississippi Basin, middle Yellow River Basin) which represent the typical geographical zones for loess deposition (Fig. 1). Typical loess may not easily be distinguished from loess-like deposits. In order to define typical loess, a list of criteria is described in this chapter, for which the articles of Pécsi (1991), Osipov and Sokolov (1995) and Catt (1995) have been taken as main references.

1.1.1 Grain size and mineral composition

Typical loess is well sorted, in contrast to the irregular grain size distributions in loess-like deposits. Generally, 50 - 70% of the loess volume are silt grains of 10-50 μm diameter. Quartz (40 -60%), feldspars (5-20%), carbonates, calcite and dolomite (2-25%), micas and chlorite (4-10%) and heavy minerals (1-6%) predominate in this grain size. The coarser fractions (medium sand fractions) consist mainly of quartz. In the pelitic fractions (2-10 μm), up to 50% of clay minerals occur, such as illite (10-30%), montmorillonite (5-15%), kaolinite (1-5%), chlorite (2-10%) and vermiculite (1-2%). In the coarse (0.6-2 μm) and medium-sized clays (0.2-0.6 μm) illite dominates (15-35%). In the fine clays (< 0.2 μm) we find mostly montmorillonite-smectite (15-50%). In addition, there are small amounts of minerals like pyrite, iron-oxides or -hydroxides and aluminium-hydroxides (0.2-3%). The allogenic minerals, such as quartz, feldspars and mica, can give information about the origin and the source of the loess-forming dust.

1.1.2 Carbonate content

A very important characteristic of loess is the presence of carbonates because of their role in the characterization of the loess texture. Two main types of carbonates are present: the primary carbonates, formed by carbonate particles (dolomite and calcite) which were transported with the rest of the loess-forming material, and secondary carbonates, which come into the loess by the flow and stagnation of hydrocarbon-bearing groundwater, precipitation, by weathering of calcareous shells and the presence of microorganisms. Secondary carbonate can also form chemically from CO_2 present in soils and groundwater and the release of calcium during weathering of anorthite - $\text{Ca}[\text{Al}_2\text{Si}_2\text{O}_8]$.

1.1.3 Lithological and structural properties of loess

Grain size, clay and carbonate content, as well as the porosity and cohesion in loess characterize the lithological properties of loess deposits. Typical loess is pale yellow. This is mainly due to limonite ($\text{Fe}_2\text{O}_3 \cdot n\text{H}_2\text{O}$) which is made of different amorphous iron hydroxides. The main components are goethite ($\alpha\text{-FeOOH}$), lepidocrocite ($\gamma\text{-FeOOH}$) and non-crystalline ironhydroxide. Its bright walnut yellow color is responsible for the pale yellow coloration. Limonite can dehydrate easily to hematite (Fe_2O_3), which is dark red colored (Mottana et al., 1982). Typical pristine windblown loess is not stratified, e.g. the grains have no preferred orientation in a specific horizon. Color, grain size and intercalation of loess layers with buried soils or sandy loess determine the stratigraphic units in loess sequences.

The cohesion of the sediment and thus its collapsibility is controlled by external (climate) and internal factors (mineral composition, structure and loess natural water content) (Osipov and Sokolov, 1995). Regarding the mineral composition, a correlation between increase of clay content and decrease of loess collapsibility has been observed. An important role is played by the microstructure, which is determined by primary grain-globules and clay-dusty aggregates. Grainy structure is typical for sandy loesses, which possess a high collapsibility. On the other hand, an increase of clay content (with a structure changing from grainy to aggregative) diminishes the collapsibility.

Porosity is another factor controlling collapsibility of loess. Three main types of

pores are found in loess: macropores (100-500 μm), intergrain and interaggregate pores (8-100 μm) and intra-aggregate pores ($< 8 \mu\text{m}$). Intergrain and interaggregate pores, with a total volume varying from 15 to 28%, and the intra-aggregate pores, with a total volume varying from 18 to 25%, are dominant. The intergrain and interaggregate pores play the most important role in loess collapsibility (Lorraine, 1971; in Osipov and Sokolov, 1995). Several factors are responsible for the pore structure in loess: organic matter, carbonate content (in carbonate free loess loam the porosity sinks from 45-60%, which is the value for typical loess, down to 20%, representing the shift from a grainy to an aggregative structure), age of the horizon (porosity decreases with time) and precipitation or artificial irrigation (porosity decrease).

Molecular (which is the weakest), capillary, ion-electrostatic and chemical forces, or structural bonds, are responsible for the cohesion of loess sediments (Osipov and Sokolov, 1995). The most important are the ionic-electrostatic bounds, which exist inside the crystals of laminated silicates, providing strong bonds between negatively charged structural layers through interlayered cations. These forces can act also between separate clay particles, forming strong ion-electrostatic contact. Chemical bonds are also strong, provided by the presence of salts (chlorite, gypsum and calcite) and sesquioxides of iron and aluminium. The water content plays an important role by controlling the strength of the structural bonds. With increasing water content, ionic-electrostatic and molecular bonds weaken faster than capillary bonds. If normal water saturation is exceeded, the capillary bonds are destroyed causing loess collapse. Water content, or moisture, is around 14-22% in loess, and is controlled by environmental conditions (moisture changes seasonally in the upper 1-3 m and reaches a maximum at 10-15 m depth), grain size and porosity. Study of collapsibility of loess, of its microstructure and physico-mechanical properties plays an important role in regions where loess covers large areas with a farming based economy, such as in China or Russia (Derbyshire et al., 1995; Osipov and Sokolov, 1995; Derbyshire et al., 1991; Wang et al., 1987).

1.1.4 Soils and paleosols

The formation of loess deposits is related to the glacial cycles in the Pleistocene. Loess dusts are transported by wind mainly during glacial periods, undergoing several abrasion and deposition processes, acquiring slowly the characteristics of a sediment as

described above. During warmer (interglacial) periods, loess is affected by new climatic conditions: higher temperature, higher precipitation, increase of chemical and biological activity on the surface and progressive transformation (pedogenesis) at depth. Formation of soils resulting from the particular climatic conditions in the region occurs. Loess deposits, such as those in the Chinese loess plateau, are interlayered with soil bodies representing the shift from cold and dry to warm and wet climatic conditions. These soil bodies are called paleosols (Ruhe, 1956).

A soil is defined as “a three-dimensional body on the surface of the earth composed of minerals and/or organic material, air and water, and formed by the impact of environmental factors acting on parent materials over a period of time to produce a sequence of horizons” (INQUA Commission 6, in Catt, 1995). Soil formation in unconsolidated sediments is controlled by the following processes: chemical weathering (decalcification, release of Fe and Al to form oxides or hydrated oxides), downward leaching of soluble material, precipitation of soluble salts in near-surface horizons because of evaporation in arid environments, decomposition and incorporation of organic material, disturbance due to biological activity, eluviation of clay and subsequent illuviation in subsoil horizons and gleying (reduction of ferric minerals to ferrous compounds) in waterlogged conditions (Birkeland, 1984). Although in loess sequences the major interest is focused on reconstructing the climatic conditions present during soil formation, it has to be pointed out that paleosol features can be modified due to other processes occurring during or a long time after the soil formation period (Catt, 1990). The original soil structure can be modified, for example, shortly after burial and pedocomplexes can form (new forming soil welded to an underlying buried soil; Ruhe and Olson, 1980). If the soil is buried deeper and pedocomplex formation is not possible anymore, diagenetic processes can change the characteristics of the soil: percolating water can reverse the effect of pedogenesis (redeposition of carbonate in decalcified horizons, change in pH, removing humic components from the A horizons). Another important diagenetic process in buried soils is dehydration, in contrast to the hydration processes observed during pedogenesis: Goethite and ferrihydrite (hydrated iron oxides) may dehydrate to hematite (Catt, 1995).

Micromorphologic studies, such as the study of microtextures, the presence of primary or secondary calcite and its modified forms, the characteristics of clay accumulation horizons, hydromorphic reactions, revealing postpedogenetic processes after burial are of great importance for obtaining reliable information on the nature and intensity of

weathering processes in loess (Bronger and Heinkele, 1989).

1.1.4.1 Climatic significance of soils and paleosols

The paleoclimatic significance of paleosols can be appreciated by understanding the processes that control soil formation. These factors are climate, presence of organisms, relief, parent material and time (Jenny, 1980). Several attempts to obtain climofunctions have been performed by taking one factor as variable and considering the others constant (Yaalon, 1975). In using Jenny's model the best results have been obtained on Holocene soils (Retallack, 1994), whereas in paleosols this quantitative approach may lead to large errors, because of changes occurring after burial.

Climofunctions may be useful climate approximations in areas where most of the soil forming factors behave uniformly, such as in the Chinese loess plateau. Even so, difficulties in using climofunctions for Holocene soils in loess deposits have been observed by Johnson et al. (1990). These authors observed gleying processes (reduction of iron to the ferrous state, typical in water saturated soil; Scheffer and Schachtschabel, 1998) above the B₁ horizon (weathered subsoil horizon with accumulation of silicate clays) in a manner independent of the soil state factors, thereby complicating the construction of climofunctions. Climofunctions for SiO₂/Fe₂O₃, for example, are useful in soils formed on crystalline igneous rocks, but cannot be used for aeolian sediments, such as loess, because the initial content of Fe₂O₃ is uncertain. Furthermore, variations by more than 25% of different soil properties have been observed over short distances (Wilding and Drees, 1983), emphasizing the difficulties in modeling reliable climofunctions. In addition, the properties of paleosols used for climofunctions may be changed upon burial. The model proposed by Jenny (1980) for recent soils cannot be applied to buried soils due to 1) the increase of the interaction between the different soil forming factors and 2) the fact that buried soils are generally polygenetic pedocomplexes and thus have a complex combination of soil state factors.

1.2 World wide loess distribution

1.2.1 Introduction

Loess deposits are the most widespread sediments on the land surface of the earth. Loess is present in both the southern and northern hemisphere, but the major sequences are found on the northern hemisphere in China, in Central Asia and Eastern Europe. Sedimentation of loess occurs in the temperate zones and at the margins of semi-arid deserts along the so-called “world wheat belt” (Liu et al., 1985). In China the major loess deposit is the central loess plateau, in the middle reaches of the Yellow River, where loess can reach a thickness > 250 m. The source material, originating from the arid basins in Qinghai province (Junggar, Tarim and Qaidam basins) was transported by strong winds blowing eastward during the Pleistocene glacial periods.



Figure 1: Worldwide loess distribution (modified after Pye, 1987).

Loess deposits in Central Asia, particularly in the Tajik depression reach a thickness > 200 m. In Europe, the thickest loess deposits (> 60 m) can be found in the Danube basin in Austria and Hungary, as well as in the Czech Republic. Loess occurs frequently in Rumania, Bulgaria, Moldavia and the Ukraine (> 40 m). In West and Central Europe loess deposits are present in Poland, Germany, France and Belgium. In North America, the most important loess deposits are situated along the Mississippi River, but are also found in Alaska. The Pampean region in South America is covered by loess.

1.2.2 Loess deposits in Europe

Loess deposits in Europe are related to the glaciations during the Pleistocene, both in the Brunhes and Matuyama magnetic polarity chrons. They are found in the periglacial realm between the Alpine glaciers and the Scandinavian ice sheets and started to accumulate ca. 1 Ma ago: the distribution of the European loess deposits is determined by the maximal extension of the ice sheets during the main glaciations recorded of Brunhes age (Kukla, 1975): they correspond to the Weichsel advance (20 ka), the Warthe advance (140 ka), the Saale advance (350 ka) and the Elster advance (550 ka). The northern limit of the loess cover is found in the South Polish uplands and in the Carpathian and Sudetes forelands and intramontaneous basins, where the main Polish loess sediments are found (Hohl, 1980). In this region loess deposits can reach thicknesses of 20-30 m with reported TL ages below ~500 ka (Nawrocki et al., 1996; Maruszczak and Nawrocki, 1991), indicating that loess accumulation began after the Matuyama-Brunhes (M/B) reversal.

In the southern part of Europe, the border of the periglacial area was delimited by the Alpine glaciers that reached the Lake of Constance and the region around Munich, determining the south-western limit of the loess deposition area. Loess is present also in Central and South Germany, especially along the lower Rhine Valley. Six to seven loess/paleosol bodies at Kärlich near Bonn have been interpreted paleomagnetically to have formed during the Brunhes epoch, with the sedimentation starting just after the B/M boundary (Brunnacker and Bönigk, 1976). In a recent paleomagnetic study, Reinders and Hambach (1995) investigated a 1.5 m thick loess sequence in Tönchesberg near Koblenz, and found negative inclinations of the natural remanent magnetization in the lower portion of the sequence. With the support of TL dating (Zöller, 1991) they were interpreted as evidence of the Blake polarity event (~118-128 ka; Jacobs, 1994).

Loess is found also in Normandy (Lautridou, 1979). Preliminary paleomagnetic measurements revealed reversed polarities for the lower part of the section, where the oldest loess horizon is considered to be either of Early Pleistocene or of the beginning of the Cromerian. In Achenheim (Alsace, France), Rousseau and Puisségur (1990) determined a chronostratigraphy using TL dating and mollusc fauna dating: The section has a thickness of ~53 m, where the oldest part (Lower Old Loess - Achenheim IV) overlies a river terrace. TL dating gives an age of 0.27 Ma (\pm 36 ka) for a layer at 35 m, which corresponds to the Middle Older Loess (Achenheim III).

The thickest European loess/paleosol sequences are found in eastern Europe (Czech Republic, Hungary, Rumania, Bulgaria, Ukraine and Precaucasus region). In the deposits at Red Hill (Cervený Kopec, Kukla, 1975) and at Krems, Austria, the M/B boundary was found below pedocomplex 9, at a depth of 65 m (Koci, 1990). The Jaramillo and Olduvai subchron have been identified in the lowermost few meters of those two sections. Hence sedimentation of loess in this region started at least just before the Olduvai subchron (1.76-1.96 Ma). A different interpretation was given by Forster et al. (1996). They argued that two sections at Red Hill which were originally considered to belong to two different stratigraphic levels are, in fact, synchronous. Their new interpretation gives a maximum age for the section at Cervený Kopec of ~0.8 Ma.

In the middle Danube basin loess deposits can reach a thickness of 60 m and more. At Paks, Hungary, the M/B boundary was found at a depth of ~44 m (Pécsi et al., 1995), in the Old Loess L₅ above the underlying paleosol PD₂, confirming the result obtained by Márton (1979). In Dunavöldvár the M/B boundary was found at ~42 m, at the same stratigraphic level as the one in Paks. It is suggested that sedimentation of the “Old” Loess along the Danube started just after the Jaramillo subchron (0.915-1.01 Ma).

In the Novaya Etulia loess/paleosol sequence (Moldova), which attains a thickness of 24 m, the B/M boundary was found at a depth of 14.5 m, below a succession of nine paleosols (Faustoff et al., 1986; Spassov, 1998). In the reversed polarity zone (from 14.5 m to 24 m) the Jaramillo and Olduvai subchrons have been detected by Russian scientists but not by Spassov (1998). In Roxolany (Ukraine) the loess/paleosol sequence on the VIII Dniestr terrace reaches a thickness of ~50 m. The M/B boundary was detected at a depth of ~35 m, between pedocomplexes PK₆ and PK₇ (Tsatskin et al., 1998). The loess/paleosol series in the foreland hills of the Precaucasus region show sedimentation rates similar to the ones observed in Central Asia and the Chinese loess/paleosol series. The Otkaznoe section near Zelenokumsk (43.5° E, 44.2° N) has a total thickness of 140 m (Virina et al., 1990). The M/B boundary was found at a depth of 72 m. The Brunhes epoch is characterized by six loess horizons interlayered with five pedocomplexes, and the Matuyama epoch by three loesses interbedded with three soils. The Jaramillo subchron (between 94 m and 104 m) was identified as the oldest polarity zone in the sequence.

1.2.3 The Chinese Loess Plateau

1.2.3.1 Introduction

The Chinese loess plateau occupies a contiguous loess area of 440'000 km² (Liu et al., 1985). If all the major loess outcrops are considered, the total area covered by loess in China amounts to about 1'000'000 km². This corresponds to 10% of the surface of China and 20% of the tillable land. Loess thus plays a very important role in the economy of China. Also the cultural development in China is related to the loess plateau, confirmed by findings which report the presence of paleolithic and neolithic cultures. In these regions the first extensive dry farming took place (He, 1969, in Liu et al., 1985).

LOESS DISTRIBUTION IN CHINA

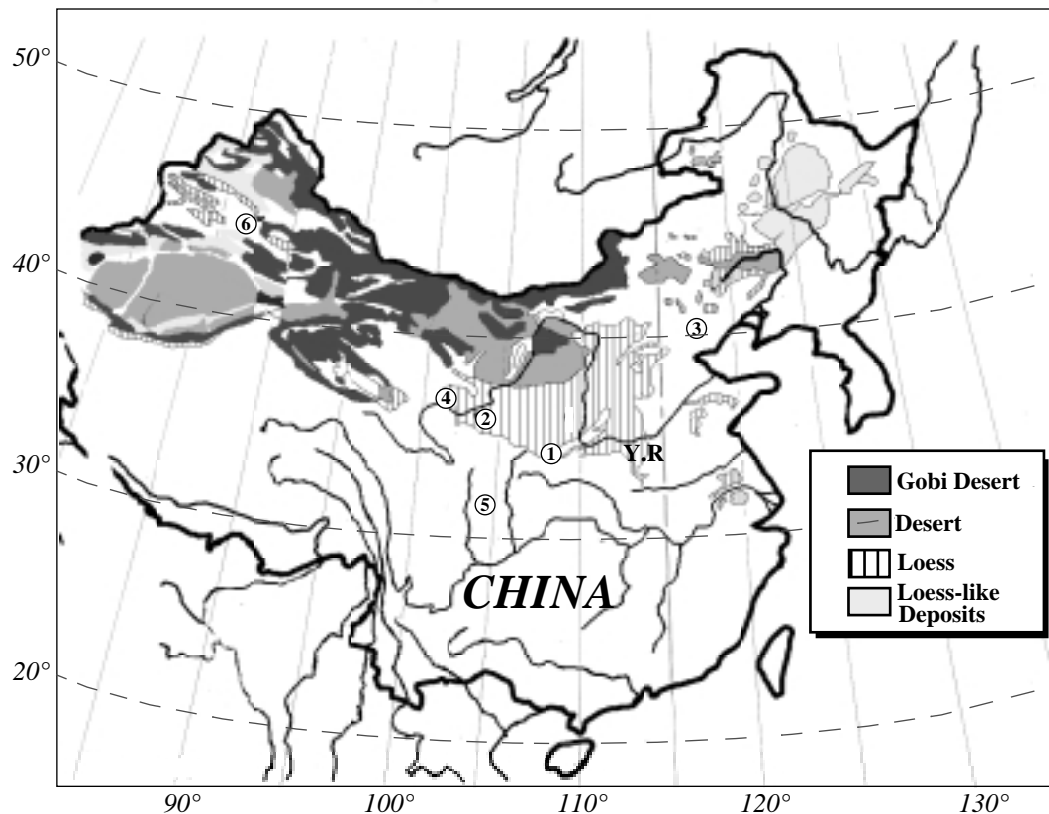


Figure 2: Sketch map showing the distribution of loess and loess-like deposits, desert and Gobi desert in China. The localities indicated are Xian (1), Lanzhou (2), Beijing (3), Xining (4), Chengdu (5), Urumqi (6); The Chinese Loess Plateau is located on the middle reaches of the Yellow River (Y.R.). Modified after Liu et al. (1987).

Several empires developed in the loess regions, from the Shang and Zhou to the Tang and Song dynasties, contributing to the transformation of the Chinese loess plateau into an important cultural area. Loess is an ideal substrate for farmland, being homogeneous, porous and loose. On the other hand it is strongly affected by erosion, which loads each year $\sim 13 \times 10^6$ tons of silt into the Yellow River.

Understanding its distribution, age, physico-mechanical properties, formation and evolution is thus of scientific and economic importance.

1.2.3.2 Regional distribution of loess

The source regions of the loess forming material may be identified by the analysis of the minerals in the loess sediments. Loess is commonly characterized by a predominance of silt-sized particles (more than 50% are quartz grains) and enrichment of carbonate (see 1.1.1). Closer inspection of quartz grains shows structures typical of mechanical fragmentation, such as conchoidal fractures, sharp edges, ruptures (Smalley, 1991). Glacial grinding is one of the mechanisms producing silt-sized quartz grains. Another process responsible for their formation takes place in deserts, due to great temperature differences and to the presence of soluble salts (Na_2SO_4) forming silt-sized quartz grains from coarser grains. It is thus possible to identify the source of the loess forming material. The deserts to the northwest of the Chinese loess plateau are supposed to be the original source region. The presence of CaCO_3 coated silt-sized quartz and feldspars grains in deserts supports this hypothesis (Liu et al., 1985).

The Chinese loess plateau has been accumulated by aeolian material transported from deserts (there are other minor sources, such as marine sediments or glacial deposits). Study of a recent dust fall in Beijing confirmed the aeolian origin of loess deposits (Liu et al., 1982). The strong relationship between origin and distribution of the Chinese loess is emphasized by the regional distribution of the grain sizes, with coarser grain sizes in the northwest near the source region (sandy loess) and finer grain sizes to the southeast (clayey loess). Figure 2 shows the distribution of loess and loess-like deposits together with deserts. The most complete loess sequences are found along the middle reaches of the Yellow River, between 34° - 40° N and 100° - 115° E. They can reach a thickness of more than 250 m (Wang et al., 1984). The loess belt is divided into three subregions, the northwestern inland basin (deposits in Xinjiang, Qinghai and northwest-

ern part of Gansu province), the central loess plateau (middle reaches of the Yellow River in Gansu and Shaanxi) and the eastern piedmont hills and plains (Shandong).

1.2.3.3 Lithostratigraphy

Red clay is found at the base of the loess deposits (Ding et al., 1998). These deposits are Late Miocene to Early Pliocene in age and overly a Pre-Tertiary basement. They consist of red-brown silty non-calcareous clays which show evidence of pedogenesis in the upper part (Kukla, 1989, Bronger and Heinkele, 1989) and are considered to be partly of fluviolacustrine origin (Kukla, 1989). Recent work by Donghuai et al. (1998) on a sequence in Pingliang (35°04'N, 107°39'E) revealed a 126 m thick Red Clay formation. The aeolian origin of the Red Clay is pointed out and related to dust accumulation that started some 7.2 Ma ago as a consequence of the uplift of the Tibetan Plateau.

The Wucheng loess (Early Pleistocene) is the oldest loess formation *sensu stricto* following the Red Clay. Deposition started at about 2.45 Ma (Heller and Liu, 1982). It is interbedded with calcareous nodule beds and fossil soils with a mineralogical composition similar to that of the Red Clay. The Wucheng loess is characterized by a higher content of silt, fine sand and calcium carbonate with respect to the paleosols. Divided into four soil units (W_{S-1} - W_{S-4}) and four loess units (W_{L-1} - W_{L-4}) (Liu et al., 1985), the Wucheng loess shows several subzones in each soil and loess unit, although soils dominate the whole Wucheng loess: up to 17 paleosols units (from S_{16} to S_{32}) are present in the Wucheng loess.

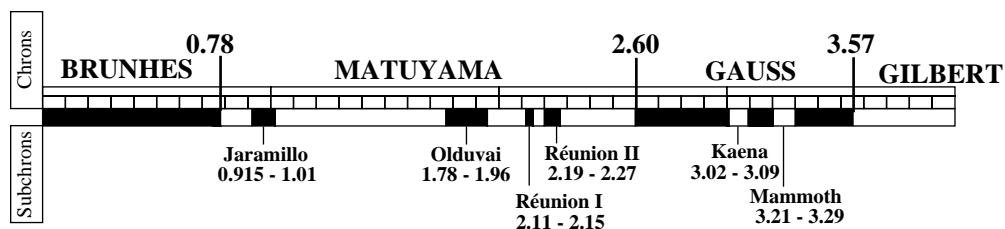


Figure 3: Geomagnetic polarity timescale for the last 4 Ma from Gilbert to Brunhes. Age of reversals after Spell and McDougall (1992) and McDougall et al. (1992).

The overlying Lishi loess (Early to Middle Pleistocene) is divided into the Lower Lishi loess (from S_5 to S_{14}) and Upper Lishi loess (from S_1 to S_4). Because of its thickness (4 - 6 m) the paleosol S_5 is used as marker to distinguish the Upper from the Lower Lishi loess: in the latter the loess beds are less developed and more dark colored than in the Upper Lishi loess, thus being similar to the Wucheng loess, whereas the paleosols are similar to those of the Upper Lishi loess. The Malan loess (Late Pleistocene) on top of the whole sequence is represented by the loess layer L_1 and can reach a thickness of 10 - 12 m in the central loess plateau. Porous and loosely cemented, the Malan loess has similar characteristics as the underlying upper part of the Lishi loess (Liu et al., 1985).

1.2.3.4 Magnetostratigraphy and the age of loess sedimentation

During the last 15-20 years, magnetostratigraphic studies in different loess/paleosol sequences have turned out to be the only realistic dating tool.

Correlation of the polarity patterns observed in the loess/paleosol sequences with the well-established geomagnetic polarity timescale (Cande and Kent, 1992) allows the start of loess deposition to be estimated. The chrons observed in the Chinese loess deposits are the Brunhes (normal polarity), Matuyama (reversed) and Gauss (normal). Well documented subchrons have also been observed (Jaramillo, Olduvai), as well as subchrons the occurrence of which is questionable (Blake, Cobb Mountain, Gilsa, Réunion).

The first complete magnetic polarity zonation was obtained from the 136 m thick loess/paleosol sequence in Luochuan (109.2°E, 35.8°N, Fig. 4), Shaanxi province (Heller and Liu, 1982, 1984; Torii et al., 1984). The M/B boundary was found in the Lishi loess at a depth of 53.05 m in paleosol S_8 . The Jaramillo subchron was observed between 67.30 m (loess L_{10}) and 72.50 m (paleosol S_{11}) and the Olduvai subchron between 107.40 m and 117.70 m (in the Wucheng loess W_{S-2}) (Heller and Liu, 1982). A starting age of 2.45 Ma for the loess sedimentation was derived. A further step in determining the beginning of loess sedimentation was the observation in Luochuan of the Gauss/Matuyama (2.60 Ma) transition in the upper part of the Red Clay underlying the Wucheng loess in Luochuan (Heller and Liu, 1984).

Further paleomagnetic studies broadly confirmed the observations made in Luochuan. A close parallel to the Luochuan section was found at the 159 m thick Baoji section (107.1°E, 34.4°N, Fig. 4), with the boundaries of the Matuyama chron at 58.5 m (loess L_8) and 157.8 m (loess L_{33}) respectively, the Jaramillo subchron between 72.0 m (loess

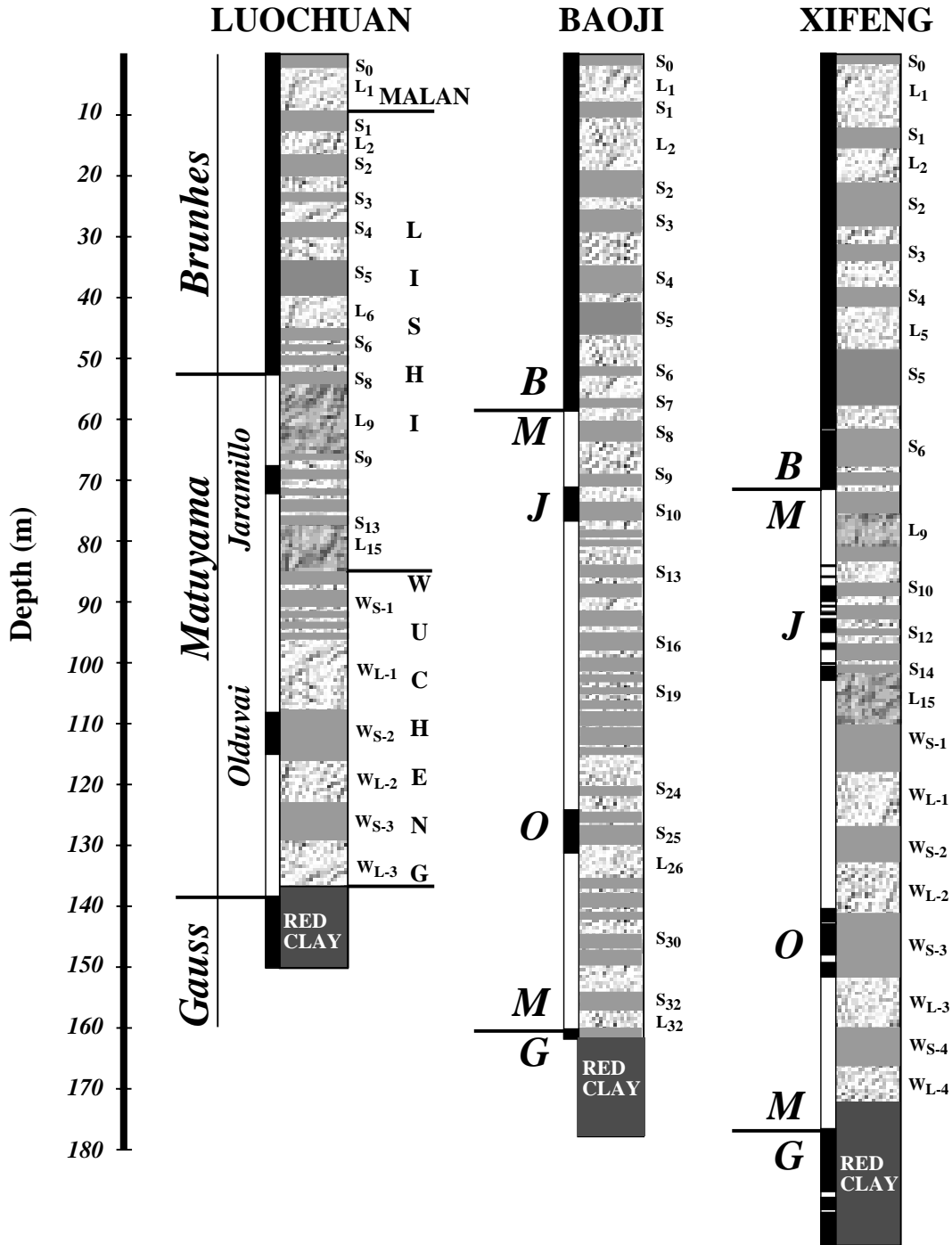


Figure 4: Magnetostratigraphy and lithology of the loess/paleosol sequences at Luochuan (Heller and Liu, 1982, 1984), Baoji (Rutter et al., 1990) and Xifeng (Liu et al., 1987, 1988). L indicates loess layers, S paleosols (S₀: Holocene soil). W indicates paleosols from the so-called Wucheng loess.

L₁₀) and 76.4 m (paleosol S₁₁) and the Olduvai subchron between 125.5 m (loess L₂₅) and 131.5 m (loess L₂₇) (Rutter et al., 1990). At Xifeng (Fig. 2, 107.6°E, 35.7°N), the magnetostratigraphy for the ~170 m thick loess/paleosol sequence (Fig. 4) revealed the boundaries of the Matuyama chron at 71 m (loess L₈) and 180 m (within the uppermost part of the Red Clay), the Olduvai chron between ~140 m (Wucheng W_{L-2}) and ~148 m (Wucheng W_{S-3}) (Liu et al., 1987; 1988). In the 195 m thick loess/Red Clay sequence at Lantian near Xian (109°12'E, 34°12'N) studied by Zheng et al. (1992), the Matuyama chron lies between ~50 m (M/B boundary in loess L₈) and 132 m (G/M boundary in loess L₃₈), 1.5 m above the Red Clay formation. With the Jaramillo subchron (from loess L₉ to loess L₁₅) and the Olduvai subchron (from paleosol S₂₆ to paleosol S₂₉), four other normal polarity subchrons were observed (B/M precursor, Cobb Mountain, Reunion I and II). These studies all suggested a starting age for loess deposition of ~2.5 Ma. The different accumulation rates and paleogeographic characteristics across the loess plateau, as well as the different sampling density and the problems related to laboratory procedures to obtain the characteristic remanent magnetization (ChRM) have to be taken into account to explain the difference in the polarity patterns observed in the Matuyama chron.

A controversy arose with respect to the magnetostratigraphic interpretation of the Jizhoutai loess/paleosol section near Lanzhou, on the Western Loess Plateau. Burbank and Li (1985) deduced a start for loess sedimentation of ~1.3 Ma, arguing that the uplift of the Tibetan Plateau prevented loess formation during the Early Pleistocene. The section is ~330 m thick, 180 m representing the Brunhes epoch and the remaining 150 m the Matuyama, down to ~1.3 Ma. An alternative magnetostratigraphic interpretation, supported by more detailed sampling, was proposed by Rolph et al. (1989). A basal age for the Wucheng loess of ~2.4 Ma was proposed, which is in good agreement with the observations made in Luochuan, which is situated in the central loess plateau. This new interpretation, related to the geomagnetic events recorded in this section, requires highly variable accumulation rates: 3.5 cm/ka from ~2.4 Ma to ~1.7 Ma, 9.3 cm/ka from ~1.7 Ma to ~0.8 Ma and 23.3 cm/ka thereafter. The uplift of the Qinghai-Tibet Plateau during the Pleistocene which had a strong effect on global climate, is thought to be responsible for these differences (Sun and Wu, 1985).

1.2.3.5 Climate evolution and the age of loess sedimentation

Various investigations (Shackleton et al, 1984; Bloemendal and De Menocal, 1989; Dodonov, 1987) document a major global cooling around 2.6-2.4 Ma. The accelerated uplift of the Tibetan Plateau during the Plio-Pleistocene epoch contributed to a global atmospheric reorganization, resulting in a global cooling, favoring loess sedimentation by enhanced wind activity associated with the link between the Siberian anticyclone and the great eastern Asian trough (Zhao and Morgan, 1985; Wang and Li, 1985; Sun and Wu, 1985).

In order to understand the starting age of loess accumulation, the properties of the underlying Red Clay formation and their difference with the overlying loess layers have to be discussed. Pedological and morphological studies of the loess/paleosol and underlying uppermost part of the Red Clay formation at Luochuan were performed by Bronger and Heinkele (1989). They could establish a Late Pliocene origin of the parent material (presence of Late Pliocene fauna) of at least the lower part of the uppermost Red Clay (between ~3-5 m below Wucheng loess W_{L-3}). In this section the Gauss-Matuyama boundary was found 2 m below W_{L-3} (Heller and Liu, 1984).

Ding et al. (1992) studied the Red Clay formation at Baoji, Xifeng and Baicaoyuan. Pedologic morphogenetic studies were interpreted to show evidence for subtropical stable environment with marked seasonal wet-dry cycles in Baoji (with rubefication as typical feature for that climate, Fedoroff, 1966). They estimated a mean rainfall of ~800-900 mm and a mean temperature $> 15^{\circ}\text{C}$. By comparing the pedologic morphogenic features of the L_{33} - L_{32} formation at Baoji (where primary calcite grains were identified) with that of the Holocene soils at Lanzhou (which show a higher degree of weathering), they concluded that the climate was drier (rainfall < 200 mm) and colder (annual mean temperature $< 5^{\circ}\text{C}$) than the present climatic conditions in Lanzhou (rainfall of ~300 mm and annual mean temperature of $\sim 6^{\circ}\text{C}$). This study also suggests that only small climatic oscillations occurred during the time of the Red Clay formation, which formed during warm climatic conditions.

1.2.4 Loess deposits in Central Asia

Bordered on the northeastern side by the Tien Shan (“shan” = mountain) and on the southeastern side by the Pamir mountain range, the Tajik depression contains the most important loess accumulation basins of Central Asia. Loess sedimented during the Pleistocene, reaching a thickness of more than 200 m (Lazarenko, 1984). Liu et al. (1985) pointed out the similar evolutionary history between the loess/paleosol sequences in Central Asia and in the Chinese loess plateau. The loess paleosol sequences of Karamaydan and Chashmanigar - both near Dushanbe (68.5°E, 38.3°N) - are the best studied sections in the Tajik depression. The Karamaydan loess/paleosol sequence is 250 m thick and shows an alternation of 35 loess/paleosol layers. The M/B boundary was found at ~117 m, between pedocomplexes IX and X. The G/M boundary was found in a borehole section at 238 m depth, whereas in the Matuyama chron the Jaramillo (beginning at a depth of ~156 m) and the Olduvai subchron (between ~192 m and ~201 m) have been recognized (Pen'kov and Gamov, 1977).

A later study by Forster and Heller (1994) confirmed the M/B boundary between pedocomplexes IX and X. They sampled the upper ~100 m of a slightly condensed natural outcrop at Karamaidan, covering a time span of < 1 Ma. The M/B boundary at a depth of ~86 m between pedocomplex IX and X can be correlate with the M/B boundary found in the Chinese loess plateau between paleosols S₇ and S₈. Similar results have been obtained in the 174 m thick loess/paleosol sequence of Chashmanigar, where the M/B was found at a depth of ~80 m, again between pedocomplexes IX and X (Dodonov et al., 1991). The Jaramillo (between 97 m and 107 m) and the Olduvai subchron (between ~160 m and ~167 m) were also detected. Other loess/paleosol sequences have been investigated near Tashkent (Dodonov, 1991). The Orkutsai loess/paleosol sequence is ~90 m thick with the M/B boundary found at a depth of ~60 m, between pedocomplexes IX and X.

1.2.5 Loess deposits on the American continents and in New Zealand

The best known loess deposits of the Northamerican continent are found along the Mississippi Valley and in Alaska. In the Gold Hill loess near Fairbanks, a section of ~32 m thickness has been studied (locality 6, 147.9° W, 64.9° N) which contains several radi-

ometrically dated tephra layers. The Kaena (3.02-3.09 Ma) and Mammoth (3.21-3.29 Ma) reversed subchrons have been recognized at depths between ~30 m and ~35 m, indicating a starting age of loess sedimentation > 3 Ma (Westgate et al., 1990).

In South America, major loess/paleosol sequences occur in Argentina along the Rio Paraná basin and in the Pampean region. The section near Balneario Cruz (57.6° W, 38.2° S) south of Mar del Plata, is ~21 m thick and is characterized by a low sedimentation rate as compared to those observed in China or Central Asia (Ruocco, 1989). The G/M and the M/B boundary, as well as the Jaramillo and Olduvai subchrons have been identified in the section. The identification of the M/B boundary is of great importance for the understanding of paleoclimatic and neotectonic processes during the Pleistocene (MacFadden et al., 1983; Nabel, 1993).

The thickness of the loess/paleosol sequences in New Zealand is comparable with the one in Argentina. A thickness of 17.4 m is reported for the loess sequences in the North Island, ~150 km west from Auckland, showing 11 loess beds containing each a soil layer. The presence of tephra layers in the sequence allowed a basal age estimation of ~0.5 Ma (Pillans and Wright, 1990).

1.2.6 Matuyama-Brunhes boundary in loess deposits

The most important polarity change recorded in loess is represented by the Matuyama-Brunhes (M/B) reversal. The M/B boundary was found in loess layer L₈ for all the studied sections in the Chinese loess plateau, except for the Luochuan section, where the M/B boundary was placed in soil S₈ (Heller and Liu, 1982; 1984). In Central Asia the M/B was found between pedocomplexes IX and X (see 1.2.4).

The Luochuan results which differ from the observations made in other sections in China and Central Asia, were explained by Zheng et al. (1992) as a result of insufficient resolution to discriminate the M/B boundary with the Matuyama/Brunhes precursor MBpc (Cao et al., 1985; Clement and Constable, 1991; Hartl and Tauxe, 1996), which they observed in the underlying soil S₈ of the section at Lantian. They argue that by a higher sampling density in Luochuan it should be possible to identify the M/B reversal also in L₈. However, a more detailed magnetostratigraphic study performed on loess layer L₈ of Luochuan and Jixian (Shaanxi Province) showed only normally magnetized

Brunhes/Matuyama boundary

<i>locality</i>	<i>depth(m)</i>	<i>unit</i>
Luochuan (CLP) ¹	53.05	S ₈
Baoji (CLP) ²	58.50	L ₈
Xifeng (CLP) ³	71.00	L ₈
Lantian (CLP) ⁴	~50	L ₈
Pingliang (CLP) ⁵	54.30	L ₈
Xian (CLP) ⁶	~48	L ₈
Weinan (CLP) ⁶	54.30	L ₁₀

Table 1: Brunhes/Matuyama boundary in different locations on the Chinese loess plateau (CLP). The depth and the corresponding unit are defined. With the exception of Luochuan, the M/B boundary is found in a loess layer (L), representing a cold period. This is in contrast with the observations made in oceanic sediment cores (see text).

¹⁾Heller and Liu, 1982, 1984; ²⁾Rutter et al., 1990; ³⁾Liu et al., 1987, 1988;

⁴⁾Zheng et al., 1992; ⁵⁾Sun et al., 1998; ⁶⁾Ding et al., 1990.

samples (Hus and Han, 1992). Zheng et al. (1992) consider the role of the magnetization acquisition mechanism, e.g. the lock-in depth as possible reason for the discrepancies observed on the different stratigraphic position of the M/B boundary.

Tauxe et al. (1996) presented a series of 19 records from marine carbonates. They estimated the age of the M/B boundary in terms of the astronomical timescale (Berger and Loutre, 1992; Hays et al., 1976, Imbrie and Imbrie, 1980). The M/B boundary is always in oxygen isotope stage 19. They show evidence for a remanence acquisition occurring in the uppermost few centimeters below the sediment-water interface.

Thus the M/B reversal is recorded in the marine environment during a warm period (stage 19, which possibly corresponds to soil layer S₇ in the Chinese loess plateau). In the Chinese loess plateau the M/B boundary is always found in loess layer L₈, except for Luochuan. The shift observed mostly in loess sediments may be explained with climatic phase lags between oceanic and continental sediments or with differential NRM lock-in depth (Forster and Heller, 1994). Tauxe et al. (1996) also tried to explain the great discrepancy in the M/B boundary placement between loess deposits and marine cores by suggesting a delayed remanence acquisition in the loess sequences.

1.3 Climatic significance of loess/paleosol deposits

1.3.1 Paleosols and susceptibility enhancement

Paleosols represent soils “formed on a landscape of the past” (Ruhe, 1956). The alternation of loess and paleosol layers observed in the loess sequences all over the world reflects changing of the interaction of the soil forming factors (see 1.1.4).

The magnetic signature of the loess/paleosol alternation also reflects climatic changes and has become an important tool for paleoclimatic reconstructions since the 1970s, when the first susceptibility measurements were performed on the Chinese loess plateau (An et al., 1977). High susceptibility values were measured in the paleosol horizons and low susceptibility values in the loess horizons (Heller and Liu, 1982, 1984; Liu et al., 1987; Kukla and An, 1989). Heller and Liu (1986) found a positive correlation between the magnetic susceptibility record in Luochuan and the marine oxygen isotope record from the Pacific Ocean core V28-239 (Shackleton and Opdyke, 1976), thus verifying the climatic significance of the susceptibility variations in loess/paleosols sequences.

	Parameters	Loess (L)	Paleosol (S)
Magnetic parameters	Coercivity (B_o) _c	13.9 mT (SD: 0.7) ¹⁾	11.4 mT (SD: 1.4) ¹⁾
	Saturation Magnetization M_s	$2.03 \times 10^{-2} \text{ Am}^2\text{kg}^{-1}$ (SD: 0.18)	$3.10 \times 10^{-2} \text{ Am}^2\text{kg}^{-1}$ (SD: 0.38)
	Susceptibility (χ)	$3.2 \times 10^{-7} \text{ m}^3\text{kg}^{-1}$ (SD: 0.3) ¹⁾	$7.6 \times 10^{-7} \text{ m}^3\text{kg}^{-1}$ (SD: 1.9) ¹⁾
Magnetic minerals	Fe_3O_4	$0.053 \pm 0.007\%$ ²⁾	$0.11 \pm 0.01\%$ ²⁾
	$\text{Fe}_3\text{O}_4 - \gamma\text{-Fe}_2\text{O}_3$	$(0.022 - 0.024)\%$ ³⁾	
	$\alpha\text{-Fe}_2\text{O}_3$	0.92% ²⁾	0.73% ²⁾
		0.88% ³⁾	

Table 2: Coercive force (B_o)_c, saturation magnetization (M_s), low field susceptibility (χ) as well as the content of magnetic minerals per unit volume are represented for loess (L) and paleosol (S) layers in different sequences on the Chinese loess plateau. (SD: Standard Deviation).

¹⁾ Xiagaoyuan, present work; ²⁾ Maher and Thompson (1992); ³⁾ Evans and Heller (1994)

The isotopic proportion $^{18}\text{O}/^{16}\text{O}$ reflects global ice volume changes. By measuring the proportion between these two oxygen isotopes in the calcium carbonates of the shells of marine foraminifers, global climatic changes have been identified. Imbrie et al. (1984) produced a composite $\delta^{18}\text{O}$ curve from 5 different cores (SPECMAP), reflecting not

only changes in the global ice volume, but also in temperature. The relation between $\delta^{18}\text{O}$ and magnetic susceptibility was confirmed in other loess/paleosol sequences (Liu et al., 1991; Forster and Heller, 1994). Different models have been proposed in order to explain the enhancement of susceptibility in paleosols. At first, Heller and Liu (1984) explained the increase of magnetic susceptibility as a result of increasing concentration of magnetic minerals due to decalcification and soil compaction. A model with constant flux of ultrafine magnetic particles from distant sources was proposed by Kukla et al. (1988). The low susceptibility values in cold periods would be due to a high input of silt with low susceptibility which is diluting the magnetic component. The high susceptibility values in warm periods would be caused by small input of silt increasing therefore the concentration of magnetic minerals. Frequent natural fires have been considered to be another reason for the magnetic enhancement (Kletetschka and Banerjee, 1995).

The presently most favored model considers postdepositional weathering processes as responsible for the formation and enhancement of magnetic susceptibility in paleosols (Zhou et al., 1990; Maher and Thompson, 1991).

The role of magnetotactic bacteria for the production of fine magnetite has been considered, in spite of the difficulty of identifying the typical chain structures in loess deposits (Evans and Heller, 1994; Maher et al., 1994).

Not only magnetic susceptibility is changing with the alternation of loess and paleosols, but also other magnetic parameters. Quantitative measurements underscore the characteristics of the magnetic mineralogy of loess and paleosols (Table 2). As discussed above, the magnetic susceptibility is enhanced in the paleosol with respect to the loess. The highest saturation magnetization M_s values and the lower coercivity $(B_o)_c$ measured in the paleosols testify to a higher concentration of “soft” magnetic minerals (magnetite/maghemite) in paleosols. A slight enrichment of magnetite (Maher and Thompson, 1992) and maghemite (considered to enhance the susceptibility together with magnetite, Evans and Heller, 1994; Eyre and Shaw 1994; Verosub et al., 1992) was observed in paleosols, as well as a higher content of “harder” hematite in the unweathered loess layers (Maher and Thompson, 1992; Evans and Heller, 1994).

1.3.2 Susceptibility enhancement and Milankovitch's theory

The sequence of glacial and interglacial periods in the Quaternary is largely controlled by the earth's orbital parameters. The planets of the solar system have an effect on the dynamics of the earth's rotation, resulting in a periodic variation of the obliquity (period of 41 ka), the eccentricity of the Earth's orbit (two cyclicities with periods of 109 ka and 413 ka) and the precession of the spin axis (describing a rosette with a period of 109 ka, that combined with the 25.7 ka period of the rotational precession gives a period of 20.5 ka). The main frequencies predicted by Milankovitch's theory (Milankovitch, 1941) were discovered in marine oxygen isotopes profiles (Hays et al., 1976). A few attempts were made to recognize periodicity in the magnetic susceptibility signal. Heller and Liu (1986) found only a peak at 40 ka (obliquity) by matching susceptibility peaks of the loess/paleosol sequence of Luochuan with the maxima of Berger's (1978) theoretical insolation curve, Wang et al. (1990) determined two peaks at 40 ka and 100 ka in the loess/paleosol sequence in Baoji using Fourier analysis. The result was confirmed and elaborated by grain size analysis of samples taken from the same section (Ding et al., 1994), confirming that to a large extent both susceptibility and grain size variation are orbitally driven.

***THEORETICAL
BACKGROUND
AND
METHODOLOGY***

Chapter 2

MAGNETISM

The following chapter represents a brief outline on the theory of rock magnetism. The works of O'Reilly (1984), Stacey & Banerjee (1974), Thompson and Oldfield (1986), Butler (1992) and Dunlop & Özdemir (1997) have been used as references.

2.1 Atomic basis of magnetism

Magnetism is exhibited by all materials, and - according to classical theory - is caused by the movement of electrons in an atom. There are two types of electron motion:

1) the orbital motion of an electron about the nucleus, which creates a magnetic moment m_{orbit} (for the hydrogen atom, with magnetic quantum number $m=1$)

$$m_{orbit} = m \frac{eh}{2m_e} = \mu_B \quad (2.1)$$

with e the electric charge of the electron, h the Planck constant, m_e the mass of the electron and μ_B the Bohr magneton as the fundamental unit in magnetism.

2) the spin motion of an electron, which gives a magnetic moment m_{spin}

$$m_{spin} = 2s \frac{eh}{2m_e} = \mu_B \quad (2.2)$$

where s is the spin quantum number with values of $\pm 1/2$.

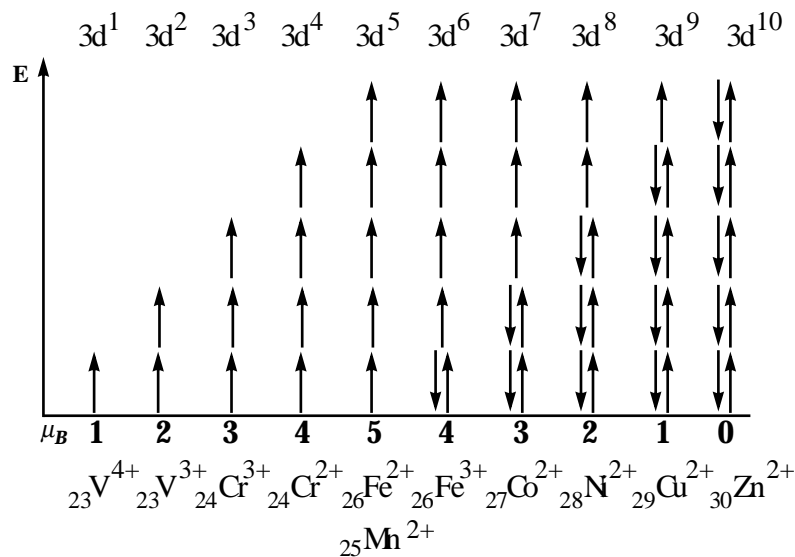


Figure 1: Electron distribution on the 3d orbitals of the transition elements. The arrows represent the spin of the electron. Each uncompensated spin corresponds to a magnetic moment of $1 \mu_B$.

Both m_{orbit} and m_{spin} express the basic unit for the magnetic moment, the Bohr Magneton (μ_B), which has a value of $9.27 \times 10^{-24} \text{ Am}^2$.

The contribution to the magnetic moment of ferromagnetic materials is caused principally by the spin of the electron rather than its orbital motion. The distribution of the electrons on the different orbitals in natural elements follows the Pauli principle (no two electrons in the same atom can have identical quantum numbers) and the Hund rules (electrons in an atomic subshell maximize their net spin). The elements having uncompensated spin moments in the 3d shell are called transition elements, among which as an example $^{26}\text{Fe}^{3+}$ has 5 unpaired electrons, and hence a magnetic moment of $5 \mu_B$ (Fig. 1).

2.2 Fundamental parameters in magnetism

It is possible to align the magnetic moments in a solid matter by applying an external magnetic field, obtaining a total magnetic moment per unit volume given by the sum of the Bohr magnetons per unit volume. This is called the magnetization M , and is expressed in the International System (S.I.) in Am^{-1} . The degree to which matter becomes magnetized is determined by the magnetic susceptibility κ

$$\kappa = \frac{M}{H} \quad (2.3)$$

with M the magnetization obtained in an applied magnetic field H . In S. I., M and H have the same dimension (Am^{-1}), giving κ as a dimensionless quantity.

2.3 Magnetic behaviour in solids

Due to the occurrence of orbital and spin magnetic moments, three main types of magnetic behaviour can be observed in nature: diamagnetism, paramagnetism and ferromagnetism.

2.3.1 Diamagnetism

Materials which exhibit an induced magnetization in the opposite sense to an

applied field are called diamagnetic (Fig. 2). Diamagnetism is present in all materials, but is easily concealed by stronger magnetic behaviour. An applied magnetic field causes a precessional mode (Larmor precession) of the electrons about the nucleus, resulting in a weak magnetic moment opposing the external field.

Hence, the diamagnetic susceptibility is negative, and in addition weak and temperature independent. Many rock forming minerals such as quartz and calcite are diamagnetic.

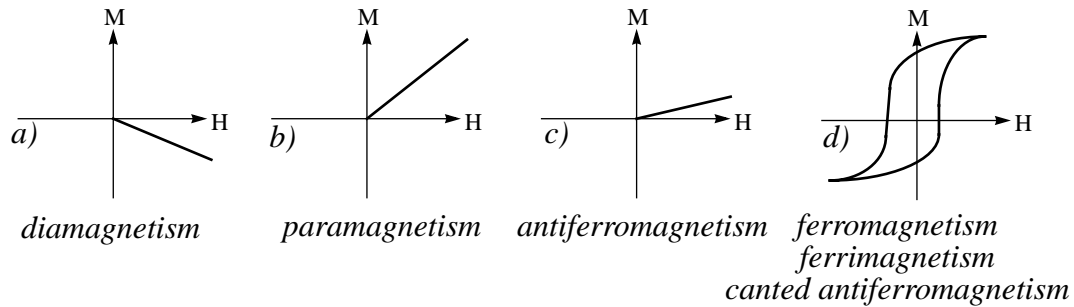


Figure 2: Magnetization M as a function of an external applied field H for diamagnetic (a), paramagnetic (b) and ferromagnetic materials (c and d).

2.3.2 Paramagnetism

Paramagnets have uncompensated spins without magnetic order in the absence of an external magnetic field (Fig. 3a). The chaotic orientation is due to thermal energy, resulting in a zero magnetization. By applying an external field H the magnetic spin moments align in the field direction, giving rise to a positive susceptibility (Fig. 2b). The latter is temperature dependent, increasing with decreasing temperature, and is described by the Langevin theory of paramagnetism. A system with N magnetic moments m per unit volume, randomly distributed and non-interacting may be considered. By applying a field H the resulting energy $E(\theta)$ for alignment of each magnetic moment is

$$E(\theta) = -m \cdot H \cdot \cos\theta \quad (2.4)$$

with θ the angle of the magnetic moment m with the applied field H .

The probability $P(\theta)$ of a magnetic moment occupying a specific energetic state is described by the Boltzmann statistics.

$$P(\theta) = e^{-\frac{mH \cos \theta}{kT}} \quad (2.5)$$

with the product of k (Boltzmann constant) and T (temperature) representing the thermal energy. The magnetic moment can be orientated in any direction so that eq. 2.4 must be integrated for values of θ from 0 to π . The resulting total magnetization M is then

$$\frac{M}{M_{max}} = \frac{Nm \int_0^\pi \cos \theta e^{-\frac{mH \cos \theta}{kT}} \sin \theta d\theta}{\int_0^\pi e^{-\frac{mH \cos \theta}{kT}} \sin \theta d\theta} \quad (2.6)$$

For $x = \frac{mH}{kT}$ the solution of eq. 2.6 is

$$\frac{M}{M_{max}} = Nm \left(\coth x - \frac{1}{x} \right) = NmL(x) \quad (2.7)$$

$L(x)$ represents the Langevin function. If the magnetic moments are small with respect to temperature and applied field, $x \ll 1$.

The series expansion of $L(x)$ for small x values, resulting in $L(x) \approx x/3$, yields a magnetization M

$$M = \frac{Nm^2 H}{3kT} \quad (2.8)$$

From this equation it is possible to obtain the susceptibility for paramagnetic materials, given by

$$\kappa = \frac{M}{H} = \frac{Nm^2}{3kT} = \frac{C}{T} \quad (2.9)$$

With the Curie constant $C = \frac{Nm^2}{3k}$. This represents the Curie law for paramagnetic minerals.

2.3.3 Ferromagnetism

Like paramagnets, ferromagnetic materials have uncompensated spins which exhibit, however, an internal magnetic order, i.e. the magnetic moments of the individual atoms

spontaneously align parallel or antiparallel. In the crystal lattice of ferromagnets the distribution of orbitals is complex and overlapping orbitals may couple the orientation of neighbouring magnetic moments leading to long-range order. Overlapping orbital and resulting direct exchange coupling (“exchange interaction”) with parallel spin alignment is characteristic of ferromagnetism “*sensu stricto*” (Fig. 3b), leading to strong macroscopic magnetization. Ferromagnetism is observed only in metals, such as iron, nickel,

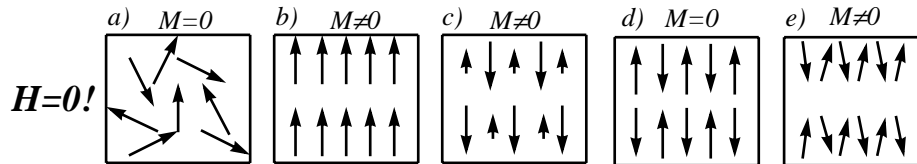


Figure 3: Magnetic spin moment ordering in paramagnetic (a), ferromagnetic (b), ferrimagnetic (c), anti-ferromagnetic (d) and canted anti-ferromagnetic (e) substances. M represents the net magnetization. Modified after Lowrie (1997).

cobalt. In rock forming ferromagnetic oxides, the exchange interactions are in effect due to interaction via the electron orbital of an interstitial oxygen ion which keeps the metal ions apart. In this case the interaction is indirect, e.g. coupled via the oxygen atom. The phenomenon is called superexchange interaction. The adjacent atomic magnetic moments are anti-parallel, and the resulting sublattice moments may be equal but opposite: no net spontaneous magnetization is observed in those antiferromagnetic substances (Fig. 3d).

Antiferromagnets may show imperfection caused by so-called spin canting, impurities or lattice defects. In this case the opposite sublattice moments will not cancel. Resulting weak ferromagnetism is observed. Spin canted antiferromagnetism occurs for instance in hematite (Fig. 3e).

If the antiparallel sub-lattice magnetic moments in an antiferromagnet are not equal, a strong permanent magnetization results. This effect is called ferrimagnetism (Fig. 3c). Temperature dependence of the magnetization is characteristic of ferromagnetic minerals.

By heating ferromagnets, the inter-atomic distances and thermal energy increase, causing a reduction of the exchange interaction and of the magnetization. The temperature at which any electron interaction is overwhelmed by thermal agitation, is called Curie temperature (T_c), and is characteristic for different ferromagnetic minerals.

2.3.4 Ferromagnetic susceptibility

Unlike paramagnetic materials, which have no remanence and can be saturated only by using very strong fields (> 100 T), ferromagnetic materials can be saturated in relatively small fields (~ 150 - 300 mT for magnetite). A remanent magnetization M_r can be measured in the absence of a magnetic field. To explain this observation, the existence of an internal molecular field that brings atomic moments near to saturation, was postulated by Weiss (1907). He proposed that in each domain the molecular field H_m must be proportional to the mean magnetization M in the same domain $H_m = \lambda M$, with λ representing the proportionality factor between M and H_m . The effective field acting is thus the sum of the applied field H and the molecular field H_m . Eq. 2.9 becomes

$$M = \frac{C}{T}(H + \lambda M) \quad (2.10)$$

If we substitute $M = H\kappa$, then the resulting susceptibility κ is described by the Curie-Weiss rule.

$$\kappa = \frac{C}{T - T_c} \quad (2.11)$$

with $T_c = \lambda C$, C = Curie constant and κ representing the ferromagnetic susceptibility.

2.4 Processes of magnetization

2.4.1 Energies in a ferromagnetic grain

The magnetization in ferromagnetic minerals is controlled by various energies which are minimized when combined in order to obtain a stable configuration of magnetization.

- **Exchange energy**

The parallel or antiparallel alignment of spin moments in ferromagnets is due to exchange interaction as already mentioned. Complete (coherent) alignment puts the energy to a minimum.

- **Magnetostatic energy**

In an uniformly magnetized sphere the magnetic moments produce a magnetic charge distribution on the surface. At the same time, the charge distribution causes an internal field in the opposite direction, the demagnetizing field H_D .

For a uniformly magnetized ellipsoid

$$H_D = -NM \quad (2.12)$$

where N is the geometric demagnetizing factor. In an orthogonal system, the sum of the demagnetizing factors in x, y and z direction equals 1.

$$N_x + N_y + N_z = 1 \quad (2.13)$$

For spherical grains:

$$N_x = N_y = N_z = \frac{1}{3} \quad (2.14)$$

The magnetostatic energy e_m describes the interaction energy between the internal demagnetizing field H_D and the magnetization M of a ferromagnet. In this case $H=H_D$

$$e_M = -\frac{\nu M H_D}{2} = -\frac{\nu M (-NM)}{2} = \frac{N \nu M^2}{2} \quad (2.15)$$

where ν denotes the volume of the particle under consideration. An incoherent (spins deviate from parallel or antiparallel alignment) magnetization minimizes magnetostatic energy. In other words, to minimize the demagnetizing field H_D , the spins should not be parallel to each other but should form closed loops (incoherent spin orientation).

- **Anisotropy energy**

The magnitude of the magnetostatic energy e_m is strongly related to the shape of a magnetic grain. Different elongations of grains in different directions result in demagnetization factors of different values. For a needle shaped grain of infinite length, N_z becomes 0 along the needle axis whereas in the cross section of the needle $N_x+N_y=1$. Thus $e_{mz}=0$ and $e_{mxy}=\nu M^2/2$. The magnetostatic energy difference Δe_m between the two directions is

$$\Delta e_m = \frac{(N_{xy} - N_z) \nu M^2}{2} = \frac{\Delta N \nu M^2}{2} \quad (2.16)$$

This shape anisotropy causes M to be aligned along the long axis. In order to force M over the magnetostatic energy barrier, an external magnetic field H has to be applied that must exceed the energy barrier Δe_m .

$$e_H = vMH > \Delta e_m \quad (2.17)$$

Magnetocrystalline anisotropy describes the energy function of the spin moments with respect to the lattice orientation of a ferromagnet. The easy directions of magnetization are defined by the crystallographic directions along which magnetocrystalline energy is minimized.

For a material with uniaxial symmetry the magnetocrystalline energy e_a becomes

$$e_a = K \sin^2 \theta \quad (2.18)$$

with K the magnetocrystalline anisotropy constant and θ the angle between the magnetization direction and the magnetocrystalline easy direction. The minimum for the anisotropy energy is obtained if the magnetization is aligned along the magnetocrystalline easy direction (coherent spins).

- **Magnetostriction and magnetoelastic energy**

By applying an external field H , a spontaneous change in the dimension of a ferro(i)magnetic grain may occur. This effect is called magnetostriction. If expansion occurs in the direction of the magnetization then the magnetostriction λ_s is positive. In magnetite, for example, λ_s is positive along the easy axis [111] and negative along a hard axis [100]. Being the magnetostriction and the magnetocrystalline energy dependent on the interionic distance, a change in the distance between ions causes a change in magnetization. This is called magnetoelastic effect and expresses the stress dependence of the magnetic anisotropy.

2.4.2 Magnetic domains

The exchange energy and the magnetocrystalline energy have a minimum with coherent spins whereas the magnetostatic energy becomes minimized through incoherent spins. To obtain an overall minimum energy status, a compromise between these competing energies has to be found. This compromise is related to the grain size of the ferro-

magnetic mineral. If a ferromagnetic grain, in a zero field environment, seeks minimization of the energy with a coherent spin structure, e.g. the magnetic moments in the grain are parallel to each other, one speaks of a single-domain (SD) grain. For equidimensional magnetite grains, the SD lower and upper size limits are 0.025-0.030 μm (Dunlop and Bina, 1977) and 0.079-0.084 μm (Enkin and Williams, 1994) respectively. In hematite the limits are 0.25-0.30 μm and 15 μm (Banerjee, 1971).

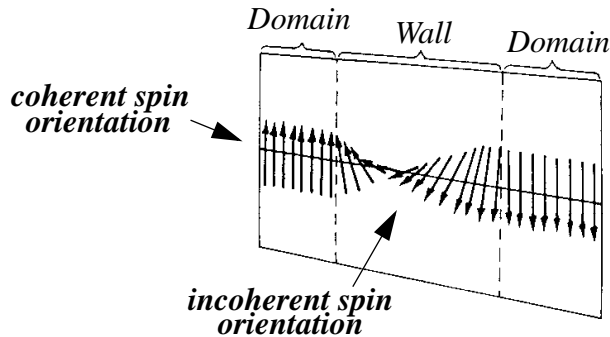


Figure 4: Coherent spin orientation in domains and incoherent orientation in domain walls. Modified after O' Reilly (1984).

If the size of a ferromagnetic mineral becomes too large to have a minimum energy with a coherent SD structure, domain walls form. These grains are called multidomain (MD) grains. In MD grains the minimization of the energy is obtained by the combination of coherent structure within domains that minimize the exchange and the magnetocrystalline energy, and incoherent structure within domain walls that tends to minimize magnetostatic energy (Fig. 4).

A special case of MD grains are those that have SD-like properties, but are larger than the critical SD size $d_0 \sim 0.08 \mu\text{m}$ (for magnetite), i.e. they have domains. These grains are called pseudo-single-domain (PSD). The main difference between PSD and MD grains is observed in their ability to acquire a thermoremanent magnetization. PSD grains with size range from $\sim 1 \mu\text{m}$ to $\sim 10 \mu\text{m}$ show a drop in TRM acquisition efficiency with respect to SD grains (Dunlop, 1981) but they can nevertheless maintain a stable TRM over geological time. On the other hand, MD grains may easily acquire a secondary component of magnetization.

2.4.3 Magnetic relaxation and superparamagnetism

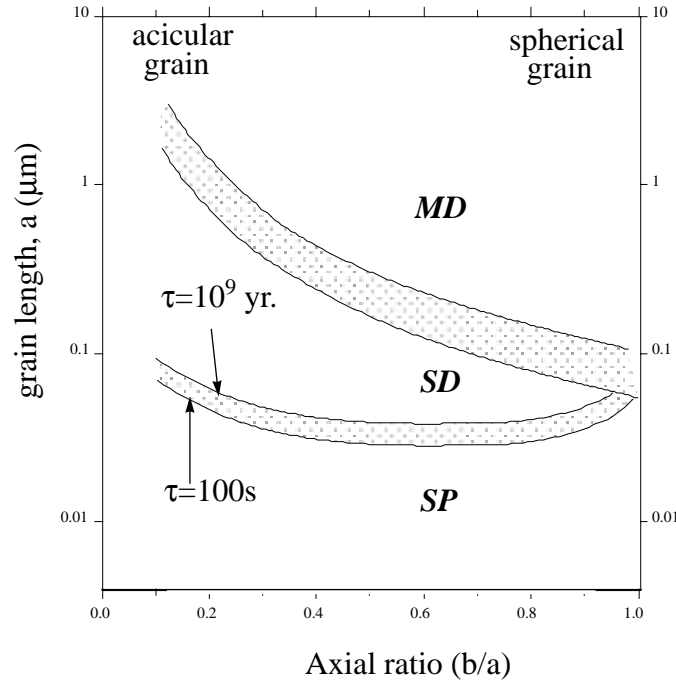


Figure 5: Ranges of grain sizes and shapes (ellipsoidal axial ratios) for single-domain (SD), multidomain (MD) and superparamagnetic (SP) behaviour in magnetite. τ is the relaxation time. Modified after Butler and Banerjee (1975).

If a grain becomes very small (Fig. 5), thermal energy may overcome the anisotropy energies. Those grains may change the direction of magnetization within short times and hence are called superparamagnetic (SP). For an assembly of SD grains, remanent magnetization M_r will decrease (in zero field) exponentially with time as described by the following equation

$$M_r = M_{r_0} \cdot e^{-\frac{t}{\tau}} \quad (2.19)$$

with M_{r_0} the initial remanent magnetization, t the time and τ the characteristic relaxation time, after which $M_r(t) = M_{r_0}/e$. The relaxation time of a grain with volume v and at temperature T is

$$\tau = \tau_0 \exp\left(\frac{v(B_0)_c M_s}{2kT}\right) \quad (2.20)$$

where $v(B_0)_c M_s$ represents the anisotropy energy, k Boltzmann's constant and τ_0 a constant of the order of $\sim 10^{-9}$ s (Néel, 1949). vM_s is the blocking energy, representing the

barrier energy to rotate the saturation magnetization M_s .

Grains with a relaxation time shorter than the measurement time will have moments which are free to rotate in an applied low field and behave similarly to the magnetic moment in paramagnetic materials.

Superparamagnetism refers to very small ferromagnetic grains that behave like paramagnets, their magnetization being thermally controlled.

2.4.4 Magnetic hysteresis

The action of the different energies in ferromagnets can be studied by applying a cycling magnetic field B . The resulting magnetization curve is called magnetic hysteresis (Fig. 6), which contains information about the mineral type, its concentration and grain size. The hysteresis loop area is a measure of the energy stored by the material and is called hardness. Materials which are easy or difficult to magnetize/demagnetize are called soft or hard, respectively. SD grains with uniaxial symmetry can have two equilibrium states of magnetization. Such grains, with their easy axis parallel to the applied field will switch between equilibrium states only when a reversed field is strong enough to overcome the anisotropy energy barrier. The result is a square hysteresis loop. If the field

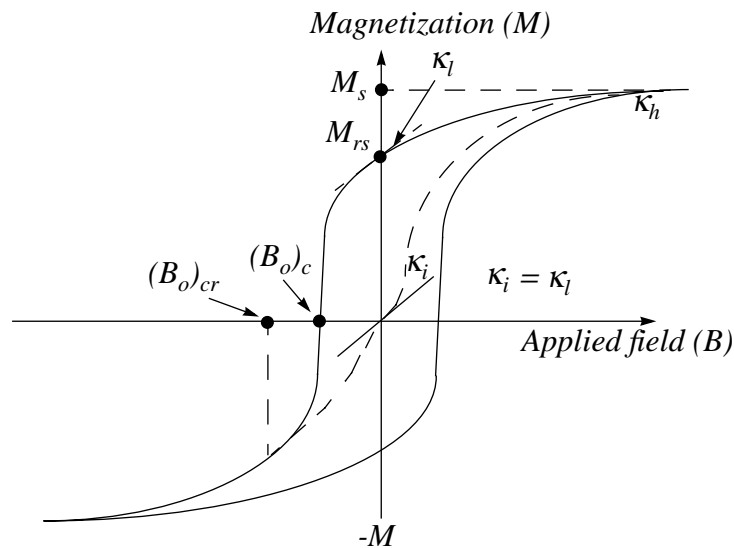


Figure 6: Hysteresis loop and standard hysteresis parameters: Saturation magnetization M_s , saturation of remanent magnetization M_{rs} , coercive force $(B_o)_{cr}$, coercivity $(B_o)_c$, high field susceptibility κ_h , low field susceptibility κ_l and initial susceptibility κ_i .

is applied perpendicular to the grains' easy axis, no hysteresis is observed, because equilibrium states have identical magnetizations in the field direction. An assembly of randomly orientated grains will show rounded loops which are intermediate between the two extremes discussed above. In multidomain grains numerous equilibrium states, which are very sensitive to the grains' previous thermal and magnetic history, are possible. Because domain wall motion is often much easier than rotation of the magnetization vector in a SD grain, hysteresis loops of MD grains are narrower ("softer").

Several parameters for a specific mineral can be obtained from the hysteresis loops. M_s (saturation magnetization) is the limiting value of magnetization at high applied fields. M_{rs} (remanent saturation magnetization) is the magnetization of a sample remaining when the applied field is reduced to zero after saturation had been achieved. The coercive force $(B_o)_c$ is the magnitude of a reversed field required to reduce the in-field magnetization to zero. The coercivity $(B_o)_{cr}$ is the reversed field required to remove any net remanence of the sample, after saturation. κ_h (high-field magnetic susceptibility) is the gradient of the linear portion of the hysteresis loop at high fields. κ_l (low-field magnetic susceptibility) is the gradient of the hysteresis loop, as it crosses the zero field axis, after the sample has been saturated. On the other hand, the initial susceptibility κ_i is the gradient of the reversible part of the magnetization curve taken through the origin for the sample in a demagnetized state.

2.5 Magnetic minerals

The most typical ferromagnetic minerals in loess/paleosol sequences are iron oxides and hydroxides which are represented by magnetite, maghemite, hematite and goethite.

2.5.1 Hematite (α -Fe₂O₃)

Hematite crystallizes in the corundum structure (Fig. 8b) in which closely-packed layers are stacked to form a hexagonal closely-packed lattice (Fig. 8c), with Fe³⁺ occupying sites with octahedral coordination. Fe³⁺ planes perpendicular to the [001] axis form an interlinked hexagonal open network such that 2/3 of the octahedral sites are occupied (O'Reilly, 1984).

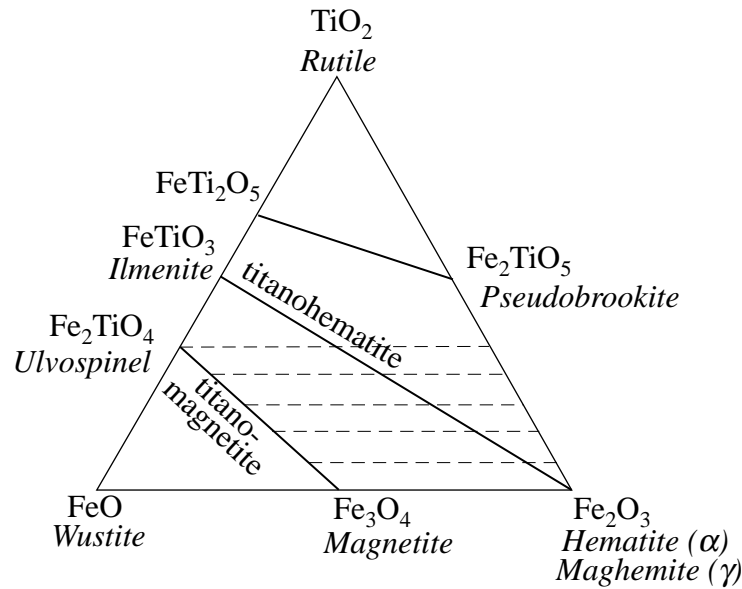


Figure 7: The ternary iron-titanium oxide system of magnetic minerals. Titanomagnetites are cubic minerals with inverse spinel structure. The titanohematites have a rhombohedral structure. Horizontal dashed lines represent the change in bulk composition during low- and high-temperature oxidation (maghemitization). Modified after Soffel (1991).

A magnetic sublattice is formed by a displacement of this network by one ion site in adjacent layers such that half of the Fe^{3+} are coupled antiferromagnetically (through superexchange interaction) to the plane below and the other half to the plane above. Superexchange also maintains parallel spins in each plane. A magnetic transition occurs on cooling pure hematite through -10°C (Morin transition T_M). Above T_M the spins are oriented in the basal c-plane (Fig. 8b) and alternate c-planes are coupled in antiparallel pairs; below T_M true antiferromagnetism occurs with spins aligned along the c-axis (Fig. 8b). Although hematite has equivalent iron sites occupied by antiparallel Fe^{3+} , it is not truly antiferromagnetic above T_M , but shows a weak parasitic ferromagnetism which arises from spin canting (Dzyaloshinski, 1958).

The sublattice magnetizations are permanently deflected through a small angle ($\sim 0.2^\circ$, Dunlop and Özdemir, 1997) in the absence of an external field. In this way a small magnetization perpendicular to the average spin axes results. In very small grains, the large surface to volume ratio can often result in a significant imbalance of uncompensated spins at the surface resulting in ferromagnetic behaviour. Although the saturation magnetization M_s of bulk hematite is weak - between $0.2\text{-}0.5 \text{ Am}^2\text{kg}^{-1}$ (Carmichael, 1989), $\sim 0.5\%$ of that of magnetite - it is magnetically extremely hard and therefore an

important remanence carrier. This is due to a magnetoelastic effect (see 2.4.1), e.g. due to the stress controlled anisotropy in the basal plane.

The Néel temperature T_N (the equivalent of the Curie temperature T_C for ferrimagnetic minerals) for hematite is 675°C. In dry, oxidizing conditions hematite is the stable end member of the iron oxide family. It can be formed by the oxidation/inversion of magnetites and by dehydration of hydroxides/oxyhydroxides. In soils and sediments it is frequently associated with goethite.

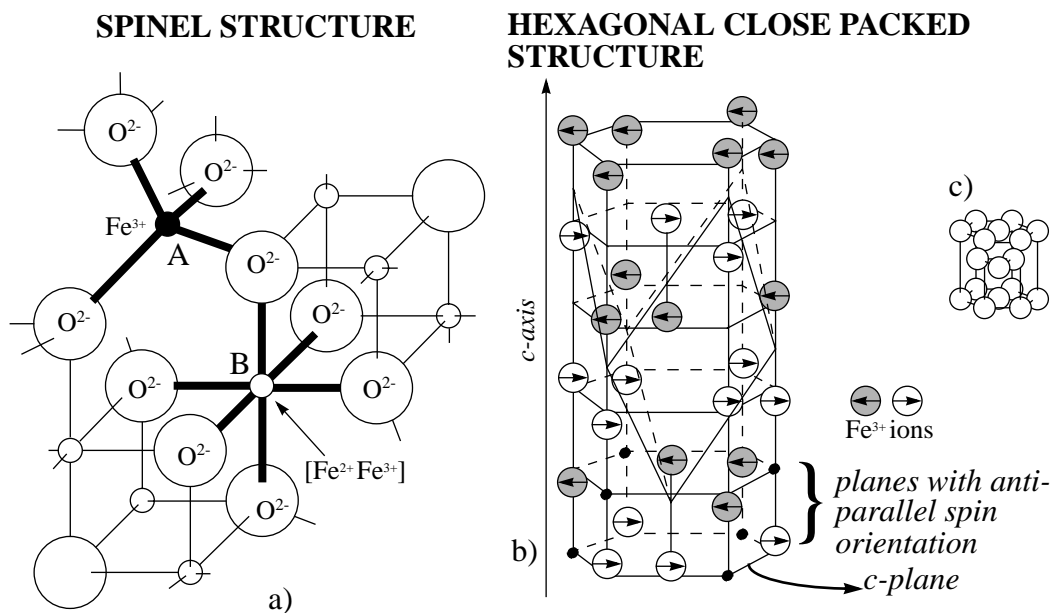


Figure 8: The spinel and the hexagonal closely packed structure is characteristic for magnetite and hematite, respectively. The spinel structure (a) presents two types of cation sites: the A site is in tetrahedral symmetry, whereas the B site is in octahedral symmetry. Hematite crystallizes in the corund structure (b) in which closely packed layers are stacked to form a hexagonal close packed lattice (c). The arrows in the Fe³⁺ ions represent the spin magnetic moment directions. Modified after O'Reilly (1984).

2.5.2 Magnetite (Fe₃O₄)

Magnetite is an iron oxide which has an inverse spinel structure with tetrahedrally coordinated (A) sites occupied by ferric (Fe³⁺) ions (8 per unit cell) and 16 octahedrally coordinated (B) sites occupied by ferric and ferrous (Fe²⁺) ions equally (Fig. 8a). Its strong spontaneous magnetization arises from the non-equal antiparallel sublattice magnetization (ferrimagnetism). The Fe³⁺ moment of $5\mu_B$ on the tetrahedral site is balanced

by the one on the octahedral site. This leaves an uncompensated moment of theoretically $4\mu_B$ of the octahedrally coordinated Fe^{2+} . Pure magnetite has a Curie temperature T_c of 578°C and a saturation magnetization M_s of $93 \text{ Am}^2\text{kg}^{-1}$ (Carmichael, 1989).

A transition from a cubic to monoclinic crystallographic structure is observed below the so-called Verwey transition which occurs at a temperature of $\sim 120\text{K}$ (T_v). Above T_v electron hopping from Fe^{2+} to neighbouring B-site Fe^{3+} converting Fe^{2+} to Fe^{3+} and vice versa, destroys cation ordering. The lattice is then perfectly cubic. The transition is characterized by a high electron mobility which converts magnetite from an electrical insulator to a semiconductor. At this temperature the effective magnetocrystalline anisotropy is zero and is characterized by a peak in magnetic susceptibility and a change in remanence (which can increase or decrease) for samples cooled or warmed through T_v . This behaviour is apparent in grains whose coercivity is controlled by magnetocrystalline anisotropy, e.g. MD grains. Anisotropy in small SD grains is generally controlled by shape, and consequently there may be no evidence of T_v in these grains. Fine grain sizes, non-stoichiometry, and foreign cation substitution are known to have an effect on T_v (Aragon et al., 1985).

2.5.3 Maghemite ($\gamma\text{-Fe}_2\text{O}_3$)

Maghemite has a cubic structure similar to that of magnetite, but with lattice vacancies. Oxidation of magnetite to maghemite involves the loss of $1/3$ of the Fe^{2+} ions per formula unit (magnetite). Magnetic properties of maghemite are similar to those of magnetite, except for its metastability. Maghemite inverts to hematite when heated above 250°C (Verwey, 1935) but inversion has been also observed at higher temperatures (up to 750°C ; Dunlop and Ödzemir, 1990). Determination of the Curie temperature is problematic due to this low temperature inversion. A T_c of $\sim 645^\circ\text{C}$ has been determined by Ödzemir and Banerjee (1984). The saturation magnetization is about $85 \text{ Am}^2\text{kg}^{-1}$ (Carmichael, 1989).

2.5.4 Goethite (α -FeOOH)

Goethite (named after J. W. v. Goethe; Schroeder, 1988) is the most significant oxyhydroxide associated with sediments, soils in particular. Goethite, a yellowish brown to red mineral (Hedley, 1971), typically forms as a weathering product in soils of humid climates. Aluminium substitution is common for pedogenetically formed goethite. Major Al-substitution is characteristic for highly weathered soils, such as in tropical and subtropical environments (formation of bauxite and saprolite) whereas minor Al-substitutions occur in reducing environments (Fitzpatrick and Schwertmann, 1982). The goethite structure consists of double chains of Fe-O-OH octahedra extending along the crystallographic z-axis. These are bound to neighboring double chains by Fe-O-Fe and H bonds (Schwertmann and Taylor, 1989).

Goethite is antiferromagnetic, but often contains a defect/imbalance moment which could be most significant for ultrafine grain sizes (Dunlop and Ödzemir, 1997). The Néel temperature (T_N) is around 120°C and the saturation magnetization is $\sim 1 \text{ Am}^2\text{kg}^{-1}$ (Carmichael, 1989). On heating in air to 250-400°C it dehydrates to form extremely fine hematite, generally superparamagnetic, thus carrying no remanence (Dunlop and Ödzemir, 1997). Goethite is magnetically extremely hard, needing strong fields to saturate (> 7 Tesla), with coercive forces up to many hundreds of mT (Dekkers, 1988).

2.6 Magnetic measurements

2.6.1 Room temperature

- **Magnetic low field susceptibility**

Low field susceptibility and its frequency dependence was measured at room temperature using a KLY-2 susceptibility bridge and a Bartington dual frequency sensor (frequencies at 0.476 kHz for the low frequency susceptibility measurement κ_{lf} and 4.76 kHz for the high frequency susceptibility measurements κ_{hf}). Small quantities of material, especially during the measurement of grain size fractions where very small amounts of material were available, sometimes caused sensitivity problems for the measurement of the frequency dependence.

- **Hysteresis measurements**

Hysteresis measurements were performed using a Princeton Measurement Corporation alternating gradient magnetometer (AGM at Gif-sûr-Yvette, France): Between 10 mg and 40 mg for each measured sample were dispersed in a non-magnetic matrix in order to prepare the individual samples. The magnetic field (B) cycled between ± 2 T, yielding a total of 500 data points for each loop. Coercive force $(B_o)_c$ was determined after subtraction of the high field susceptibility signal. Back field measurements with peak fields of 2 T at steps of 40 mT on the same instrument were performed to measure coercivity of remanence $(B_o)_{cr}$. High field susceptibility (κ_h) was obtained from the gradient of the magnetization at high fields (~ 1.5 -2.0 T).

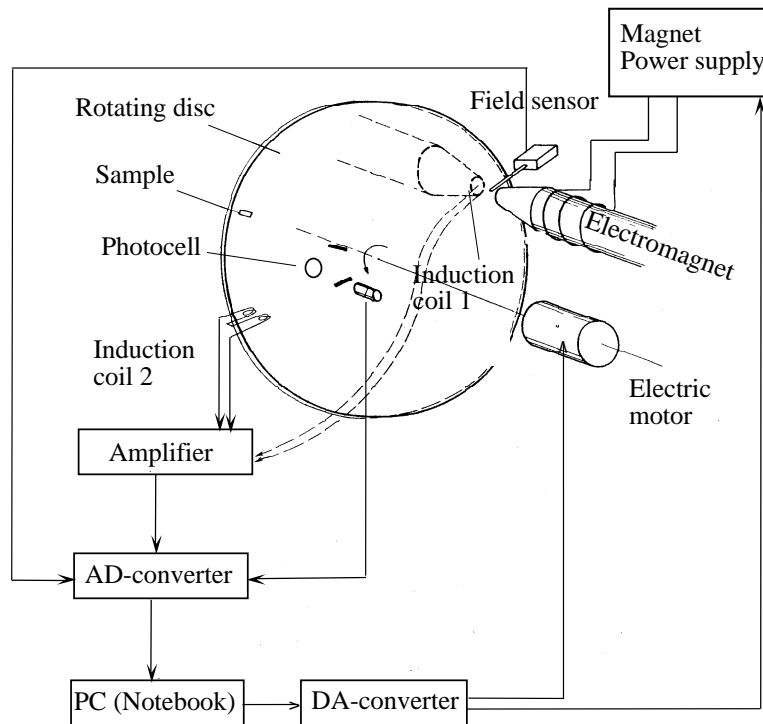


Figure 9: Diagram of the coercivity spectrometer. Induction coil 1 measures induced magnetization (estimated lower sensitivity limit: 0.05 Am^{-1}). Induction coil 2 measures remanent magnetization (estimated lower sensitivity limit: 0.005 Am^{-1}).

The hysteresis parameters were also measured with a modernized coercivity spectrometer (a precise description of this instrument can be found in Burov et al., 1986). The instrument consists of a non-magnetic disk housing a sample and rotating with a speed of about 22 Hz (see Fig. 9). The peripheral part of the disk where the sample is inserted

goes through two measurement every rotation cycle. The first device is composed of the induction coil 1 and an electromagnet that produces a continuously changing magnetic field, while the second device comprises the induction coil 2 in a magnetically shielded space. In the first coil, the induced magnetization (M_i) of the sample is measured since the measurement occurs inside the applied field. Thus, the saturation magnetization (M_s), if saturation can be achieved, and the coercive force $(B_o)_c$ determined. The induction coil 2 measures the sample remanent magnetization M_r outside the applied field a fraction of a second after M_i was measured. Thus, the saturation remanence (M_{rs}), (also called the saturation isothermal remanent magnetization, SIRM) and the coercivity of remanence $(B_o)_{cr}$ will be determined if saturation is achieved.

During the first stage of the measurement, the applied field is continuously increased until it reaches its maximum value ($B = 300$ mT). Then, the field is decreased during the second stage, passes zero and is increased again in the opposite direction for the third stage of the measurements until it reaches $(B) = -300$ mT.

M_i and M_r are being continuously measured during all three stages of the measurements, a mean value of both parameter is then calculated every 0.5 mT. Thus, the output file of every measurement cycle comprises 1800 average readings.

Since M_{rs} depends on both concentration and grain size, its normalization with M_s , which is solely dependent on the particle concentration, forms a new parameter (M_{rs}/M_s) that only reflects the grain size, for a given ferromagnetic mineral type. Thus, high values of (M_{rs}/M_s) indicate grains that have relatively long relaxation times (stable single domain), while MD-grains have low values of the magnetization ratio (see next section). The combination of the coercivities also produces a parameter reflecting the grain size, but with less discrimination power than (M_{rs}/M_s) . The coercivity of remanence and the coercive force have indeed comparable values in the SD size range, becoming however progressively divergent for larger grain sizes. Thus, small values of $(B_o)_{cr}/(B_o)_c$ are diagnostic for SD-grains, while higher values of this ratio indicate MD-behaviour. A Day plot (Day et al., 1977) may be used to represent the grain size characteristic of magnetic minerals.

- **Isothermal remanent magnetization (IRM)**

IRM refers to the magnetization acquired in a DC field at constant temperature and was measured with a 2G superconducting rock magnetometer (Goree and Fuller, 1976).

The increase of IRM with increasing field continues to a maximal value, the saturation of IRM (SIRM). SIRM intensity depends on the minerals and on their concentration in the measured sample. The distribution of coercivities in the magnetic minerals present in the sample determines the shape of the IRM acquisition curve.

- **Anhyseretic remanent magnetization (ARM)**

ARM was produced by superimposing an AC magnetic field on a small DC field using homemade equipment (Sharma, 1963). All the magnetic grains with coercive force up to the maximum amplitude of the alternating magnetic field (usually 120 mT) used to impart the ARM are carrying the ARM. The anhyseretic susceptibility (κ_{ARM}) is obtained by dividing the ARM with the applied DC field value (generally the earth's magnetic field, ~ 0.047 mT in Zurich).

- **Determination of the characteristic remanent magnetization (ChRM)**

The natural remanent magnetization (NRM) of a sample - also measured using 2G SQUID magnetometer - may contain several components, some related to the geological history of the rock and others to the sampling and handling procedure. It is necessary to demagnetize the samples so that the structure and composition of the NRM can be analyzed (principle component analysis, Kirschvink, 1980) and stable and characteristic components can be isolated, the characteristic remanent magnetization (ChRM).

- **Alternating field (AF) demagnetization**

When a rock sample is placed in an alternating magnetic field, the magnetizations of all domains with coercivity less than the peak AF field are remagnetized. If the field is then slowly reduced to zero in a DC field free environment, part of the rock magnetization is randomized (Creer, 1959). If this procedure is carried out in progressively increasing peak fields, a different decay of NRM components can be recognized. The equipment used, a Schonstedt Model GSD-1 AC demagnetizer, has a peak field of 100 mT. Thus it is not possible to demagnetize high coercivity minerals such as hematite and goethite, but it is useful for samples in which magnetite or maghemite carries the remanence.

- **Thermal demagnetization**

Thermal demagnetization (Thellier, 1938) is an alternative method to the AF demagnetization and was performed with a Schonstedt Model TSD-1 Thermal Demagnetizer. It consists of stepwise heating a sample to a demagnetizing temperatures T_d below T_c of the constituent ferromagnetic minerals, and cooling after each heating step down to room temperature in zero magnetic field. During heating the magnetic grains with blocking temperatures $T_b \leq T_d$ acquire a thermoremanent magnetization in zero field (i.e. the magnetic moments are randomly distributed), erasing the NRM component carried by these grains. In other words, the remanence of the magnetic minerals with low T_b is removed, whereas the magnetic grains with higher T_b keep their stable magnetization.

During stepwise thermal demagnetization, the heating and cooling cycles are repeated with progressively higher maximum temperatures. Progressive destruction of the magnetization reveals the components present in the NRM (carried by the grains with the highest T_b), and only the ChRM remains. This method is more powerful than AF demagnetization because the range of temperatures needed to destroy all of the NRM is below 700°C. Problems can arise if thermodynamically metastable or unstable magnetic minerals are present.

2.6.2 Low temperature measurements

Low temperature measurements were performed using a cryogenic SQUID-magnetometer S-600 (Cryogenic Ltd., U.K.). This highly specialized magnetometer was accessible at the Centre d'Etude Atomique in Saclay (France). A holder with a few milligrams of fractionated material was put in a tube which is thermally isolated. Concentric reservoirs around this tube are filled with liquid helium and liquid nitrogen. This allows measurements of the magnetic moment between 1.5 K and 330 K. The applied magnetic field, which can reach a strength of 6 T, is produced by a superconducting coil powered by a DC power supply, coupled in parallel with a superconducting short circuit. The sample in the tube is moved along the detection coils axes. This movement gives a magnetic flux variation, which is transmitted to the SQUID sensor and transformed into a voltage variation (Pierron-Darbonne, 1995).

Zero Field Cooling (ZFC) measurements were performed using bulk samples and

fractionated samples: the sample was cooled down in zero field from room temperature to 10 K. A weak field (0.1 mT) is then applied and the magnetization is measured as a function of temperature during the subsequent warm up. Experiments with low temperature thermoremanent magnetization (TRM) were also performed: the sample is cooled in a field (1 mT and/or 8 mT) from room temperature to 10 K. The applied field was then cancelled (virtually zero) during subsequent warm-up of the sample. The strength of the applied fields chosen for this experiments depended on the ability of the samples to acquire a magnetization, so that 1 mT was chosen as the smallest field for our experiments.

Hysteresis loops were also measured at lower temperatures (130 K, 10 K) using the SQUID-magnetometer S-600, with a magnetic field (B) cycling between ± 0.3 T, yielding a total of 250 data point for each loop

Chapter 3

GRAIN SIZE ANALYSIS

3.1 Introduction

Grain size analysis can be performed using different methods, depending on the purpose of the analysis. Sedimentation and centrifugation have been used in this work to obtain magnetic and geochemical information on 10 grain size fractions of loess and paleosol samples. The grain size distribution itself has been determined using the Mastersizer (laser scattering instrument). This method is much faster than the previous, but does not connect the grain size distribution with other physical properties.

3.2 Stoke Law

Stoke law is used in fractionating methods to calculate the grain size as a function of sedimentation time during sedimentation or centrifugation. The following forces act on a spherical particle in a fluid solution: the frictional force f_v , which is given by the viscous drag of the surrounding fluid, the gravitational force mg (m = mass, $g = 9.81 \text{ ms}^{-2}$), and the liquid buoyancy $-(mg)_l$. The particle acceleration is then

$$m \frac{du}{dt} = mg - (mg)_l - f_v \quad (3.1)$$

With increasing velocity the frictional force also increases, eventually reducing the acceleration to zero, and achieving terminal velocity (U_t)

$$f_v = BU_t \quad (3.2)$$

where $B = 6\pi\eta r$, with the viscosity η and the radius r .

3.3 Sedimentation and centrifugation

3.3.1 Sedimentation

The following practical steps have been carried out (Fig. 1):

- 1) Ca. 15g of sediment were poured into a 250 ml PVC-bottle. 50 ml of sodium hexamellphosphate 2% (Calgon) are added using a syringe with a $0.45 \mu\text{m}$ filter.
- 2) The bottle is strongly shaken for about 1 minute and ultrasounded for about 10 minutes.
- 3) The grain sizes $> 50 \mu\text{m}$ are removed using a metallic sieve of $50 \mu\text{m}$ mesh. This oper-

ation is performed on the top of a 1000 ml graduated glass cylinder, where the grain sizes $< 50 \mu\text{m}$ are in solution. The metallic sieve has to be rinsed using distilled water, allowing the fractions $< 50 \mu\text{m}$ to pass through the sieve. The residue on the sieve is then dried at ca. 80°C . This coarse fraction is designated as fraction “I”.

4) The graduated cylinder containing the remaining sediment is then filled up to 1000 ml using distilled water. Ultrasonic mixing is performed for about 5 minutes.

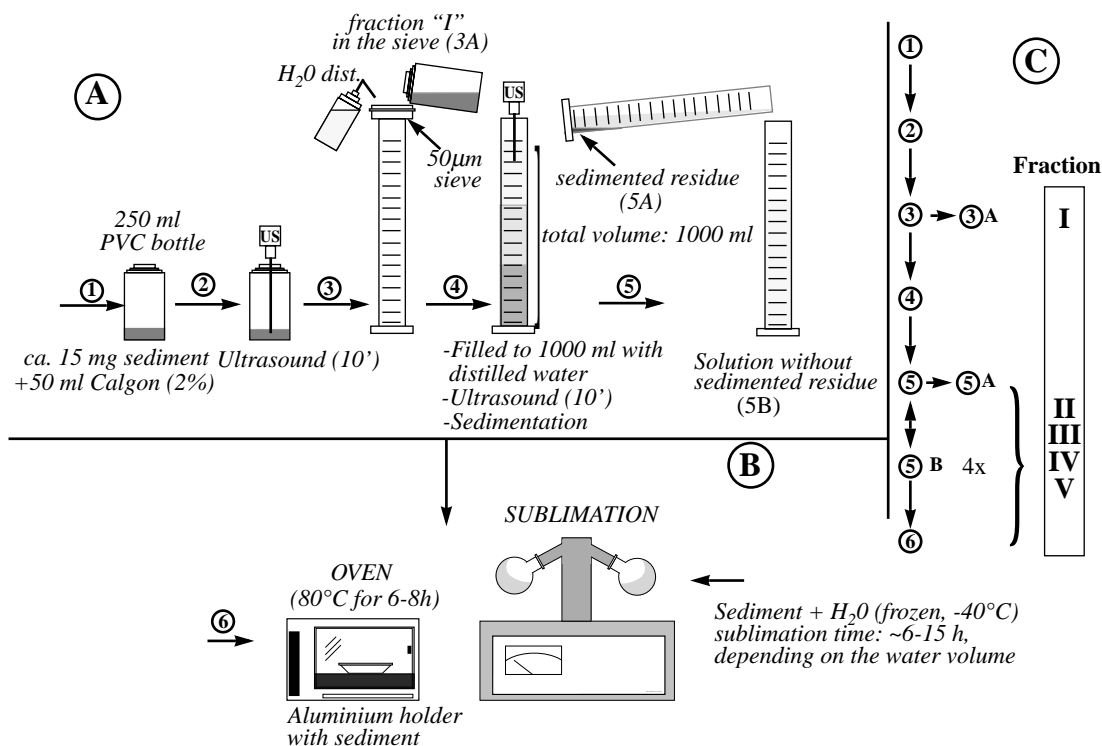


Figure 1: Sedimentation procedure. A) At step 5 the solution is poured into a new graduated cylinder (5B) and the residue (5A) is dried or sublimated (fraction “II” is obtained). The remaining solution (5B) undergoes further sedimentation to obtain fraction “III”, “IV” and “V” (step 5 repeated four times). The residue is either dried (6A) or sublimated (6B, before sublimation the residue is frozen in a methanol bath). C) Schematic representation of the repetitive sedimentation procedure.

5) The graduated cylinder has to be shaken for several seconds before the sedimentation starts. The correlation between grain size and time can be obtained from Stoke law

$$d^2 = \frac{18\eta s}{tg\Delta\rho} \quad (3.3)$$

d particle diameter (m)

s	sedimentation distance in the cylinder (m)
η	water viscosity (η) = 9.50×10^{-4} , at 20°C
t	fall time (s)
$\Delta\rho$	density difference between sediment and water ($2.65 \text{ g/ml} - 1.00 \text{ g/ml} = 1.65 \text{ g/ml}$)
g	gravity acceleration (9.81 m/s^2)

By changing the fall time it is possible to define the grain size range for the different fractions (see tab. 1).

The decantation has to be carried out with care, in order to avoid the residue going back into the solution. The residue can be dried in porcelain or aluminium holders in an oven at ca. 80°C . Alternatively the distilled water and the sediment can be frozen at -40°C in a methanol bath. By sublimation a fine powder is obtained for further analysis.

3.3.2 Centrifugation

The sedimentation method should not be used for fall times t longer than 24 hours because of decreasing precision. For grain size below $2.2 \mu\text{m}$ the centrifugation method was applied using a Swing-out Rotor TST 28.08/17 of Centrikon Kontron. Stokes law again estimates the sedimentation times for different grain size fractions.

$$d^2 = \frac{18\eta s}{ta\Delta\rho} \quad (3.4)$$

$d, s, \eta, t, \Delta\rho$ see equation 3.3

a $\omega^2 r$; $\omega = 2\pi n$ ($n = \text{U/min} / 60$); $a = 4\pi^2 n^2 r$ ($r = (r_{\min} + r_{\max})/2$)
 $r_{\min} = 7.4 \text{ cm}$, $r_{\max} = 17.16 \text{ cm}$

r_{\max} represents the distance between the centrifuge rotation axis and the bottom of the centrifuge tube, and r_{\min} is the distance from the centrifuge rotation axis and the top of the centrifuge tube.

	I	II	III	IV	V	VI	VII	VIII	IX	X
a		3.5 min	15 min	120 min	20 h					
b						5'	15'	15'	15'	120'
c						4000	4000	10000	28000	28000
d	> 50	50.0 - 41.8	41.8 - 20.0	20.0 - 7.0	7.0 - 2.2	2.2 - .396	.396 - .228	.228 - .091	.091 - .032	.032 - .0115

Table 1: Sedimentation time in minutes (a), centrifugation time in minutes (b) and centrifugation speed in revs per minute (c) for the 10 grain size fractions (d) in mm. The centrifugation time (b) does not include the acceleration and deceleration time (no braking after centrifugation time).

The following practical steps were carried out (Fig. 2):

- 1) The grains $< 2.2 \mu\text{m}$ was dispersed in water (total volume = 1000 ml) and exposed to ultrasonic mixing.

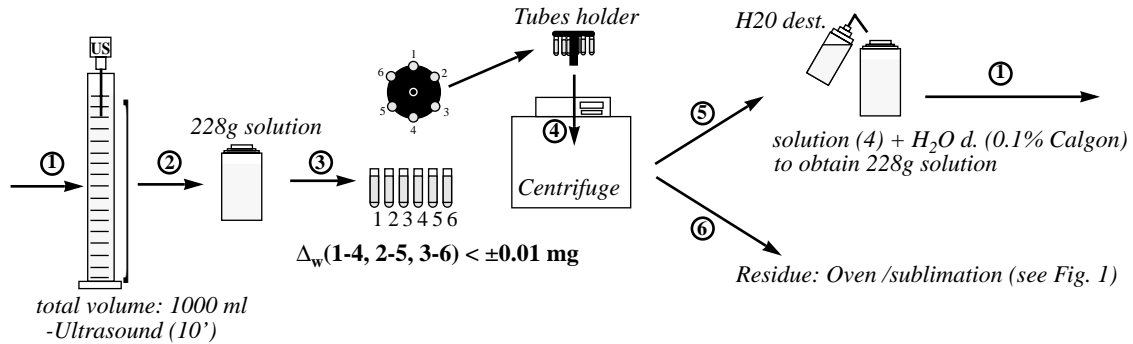


Figure 2: Centrifugation procedure (see text for details).

- 2) 228 g of the solution is put in a 250 ml PVC bottle.
- 3) The solution is divided into six equal weight fractions ($\Delta_w < 0.01 \text{ g}$) which are filled into 6 centrifuge tubes.
- 4) The tubes with the sediment are centrifuged at a defined speed and time depending on the grain size range.
- 5) The solution is decanted in a 250 PVC bottle. Distilled water with 0.1% Calgon is added to obtain again a weight of 228 g. The above procedure was repeated for the next grain size fraction using this solution.
- 6) The residue was dried in an oven using aluminium holders or was sublimated.

3.4 Mastersizer

The Mastersizer (Malvern Instrument Ltd.), as all particle sizers, is based on the principle of laser ensemble light scattering. It is classified as non imaging optical system: the sizing is accomplished without forming an image of the particle onto the detector.

The principle is that of a low-power Helium-Neon laser used to form a collimated and monochromatic beam of light, typically 18 mm in diameter. The particles are introduced in a recipient with distilled water and Calgon (0.1%) and then sprayed into the measurement area using a pump. The analyser (laser) beam is then scattered by the pres-

ence of the measured particles. The light scattered by the particles and the unscattered remainders are incident to a receiver lens, the so-called range lens (in this work a lens with a focus of 100 mm is used, allowing the measurements in a size range between 0.5 μm and 180 μm). This operates as a Fourier transform lens forming the far field diffraction pattern of the scattered light at its focal plane. Here a custom-designed detector, in the form of 31 concentric annular sectors, gathers the scattered light over a range of solid scatter angles. Wherever a particle is located in the analyser beam, the range lens configuration keeps its diffraction pattern stationary and centered on the range lens optical axis. During the measurements many particles are present simultaneously in the analyser, so that the system inherently measures the integral scattering of all particles present in the beam. The energy measured on the different annular sectors of the detector depends on the diameter of the particles present, with large (respectively small) particles having energy peaks at low (respectively high) angles. A distribution of energy values over the 31 concentric annular sectors is obtained, from which the grain size distribution is calculated.

The unscattered light is brought to a focus on the detector and passes through a small aperture in the detector and out of the optical system. The total laser power passing out of the system allows the sample volume concentration to be determined.

The main advantage of this method is that a grain size spectrum for a given sample is obtained in a few minutes. The disadvantage, with respect to sedimentation and centrifugation, is due to the fact that the measurement is destructive.

Chapter 4

BERYLLIUM-10

The comprehensive descriptions of Lal and Peters (1967) and McHargue and Damon (1991) have been used as fundamental references in this chapter.

4.1 Cosmogenic Isotopes

4.1.1 Cosmic Rays

Coming from outer space, cosmic radiation interacts with extraterrestrial and terrestrial matter in the atmosphere, on the earth's surface and within the crust, thus forming a variety of different isotopes by nuclear reaction. The cosmic particles consist of protons (87%), α -particles (12%) and heavier nuclei (1%) (Masarik and Beer, 1999). The isotopes generated in the atmosphere are used in the geosciences for dating and tracing various events and processes in the environment.

4.1.2 Primary particles

The corpuscular radiation has a galactic and a solar component, both showing different energy distribution, intensity and time modulation. The galactic cosmic radiation can be considered constant in time (Vogt et al., 1990), but the flux reaching earth is modulated by the heliomagnetic and the geomagnetic field intensity. Sunspot cycles and intensity variation of plasma cloud emission from the Sun can cause a reduction by an order of magnitude of the flux of galactic particles entering with energies below 10 GeV/nucleon (Fig.1) (Masarik and Beer, 1999). These reductions are due to "shielding" inhomogeneities, currents and magnetic fields in the interplanetary medium. At higher energies (above 20 GeV), the spectra are insensitive to this effect (Fig. 1). Near the earth's surface these energy spectra can be observed only in the polar troposphere. At lower latitudes the geomagnetic coordinates, as well as the angle of incidence and the rigidity (ratio of the particle's momentum and charge) strongly control the energy.

Although the relative abundance among the complex nuclei remains almost constant, the ratio between protons and complex nuclei may sensitively change for different coronal mass ejections (CME). In view of this behaviour and of the stochastic distribution of the events, it is difficult to quantify their effect on the production of isotopes in the atmosphere.

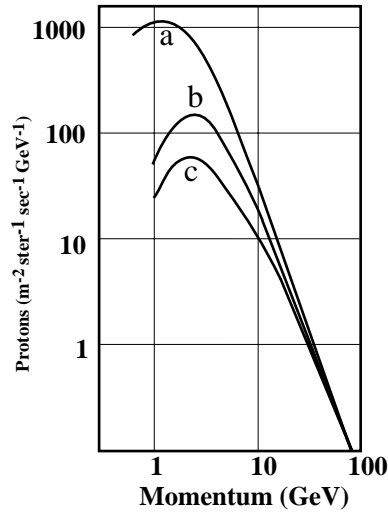


Figure 1: *Differential momentum spectra of cosmic ray protons at three different periods during a solar cycle. Curve a) during a sunspot minimum, curve b) during a sunspot maximum and curve c) during a series of Forbush decreases (July '59), (from Lal and Peters, 1967) .*

4.1.3 Interaction of cosmic rays with the atmosphere

The primary cosmic rays interacting with the top of the atmosphere consist mainly of protons with energies above 0.1 GeV. The collision of protons with the atmosphere leads to the formation of secondary particles, many of which have enough energy to subsequently interact with the atmosphere. This process leads to a particle cascade, which ends when the energy of the particles are too low for further reaction. The particle cascade results in a decrease of primary cosmic-ray particles and an increase of secondary particles with increasing atmospheric depth.

It is possible to calculate the number of interactions occurring in the atmosphere, for a given latitude and a defined incident direction, which permits one to determine the energy removed from the incident primary beam for a given power function representing the energy distribution of the primary particles (Fig.1). By integrating over all angles of incidence the total number of interactions is obtained. The interaction between primary cosmic rays and the atmosphere may generate neutrons which are causing spallation reactions about 2-3 times more effectively than protons (a large part of protons with energies below 0.5 GeV are stopped due to ionization processes in the upper atmosphere). Low energy neutrons ($E < 1$ eV) are captured, forming new isotopes. Apart from

spallation reactions, for energies above 500 MeV there are nuclear collisions forming pions. Because of their relatively low energy ($E \approx 400$ MeV) and very short half-life (2×10^{-8} s), they do not contribute to the isotope formation, instead they decay to muons and neutrinos. If we consider the major sources for isotope production (neutrons n , protons p , gamma rays γ , muons μ), their relative contribution to the isotope production in the atmosphere is

$$n : p : \gamma : \mu = 100 : 10 : 0.5 : 0.003$$

4.1.4 Production of isotopes in the atmosphere

Nitrogen, oxygen and argon are the main target nucleids (tab. 1), although the isotopes produced by argon spallation are difficult to detect because of the low argon concentration ($\sim 1\%$ of the total atmosphere volume).

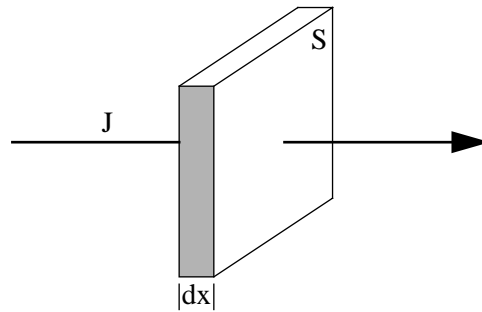


Figure 2: Schematic representation of cross section measurements. The number of reactions R depends on the flux J of the radiation and on the number of nuclei n on a surface S .

Nuclei production can be calculated mathematically. The probability w for a reaction (nuclei production) is given by

$$w = \frac{n \cdot \sigma(E)}{S} \quad (4.1)$$

n represents the number of nuclei on Sdx , and $\sigma(E)$ the cross-section (unit: 1barn = 10^{-24} cm²) (Fig. 2).

Cross section measurements are performed using particle accelerators.

The number n_0 of nuclei per cm³ is given by

$$n_0 = \frac{n}{Sdx} = \frac{\rho L}{A} \quad (4.2)$$

with ρ the density of the target, A the atomic weight and L the Losschmidt number.

The flux variation dJ depends on the initial flux J and probability w of a reaction

$$J = -Jw dx \quad (4.3)$$

$$\frac{dJ}{dx} = -wJ = -n_0 \sigma J \quad (4.4)$$

Then an exponential function for the cosmic flux

$$J = J_0 \exp(-n_0 \sigma x) \quad (4.5)$$

and a reaction rate R is obtained

$$R = \frac{J_0 L \sigma x}{A} \quad (4.6)$$

where A is the atomic weight. Using the cross section function it is possible to calculate the production rate $C_j(x, \lambda)$ for an isotope j at an altitude x and geomagnetic latitude λ

$$C_j(x, \lambda) = \sum_T \frac{LK_T}{A} \int \int \int \sum_i J_i(x, E, \lambda, \theta, \phi) \sigma_{i,j,T}(E) d\cos\theta d\phi dE \quad (4.7)$$

K_T	fractional abundance by weight of a particular target nuclide T
$\sigma_{i,j,T}(E)$	cross section function for the production of the isotope j in the collision between a particle i with T as target and with energy E .
$J_i(x, E, \lambda, \theta, \phi)$	differential energy spectrum of the particle i of the cosmic radiation dependent on the altitude x , the energy E of the incident ray, on the geomagnetic latitude λ and on the angle of incidence θ and ϕ .

By knowing the number and type of cosmic rays, their energy spectrum and the partial cross section for the production of a specific nuclide, the amount of produced cosmogenic isotopes can be quantified at a given position in the atmosphere.

4.2 Beryllium - 10 (¹⁰Be)

4.2.1 ¹⁰Be production rate

The half-life for ¹⁰Be is $(1.51 \pm 0.06) \times 10^6$ yr (Hofmann et al., 1987). Incident nucleons with an energy above ~10 MeV react with N and O to produce ¹⁰Be.

Other Beryllium isotopes, such as ⁶Be, ⁸Be, ¹¹Be and ¹²Be, are also produced but they decay in less than a second. ⁷Be has a half-life of ~53 days and can therefore be used as a tracer for cosmogenic beryllium in the atmosphere and surface waters.

Although theoretical calculations of production rates are easy to perform, their accuracy depends on the cross-section calculation. Several cross section calculations with different models (considering the effect of solar activity and variations of the earth magnetic field) have been performed. The obtained production rates (atoms/m²s), show differences that can exceed 100% depending on the calculation methods used (Blinov, 1988; O'Brien, 1979; Masarik and Reedy, 1995). Masarik and Beer (1999) obtained a value of 0.57×10^6 atoms/m²s.

Isotope	Half-life	Main Target Nuclide(S)
³ He	stable	N, O
¹⁰ Be	1.5×10^6 yr.	N, O
²⁶ Al	7.4×10^5 yr.	Ar
³⁶ Cl	3.1×10^5 yr.	Ar
⁸¹ Kr	2.1×10^5 yr.	Kr
¹⁴ C	5730 yr.	N, O
³² Si	500 yr.	Ar
³⁹ Ar	270 yr.	Ar
³ H	12.3 yr.	N, O
²² Na	2.6 yr.	Ar
³⁵ S	87 d	Ar
⁷ Be	53 d	N, O
³⁷ Ar	35 d	Ar
³³ P	25 d	Ar
³² P	14.3 d	Ar

Table 1: Isotopes with half-life > 1 day produced by cosmic rays in the atmosphere. After Lal and Peters (1967)

4.2.2 ^{10}Be in the atmosphere and transportation processes

Several factors, such as stratospheric-tropospheric exchange or intratropospheric mixing, control the residence time of ^{10}Be in the atmosphere (Lal and Peters, 1967). ^{10}Be and ^7Be are scavenged by aerosols present in the atmosphere (mostly sulfates, Young and Silker, 1980; Meszaros, 1981). The path followed by these aerosols depend on mixing processes in the atmosphere during the year. The residence time of ^{10}Be and ^7Be in the stratosphere is between 1-2 years, and in the troposphere between 15 and 35 days, as it can be estimated from the production value of $^{10}\text{Be}/^7\text{Be}$ (~ 0.5) and their half-lives and from the transport processes of the aerosol in the atmosphere.

The subsequent deposition of ^{10}Be depends on precipitation, which occurs after water condensation on the sulfate particles in the atmosphere. The precipitation rate (which also depends on the latitude) is thus a factor controlling the concentration of ^{10}Be : high precipitation in the tropics causes low ^{10}Be concentration in the clouds due to dilution. Over Antarctica, for example, low rainfall (snowfall) concentrates ^{10}Be in the precipitates.

After sedimentation, ^{10}Be follows either the water circulation path (where it can be dissolved or remain in marine sediments) or is absorbed by sediment particles (generally silicates with a diameter between 0.1 and 10 μm) and may be reintroduced in the atmosphere with dust. Further precipitation brings ^{10}Be back to the earth's surface. Figure 2 summarizes the cycle of the cosmogenic ^{10}Be in nature.

4.2.3 ^{10}Be in soils

^{10}Be deposited on land will be washed into soils or transported by rivers. Moller and Wagener (1967) suggested that soils can fix ^{10}Be transported by precipitation. This observation was confirmed by further studies showing that ^7Be also becomes attached to soil particles (Brown et al., 1981).

Iron hydroxides strongly scavenge ^{10}Be , as do organic matter and clays, which provide exchange sites for ^{10}Be to be absorbed (McHargue and Damon, 1991). Generally, two main processes are responsible for the mobility of ^{10}Be : movement of particles to

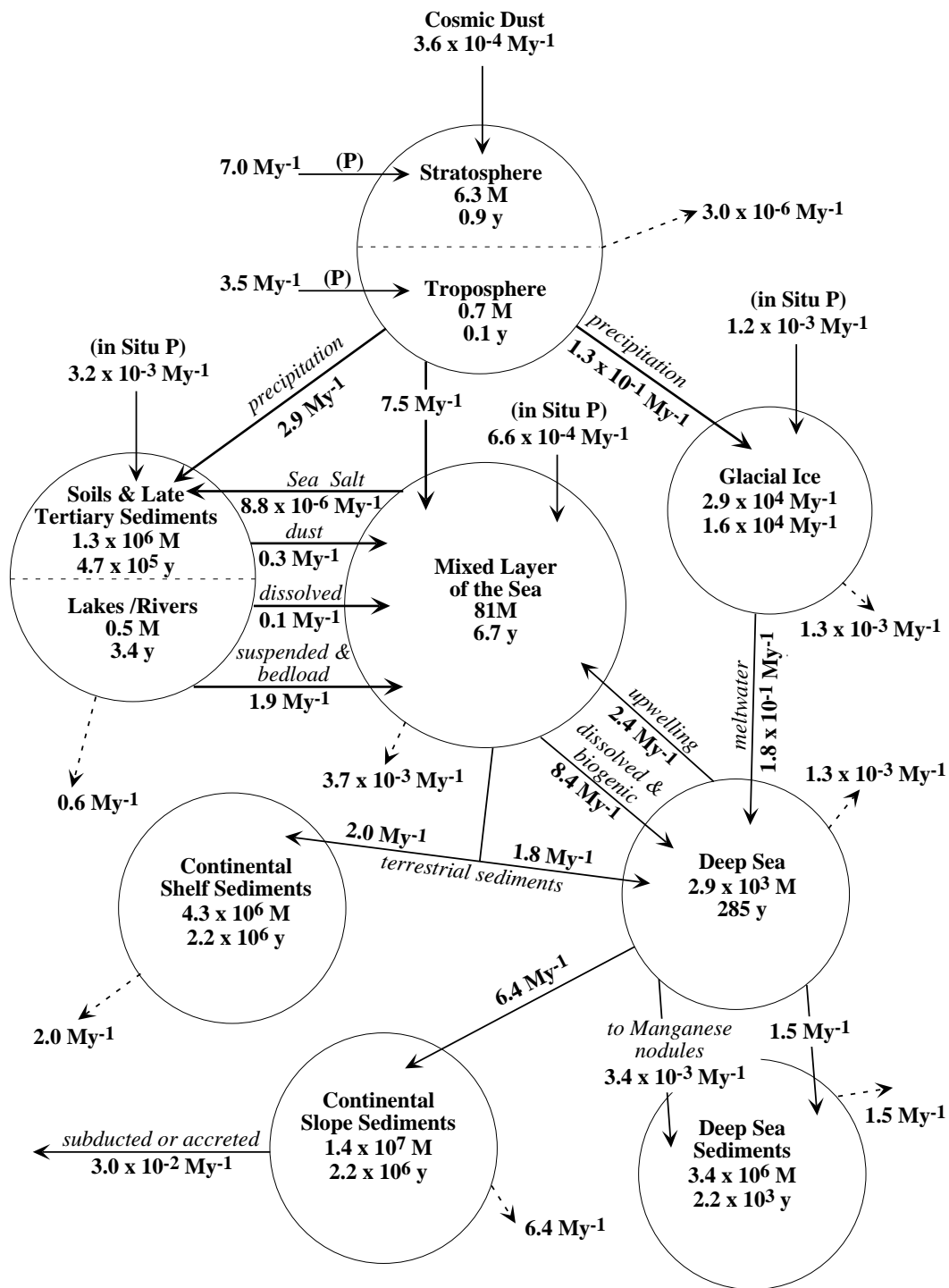


Figure 3: The cycle of cosmogenic ^{10}Be in nature. The inventory for each reservoir (circles) is expressed in moles (M), the residence time in years (y), and the flux in moles per year (My^{-1}). Cosmogenic production of ^{10}Be is indicated by a (P). Decay is represented by dashed arrows. Modified after McHargue and Damon (1991).

which ^{10}Be is attached (percolating water or mixing processes) and leaching processes. Shen et al. (1992) showed that

^{10}Be is mobilized by leaching only at very low pH values (1/3 of the ^{10}Be in a paleosol sample was removed in a solution of pH ~ 1). Carbonate dissolution also does not contribute much to the mobility of ^{10}Be (Shen et al., 1992). For pH > 5.3 , adsorption in soil occurs rapidly. On the other hand, for a stable pH, the solubility of ^{10}Be increases with increasing salinity (increased ^{10}Be solubility as ion competition for exchange site is increased, McHargue and Damon, 1991).

To evaluate the mobility of ^{10}Be in soils due to translocation processes, the distribution with depth of ^{10}Be in several soils was measured. Pavich et al. (1986) measured the ^{10}Be concentration in different soil terraces. The clay-rich B horizons showed the highest ^{10}Be concentration with a variation within the B horizon proportional to the clay content. The mobility of ^{10}Be depends on the soil forming processes: permeability of the soil decreases with time because of clay formation, and ^{10}Be translocation to depth may occur through fractures in the soil.

4.2.4 ^{10}Be , magnetic susceptibility and paleoprecipitation

Paleoprecipitation reconstruction in Chinese loess represented an important goal for environmental magnetists during the last decade. Quantitative determination of paleoprecipitation using magnetic and/or geochemical and sedimentologic climate proxies is the goal. In this section two methods will be considered: 1) the combined use of ^{10}Be and susceptibility and 2) the use of susceptibility alone. These methods are explained here as an introduction to the new results presented later in this work.

The first method takes into account the accumulation rate of ^{10}Be in loess sediments during the last 135 ka for the loess/paleosol sequence at Luochuan (Beer et al., 1993). The model separates the total ^{10}Be flux (F_B) in two components: a component brought in by the original loess dust (dust flux F_D) and an atmospheric flux component F_A . The total ^{10}Be flux F_B is given by the sum of F_A and F_D , with F_A being assumed constant. As pointed out by Beer et al. (1993), F_A is not constant, but linked to the intensity of the geo-

magnetic field, which causes important variations in the production rate of ^{10}Be (Bard et al., 1990). Another aspect to consider is the grain size dependence of ^{10}Be concentration: during cold periods the loess-forming particles are coarser, so an overestimation of the ^{10}Be flux during glacial periods may be possible (recalling that for spherical grains the ratio between surface and volume is inversely proportional to the radius).

The next step is to establishing a relationship between susceptibility and ^{10}Be . The total susceptibility flux F_S can be considered as the sum of a dust flux ($F_{D'}$) and an unknown flux component F_X , originating from *in situ* activity. To quantify F_X the following assumption was made: $F_{D'} = \alpha F_D = \alpha(F_B - F_A)$. The relative contribution of F_X to F_S is then: $F_X/F_S = (1 - \alpha(F_B - F_A)/F_S) \times 100$. Estimates made in this way indicate high F_X susceptibility components during interglacial periods (up to 80%) and low F_X during glacial periods (peak up to 45% for oxygen isotope stage 3, far below 30% for stages 2 and 4).

This approach to separating the pedogenic from the detrital susceptibility was used by Heller et al. (1993) to estimate the paleoprecipitation during the last glacial/interglacial cycle. A linear relationship between susceptibility measured in 3 different horizons (S_0 , S_5 and L_9) and present day mean precipitation was observed in four different loess/paleosol sequences in China. Using this calibration, paleoprecipitation was reconstructed for the last 130 ka at Luochuan (tab. 2).

Methods which use susceptibility only were first proposed by Maher et al. (1994). The following assumptions are involved in these models:

- A strong correlation exists between the enhancement of susceptibility in modern soil of China and the contemporary annual rainfall. The enhancement of susceptibility (in the soil B-horizon) was calculated by subtracting the susceptibility measured in the C-horizon of the most unaltered loess l_9 from the maximum value measured in the B-horizon in 9 different modern soils of the central and western Chinese loess plateau. The correlation between annual rainfall and the logarithm of the difference B-C was then expressed using a logarithmic function.

- Susceptibility enhancement reaches a steady-state relatively quickly. It was assumed that susceptibility enhancement, as well as the build up of organic matter, occurs over a few centuries or millennia. The similarity between susceptibility values measured in modern soils and in paleosols supports this assumption. The paleoprecipita-

tion values obtained by Heller et al. (1993) and Thompson and Maher (1995) are given in table 2.

Locality	last 40 years	S ₀ (11 ka)	L ₁ (60 ka)	S ₁ (58 ka)
Linxia	431	621	429	608
Xifeng	522	642	470	689
Luochuan	537	661	344	693
Luochuan*	537	600* (-9.2%)	310* (-9.9%)	540* (-22.1%)
Quinjiazhe	537	644	419	682
Baoji	565	638	559	695

Table 2: Reconstructed paleoprecipitation for the last glacial/interglacial cycle for 5 sites from the Chinese loess plateau. Data from Thompson and Maher (1995), except * (Heller et al., 1993). The duration of S₀, L₁ and S₁ is given in the column headers.

4.2.5 Chemical extraction of ¹⁰Be from loess sediments

The chemical extraction procedure used in this work is based on the work of Shen (1986). Because of the presence of Al(OH)₃ together with Be(OH)₂ solution this protocol was changed. An ion-exchange method, which is commonly used for the extraction of ¹⁰Be from ice core samples (Baumgartner, 1995) and for quartz samples (Ochs, 1996), was added. In general the extraction is performed on 16 samples in parallel, and the entire procedure takes 9 days (without measurement using an accelerator mass spectrometer (AMS)).

- **Day 1**

- a) Sample preparation

1.1) Ca. 1g of sediment is dried (80°C for ~12 hours), powdered using a mortar and poured into a 50 ml centrifuge tube.

- b) Leaching

1.2) 1 ml of ⁹Be-carrier (0.3 mg/ml) is added to the sediment using an Eppendorf autopipette.

1.3) 1 ml of H₂O₂ and 1 ml of HCl (32%) are added.

1.4) After ca. 5 min of stirring, 8 ml HCl (32%, HCl:H₂O=1:1) are given to the solution

which is then stirred.

- **Day 2**

2.1) The solution 1.4 is centrifuged for ~10 min at a speed of 4000 revs/min and the solution obtained is poured in a beaker.

2.2) The precipitated material in 2.1 is dissolved by adding 5 ml HCl (32%, HCl:H₂O=1:1) and stirred.

- **Day 3**

3.1) Solution 2.2 is centrifuged again for ~10 min at a speed of 4000 turns/min. The precipitated material will not be used again (¹⁰Be is in solution).

3.2) Solution 3.1 and solution 2.1 are dried in a beaker at ~ 80°C on a heating plate (4-5 hours).

3.3) 1 ml HNO₃ (65%) is added to the solution (stirring for ~ 5').

3.4) 1 ml HCl (35%) is added to the solution (stirring for ~ 10').

At this point all the material is in solution, which is then centrifuged in 10 ml -PP- centrifugal tubes for ~10' at a speed of 4000 revs/min. The solution is then separated from the precipitated material and put in a new beaker. At this point the majority of the Beryllium and metals present in loess are in solution.

3.5) NaOH (160g/l) is added to the solution to reach pH ~2.

3.6) 1 ml EDTA (10%) is added to the solution.

3.7) After ~30' NaOH is added to reach pH ~8.

A dense orange precipitate is obtained, which includes Be(OH)₂, Al₂(OH)₃, FeOH, MnOH.

- **Day 4**

4.1) The solution 3.7 is centrifuged in 10 ml -PP- centrifugal tubes (for ~10' at a speed of 4000 revs/min).

4.2) 5 ml NaOH (160g/l) are added, causing an increase of the pH up to ~14. Be(OH)₂ becomes redissolved.

- **Day 5**

5.1) The solution is centrifuged (for ~10' at a speed of 4000 revs/min). $\text{Be}(\text{OH})_2$ remains in solution, while the other hydroxides remain solved.

5.2) HCl (32%) is added to the solution to lower the pH down to ~ 2.

5.3) 1 ml EDTA (10%) is added.

5.4) After ~30' N_4HOH is added to reach pH ~ 8, so that $\text{Be}(\text{OH})_2$ precipitates.

- **Day 6**

6.1) The solution 5.4 containing $\text{Be}(\text{OH})_2$ is centrifuged and only the precipitate is used for the next steps. At this point the sample needs further cleaning to separate ^{10}Be and ^{10}B (Finkel and Suter, 1993). ^{10}B interferes in the AMS measurement, and has to be kept at a low level (see below). ^{10}B occurs commonly in dust and tap water (Brown, 1992). Rinsing the labware with distilled water lowers its concentration.

Demineralized water is added to the 10 ml-PP- centrifugal tube containing $\text{Be}(\text{OH})_2$ and stirred for ~1'. The solution is then centrifuged and only the precipitate $\text{Be}(\text{OH})_2$ is kept. The rinsing operation is performed 3 times. To clean the sample from the presence of $\text{Al}_2(\text{OH})_3$, a cation-exchange method is introduced.

Speciation function and elution efficiency test was performed by Ochs and Ivy-Ochs (1997) and Baumgartner (1995), who determined an elution efficiency of 87(\pm 1)%.

6.2) The solution containing $\text{Al}_2(\text{OH})_3$ and $\text{Be}(\text{OH})_2$ is brought to pH ~4 and poured in the 7 ml resin column (Biorad analytical grade Ag50W X 8 cation exchange column) which are positively charged.

6.3) The resin is penetrated with 1 column water 1 M HCl (~24 ml)

6.4) After a few minutes, the water column 1 M HCl is eluted into a 100 ml centrifuge tube. Be is detached from the resin and eluted with the water column in the centrifuge tube.

6.5) ~8 ml N_4HOH are added to the solution (that became in the meantime alkaline after having left H^+ in the resin column) and the pH rises up to ~11.

- **Day 7 and 8**

5.1) The solution is centrifuged (for ~10' at 4000 revs/min). $\text{Be}(\text{OH})_2$ precipitated at pH ~11 (step 6.5). The solution is decanted without pouring out the precipitated $\text{Be}(\text{OH})_2$. By adding distilled H_2O and successively stirring and centrifuging (twice) the solution is neutralized (pH ~8).

6.6) The residue ($\text{Be}(\text{OH})_2$) is transferred to a quartz crucible (0.4 cm diameter, 0.6 cm length) using a 0.5 disposable pipette and dried under infra-red heat lamps for ~2 hours.

6.7) Using tweezers, the crucible is moved to a quartz sled and covered with a quartz lid. The sample is placed in a muffle furnace and heated 2 hours at 150°C (final drying) and 2 hours at 850°C . The whole oxidation requires ~8 hours.

- **Day 9**

BeO is mixed with pure copper (ratio 1:4) and pressed into the 1 mm hole of the final target, a copper disk used at the PSI/ETH AMS. BeO is highly toxic (toxicity class 1) and may cause pulmonary disease with a mortality of ~10% in 224 observed cases (Baumgartner, 1995). For this reason the samples are pressed inside of a laminar in-flow dust cabinet.

4.2.6 Accelerator mass spectrometer (AMS)

The ^{10}Be concentrations are measured with an accelerator mass spectrometer, which facilitates measurements of very small amounts of isotopes (isotopic ratio of 10^{-15}). A technical description of the AMS is given in Synal et al. (1997).

Positive cesium ions strike the target surface, producing neutral, positive and negative BeO . The negative ions are then accelerated by using an electrostatic field and are focused into a beam, which will be analyzed by a first magnet. This analyzer selects the different ions with different mass. At this stage, ^{10}BeO and ^9BeO ions are moving into the tandem accelerator.

In the Tandem accelerator (Tandem Van-de-Graaff) the negative ions are accelerated from ground potential to the positively charged terminal (5.4 MeV), in order to obtain positive ions. This happens in the middle part of the Tandem accelerator, where the negative ions are stripped of some of their electrons. At this point, the now positive ions are

again accelerated and leave the accelerator with several tens of MeV.

In the following electrostatic deflector the charge state 3^+ is selected. In the magnetic mass analyzer the different masses are split into separate beams. ^9Be is measured in the Faraday cup and ^{10}Be is measured in a proportional counting chamber. To obtain a value for the $^{10}\text{Be}/^9\text{Be}$ ratio, the system is switched from ^{10}Be to ^9Be (by applying an additional voltage in the initial deflection magnet).

An isobaric atomic interference can be caused by ^{10}B . In other word, ^{10}Be and ^{10}B have the same behaviour in the accelerator, so that ^{10}B and ^{10}Be can not be discriminated. To diminish this effect, a passive absorber cell is placed in front of the ^{10}Be detector to absorb ^{10}B , although part of it forms ^7Be , a disturbing background signal due to the reac-

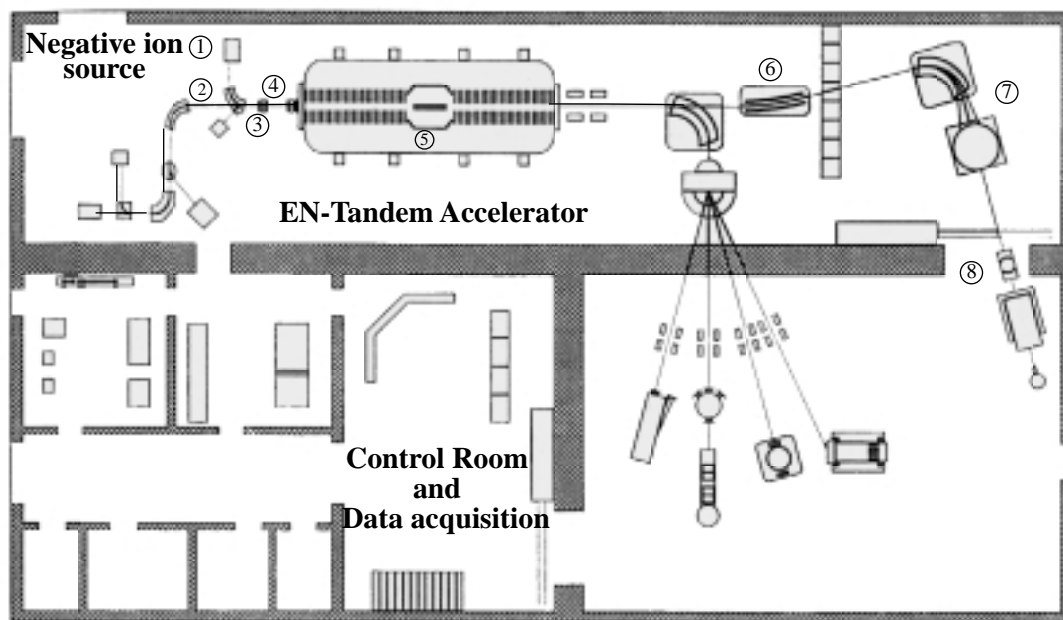


Figure 4: Floor plan of the PSI/ETH accelerator facility. The system is based on a 6 MV EN Tandem accelerator and is used for AMS (85%) and for material sciences (15%). 1) Cs gun ion source; 2) electrostatic deflector (90°); 3) Einzel lenses; 4) LE-Faraday cup; 5) Stripper; 6) Electrostatic deflector (15°); 7) Magnetic mass analyzer; 8) counting chamber (7 and 8: ^{36}Cl set up), (Modified after Synal et al., 1997).

tion $^{10}\text{B}(\text{H}, ^4\text{He})^7\text{Be}$. Nevertheless the background of the Zurich AMS system is $\sim 10^{-14}$, two orders of magnitude smaller than the measured $^{10}\text{Be}/^9\text{Be}$ ratio of 10^{-12}). The $^{10}\text{Be}/^9\text{Be}$ ratios measured with the Zurich AMS facility are not absolute. For this reason the

obtained results are normalized using standard samples. For $^{10}\text{Be}/^9\text{Be}$ the standard S555 is used ($^{10}\text{Be}/^9\text{Be S555} = 95.5 \times 10^{-12}$).

Each measurement is performed at least twice. Errors may result from counting errors (according to Poisson statistics the error can be estimated from the square root of the number of counts. The maximal value chosen in this work is 6%), from the Bor correction (varying between 0-4% for 80% of the measurements and between 4-10% for the remaining 20% of the measurements) and from the standard error (between 1-2%).

Chapter 1

DETERMINATION OF THE MATUYAMA/BRUNHES BOUNDARY (M/B) AND MAGNETIC PROPERTIES OF LOESS GRAIN SIZE FRACTIONS FROM THE SECTION AT PAKS (HUNGARY)

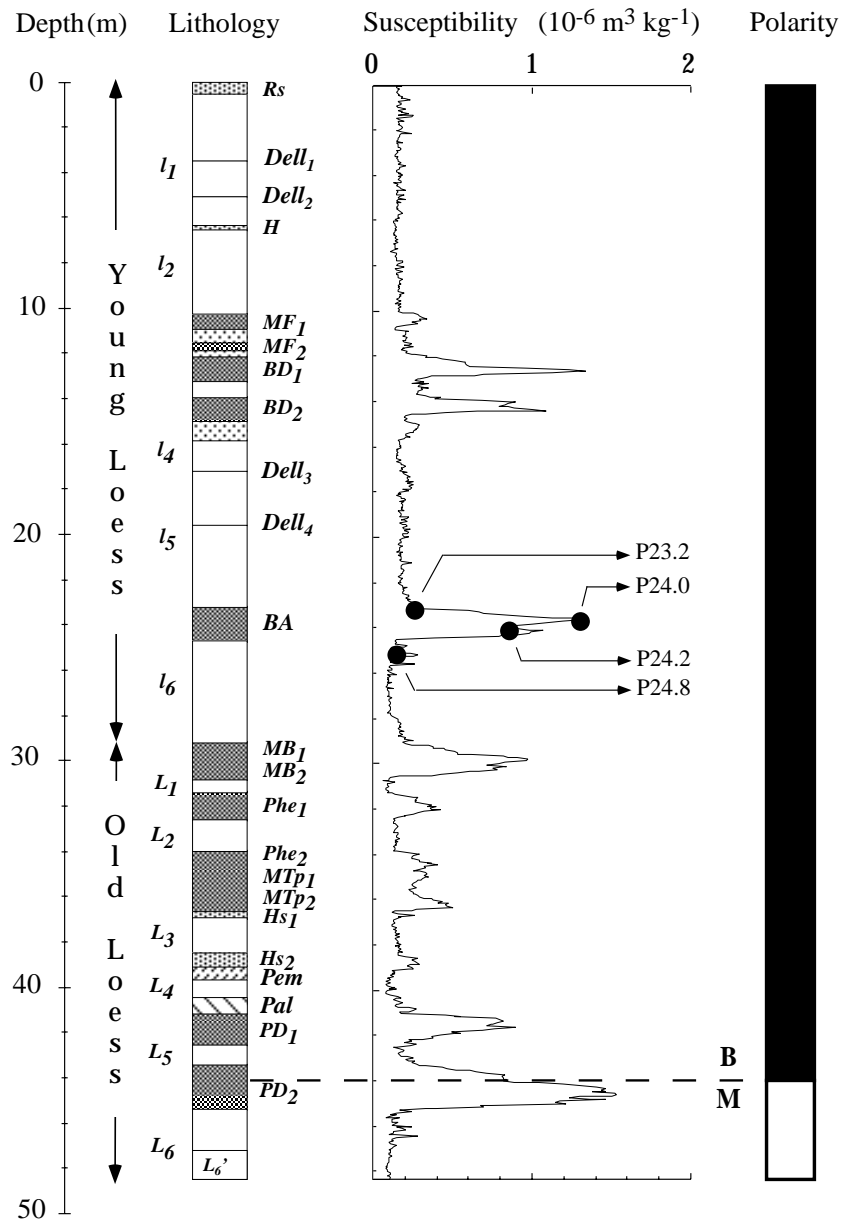
1.1 Introduction

Hungarian loess-paleosol sequences have been extensively studied during the last decades in an attempt to reconstruct the Quaternary climate changes in the middle Danube basin.

The most complete sections studied in this region (over 50; Hahn, 1987) expose 12-13 loess units, 8-13 paleosols and 2-3 sand layers (Pécsi, 1987). They are similar to the present loess-paleosol sequence at Paks brickyard (46.6°N, 18.8°E), which is 49 m thick and has been subdivided into the “young loess” series (uppermost 30 m) and the “old loess” series (Pécsi, 1979). The “young loess” contains 6 loess layers (numbered I1 to I6) interbedded with the paleosols MF₁ and MF₂ (Mende upper), BD₁ and BD₂ (Basaharc double) and BA (Basaharc lower). In this part of the section, loess layers are predominant (only 25% of the “young loess” are paleosols or embryonic soils). In the “old loess”, thin loess layers (L₁ to L₆ and L'₆, thickness < 2 m) are intercalated with the paleosols MB₁ and MB₂ (Mende Base), Phe₁ and Phe₂, MTP₁ and MTP₂, PD₁ and PD₂ (Paks Lower Double).

The major problem is establishing a reliable chronology and several interpretations have been proposed. Our recent paleomagnetic investigations place the Matuyama/Brunhes boundary at a profile depth of nearly 44 m (Heller et al., 1996) confirming in principle the earlier results of Márton (1979). In order to obtain reliable age data for the youngest interglacial paleosols, different methods are needed, but the results are still in conflict. Using thermoluminescence (TL) and infrared stimulated luminescence (IRSL) dating, Frechen et al. (1997) determined that MF₁ formed during the interstadial corresponding to oxygen isotope stage 3. For paleosol MF₂ an age corresponding to the penultimate glaciation was measured (oxygen isotope stage 7), which implies a considerable time gap of ~70 ka between MF₁ and MF₂. According to these observations the paleosols BD₁ and BD₂ did not form during the last interglacial as previously claimed (Pécsi, 1991; Zöller and Wagner, 1990), but are older.

Thermoluminescence dating by Zöller et al. (1994) yields a formation age for paleosol BA corresponding to marine $\delta^{18}\text{O}$ stage 9 or paleosol S₃ on the Chinese loess plateau (e.g. Heller and Evans, 1995). An aminostratigraphic investigation by Oches and McCoy (1995) confirms this result: the boundary between BA and I₆ at Paks corresponds to Kukla's (1977) termination 4 at the beginning of glacial cycle D with a SPECMAP age



P23.2 $\chi = 21.6 \times 10^{-8} \text{ (m}^3\text{kg}^{-1}\text{)}$	P24.0 $\chi = 126 \times 10^{-8} \text{ (m}^3\text{kg}^{-1}\text{)}$
P24.2 $\chi = 101 \times 10^{-8} \text{ (m}^3\text{kg}^{-1}\text{)}$	P24.8 $\chi = 14.8 \times 10^{-8} \text{ (m}^3\text{kg}^{-1}\text{)}$

Figure 1: Lithology (after Pécsi et al., 1995), specific magnetic low field susceptibility χ and interpreted magnetic polarity of the loess sequence at the Paks brickyard as a function of profile depth. The section is divided into the upper part of the "young loess" sequence (l layers) and the lower part of the "old loess" sequence (L layers). Both sequences contain a number of paleosols (shaded) which usually are named according to Hungarian type localities (for nomenclature of paleosol abbreviations see Pécsi, 1979). The Matuyama/Brunhes boundary was determined at 44.1 m depth, in the top of pedocomplex PD₂ ("Paks Double 2"). The positions of the four analyzed samples (P23.2, P24.0, P24.2, P24.8) in and around the paleosol BA ("Basaharc Lower") are indicated on the susceptibility profile.

of 339 ky (Imbrie et al., 1984).

Rock magnetic measurements were performed on samples collected in the paleosol BA and in the loess layers l_5 and l_6 , on the upper and lower limits of paleosol BA (Fig. 1). The faintly weathered sample P23.2 was extracted from the very bottom of the well structured loess layer l_5 which is characterized by the presence of calcareous nodules and low bulk susceptibility. Samples P24.0 and P24.2 were collected in the paleosol BA ("Basaharc Lower"), a chernozem-like forest steppe soil, containing krotovinas with diameters up to 20-30 cm and exhibiting clearly enhanced susceptibility. Sample P24.8 was taken in the underlying loess layer l_6 which is distinguished by intrusion of calcareous concretions from the overlying paleosol BA.

In general, low field susceptibility and other magnetic parameters are enhanced in the paleosols and weathered loess beds which were produced or altered during warmer and more humid climate episodes, most probably due to *in situ* formation of new ferri-magnetic minerals (Zhou et al., 1990). This enhancement is closely connected to strong frequency dependence of the susceptibility signal which indicates predominance of very fine grained (≤ 30 nm diameter) superparamagnetic ferrimagnetic minerals (Forster et al., 1994). Because of the potential for paleoclimatic modeling, the type and grain size distribution of these minerals need to be investigated in great detail in both loesses and paleosols in order to foster future models which aim to establish a quantitative correlation between magnetic properties and paleoclimate factors such as precipitation and temperature: for this reason, all four samples have been fractionated and grain size fractions spanning from 50 μm to 30 nm were obtained and their magnetic properties were studied.

1.2 Lithology

The 49 m thick loess/paleosol profile at the Paks Brickyard is divided into a "young loess" (the upper 29.3 m) and an "old loess" sequence (Fig. 1). The following description and the lithological, chemical and sedimentological data in figure 2 are based on the work of Pécsi et al. (1995).

1.2.1 Young Loess

The uppermost part of the young loess is formed by a 0.5 m thick zonal chernozem type soil (Rs), with typical carbonate accumulation horizons. Small calcretes are scattered down to 1.5 m depth into the typical loess l_1 , which is a structured fine sandy loess, with calcareous mycelia, scattered manganese patches, small calcretes, rootprints, earthworm burrows and occasional thin fine sand intercalation, representing layered delle infillings. Loess layer l_1 , divided from l_2 by a structured steppe embryonic soil (H), is weakly or moderately structured. Loessification was more effective in loess layer l_2 , due to a relatively slow accumulation of minerals.

The double soil MF_1 and MF_2 below loess layer l_2 is a crumbly chestnut steppe soil (MF_1), a well developed calcareous loess accumulation horizon (genetically regarded as a part of the soil) and a highly crumbly soil (MF_2) with numerous krotovinas in its accumulation horizon.

In a large part of the Paks Brickyard section, the soils MF_1 and MF_2 are completely missing as a result of erosion, confirmed by the presence of a minor stratigraphic hiatus corresponding to the formation of paleosol MF_2 . The loess underlying the MF_2 paleosol is ~20 cm thick. Probably it was also partly removed by erosion.

The paleosol BD_1 follows at 12.4 - 13.36 m showing a C_{ca} horizon. The soil is strongly crumbly and greyish brown. Its lower part is of dark chestnut color and contains rootprints, earthworms, insect burrows and krotovinas of some cm diameter. A similar steppe paleosol BD_2 was formed at 14.2-15.1 m, containing krotovinas in the accumulation horizon. Paleosol BD_1 lies on the top of a loess of some dm thickness with reworked soil fragments. Below, the first loess is encountered containing calcareous concretions of 2 to 5 cm size at 16.4-16.5 m.

In the lower part of the “young loess”, between 16-23.1 m, loess units l_4 and l_5 consist of fine sandy loess, typical loess and loessy sand layers. It is interpreted as a typical layered sandy slope loess infilling of a major delle between 20-23 m, the “young loess” is well structured, with manganese precipitation and small calcretes, with major calcareous nodules occurring at 23 m depth, similar to those found in the old loess sequence. A reworked soil containing loess of solifluction origin is observed at 22.3 m and 23.3 m.

The paleosol BA, between 23.3-25.1 m, is a chestnut, chocolate colored, structured

steppe soil with large (20-30 cm in diameter) krotovinas. Pale and dark brown soil fragments at 23.5-23.9 m result in a characteristic variegated color and fabric (semipedolith). The BA soil is strongly bioturbated by earth worms. These give a characteristic appearance to the paleosol not only in Paks but in other key loess section in Hungary as well.

The accumulation horizon of the BA soil with big calcareous concretions (“loess dolls”) intrudes into the underlying loess l_6 as deeply as 1 m. Between 26-29 m there is a moderately structured, compact, old loess containing micas and snail remains with small calcretes and manganese patches. At 28.1-28.9 m l_6 is intercalated by two thin embryonic soil or semipedolith horizons; this is a transitional layer to the underlying MB paleosol.

1.2.2 Old Loess

A distinguishing characteristic of the “old loess” series are the densely packed reddish-brown “mediterranean-type” forest soils, resulting from warmer and wetter climate. The lower susceptibility values measured in these paleosols with respect to paleosols BD and BA reflect observations made at other eastern European loess/paleosol sequences (Tsatskin et al., 1998; Spassov, 1998), where a major susceptibility enhancement for the youngest paleosols was measured.

The upper part of the “old loess” is represented by the strikingly crumbly, chestnut MB paleosol, with steppe type krotovinas, and earthworm burrows filled with light or dark colored soils. An accumulation horizon with vertical carbonate nodule separates the paleosol MB_1 and MB_2 . The main part of the C_{ca} horizon of MB_2 is represented by the calcareous “old loess” layer L_1 (Fig. 2a).

The next paleosol at 31.37-32.6 m is a crumbly light grey steppe soil, designated Phe_1 . Its upper part is a structured embryonic soil, with carbonate tubes and manganese patches.

Phe_2 , between 34.2-35.1 m is a moderately crumbly, rusty brown sandy forest steppe soil, formed on a sand layer, with its lower part containing 52% sand grains (Fig. 2d). Its lower boundary is very sharp. An erosional hiatus is assumed here. The old loess L_2 between Phe_1 and Phe_2 is well structured, with few manganese patches and carbonate tubelets. It includes two horizons with large calcareous concretions (loess dolls). Two paleosols (MTP_1 and MTP_2) are superimposed on each other at 35.1-35.9 and 35.9-36.8

m. The upper one is a crumbly steppe soil with krotovinas. Its sand and clay content are both 31%. This passes to the strongly clayey soil unit MTp₂, which is a dark brown, crumbly meadow chernozem soil with many calcareous mycelia and calcretes. Sporadica-

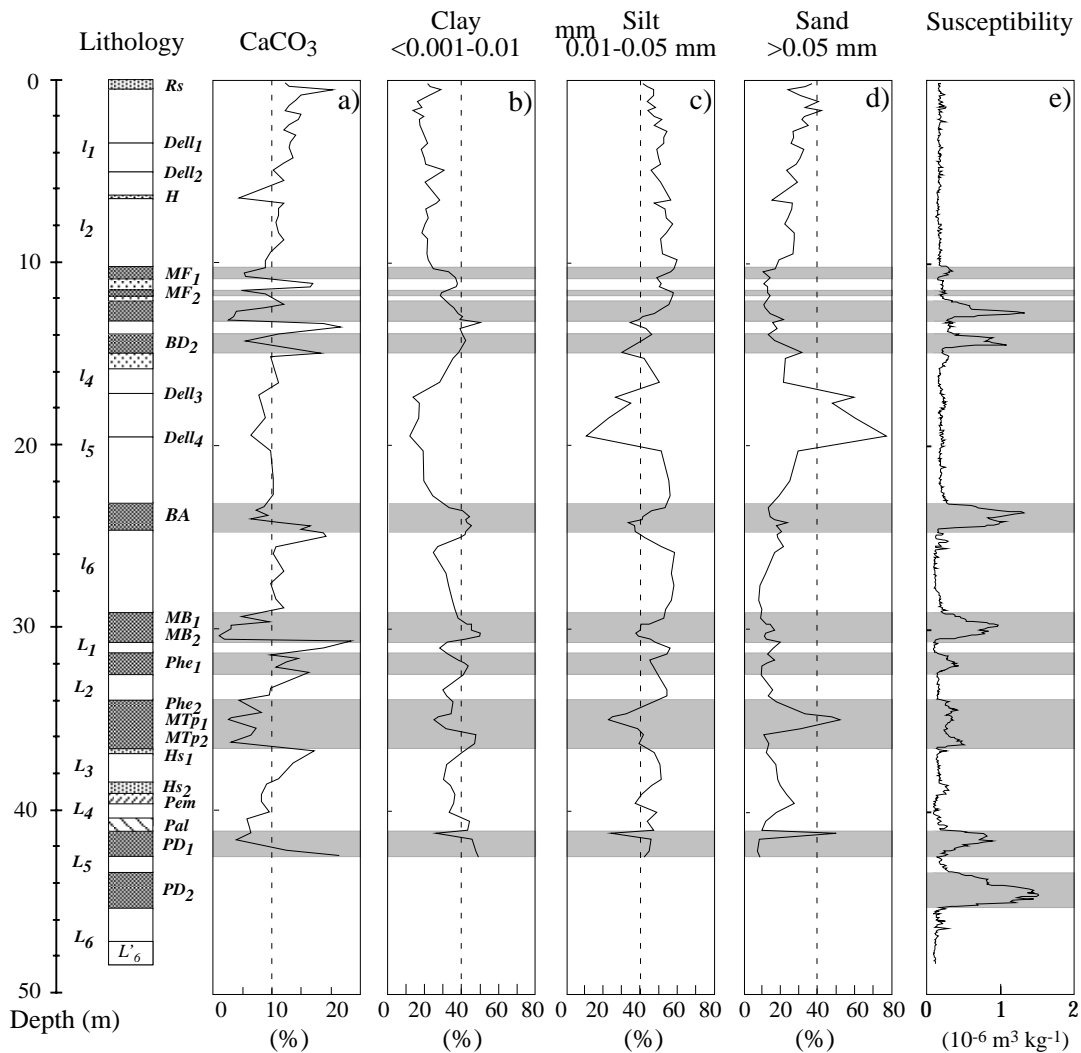


Figure 2: Carbonate content (a), granulometric composition (b, c, d), and susceptibility (e) as a function of depth of the loess/paleosol profile at Paks Brickyard. 104 block samples of a mean thickness of 13 cm were used for the granulometric and carbonate analysis. The median point of each block was used as reference depth. Clay fractions represent a grain size < 0.01 mm, the silt fraction grain sizes between 0.01-0.05 mm and the sand fraction grain sizes > 0.05 mm (from Pécsi et al., 1995).

lly it contains rusty patches, and has a clay content of 47%. The accumulation horizon of the soil is a 30 to 40 cm thick carbonate layer. Pécsi (1987) defines MTp as a gleyed hydromorphous soil. This interpretation was made on a previous studied section at Paks, because the low susceptibility values are not typical for a chernozem-type soil.

Layered old loess L_3 is found at 36.8-38.4 m. Its upper part is a brownish grey, strongly calcareous, crumbly, pedogenically altered old loess H_{S1} (embryonic soil), with numerous calcareous mycelia. The entire layer is transected by vertical earthworm burrows infilled with material of paleosol MTP_2 . The slightly altered layer H_{S2} , between 38.4-39.45 m, with many manganese patches, sporadically with carbonate concretions and loess dolls, and the embryonic soil Pem (Pem: Paks embryonic soil) define the transition from L_4 to L_3 . Below L_4 , at 40.4-41.2 m, the Paks alluvial soil (Pal) was identified, a chocolate brown valley-bottom floodplain paleosol, sporadically with carbonate concretions and thin sand layers.

Between 41.2-41.45 m a stratified coarse sand was found, which is slightly clayey. It is sharply delimited from the underlying PD_1 , a chestnut steppe soil (Fig. 2d). The thickness of the sand may exceed one meter at the central part of the Paks brickyard wall. It represents a significant erosional hiatus.

The pale yellow old loess L_5 continues the section downwards between 41.2-43.7 m. It is moderately structured, contains grey patches, due to reduction and carbonate tubellets of rootprints origin, and big calcareous concretions in two levels as well as earthworm burrows throughout the entire layer, filled with material of paleosol PD_1 . L_5 is mainly the accumulation horizon of the PD_1 paleosol, which has a chestnut steppe soil character between 41.2-42.3 m. The reddish chestnut steppe soil PD_2 between 43.7-45.2 m is darkening downwards, strongly crumbly, with krotovinas. The upper- and lowermost 20 cm of this soil are built of light and dark soil fragments (pedosediment).

A moderately structured loess is situated between 45.2-48.9 m. Its one meter thick upper part is the accumulation horizon C_{ca} of the overlying soil PD_2 , with snails, krotovinas and concretions, down to 47.7 m. At this level, a hiatus is marked by the horizontally arranged concretions. This is the upper boundary of the old loess L'_6 .

1.3 Experimental results

1.3.1 Natural remanent magnetization (NRM)

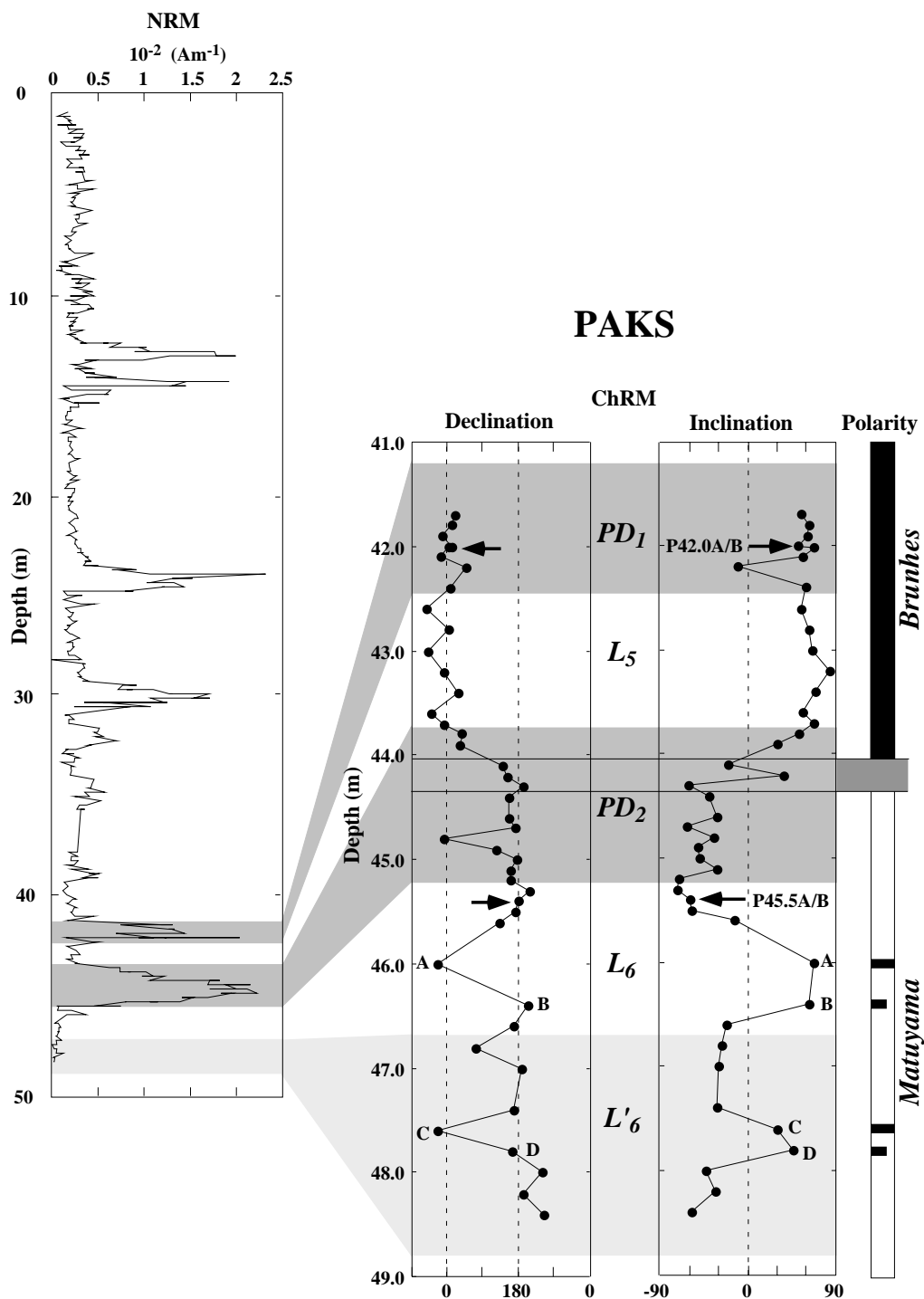


Figure 3: NRM intensity, ChRM declination and inclination and interpreted polarity of the lower part of the “old loess” sequence at Paks brickyard as a function of profile depth. The abbreviations indicate the loess (L_5 , L_6 and L'_6) and the paleosol layers (PD_1 and PD_2) according to the description given in figure 1. The letters A, B, C and D indicate samples with anomalous declinations and inclinations.

NRM intensity measured through the profile show high intensities in correspondence to the paleosol layers, with peak values $> 20 \text{ mAm}^{-1}$ in the chestnut steppe soil BA, PD₁ and PD₂. The forest soils BD₁ and BD₂ in the “young loess” series, MB, PD₁ and PD₂ in the “old loess” series show values between 15 and 20 mAm^{-1} . Values below 0.5 mAm^{-1} are characteristic for the loess layers (Fig. 3).

Alternating field and thermal magnetization was performed on 43 samples between 41.7-48.4 m depth (Fig. 3), using as reference the previous paleomagnetic investigation performed on Hungarian loess, which placed the M/B boundary in the lower part of the sequence (Márton, 1979). In this interval, high NRM intensities are observed in the paleosols (average: 11.4 mAm^{-1} for PD₁ and 15.3 mAm^{-1} for PD₂) and lower values in the loess layers (average: 3.4 mAm^{-1} for L₅ and 2.1 mAm^{-1} for L₆ and L'₆).

Only normal magnetization directions, i.e. north and downward directed components, characterize two samples taken at 42.0 m depth (P42.0 a, b, Fig. 4) during both demagnetization procedures. At 45.5 m depth, thermal demagnetization removes a normal NRM component up to 300°C, and reveals a reversed characteristic magnetization which is stable up to 575°C (Fig. 4b'). AF demagnetization is not successful in evaluating this reversed component. Even at higher fields ($\leq 60 \text{ mT}$, Fig. 4b) the normal NRM persists. This is taken as evidence that a high coercivity overprint could not be removed and that the ChRM at least partly resides in hematite with a wide range of unblocking temperatures probably from room temperature up to 600°C.

The uppermost sample with reversed polarity was observed at a depth of 44.1 m. The transition from the Matuyama to the Brunhes period, however, is not without uncertainties because a few samples at greater depth (A, B, C and D in Fig. 3) are still normally magnetized. It is difficult to decide whether they are completely remagnetized during the Brunhes epoch or if they give further support to the existence of a M/B precursor event as postulated by Clement and Constable (1991).

During thermal demagnetization the magnetic properties of the sediment can be disturbed by the formation or destruction of magnetic minerals. For this purpose low field susceptibility was monitored during stepwise heating for the paleosol layers PD₁ and PD₂ (7 and 12 samples, respectively) and the loess layers L₅ and L₆ (+L'₆) (6 and 13 samples, respectively)(Fig. 5). The susceptibility of the samples from paleosols PD₁ and PD₂ as

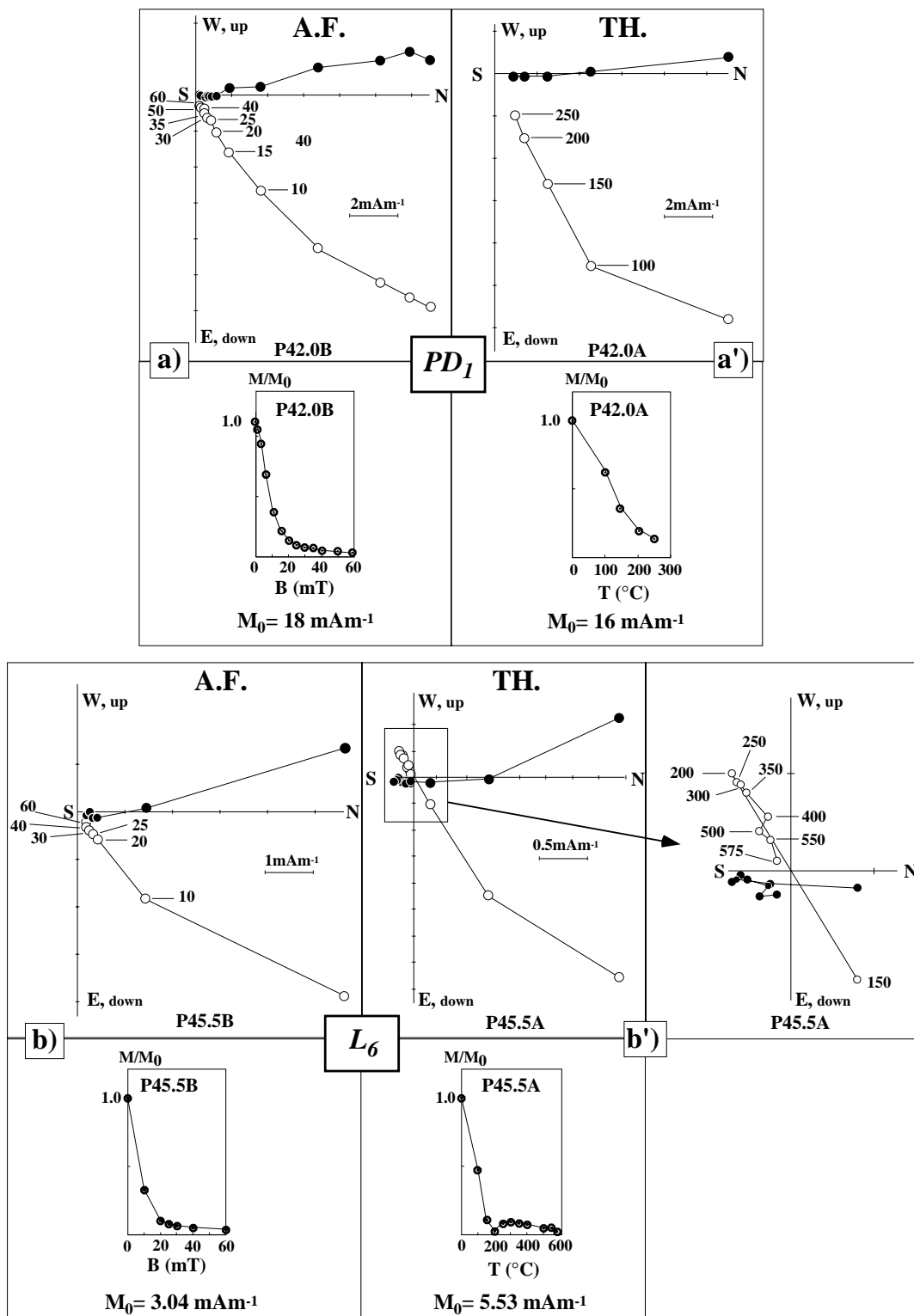


Figure 4: NRM vector and intensity of four samples during stepwise thermal and AF-demagnetization. Two samples originating from the Brunhes epoch (P42.0 A and B from paleosol PD₁) and two from the Matuyama epoch (P45.5 A and B from loess L₆) were taken as representative examples to show the different behaviour during AF-demagnetization (a and b) and thermal demagnetization (a' and b'). The number in the sample code represents the profile depth (see figure 3).

well as those of the loess L_5 and $L_6(+L'_6)$ varies little below 300°C . At 300°C , susceptibility increases slightly in the paleosol samples (between 5 and 12% for PD_1 and between 2 and 15% for PD_2) in contrast to the loess samples in which susceptibility is strongly enhanced (between 21 and 63% for L_5 and between 19 and 72% for $L_6(+L'_6)$).

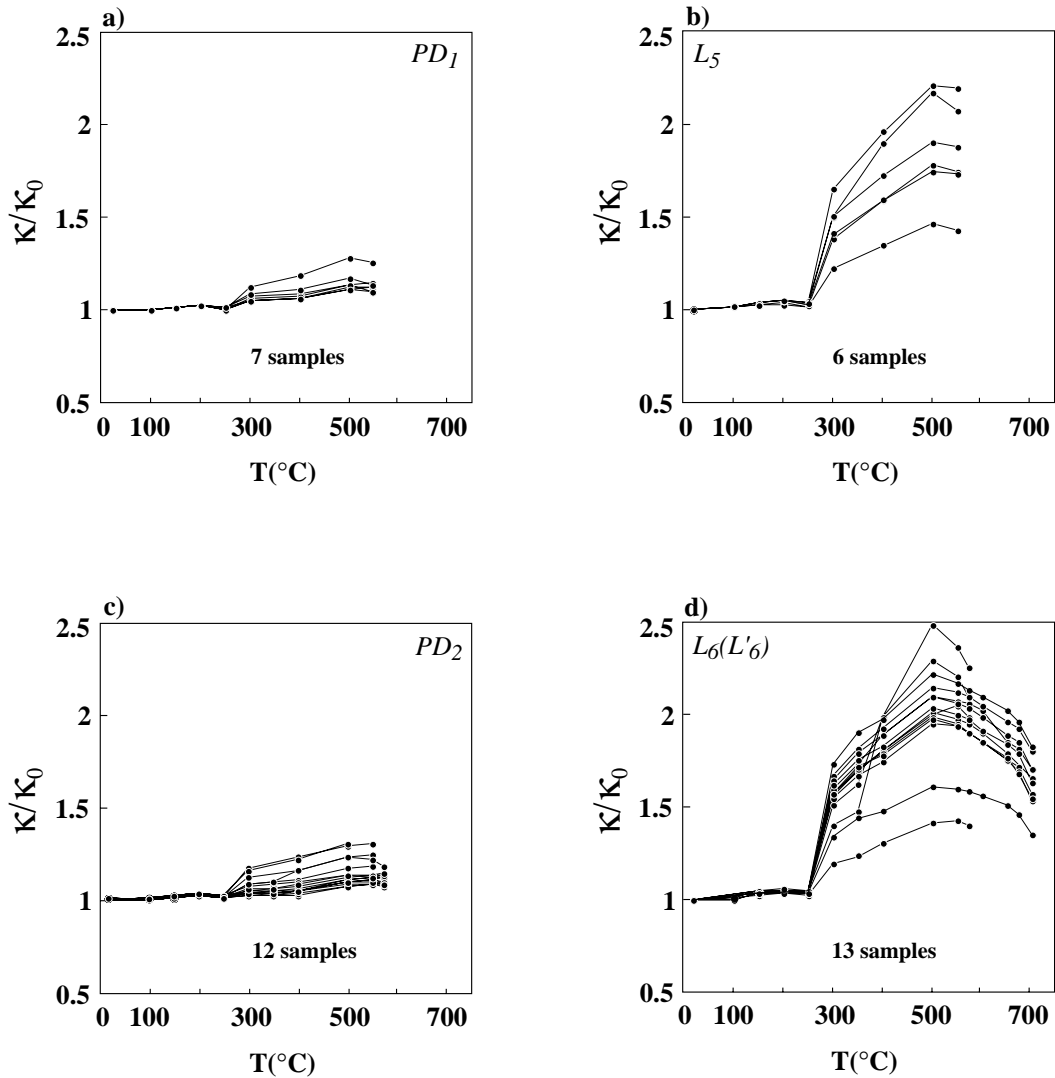


Figure 5: Normalized susceptibility variations during stepwise heating of the samples used for determination of the ChRM (figure 3). The samples are heated up to 550°C (700°C for loess $L_6(+L'_6)$), the heating steps varying between 25° and 100°C . Weak susceptibility increase was measured in the paleosol layers (a and c), while in the loess layers (b and d) the increase can exceed a factor 2. The values at room temperature were used to normalize (κ_0).

Possibly lepidocrocite (γ -FeOOH) converts to maghemite between 250-350°C (Ödземir and Dunlop, 1993), or forms new magnetite grains. The susceptibility increase in the loess samples may be due to an important neoformation of magnetite.

At higher temperatures, susceptibility increases further by a max. 30% in the paleosols, but up to 150% in the loesses. The peak values for all samples are reached at 500-550°C. In the loess L₆ (+L'₆) a steady decrease follows from 550 to 700°C, probably being due to partial oxidation of magnetite/maghemite to hematite.

1.3.2 Low field susceptibility (χ) as a function of grain size

The susceptibility (χ) of the two samples P24.0 and P24.2 from the Lower Basaharc paleosol horizon BA is enhanced by a factor 5 - 8 compared to the loess samples P23.2 and P24.8 (Fig. 1). The susceptibility of the fractionated samples depends strongly on grain size (Fig. 6). It increases from extremely small values in the coarse fractions to maximum values in the fraction “VIII” (see also chapter 3, Part I).

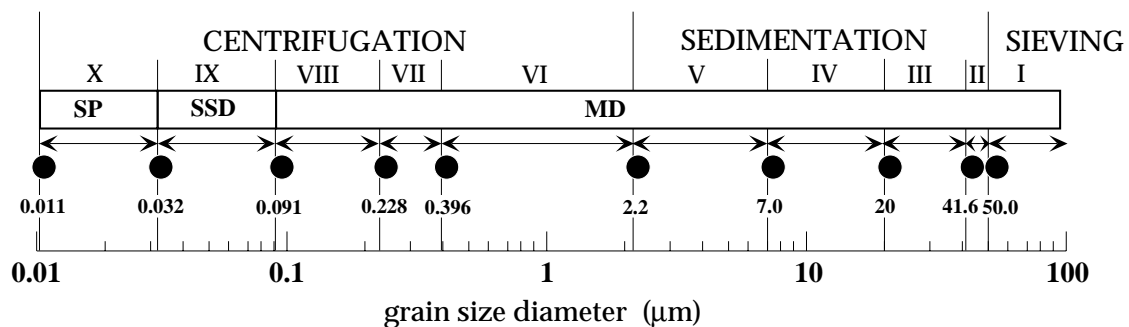


Table 1: Ten grain size fractions have been obtained by sieving (one fraction with grains > 50 μm), fractional sedimentation (four fractions with a grain size distribution between 50 μm and 2.2 μm) and fractional centrifugation (five fractions with grain size distributions between 2200 nm and 11.5 nm). Each fraction is represented by a roman number, from "I" for the largest fraction to "X" for the finest fraction. The grain size for fractions "II" to "X" corresponds to their hydrodynamic diameter, obtained from Stokes' law for sedimentation and centrifugation processes. If fractionation is perfect, superparamagnetic (SP) grains should be found in the finest fraction "X" with grain sizes < 30 nm (e.g. Forster et al., 1994), stable single domain (SSD) grains in fraction "IX" with magnetic grains between 30 and 100 nm (e.g. Maher, 1988), and multidomain (MD) grains in the remaining larger fractions "VIII" to "I". The black dots indicate that the fraction properties are always plotted at the lower grain size limit of each fraction. For details see part I, chapter 3.

Susceptibility decreases again in the two finest fractions ("IX" and "X", see table 1) of all samples. The susceptibility changes in the fine fractions are much more pro-

nounced in the paleosols.

Susceptibility enhancement in the loess samples increases nevertheless clearly from the grain size fraction "VI" to "VIII" and susceptibility decreases again in the two smallest fractions. The mass distribution in the loess samples is irregular but reaches nearly 50% in the silty fraction "II" (41.6 – 50 μm) of loess sample P23.2 whereas the fine fractions below 0.396 μm contribute less than 1 % of the total mass of loess sample P24.8.

The pedogenically most strongly developed paleosol sample P24.0 has a significant mass contribution with > 10% in the fine fractions below 0.396 μm and the silty fraction "II" is reduced to < 35%. In the loess samples, the mass distribution is the critical factor controlling the susceptibility contributions of the fractions to the total susceptibility, i.e. susceptibility contribution follows closely the mass distribution and contribution maxima are observed in the coarser fractions.

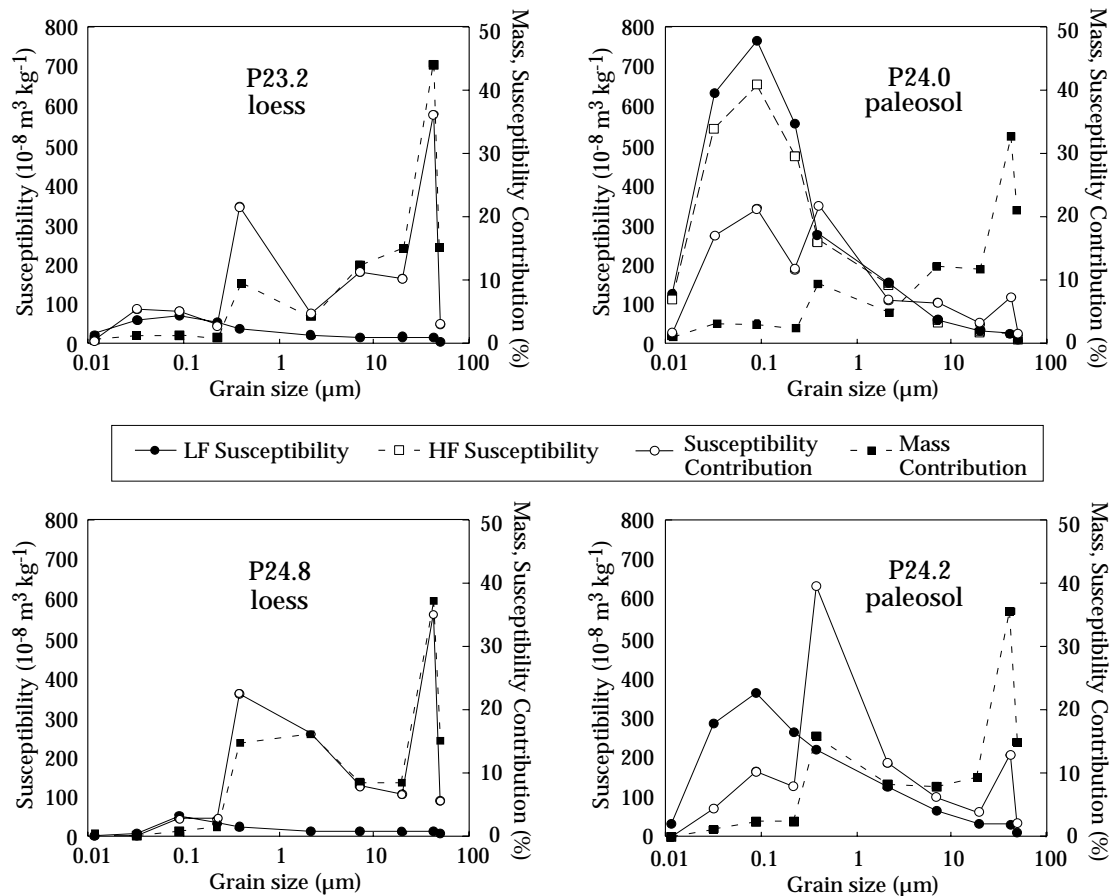


Figure 6: Low field susceptibility measured at low frequency (KLY-2: 980 Hz), mass distribution and susceptibility contribution of the grain size fractions for the loess (P23.2 and P24.8) and paleosol samples (P24.0 and P24.2) from Paks. High frequency susceptibility (Bartington: 4.7 kHz) is clearly reduced in the fine grained magnetically enhanced fractions of paleosol sample P24.0.

In the paleosols, however, maximum susceptibility contributions are migrating towards the finer fractions between 2.2 μm and 0.091 μm with increasing susceptibility enhancement. About 70% of the susceptibility signal resides in the fine grained fractions "VI" to "IX" of the strongly enhanced paleosol P24.0.

The Bartington dual frequency sensor was sensitive enough to determine the susceptibility frequency dependence of the grain size fractions of the most strongly magnetized paleosol (P24.0). The superparamagnetic grains are concentrated in the fine fractions ("VI" to "VIII") where the F-factor ($\chi_{\text{FD}} = 100 (\chi_{\text{LF}} - \chi_{\text{HF}}) / \chi_{\text{LF}}$) varies between 12.1% and 14.5% (Table 2).

SAMPLE P24.0

Fraction	I	II	III	IV	V	VI	VII	VIII	IX	X
F(%)	6.3	5.0	5.1	4.5	9.5	15.0	14.5	12.1	—	—

Table 2: Susceptibility frequency dependence (F-factor) of the grain size fractions of sample P24.0. An increase toward the finest fraction is observed. Fractions IX and X could not be measured due to the limiting sensivity of the Bartington dual frequency sensor.

1.3.3 Hysteresis parameters as a function of grain size

Low field susceptibility, coercive force $(B_o)_c$ and coercivity $(B_o)_{cr}$, plotted against grain size for loess sample P23.2 and for paleosol sample P24.2 behave differently according to lithology (Fig. 7). In the strongly weathered paleosol sample P24.2 with enhanced bulk susceptibility (Fig. 1), $(B_o)_c$ and $(B_o)_{cr}$ have their maximum values in the coarser fractions ($(B_o)_c \approx 12$ mT; $(B_o)_{cr} \approx 32$ mT). Both coercivity parameters decrease rather smoothly with decreasing grain sizes and reach minimum values between 0.1 and 1 μm at $(B_o)_c \approx 7$ mT and $(B_o)_{cr} \approx 20$ mT. In the smallest grain size fractions ("IX" and "X", tab.1), where susceptibility becomes very small, $(B_o)_c$ and $(B_o)_{cr}$ increase again to values similar to the maximum values in the coarse fractions. In the little altered loess sample P23.2, $(B_o)_c$ and $(B_o)_{cr}$ again vary inversely with susceptibility except that the two finest fractions ("VIII" and "IX") decrease continuously. Fraction "X" could not be measured because of the extremely tiny amount of material available. The hysteresis parameters of the coarse grained fractions between 1 and 50 μm are high and fairly constant ($(B_o)_r \approx 17$ mT; $(B_o)_{cr} \approx 60$ mT) and drop rapidly with decreasing grain size to values of $(B_o)_c \approx 3$ mT and $(B_o)_{cr} \approx 8$ mT.

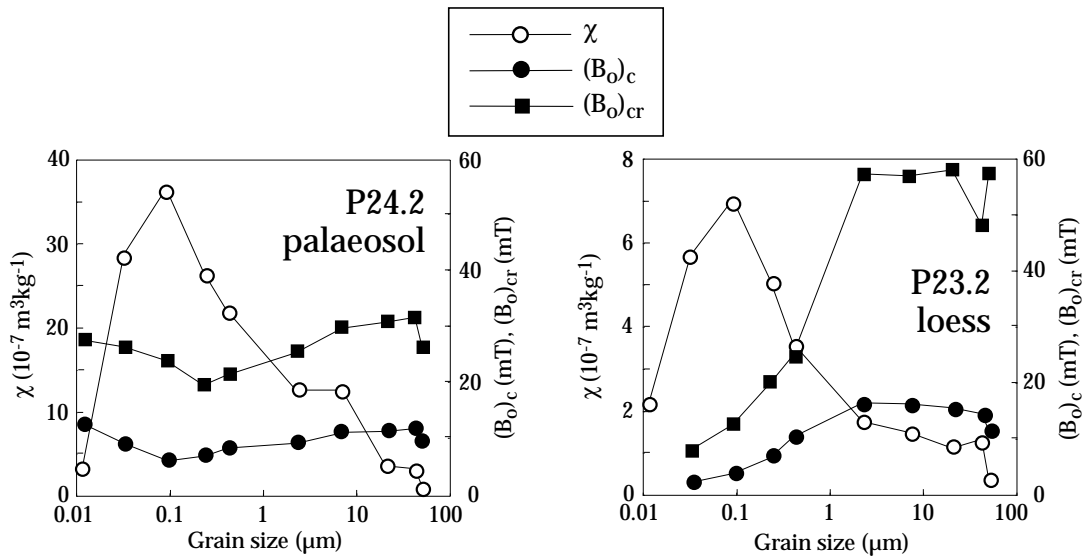


Figure 7: Low field susceptibility, coercivity (B_{0c}) and coercivity of remanence (B_{0cr}) as function of grain size for the slightly weathered loess sample P23.2 and palaeosol sample P24.0.

High field susceptibility (χ_h) was determined on bulk samples taken from different layers in the Paks sequence (Fig. 8). No significant correlation of χ_h with the low field susceptibility is observed (cf. Forster and Heller, 1997). χ_h varies very little between 0.016 and 0.061 x 10⁻⁶ m³kg⁻¹ over the whole low field susceptibility range.

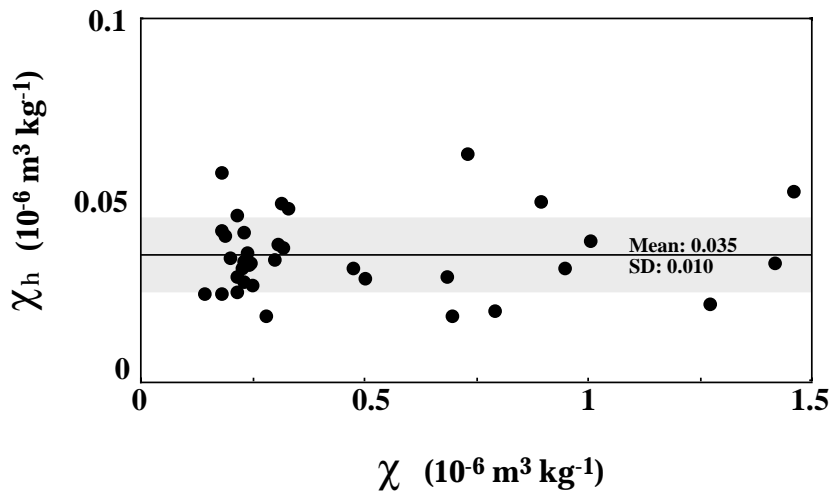


Figure 8: High field susceptibility (χ_h) as a function of low field susceptibility (χ) for a number of arbitrarily selected samples from the loess sequence at Paks.

1.3.4 Low temperature TRM

TRM experiments (Fig. 9) were carried out using the bulk loess sample P23.2 and three of its grain size fractions (fractions "III", "V" and "VIII") in fields of 8 mT or 1 mT. The strength of the applied field strongly influences the shape of the TRM curves. The 1 mT TRM of fraction "VIII" decays almost linearly with increasing temperature whereas the temperature dependence of the 8 mT TRM decay has a distinctly concave shape. The TRM curves for the bulk sample and the fraction "V" are also field dependent with different gradients especially above 120 K. A kink in the TRM(T) curve between 100 K and 120 K for the bulk sample is interpreted as evidence of the magnetite Verwey transition (cf. Banerjee et al., 1993). This kink is also seen faintly in the fraction "III", but is virtually absent in the finest fractions "V" and "VIII".

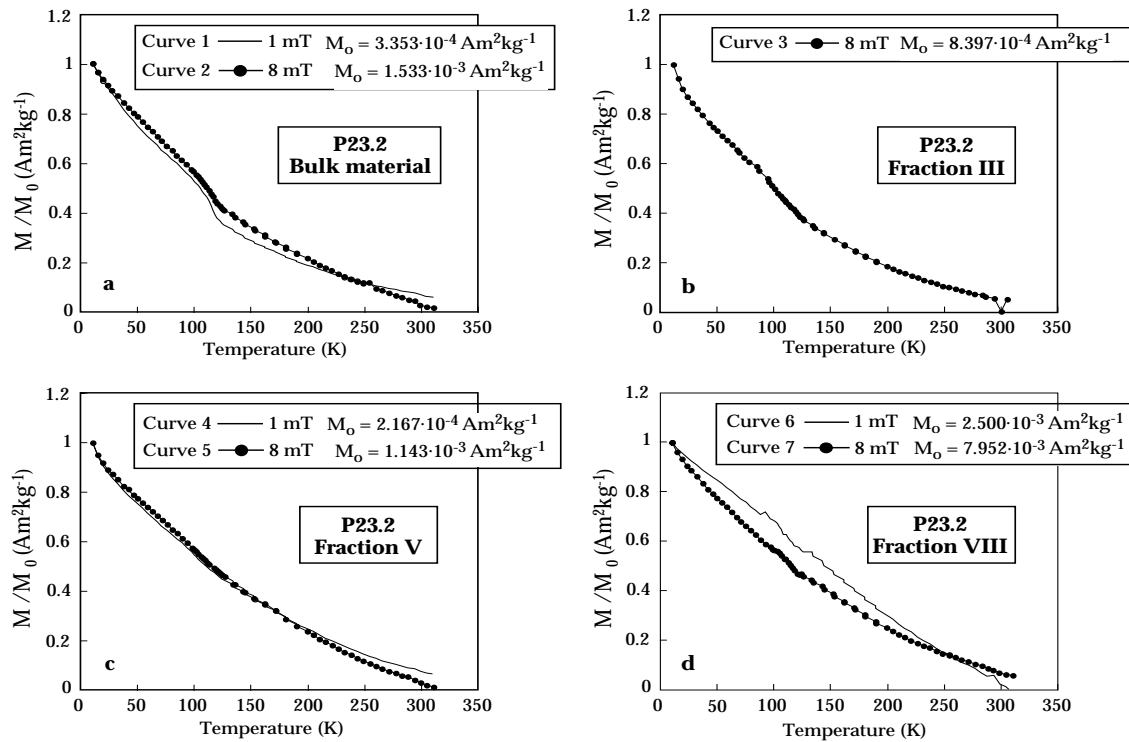


Figure 9. Low temperature thermoremanent magnetization curves of loess sample P23.2 measured upon warming from 10 K to room temperature in zero field. The applied field during the foregoing cooling to 10 K was either 8 mT or 1 mT. The maximum remanence M_0 for all magnetization curves is indicated.

1.3.5 Zero Field Cooling

The loess sample P23.2 and the paleosol sample P24.2 were subjected to zero field cooling (ZFC). The bulk material and three grain size fractions have been measured (Fig. 10). All the curves obtained from the loess sample (Fig. 10a) have the highest susceptibility signal at 10 K, which varies from $1.12 \times 10^{-6} \text{ m}^3\text{kg}^{-1}$ for the bulk material to $2.40 \times 10^{-6} \text{ m}^3\text{kg}^{-1}$ for very fine fraction "VIII". Susceptibility decreases in these loess separates from 10 K to about 50 K and stays almost constant from 90-100 K to room temperature for the coarser fractions and the bulk material. In fraction "VIII", however, an almost linear increase of susceptibility above 50 K until room temperature is observed. The four subsamples of paleosol P24.2 show a similar initial decrease of susceptibility from 10 K to 20-30 K (Fig. 10b), but the absolute values measured at 10 K ($8.11 \times 10^{-7} \text{ m}^3\text{kg}^{-1}$ for the bulk material to $1.47 \times 10^{-6} \text{ m}^3\text{kg}^{-1}$ for fraction "VIII") are lower with respect to the values measured at the same temperature in the correspondent fractions of the loess sample (Fig. 10a).

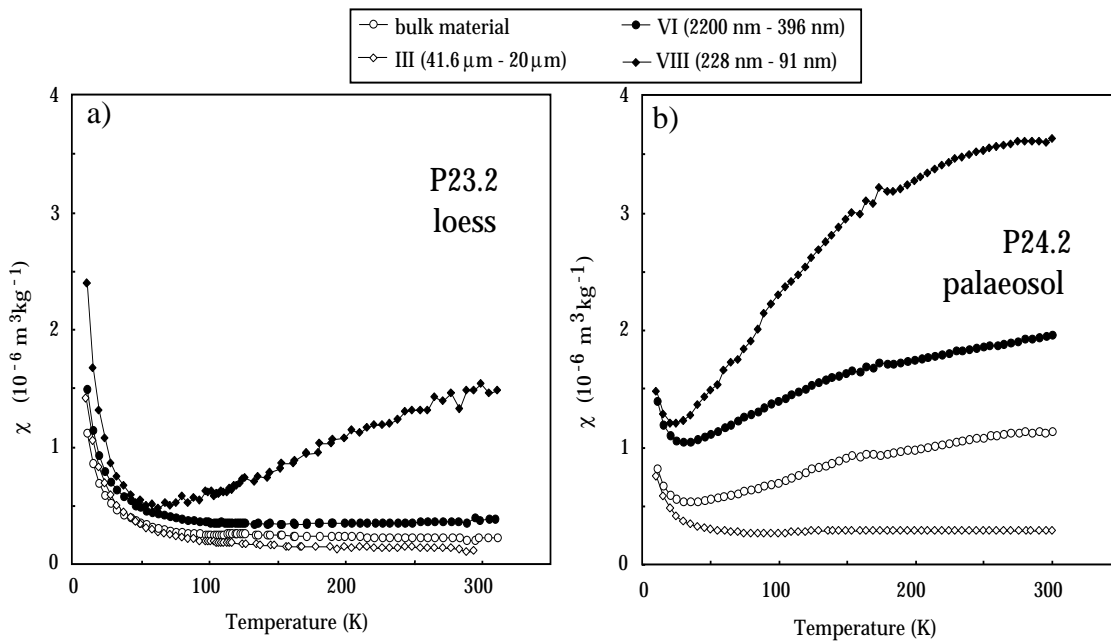


Figure 10: Magnetic susceptibility as a function of temperature between 10 K and 300 K. Zero Field Cooling (ZFC) measurements performed on four separates each (bulk material, fractions "III", "VI", "VIII") from loess sample P23.2 and from paleosol sample P24.2. The SP particles in the finest fractions unblock during warming and susceptibility increases according to the SP grain size spectra present. The increase is very pronounced in the pedogenetically strongly altered paleosol. The coarse grained fraction do not contain SP proportions and behave paramagnetically to a large extent.

The magnetic susceptibility remains almost constant from 80 K to room temperature in the paleosol fraction "III", whereas the magnetic signal of the bulk material and the finer fractionated paleosol samples "VI" and "VIII" increases strongly beginning at 20 K to 30 K. The gradients of these curves are variable and flatten off towards room temperature especially in the finest fraction "VIII". The susceptibilities at room temperature are much higher in the fine fractions and the bulk material of the paleosol sample (P24.2) than the corresponding values of the loess sample (P23.2).

1.4 Discussion

1.4.1 Magnetostratigraphy

An early study by Márton (1979) defined the position of the Matuyama/Brunhes boundary in the loess layer beneath the PD-soil complex. In this work the same interval was chosen for an investigation of the ChRM (Fig. 3). The upper part of our interval (from 41.7 to 44.0 m), which includes the paleosol layer PD₁ and the loess layer L₅, has normal polarity throughout and is interpreted as having been formed during the Brunhes epoch.

The M/B boundary is located between 44.1 and 44.3 m. In this interval (3 samples) declinations are pointing toward south, while inclinations are mixed (2 negative, 1 positive). An anomalous declination, directed toward the north, was observed at 44.8 m depth. It has to be pointed out that all the samples at a depth between 44.1 and 45.5 have secondary normally directed components which decay rapidly in peak fields up to 20 mT. This is probably due to remagnetization of low coercivity minerals (carrying the main contribution to the NRM in PD₂) during the Brunhes epoch.

In the lower part of the detailed section (loess layers L₆ and L'₆) several anomalous directions were detected (Fig. 3: Points A, B, C and D). At point B and D normally oriented declinations and inclinations are observed, whereas for A and C the inclinations are normally oriented with declinations toward south. During thermal demagnetization a strong increase of susceptibility above 250°C occurred, so that the formation of new magnetic minerals could be responsible for these observed anomalous directions. Even though a secondary component carried by low coercivity minerals was removed using AF demagnetization (with peak field between 20 and 30 mT), a component carried by

minerals with coercivities > 60 mT is present. The presence of hematite as a high coercivity mineral in the loess layers L_5 and L'_6 is testified by the unblocking temperatures above 650°C during thermal demagnetization, whereas the samples from paleosol PD_2 have unblocking temperatures that do not exceed 600°C , indicating magnetite as the carrier of the ChRM.

1.4.2 Room temperature measurements

The magnetic enhancement processes in the loess sequence at Paks were shown by Forster and Heller (1997) to be due to the increasing amount of a pedogenic ferromagnetic admixture, which strengthens the magnetic signal of the original magnetic mixture. The composition of the pedogenic component remains fairly constant throughout the sequence. We therefore assume that the enhancing processes that led to the magnetic signatures measured in our four samples, are typical for the whole Paks loess/paleosol sequence.

Different methods have been used to study the grain size dependence of magnetic properties. Synthetically grown minerals (Maher, 1988; Heider et al., 1996) or crushed natural minerals (Cui et al., 1994) with specific grain sizes can be used. The method used in the present work is gravitational grain size fractionation, which implies that the sediment composition within the fractions is maintained even if some material is lost during separation. This contrasts the extraction method of Hounslow and Maher (1996) who tried to collect quantitatively the whole grain size spectrum of magnetic minerals in one sample.

Possible clumping of individual magnetic grains and the electrostatic forces between clays and magnetic minerals can cause a discrepancy between the theoretical and the actual magnetic grain size fraction distribution. Fine grained superparamagnetic (SP) and stable single domain (SSD) ferromagnetic grains may contaminate the coarser grain size fractions. For example, the grain size fractions obtained from paleosol sample P24.0 (Fig. 6) have an F-factor varying between zero and 3.44% for the fractions with grain sizes $> 2.2 \mu\text{m}$, and between 9% and 14.7% for fractions with grain sizes $< 2.2 \mu\text{m}$. This indicates that the coarser fractions are not completely devoid of magnetic grains that behave superparamagnetically at room temperature. The majority of SP material, however, is concentrated in the finest fractions; in fractions "VII" and "VIII", the F-factor exceeds 14% and in the two finest fractions ("IX" and "X") it lies between 11 and 12%.

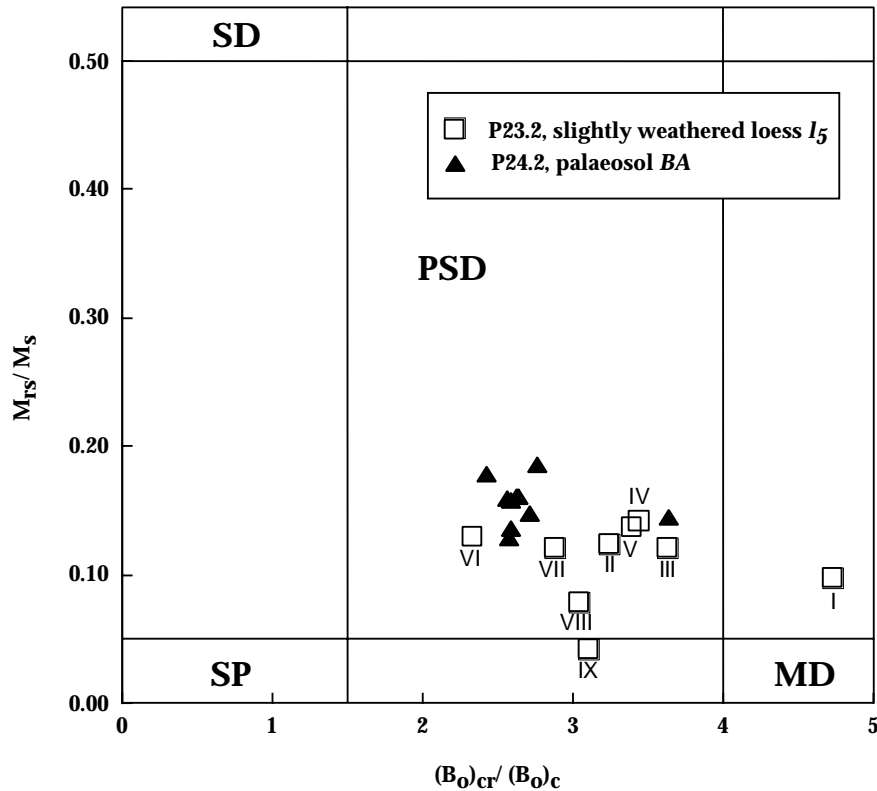


Figure 11: Hysteresis parameters of the sized fractions obtained from samples P23.2 (squares, loess layer I_5), P24.2 (triangles, paleosol layer BA) plotted on a Day diagram (Day et al., 1977). The roman numerals correspond to the grain size fraction for the loess sample I_5 .

The hysteresis parameters $(B_0)_c$ and $(B_0)_{cr}$ of the loess sample P23.2 and the paleosol sample P24.2 have the highest values in the coarse fractions decreasing towards the fine fractions, thus behaving inversely with respect to susceptibility. Theoretically, the coercivity maxima is expected near $0.1 \mu\text{m}$ (i.e. fraction "VIII"), where SSD magnetite grains with the highest coercivity should occur (e.g. Heider et al., 1996). The shift of the coercivity maxima towards coarser grain size in our samples may indicate that the fractions are indeed contaminated with finer SSD grains which were not separated out completely. Alternatively, the coarser grained magnetite is detrital and inherited from loess source rocks and hence may be at least partly oxidized as has been observed optically in Chinese loess (Heller and Liu, 1984). Oxidation may enhance magnetite coercivity substantially (van Velzen and Zijdeveld, 1995). Therefore unusually high coercivities could be observed in the fractions $> 1 \mu\text{m}$ especially in the loess sample which is less affected by pedogenesis.

Pedogenesis may also be responsible for the increase in coercivity seen in the finest

fractions of the paleosol sample. We speculate that extremely fine grained hematite which causes the reddish coloration and is present in Chinese paleosols in much larger quantities than the ferrimagnetic minerals (Evans and Heller, 1994), has a measurable influence and "hardens" the coercivity spectrum.

The grain size characteristics of the magnetic minerals in our samples are emphasized in a Day diagram (Fig. 11). The loess sample fractions are distributed across a relatively wide range of coercivity ratios from the MD field into the PSD (pseudo-single domain) field. The rightmost outlier represents the coarse fraction "I" with grain sizes $> 50 \mu\text{m}$. The data of the strongly altered paleosol plot in the centre of the PSD field. The paleosol contains a thorough mixture of fine grained (SP + SSD) pedogenic magnetic minerals whereas the sized fractions of the only slightly altered loess sample P23.2 show the increasing influence of pedogenesis fraction.

1.4.3 Low temperature measurements

The behaviour of the low temperature susceptibility (ZFC) and TRM curves provides information on different types of magnetic materials contributing to the total signal, allowing estimation of the paramagnetic contribution, of the type and grain size of the ferromagnetic minerals that contribute to the magnetic signals, and - in principle - of the smallest unblocking volumes of the ferromagnetic minerals. In ZFC experiments, the sample is cooled down to a few degrees Kelvin causing all the SP grains to be blocked and thus to behave like SSD-grains. During warm up to room temperature in a steady field, the grains eventually reach their unblocking temperatures and turn into SP grains: their moments can then align in the direction of the applied field and increase the magnetic signal. Thus ZFC curves represent a cumulative distribution of unblocking temperatures. We have also to consider the loss in magnetization of these SP grains responsible for the enhancement of the magnetic signal. They behave now like paramagnetic minerals, and lose magnetization with increasing temperature. The magnetization increase due to further unblocking SD grains therefore may be partly compensated by a paramagnetic magnetization decrease of the already unblocked SP grains (Sappey et al., 1997). A quantitative analysis of the ferromagnetic grain size spectra in our natural samples from ZFC measurements alone does not seem to be possible at present.

Qualitative remarks about these contributions, however, can be made for the loess/paleosol samples under consideration. Paramagnetic and superparamagnetic susceptibili-

ties mainly control the total signal (Fig. 10). The paramagnetic drop with increasing temperature is observed most clearly at temperatures below 30 K to 100 K (e.g. fraction "III" of loess P23.2 with negligible influence of SP grains). The unblocking of SSD susceptibility with increasing temperature resulting in growing SP susceptibility towards room temperature is recognized best in the fine material fractions (e.g. fraction "VIII" of paleosol P24.2). Thus loess/paleosol bulk susceptibility is mainly a mixture resulting from contributions of paramagnetic mineral fractions and superparamagnetically controlled fine fractions.

Sample	Bulk	Fraction "III"	Fraction "VI"	Fraction "VIII"
Loess P23.2	5.50	5.82	7.36	8.46
Paleosol P24.2	4.60	4.10	9.26	10.04

Table 3: Paramagnetic susceptibility ($\times 10^{-8} \text{ m}^3\text{kg}^{-1}$) at 300 K for loess P23.2 and paleosol P24.2 bulk samples and selected grain size fractions as derived from the susceptibility changes at very low temperature reported in figure 10. Values have an estimated error of $\pm 10\%$.

Even the bulk material of paleosol sample P24.2 shows the SSD \rightarrow SP conversion with temperature because the total susceptibility is strongly influenced by SP material which produces a very strong susceptibility signal at room temperature in the finest fractions ($\chi > 350 \times 10^{-8} \text{ m}^3\text{kg}^{-1}$). In this fraction ("VIII") strong SP influence is also observed in the slightly weathered loess sample P23.2.

The paramagnetic contribution to the ZFC total signal can be estimated by considering the portion at the lowest temperatures as purely paramagnetic. It is almost perfectly linear when plotted vs. $1/T$ for $T < 30 \text{ K}$, even though the influence of very small ferromagnetic minerals being still SP in this temperature interval cannot be completely excluded. The gradient of the best fitting line for the $1/T$ tail provides an estimate for the paramagnetic signal. The temperature-independent value may be taken as the non-paramagnetic contribution present in the sample which includes ferromagnetic SSD and MD grains and SP grains blocked at low temperature. The analysis in Table 3 shows - in agreement with Fig. 8 - that the paramagnetic contribution is generally similar in loess and paleosol samples. The paramagnetic contributions increase towards the finer grains size fractions which contain the paramagnetic clay minerals. The enrichment of fine grained clays in the paleosols is documented by the strong increase of paramagnetic susceptibility in the fractions "VI" and "VIII" of paleosol P24.2. The relative paramagnetic

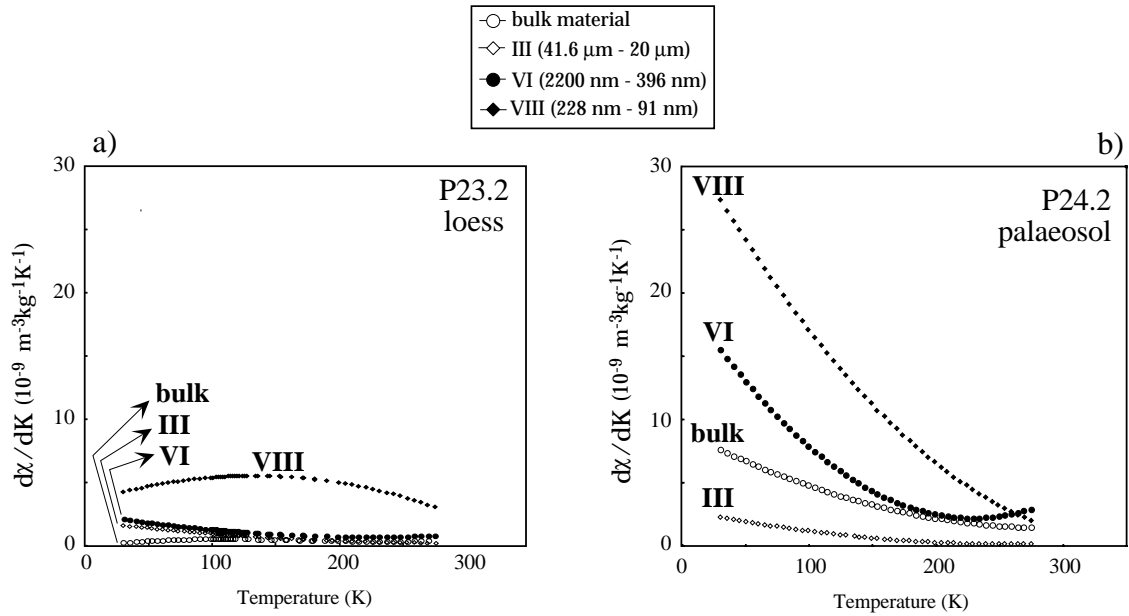


Figure 12: Gradients of the ZFC susceptibility curves (cf. Fig. 10) as a function of temperature after subtraction of the paramagnetic susceptibility signal.

susceptibility decrease in fraction "III" of this paleosol sample possibly indicates destruction of paramagnetic minerals due to weathering and pedogenesis.

After subtraction of the paramagnetic signal, the ZFC curves of Fig. 10 were fitted to polynomial functions between 25 K and 260 K. The gradients of the fitted functions (which also smooth the measured curves) give qualitative information about the grain size distribution of the SSD grains (Fig. 12). The high gradients measured at the lowest temperatures for the bulk sample and the fine fractions of paleosol sample P24.2 indicate that large amounts of SSD grains turn to SP behaviour in this temperature range.

The coarser fraction "III" shows only low gradients, suggesting a virtual absence of SSD grains. The loess P23.2 bulk sample and its two coarser fractions display very small gradients only and are largely devoid of SP influence. Only the finest fraction "VIII" shows minor SP grain contributions.

Özdemir and Dunlop (1993) suggested that the observation of remanence changes in the interval corresponding to the Verwey transition as a function of grain size can be used as a tool for detecting oxidation (magnetization) in sediments. The TRM curves of figure 6 clearly demonstrate the presence of magnetite in the loess bulk material and in the coarse fraction (P23.2: "III"). No evidence of the transition is seen in the finest fraction which contains substantial amounts of pedogenic SP grains. Thus it is suggested that

oxidation affects the pedogenic component strongly which mainly consists of maghemite (Banerjee et al., 1993) whereas the detrital ferrimagnetic material at least partly consists of magnetite. The different shape of the TRM(T) curves in fields of variable magnitude is caused by changing and broadening of the blocking temperatures with increasing fields (Sugiura, 1980).

1.5 Conclusions

The Brunhes/Matuyama boundary was found in the upper part of the paleosol PD₂ at a depth of 44.1 - 44.3 m. The B/M boundary represents the most reliable chronostratigraphic marker in this profile, in consideration of the observations made in other Hungarian sections (Pécsi et al., 1995), while other attempts to obtain a chronostratigraphic subdivision of the Young Loess and Old Loess resulted in discrepant age assignments (Kukla, 1977; Bronger and Heinkele, 1989a; Pécsi, 1992; Pécsi 1995; Oches and McCoy, 1995). This is mainly due to the limitation of the TL dating methods (Frechen, 1997) and to the complexity of the loess section at Paks brickyard, which is caused by several gaps (“delle” erosion) and superimposed soils complicating the chronostratigraphic classification (superimposed soils: MB₁ + MB₂, Phe₂ + Mtp₁ + Mtp₂; polygenetic soils: MB₁ + MB₂).

The Brunhes-age loess/paleosol sequence at Paks resembles the paleoclimatically induced rock magnetic variations found in many “dry” loess sections of Europe, Central Asia or China which are characterized by distinct magnetic enhancement in the paleosols due to weathering and pedogenesis.

Grain size fractionation is a useful approach in order to obtain information on the sediment magnetic properties as a function of their grain size distribution, especially for the very fine SP grains, which cause magnetic susceptibility enhancement. Low field susceptibility and coercive force show a distinct grain size dependence with susceptibility peak values in the 0.091 - 0.228 µm fraction in both loesses and paleosols. The low temperature dependence of susceptibility offers the possibility of separating paramagnetic and ferromagnetic contributions to the total magnetic signal.

The often observed susceptibility enhancement in paleosols (cf. Fig. 1) is due to neoformation of fine grained iron oxides (possibly mainly maghemite) by destruction and at the expense of the paramagnetic minerals of the loesses. Slight kinks in the TRM

low temperature decay curves at about 130 K indicate the presence of pure (probably detrital) magnetite. The strong TRM decay and the increase of susceptibility during warming between 10 K and 300 K indicates wide SD-SP grain size spectra of oxidized magnetite which occurs in different types. Unusually high coercivity in the coarser grained sediment separates points to oxidation of coarser grained detrital magnetite (cf. Heller and Liu, 1984). The “smeared“ appearance of the Verwey transition in loess bulk material (Özdemir and Dunlop, 1993) and the total absence of the Verwey transition in the grains sizes < 228 nm indicates oxidation of the pedogenic ferrimagnetic mineral admixture. Increasing coercivity in the very fine fractions which contain mixtures of ferrimagnetic SP-SD grains, may point to the presence of in situ formed fine grained (pigmentary) hematite.

The total iron content in loess/paleosol sequences does not vary extensively. A slightly higher iron content has been analyzed in Brunhes-aged Chinese paleosols as compared to the loesses (Bronger and Heinkele, 1989). This applies also to the Paks section (Pécsi, 1990) and may be explained by relative enrichment due to mass compaction of the soils during pedogenesis. The reduction of the paramagnetic susceptibility in the coarser grained fraction and the concomitant increase of superparamagnetic and single domain ferrimagnetic oxides in paleosol P24.2 as compared to the loess sample P23.2 lends support to the hypothesis that the iron oxides leading to enhanced susceptibility of paleosols have been formed *in situ* by weathering of iron-bearing paramagnetic minerals (e.g. Zhou et al., 1990, Heller et al., 1991) and/or iron-hydroxides which are abundant in Paks with up to 3 percent by volume (Pécsi, 1990) although magnetic methods have failed to identify the presence of the latter minerals.

Chapter 2

MAGNETIC PROPERTIES AND CHRONOLOGY OF THE LOESS/PALEOSOL SEQUENCE AT ROXOLANY (UKRAINE)

2.1 Introduction

The outcrop located near the village of Roxolany (30.4°E, 45.8°N), about 50 km west of Odessa on the eastern bank of the Dniestr estuary, represents one of the most complete Quaternary records in the Black Sea area. It is characterized by several well developed paleosols which alternate with thick loess units. The sequence overlies alluvium of the VIII Dniestr terrace (Tsatskin et al., 1998).

Recently, a new pedostratigraphic division was obtained when the loess-soil variability was investigated using magnetic susceptibility (MS), saturation magnetization and micromorphology analysis (Tsatskin et al., 1998). Susceptibility curves, derived from the thickest terrestrial records of Quaternary climate change on the Chinese Loess plateau (Liu, 1985; Heller and Liu, 1986; Maher and Thompson, 1991; Derbyshire et al., 1995) and in Central Asia (Forster and Heller, 1994), match well with the marine oxygen isotope record (Shackleton et al., 1990). Periods of enhanced dust accumulation, exhibited by loess layers with low values of MS, relate to global cooling, while intercalated paleosols with high MS are proxy evidence of warm periods. Zhou et al. (1990) amongst others suggested that the high MS signal in soils results from the *in situ* production of fine-grained magnetite in the course of pedogenesis and biomineralisation. Broad similarities between paleoclimatic records in the European loess and oceanic sediments, first suggested by Kukla (1977), are being increasingly recognised from detailed MS studies (Forster et al., 1996; Oches and Banerjee, 1996). It is anticipated that the same may hold true for the loess-soil sequences of the Black Sea area.

In the present study, in addition to the magnetic properties measured by Tsatskin et al. (1998) and partly in cooperation with Jacques du Pasquier (1998), hysteresis and remanence parameters were measured throughout the profile. Previous paleomagnetic studies gave ambiguous results regarding the stratigraphic depth of the Matuyama/Brunhes boundary (Tretyak and Volok, 1976; Trubikhin and Chepalyga, 1986). Heller et al. (1996) locate the boundary at 34-35 m depth, at the top of pedocomplex PK₇.

Another objective is to obtain information on the magnetic mineralogy and its origin and to verify if the climate variability during the Quaternary also controls the magnetic grain size distribution along the sequence at Roxolany. Obviously, the original magnetic signal is modified during interglacial periods, which are characterized by soil forming processes that lead to the formation of new magnetic minerals (e.g. Zhou et al., 1990). The

different conditions under which the various paleosols formed may enhance or deplete the sediment magnetism. The original detrital magnetic component can be studied in the loess layers, formed during cold periods: the variability of the hysteresis and remanence parameters in a cold and dry environment may reflect the wind variability responsible for the transport of dust from which loess sediments form.

2.2 The Roxolany loess-soil sequence

The profile is divided into 6 units (Tsatskin et al., 1998), numbered from top to bottom. Each unit comprises an upper paleosol and an underlying loess layer, except for units V and VI where three and two such soil-loess successions are present, respectively. The paleosol layers are designated as “PK”, from the German word "Pedokomplex" emphasizing their complex morphology, while loess layers are simply designated by “L”. Magnetic low field susceptibility (χ) was measured at two frequencies (0.47 kHz and 4.7 kHz) on cylindrical samples of 3.35 cm³ volume taken every 5 to 10 cm down the profile. The susceptibility value and the difference between the low and high frequency values ($\Delta\chi$) are plotted as a function of depth and lithology in Fig. 1.

2.2.1 Unit I

Unit I, which includes the surface soil and the underlying loess, is about 3 meters thick. PK₁ consists of A (humic), AB_{ca} (transitional, calcareous, with biotic perturbation) and BC_{ca} (reworked parent material) horizons. The A horizon is a 0.3 meter thick dark grey silty loam; it is a crumbly and porous layer. The AB_{ca} horizon is a 1 m thick sandy/silty loam and has been strongly biologically reworked. It grades downward into a BC_{ca} horizon, the upper part of the parent material, here a heterogeneous yellowish loess. The magnetic susceptibility of this chernosem at Roxolany is about 4 times the loess average susceptibility of $8 \times 10^{-8} \text{ m}^3\text{kg}^{-1}$ (Fig. 1).

2.2.2 Unit II

Unit II lies between 4 m and 6.8 m depth and includes paleosol PK₂ developed upon the silty yellowish loess horizon L₂. PK₂ comprises an uppermost brown A horizon and a

ROXOLANY

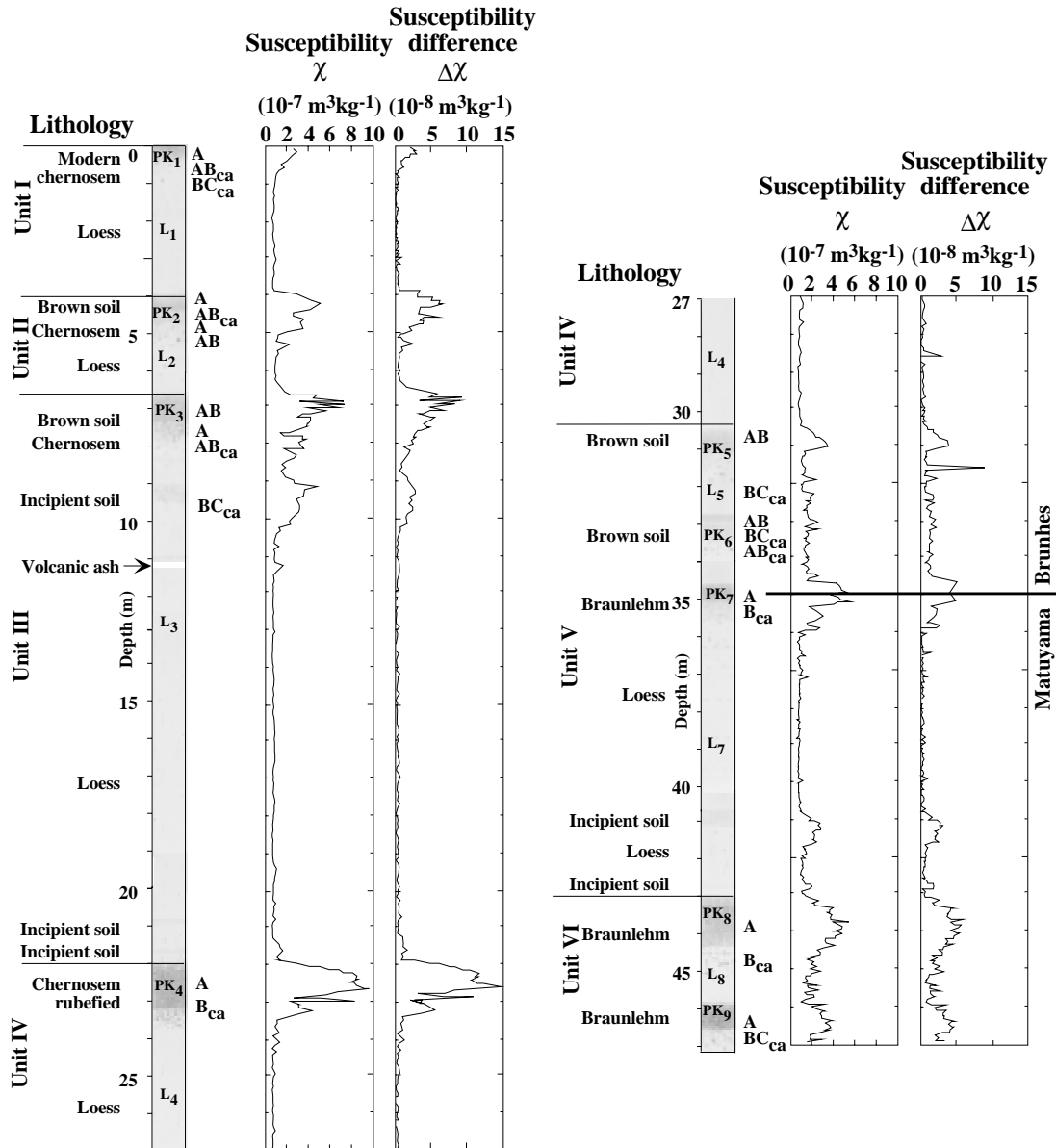


Figure 1: Roxolany loess/paleosol sequence with approximate position of the Matuyama/Brunhes (M/B) boundary. Lithology: Units as defined in the text with L=loess and PK=pedocomplex layers; specific low field susceptibility (χ) and susceptibility difference ($\Delta\chi$, specific susceptibility measured at 0.47 kHz - that measured at 4.7 kHz) are plotted as a function of depth. Susceptibility and susceptibility difference peaks correspond to the paleosol layers, while low values are characteristic for the loess layers.

thick calcareous AB_{ca} horizon below. Another greyish A horizon follows which lies on the top of a totally reworked

AB horizon of similar morphology to that of the surface soil. There are therefore two morphologically different paleosols in PK₂, called PK₂₋₁ and PK₂₋₂. This is confirmed by variations of the magnetic properties (Fig. 1). The A horizon of PK₂₋₁ shows an strong increase in susceptibility and susceptibility difference. In PK₂₋₁, these values drop in the AB_{ca} horizon and then increase again in the A horizon of PK₂₋₂.

Susceptibility differences increase strikingly in PK₂ (as in other pedocomplexes) reaching 15% of the bulk susceptibility signal.

This increase attests to the additional contribution of superparamagnetic ferrimagnetic minerals, as has been observed previously in Chinese loess (e.g. Heller and Liu, 1986; Zhou et al., 1990). The total Fe content, estimated from Mössbauer spectra (Gendler et al., 1997), is about 1.4 times higher in the A horizon of PK₂₋₁ than that of the modern chernosem.

2.2.3 Unit III

Unit III consists of a thick weathered layer, PK₃, on top of the thick yellowish loess L₃ with sandy silt texture containing a thin layer of volcanic ash (tephra layer) at about 11.2 m depth. PK₃ can be subdivided into three closely spaced paleosols:

PK₃₋₁ comprises a bright brown AB horizon and an underlying horizon that is strongly enriched with diffuse carbonates. PK₃₋₂ includes a grey humic A horizon with patches of diffuse carbonates and a calcareous AB_{ca} horizon composed of a strongly bioturbated silt. PK₃₋₃ has only a distinct BC_{ca} horizon at about 9.5 m depth. However, a slightly darker horizon at 8.9 m depth can be recognised which was interpreted as an incipient soil.

Magnetic susceptibility variations in PK₃ are in concert with the field observations of pedogenic alteration. The susceptibility values increase sharply in PK₃₋₁, whereas moderate enhancement is observed in PK₃₋₂ and in the PK₃₋₃ paleosol which is hardly recognisable in the field.

L₃ is a typical yellowish loess of sandy silt texture with nearly 15 m thickness and with typical low susceptibility. The tephra layer with slightly enhanced susceptibility is well identified by a strong white colour and more prominently by very high saturation magnetization (see Fig. 7).

At least two incipient paleosols are encountered at depths of about 21 m and 21.8 m. These paleosols have slightly darker hues in the A horizon which is about 10 cm thick, above a whitish B_{ca} horizon strongly impregnated with diffuse carbonates.

2.2.4 Unit IV

Unit IV is represented by the strongly developed paleosol PK₄ at approximately 22 m depth and loess L₄, from which it developed. PK₄ is a strongly red-brown polygenetic paleosol, which includes a 0.9 m thick A horizon and a B_{ca} horizon of silty loam. Susceptibility values in the red-brown A horizon are 5 times higher than in the underlying loess, and display three pronounced peaks, with the maximum at the top: $9.5 \times 10^{-7} \text{ m}^3\text{kg}^{-1}$ (Fig. 1).

2.2.5 Units V and VI

The beds below 30 m, underlying Unit IV, show a more complex pattern of loess and soil cyclicity. They contain strongly developed red-coloured paleosols (braunlehms), instead of the grey- or brown-coloured paleosols (chernosems) that occur in the upper part of the Roxolany outcrop. PK₅ lies at about 31 m depth with a hard reddish-brown AB horizon and a greenish-yellow BC_{ca} horizon upon loess L₅. PK₆ lies approximately 1.6 meter below and is interpreted as a bisquential paleosol with two humic horizons: an upper AB horizon underlain by the whitish BC_{ca}, impregnated with diffuse carbonate, and a lower light brown AB_{ca} horizon. PK₇, the best developed paleosol in unit V, is located at about 35 m depth. Its A horizon is a pink brown loam. L₇ is an olive-yellow sandy silt that contains five incipient soils between 37 and 43 m. Only two of them (at 41 and 42.8 m) are accompanied by a humic A horizon.

Unit VI comprises the two oldest major red paleosols of the Roxolany outcrop. PK₈ lies at approximately 43.2 m depth and consists of a reddish dark-brown A horizon that contains several superimposed humic horizons under which a BC_{ca} horizon is found. The lowermost semihydromorphic PK₉ appears at 46.3 m depth under the thin L₈ layer. It has a red sandy clay A horizon, grading down to a BC_{ca} horizon, represented by a greenish sand. This then grades to a silty alluvial loess, which overlies the channel gravels of the VIII Dnjestr terrace.

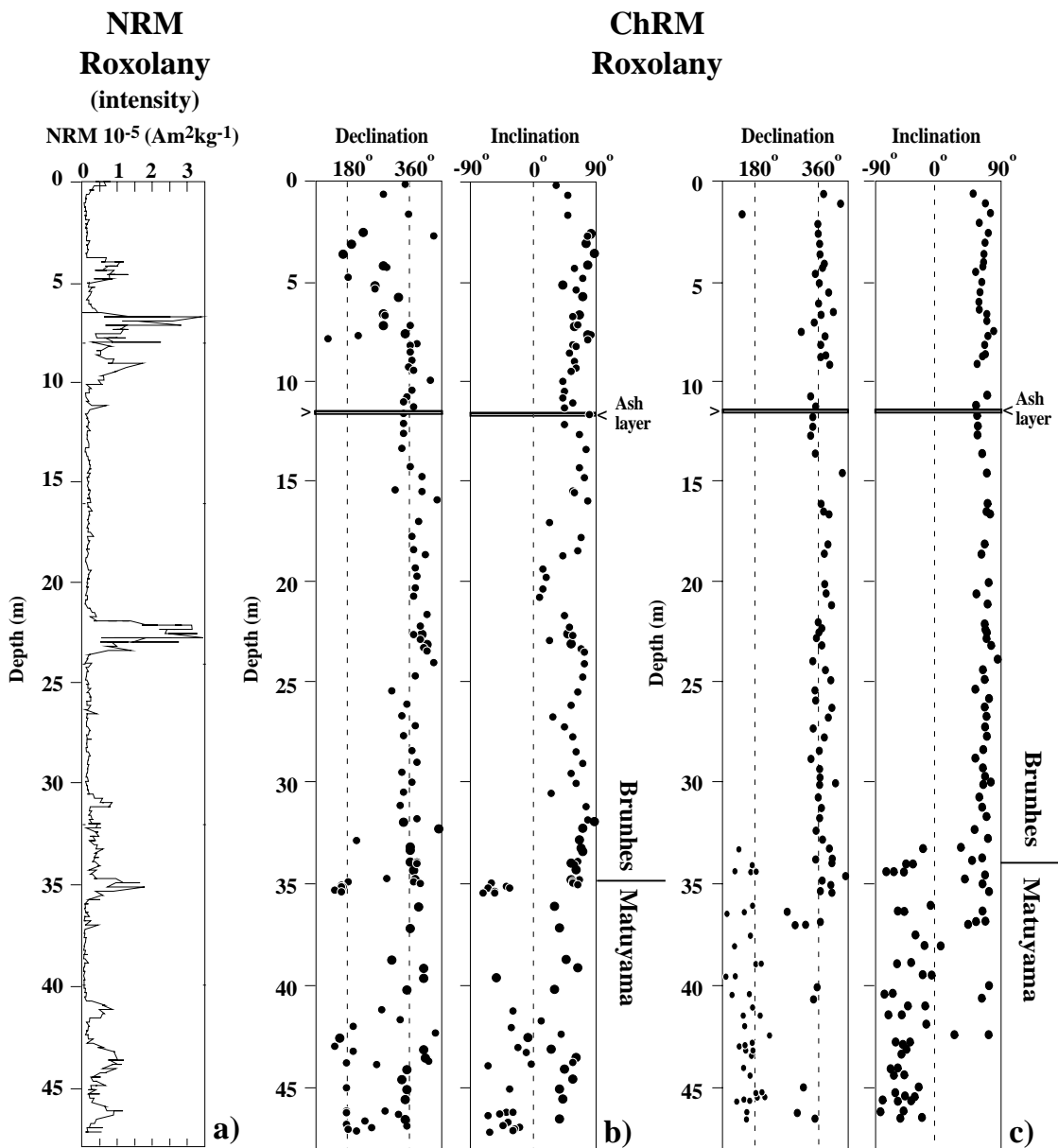


Figure 2: NRM intensity and comparison of two magnetostratigraphic profiles of the Roxolany loess sequence. Fig. 2b represents data measured in Zurich using A.F (for loess samples) and thermal demagnetization (for paleosol samples), while Fig. 2c represents data obtained only by thermal demagnetization (kindly provided by Dr. J. Hus). The Matuyama/Brunhes boundary is situated at a depth between 34 m and 35 m. At a depth of ca. 11.2 m a tephra layer was identified, which has not yet been dated.

Relatively weak susceptibility values in Unit V show more frequent fluctuations than in the upper units of the section. PK₇ has the highest susceptibility value of all soils in this unit, but less than half the highest susceptibility signal of PK₄ (Fig. 1).

In the younger paleosols, in particular in the chernosems PK₃ and PK₄ of Unit II and III the values exceed $3 \times 10^{-5} \text{ Am}^2\text{kg}^{-1}$, clearly higher than the older brown soils and braunlehms (PK₅, PK₆, PK₇, PK₈ and PK₉) which have values between 0.7 and $1.8 \times 10^{-5} \text{ Am}^2\text{kg}^{-1}$.

2.3 Determination of the Matuyama-Brunhes boundary

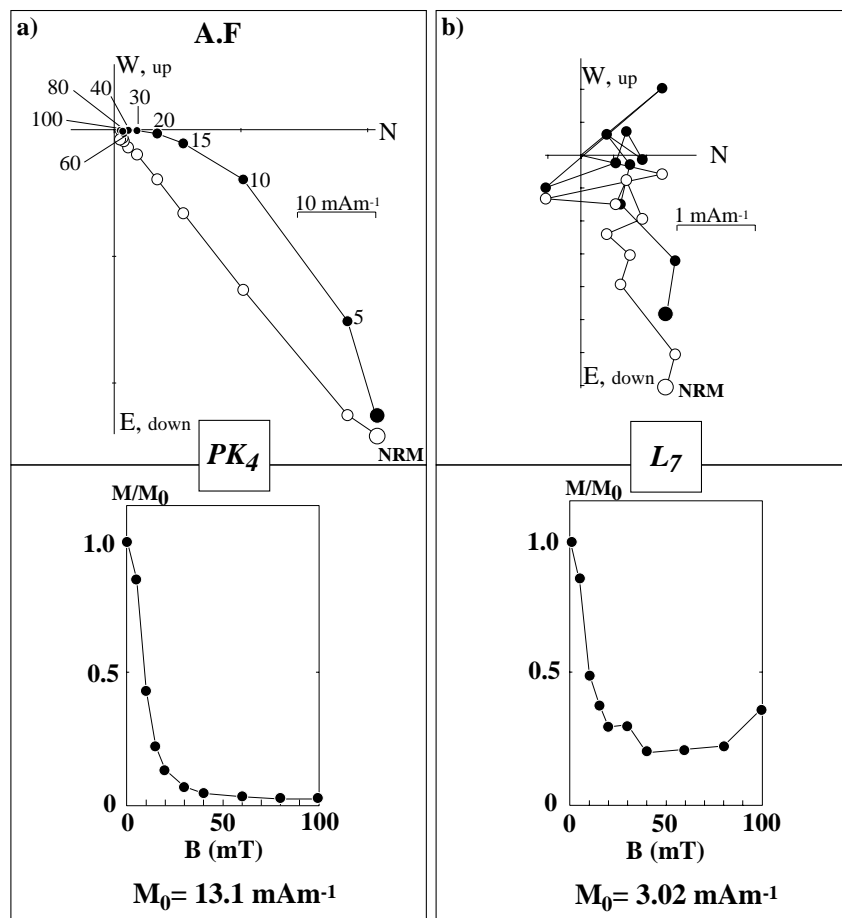


Figure 3: NRM vector and intensity of a paleosol sample collected at 22.3 m depth (paleosol PK₄) and a loess sample collected at 37.85 m depth (loess L₇) during stepwise A.F demagnetization. PK₄ is within the Brunhes normal polarity chron and L₇ within the reversed Matuyama chron. Black dots in the vector diagrams represent NRM vector end points projected onto the horizontal plane, white dots NRM vector end points projected onto the vertical plane.

NRM intensities vary in a very similar manner as the susceptibility and reach the highest values in the paleosol layers ($1-3 \times 10^{-5} \text{ Am}^2\text{kg}^{-1}$), while in loess layers the values are one order of magnitude lower (mean: $1.2 \times 10^{-6} \text{ Am}^2\text{kg}^{-1}$) (Fig. 2a).

The most important point in the chronological division of the Roxolany loess section is the occurrence of the Matuyama/Brunhes (M/B) polarity boundary. In order to determine the characteristic primary component of the NRM and thus to define the Matuyama/Brunhes boundary, a total of 118 samples were treated using A.F. and thermal demagnetization. Since most of the material is fragile, the samples have to be kept in the plastic sampling box, which cannot be heated to temperatures $> 150^\circ\text{C}$. For this reason A.F. demagnetization had to be applied mostly.

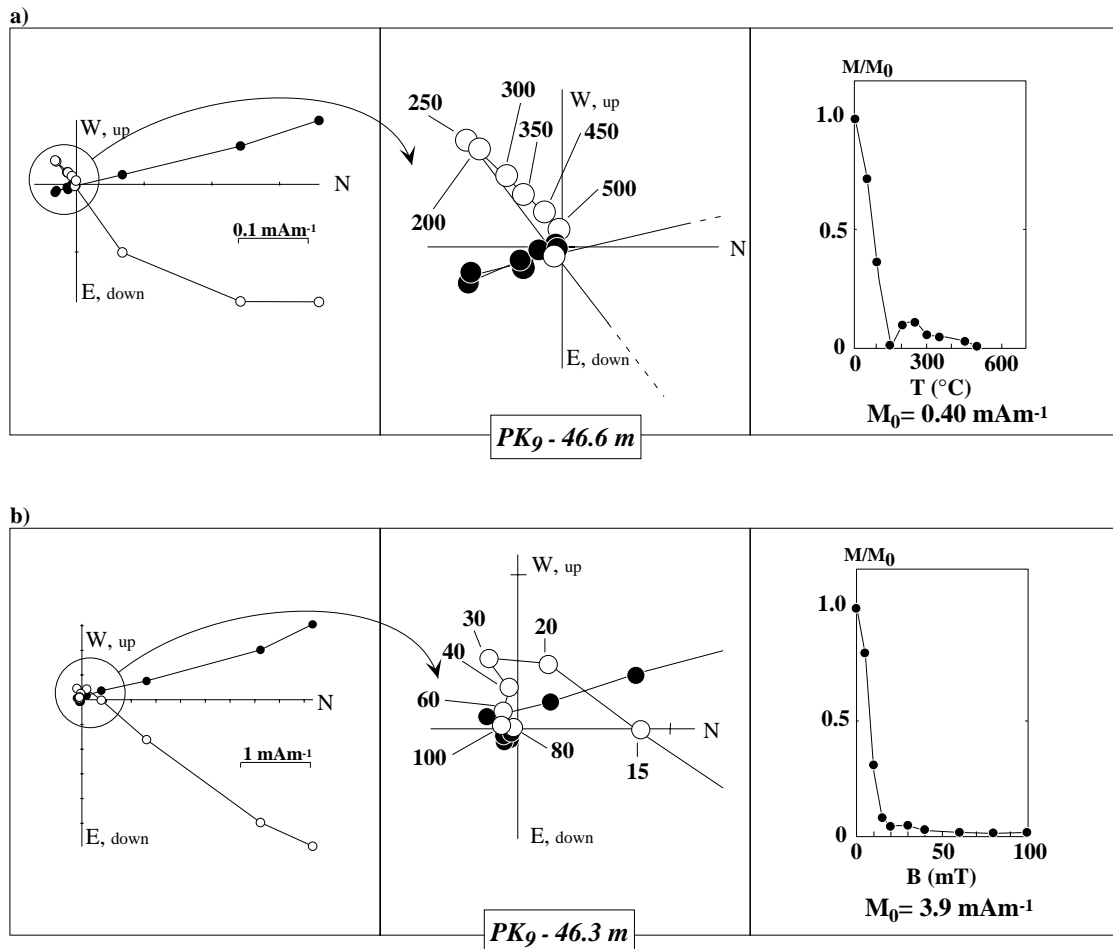


Figure 4: NRM vector and intensity of two paleosol samples collected at 46.6 m (4a) and at 46.3 m depth (4b) during stepwise thermal (4a) and A.F. demagnetization (4b). Both samples belong to paleosol PK_9 that originate from the Matuyama reversed polarity chron. For both samples a detail of the low NRM intensity part of the orthogonal vector diagram show the reversed principal component.

The ChRM directions (Fig. 2b) were then compared with those obtained using only thermal demagnetization (kindly provided by Dr. J. Hus) (Fig. 2c). Both profiles have similar positive inclination and northerly declination values for the upper ~34 m, although the data provided by Hus are less scattered. Larger deviations from the expected mean inclination value (ca. 63° at Roxolany) are observed in many AF demagnetized loess samples at a depth between 15 m and 30 m, with values ranging from almost 0° to 90°, whereas the thermally cleaned samples keep steady inclinations at 65°±10°.

Thermal and alternating field demagnetization removes a strong, probably, viscous overprint, the characteristic component in many samples being less than 5% of the initial NRM. Incomplete removal of the viscous component produces a wide scatter of the cleaned NRM directions. Nevertheless a fairly clear magnetic polarity stratigraphy emerges: data from the thermally cleaned samples (Fig. 2 c) suggest a major polarity change at a profile depth between 34 and 35 m which is interpreted as evidence of the Matuyama/Brunhes (M/B) polarity boundary. The Jaramillo subchron -if present- cannot be clearly identified in the Roxolany profile.

Two examples of AF demagnetization are given, for paleosol layer PK₄ and L₇ (Fig. 3a, b, respectively). Two superimposed NRM components are present on the orthogonal vector diagram for the PK₄ paleosol sample (22.3 m depth). The secondary component overprint is demagnetized at 20 mT. At higher fields the characteristic component decays linearly towards the origin, with normal directions indicating the formation of PK₄ during the Brunhes chron.

The sample from layer L₇ (Fig. 3b) was taken at a depth of 37.85 m below the M/B boundary (Fig. 2) and should thus have the reversed polarity of the Matuyama chron. The secondary component (up to 20 mT) is followed by a noisy signal and no stable direction for the primary component can be identified. The demagnetization curve decreases in intensity up to a field of 40 mT. Then a small increase follows up to fields of 100 mT. The A.F. demagnetization procedure seems not to be suitable for isolating the characteristic component carried by this loess sample.

The same procedure was applied to a paleosol sample from braunlehm PK₉ (collected at a depth of 46.3 m), also formed during the Matuyama chron (Fig. 4b). The secondary component is demagnetized when the AF exceeds 20 mT. The presence of a reversed direction is characterized by a small increase of intensity at a field of 30 mT above which the reversed ChRM direction is clearly depicted. In the paleosol samples at Roxolany, the

overprint is carried by low coercivity minerals that can be demagnetized using A.F. demagnetization. Another example from paleosol PK₉ (Fig. 4a) demonstrates that thermal demagnetization also clearly indicates the presence of a reversed characteristic direction which is overprinted by a normally oriented secondary component. The latter is completely demagnetized at 250°C, revealing the ChRM and its reversed direction.

An interesting observation with regard to the Matuyama/Brunhes boundary is that Hus's thermally demagnetized data (Fig. 2c) apparently determine the polarity change in the loess layer L₆, just above paleosol PK₇, while the youngest AF cleaned reversed samples occur in the paleosol PK₇. This small discrepancy can be attributed to the different demagnetization methods used. Most probably, however, it results from different sample positioning during the joint sampling campaign. Hence, it is concluded that both reversal positions coincide closely and fall into the top part of PK₇.

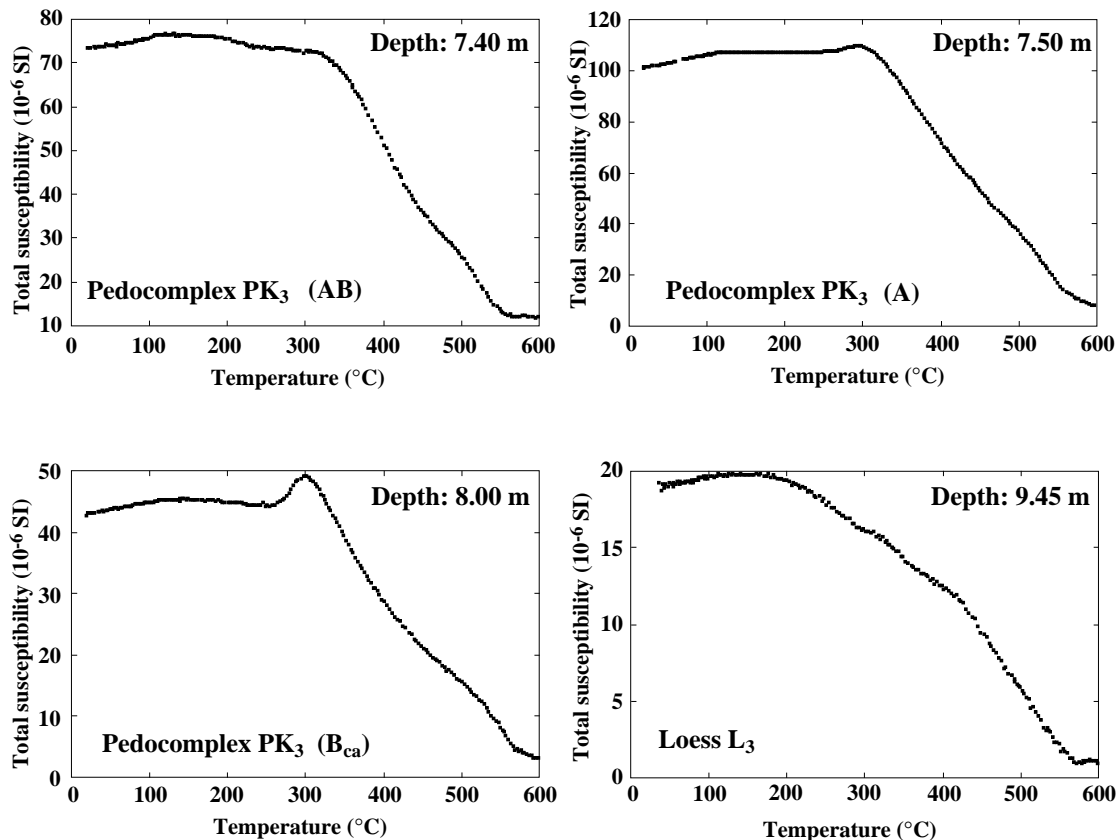


Figure 5: Temperature dependence of magnetic susceptibility of 3 paleosol samples (from the AB, A and B_{ca} horizon of chernosem PK₃) and a loess sample (from loess layer L₃).

Magnetic susceptibility as a function of temperature was measured for four samples from unit III (Fig. 5). The susceptibility of all four samples increases initially up to 100°-200° C. This effect is attributed to superparamagnetic grains. The susceptibility decreases consistently from 300° C in the paleosol samples, while the decrease starts at temperatures between 100° C and 200° C in the loess sample. All samples show a Curie temperature around 560° C - 580° C, indicating the presence of magnetite in all samples.

A susceptibility peak at 300° C is observed in the PK₃ paleosol samples (horizons A and B_{ca}). Siderite (FeCO₃), a paramagnetic mineral common in carbonate sediments (Ellwood et al., 1986) that rapidly oxidizes at 300° C to magnetite, maghemite and then to hematite, could explain this increase in susceptibility.

2.4 Hysteresis and ARM

2.4.1 Hysteresis parameters

Hysteresis parameters were measured on 479 samples using a modernized coercivity spectrometer (Burov et al., 1986), in order to determine the concentration and the granulometry of the magnetic minerals present (du Pasquier, 1999). The pedological investigation of the loess/paleosol sequence at Roxolany emphasized different characteristics of the paleosols encountered. While the paleosols in units I to IV are chernosems or chernosem-like, showing A, B and C horizons with signs of intensive biotic perturbation and carbonate accumulation, the paleosols in the older units V to VI are red coloured braunlehms, containing also calcareous, bioturbated BC horizons, with Mediterranean soil characteristics.

Paramagnetic minerals have a strong influence on the hysteresis parameters, resulting in a wide spectrum of coercivity ratios in paleosol (values from 3.2 to 4.3, with the exception of two isolated samples with a coercivity ratio between 2 and 3) but especially in the loess samples (from 3.3 up to 6) (Fig. 6). After subtraction of the paramagnetic contribution (calculated from the slope of the linear portion of the hysteresis in the field interval between 250 and 300 mT) a general grouping in the PSD field is observed (Fig. 6). This concentration is stronger in the loess samples because the relative contribution of paramagnetic minerals in the hysteresis parameters is higher than in the magnetically enhanced paleosols. The Day-plot alone cannot be used to discriminate magnetic grain size

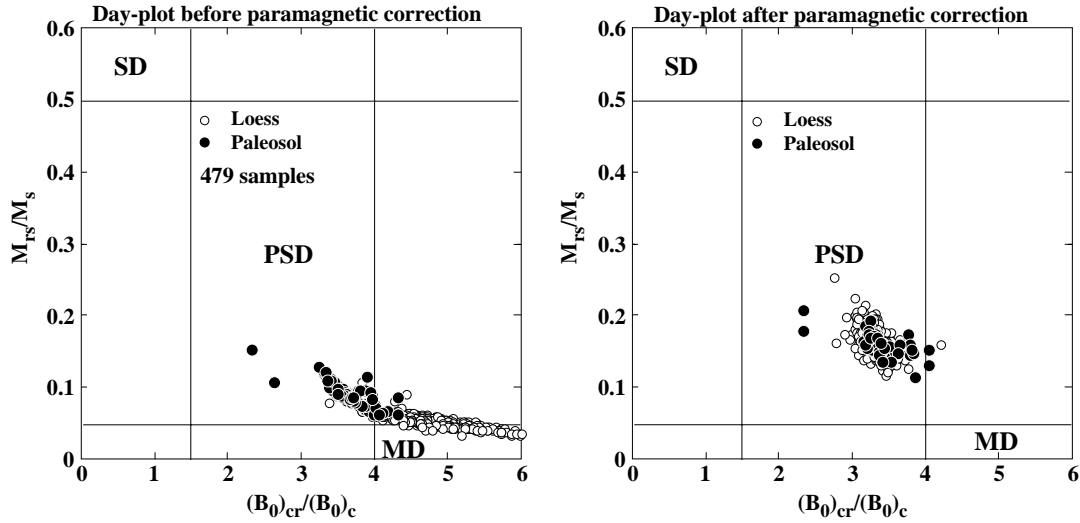


Figure 6: Day plot (Day et al., 1977) of the loess and paleosol samples from Roxolany, before and after paramagnetic correction.

population between loess and paleosols. Susceptibility differences (Fig. 1) suggest the presence of SP grains in the paleosol layers, which are probably responsible for the overlap of loess and paleosol samples in the Day-plot.

In figure 7 the distribution of the saturation magnetization M_s , the saturation remanence (M_{rs}), the coercive force $(B_0)_c$ and the coercivity of remanence $(B_0)_{cr}$ for the whole Roxolany profile are shown. The lithology sequence is also plotted for comparison. Both magnetizations are higher in the paleosols as compared to the loess layers. The saturation magnetization depends purely on the concentration of ferromagnetic minerals and demonstrates that the paleosol layers have significantly higher (up to 20 times) ferromagnetic particle concentration than the unaltered loesses.

The maximum saturation magnetization measured in PK₄ (about 0.02 Am²/kg) corresponds to a concentration of 0.22 mg/g for pure magnetite and the minimum value found in L₄ to a pure magnetite concentration of 0.01 mg/g. The saturation remanence is also influenced by the concentration, but depends also on grain size and shape. The very high values of M_s and M_{rs} reached for the tephra layer (about 11.2 meter depth) are remarkable. This expresses the very high concentration of magnetic particles in this layer. Both coercive force and coercivity of remanence depend on the magnetic granulometry and correlate well with lithology. $(B_0)_c$ and $(B_0)_{cr}$ have smaller values in paleosols than in loess, hence, an inverse distribution with regard to the magnetization profiles is observed, indi-

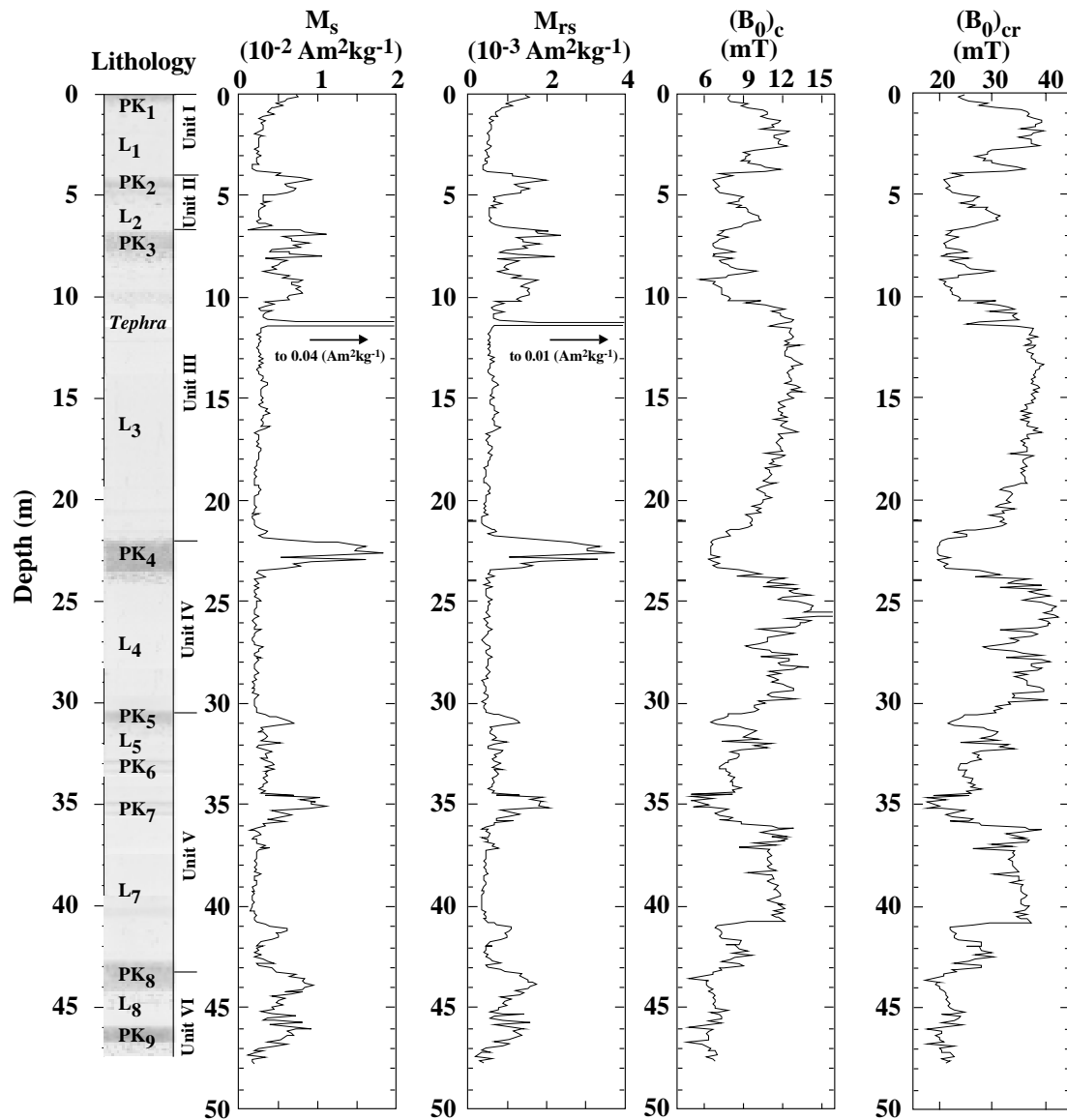


Figure 7: Saturation magnetization M_s , saturation of remanence M_{rs} , coercive force $(B_0)_c$ and coercivity $(B_0)_{cr}$ measured along the Roxolany loess/paleosol sequence.

cating that the magnetic enhancement is controlled mainly by low coercivity minerals. The coercivity-related curves detect features that can not be derived from the M_s and M_{rs} curves, especially in the loess layers, where important changes in coercivity (up to 100%) and almost constant ferromagnetic concentrations were measured.

A minimum at 3 m depth, for example, cannot be related to any observed pedologic horizon. It probably reflects an incipient soil and may be due to a warming during the glacial period corresponding to layer L_1 . The coercivity properties of loess L_3 are not as homogeneous as the L_3 magnetization profiles, indicating that the magnetic grain size

may change because of a change of the source material and not because of pedogenic processes. A maximum for the coercivity values is observed around 14 m depth, then $(B_0)_c$ and $(B_0)_{cr}$ decrease slightly while approaching PK₄.

In loess L₄, coercivities also vary much more than magnetization. One peak at 27 m depth and another smaller peak at 28.5 m depth indicate a variation in magnetic properties in the direction of soil-like characteristics. PK₆ can be better recognized in the coercivity profiles. The oldest three peaks, caused by an incipient soil, PK₈ and PK₉, show a progressive coercivity decrease. Loess L₈ has soil like coercivity values.

These observed variations of the four measured hysteresis parameters reflect different concentrations and grain sizes of the magnetic particles in loess versus paleosol. It appears that magnetization values reflect well the climatic changes during interglacial periods (increasing values), but are not sensitive enough to give evidence of smaller climate changes occurring during glacial periods, whereas coercivity reacts much more sensitively to minor environmental variations.

2.4.2 Anhysteretic remanent magnetization (ARM)

Strong ARM differences between paleosol and loess are observed (Fig. 8a) with values over an order of magnitude higher in the paleosol than in the loess samples.

Higher intensities ($> 1.5 \times 10^{-4} \text{ Am}^2\text{kg}^{-1}$) were measured at 120 mT for the younger paleosols PK₄ and PK₃, while the older paleosols (PK₇ and PK₈) have values between 0.6 and $0.7 \times 10^{-4} \text{ Am}^2\text{kg}^{-1}$. A difference in concentration of the magnetic minerals is the origin of the intensity difference, confirmed by the higher susceptibilities and saturation magnetization measured in the younger paleosols (Fig. 1). In the loess samples (Fig. 8b) ARM intensities at 120 mT are quite similar for all four samples (between 5 and $7 \times 10^{-6} \text{ Am}^2\text{kg}^{-1}$) but saturation is not achieved at 120 mT.

This is related to the presence and relatively higher contribution of magnetically harder minerals in the loess than in the paleosols. In the paleosols, the acquisition curves are flattening at fields > 80 mT, indicating that ARM is carried mainly by magnetically soft minerals. ARM acquisition rates for PK₄ and PK₃ (younger paleosols) and for PK₇ and PK₈ (older paleosols) are almost identical (Fig. 8c), with a maximum value at 20 mT, indicating that the differences in ARM intensity are a result of an increased concentration of ARM-carrying minerals (SSD and small PSD magnetite grains) in the younger

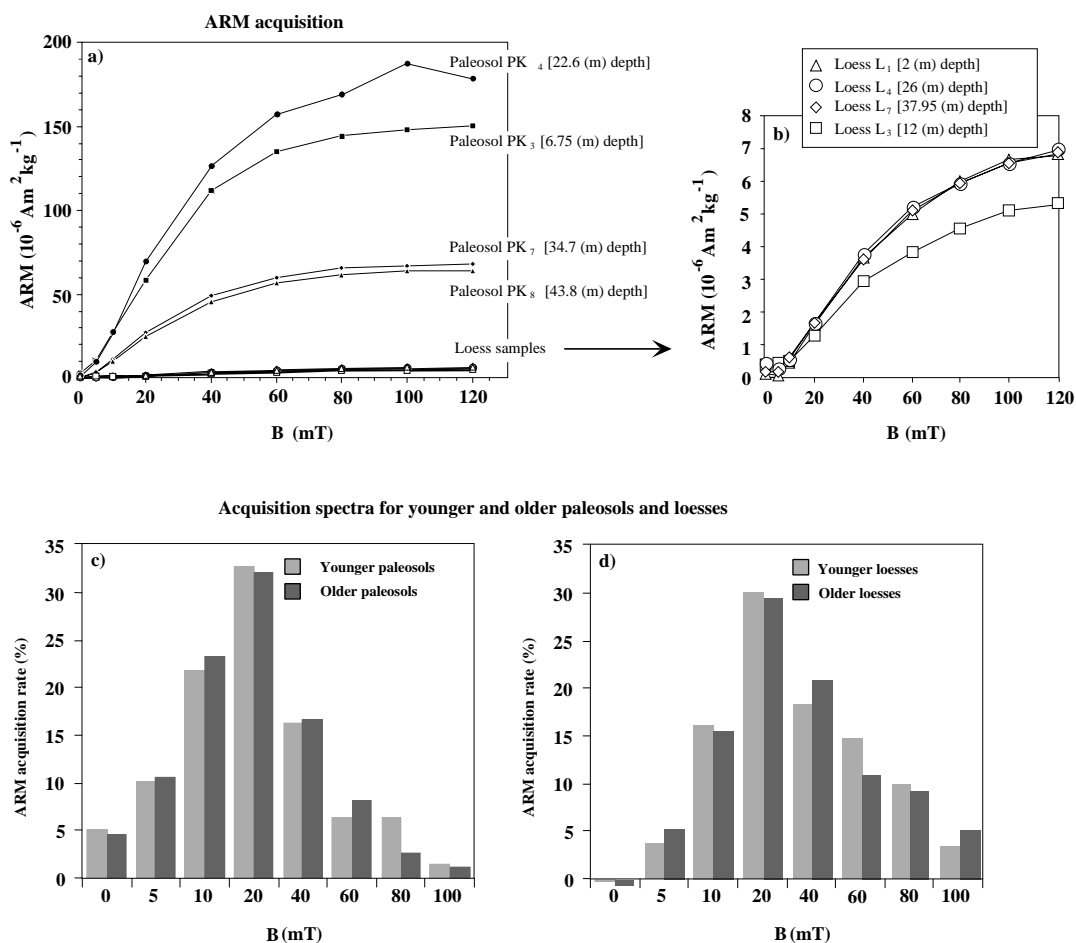


Figure 8: ARM acquisition for four paleosol (a) and four loess (a, b) samples. The samples were chosen in order to represent the different types of loess and paleosols, but also those of younger and older paleosols. ARM acquisition spectra for 2 young and 2 old paleosols and loesses each (averaged values) have all maxima at 20 mT (c, d).

paleosols. No distinct qualitative difference can be recognized. A different result is obtained from the young loesses (L₁ and L₃) and from the old loesses (L₄ and L₇), where the contribution of harder magnetic minerals is expressed by a lower ARM acquisition rate below 20 mT and higher above 40 mT (Fig. 8d). and the very soft contribution below 5 mT is hardly visible.

The variations of the ARM intensity through the Roxolany outcrop as well as the lithology of the profile have been plotted in figure 9. ARM and lithology correlate very well. Every pedocomplex from PK₁ to PK₉ can be easily recognized by enlarged ARM values. A closer look at the ARM profile allows additional considerations to be made. The ARM intensity of PK₁ is about half that of the next two paleosols PK₂ and PK₃. PK₃

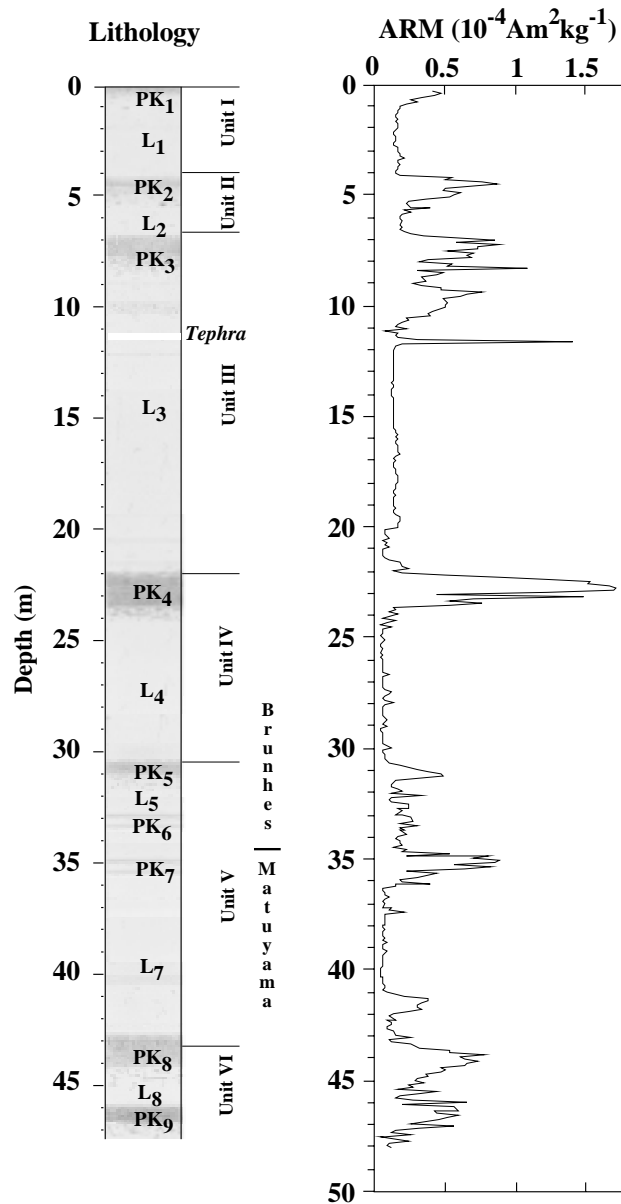


Figure 9: ARM intensity (at 120 mT) profile and lithology for the loess/paleosol sequence at Roxolany.

has a complex ARM progression, with three distinct peaks being recognizable, reflecting exactly the three closely spaced paleosols PK₃₋₁, PK₃₋₂ and PK₃₋₃ mentioned in section 2.2.3. The sharp peak at 11.2 meter depth is due to the tephra layer. PK₄ has the highest ARM intensity of the whole profile. PK₆ has the lowest ARM value among the paleosols in the outcrop. Compared with PK₇, the best developed paleosol in unit V, its ARM intensity values are three times lower. A peak at 41 meter depth is not correlated with any of

the nine defined pedocomplexes. It corresponds to one of the incipient soils mentioned in section 2.2.5. The enhanced magnetic behaviour of the paleosols as compared to the loesses is thus reconfirmed.

2.4.3 Loess/paleosol discrimination

It was shown in section 2.4.1 that the Day plot is not a powerful tool to clearly discriminate the magnetic grain size distribution in loess and paleosols. Hence, other parameters have to be tested in order to distinguish the sediment types magnetically. SIRM has been plotted versus χ_{lf} in Fig. 10.

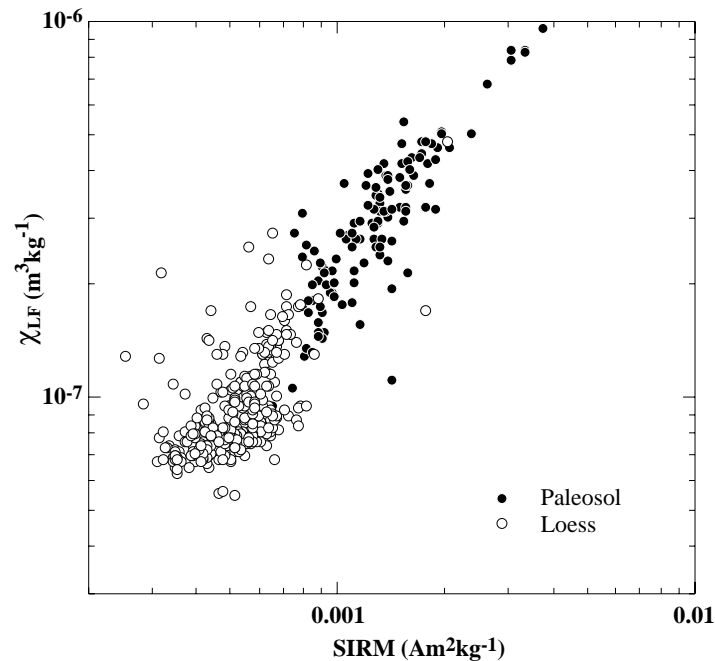


Figure 10: Bilogarithmic plot of saturation remanence *SIRM* versus low field susceptibility χ_{lf}

High ferromagnetic grain concentrations are characterized by high SIRM and χ_{LF} values and thus plot toward the top right while low concentrations plot toward the bottom left corner of the diagram. The grain size dependence of these two parameters was empirically quantified for pure magnetite by Thompson and Oldfield (1986). Since the ferromagnetic fraction of the loess and paleosol samples from Roxolany does not only comprise magnetite grains, the absolute magnetite content and its grain size distribution cannot be determined according to the Thompson and Oldfield (1986) method. The paleosol samples clearly tend to plot towards the upper right field of the diagram, while

the loess samples plot in the lower left field. Hence, the relative higher ferromagnetic concentration of SSD and MD grains in paleosols is confirmed, Further mineral differentiation can be attempted by plotting $SIRM/\chi_{LF}$ versus $(B_0)_{cr}$ as suggested by Thompson and Oldfield (1986).

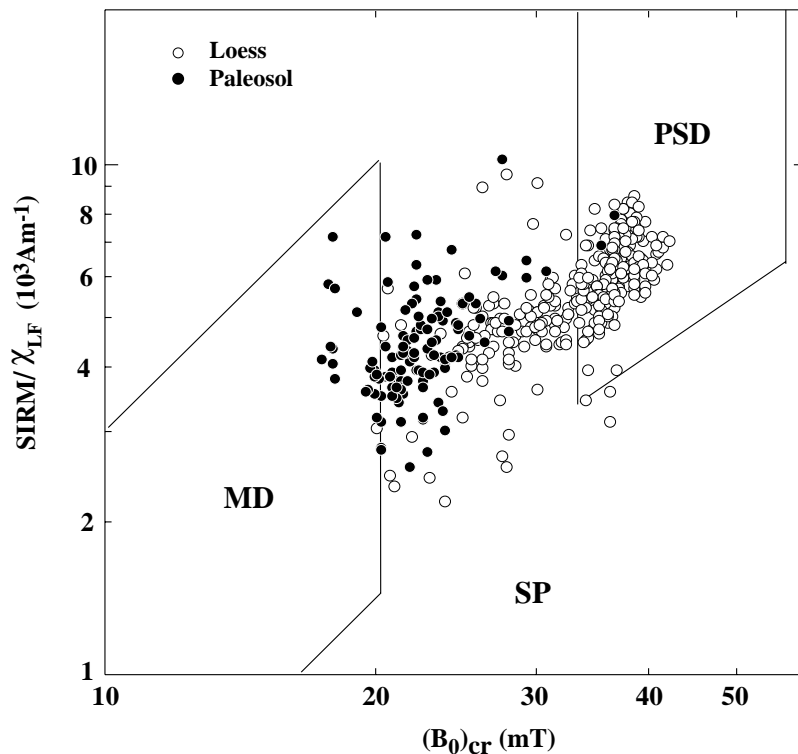


Figure 11: $SIRM/\chi_{LF}$ versus $(B_0)_{cr}$. The relatively high $SIRM/\chi_{LF}$ values measured for the paleosols (where a large contribution is given by the SP grains) could result from oxidized magnetite (maghemitization), resulting in relatively low susceptibility values.

In Fig. 11, the loesses have a strong tendency to plot in the PSD region while the paleosols tend to plot towards the MD region of the diagram. The rather wide distribution is not surprising and is due to the increasing influence of SP grains in the paleosols. The distribution along the ordinate, however, does not reflect the strong SP contribution that has been suggested in the previous sections. The data points are expected to plot at the lower end of the depicted domain state regions. The offset may be caused by "maghemitization" of the magnetic fraction. Indeed, it is likely that a substantial amount of magnetite grains has been oxidized into maghemite during the pedogenic transformation processes, as was discussed for the Hungarian loess/paleosol sequence at Paks (Chapter 1). Since the domain state regions in the $SIRM/\chi_{LF}$ versus $(B_0)_{cr}$ diagram were determined for pure magnetite (Thompson and Oldfield, 1986), it can be suggested that the presence of

maghemite would lead to an upward shift of these regions, because of the lower χ_{LF} values of maghemite caused by oxidation of magnetite (cf. Van Velzen and Zijdeveld, 1995).

2.4.4 Magnetic profiles

In order to refine the results obtained in the previous three sections, the various magnetic parameters may be combined, including ARM/SIRM (where an increase indicates a relative increase of SSD grains), $\chi_{LF}/SIRM$ (where an increase indicates a relative increase of SP and/or MD grains), χ_{ARM}/χ_{LF} (which indicates the relative contribution of SSD grains to the magnetic signal as compared to that of SP grains) in order to shed more light on the variability of the ferromagnetic mineralogy along the profile in Roxolany. In addition, low field susceptibility χ , saturation magnetization M_s and coercive force $(B_0)_c$ are presented (Fig. 12).

• Unit I

Susceptibility and M_s show the highest values in the humic (A) horizon of PK₁ (the magnetic susceptibility of this chernosem at Roxolany is about 4 times the loess average susceptibility of $8 \times 10^{-8} \text{ m}^3\text{kg}^{-1}$, Fig. 1). indicating an increased concentration of magnetic minerals. These decrease in the AB_{ca} and BC_{ca} horizons and remain almost constant with low values throughout loess layer L₁ (Fig. 12).

$\chi_{LF}/SIRM$ has a minimum at 1 m depth, corresponding to the lower part of the AB_{ca} horizon of PK₁, which is characterized by abundant calcite nodules. It indicates a minimum in SP or MD magnetic grains. A minimum of SSD grains is also indicated by low ARM/SIRM ratios.

Throughout loess layer L₁ a variable distribution of magnetic grain sizes is indicated by the coercive force variations $(B_0)_c$ and $(B_0)_{cr}$ (see Fig. 7). The synchronous increase of ARM/SIRM and of $\chi_{LF}/SIRM$ indicates that in the lower part of L₁ the SSD and SP contributions are slightly increased.

• Unit II

Two distinct peaks of susceptibility, M_s , and $\chi_{LF}/SIRM$ occur (Fig. 12), which are related to the two already mentioned humic A horizons of the welded pedocomplexes

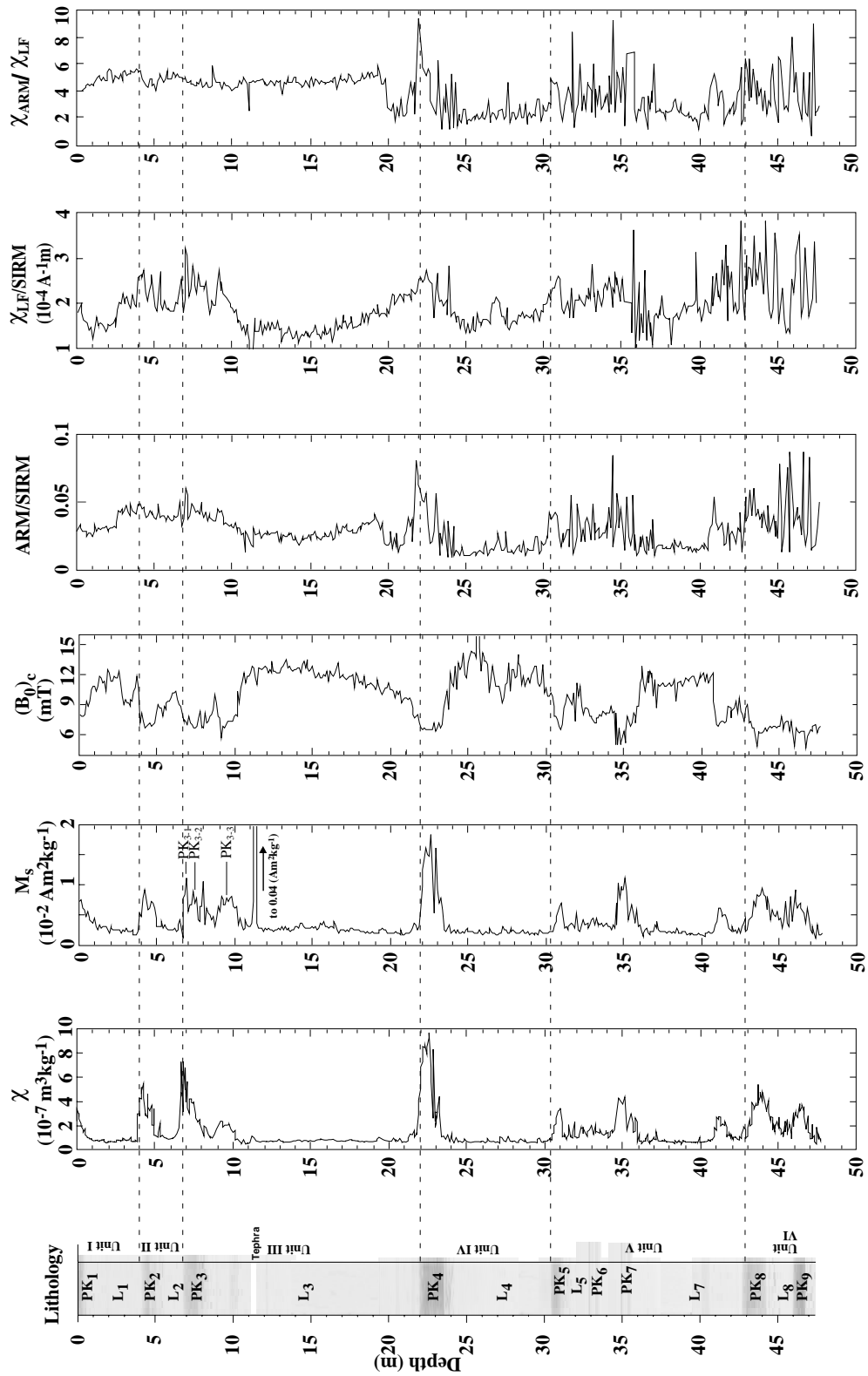


Figure 12: Susceptibility (χ), saturation magnetization (M_s) coercive force $(B_0)_c$, ARM/SIRM, $\chi_{LF}/SIRM$ and χ_{ARM}/χ_{LF} in Roxolany plotted as function of depth and lithology.

PK₂₋₁ and PK₂₋₂. The major susceptibility peak in the younger A horizon can be explained by a larger increase of SP grains because $\chi_{LF}/SIRM$ increases ($\Delta\chi$ increases strikingly in PK₂ (as in other pedocomplexes) reaching 15% of the bulk susceptibility signal, see Fig. 1).

There is no significant change of SSD grains (ARM/SIRM) from PK₂ to the overlying L₁. The increased contribution of SP grains is also shown by the small decrease of χ_{ARM}/χ_{LF} from 4 m to 5 m.

The horizon with low susceptibility values between the two A horizons is the carbonate rich AB_{ca} horizon of PK₂₋₁. The decrease in susceptibility may be due to dilution effects, while magnetic grain size differences are not indicated by any large variation in coercivities.

The underlying loess layer L₂ has a susceptibility similar to loess L₁, but lower coercivity values. The $\chi_{LF}/SIRM$ peak associated with a small increase of χ_{ARM}/χ_{LF} indicates an increase of MD and/or SP grains. This behaviour is probably related to the evolution of the overlying pedocomplex rather than a climate signal during the cold period corresponding to L₂.

• Unit III

At a depth of 11.2 m a tephra layer was identified, marked by a strong M_s peak. Higher susceptibility values were measured in PK₃ (max.: $\sim 7 \times 10^{-7} \text{ m}^3\text{kg}^{-1}$) with respect to PK₂ (max.: $\sim 5.2 \times 10^{-7} \text{ m}^3\text{kg}^{-1}$) and PK₁ (max.: $\sim 3 \times 10^{-7} \text{ m}^3\text{kg}^{-1}$), but coercivities are similar to those of pedocomplex PK₂. While χ_{ARM}/χ_{LF} remains almost constant also throughout unit III, strong variations are observed in M_s (change in concentration) and $\chi_{LF}/SIRM$ (change in SP/MD contribution) in correspondence with the observed structure of the pedocomplex PK₃. Maxima of these parameters are actually observed in the AB horizon of PK₃₋₁, the humic A horizon of PK₃₋₂ and in the [A] horizon of PK₃₋₃ (Fig. 13), suggesting a correlation between superparamagnetic enhancement and humus content (see Virina et al., 1997).

Coercive force changes clearly in loess layer L₃ (Fig.12). From the top to the bottom of L₃ (B_o)_c decreases constantly from a maximum just below the tephra layer to the top of underlying PK₄. The inverse pattern is observed in $\chi_{LF}/SIRM$, with the minimum occurring just below the tephra layer. SP grains are virtually absent in L₃, and the SSD grain

content is almost constant (see ARM/SIRM) throughout (except for the lowest 2 m, where the decrease of $\chi_{\text{ARM}}/\chi_{\text{LF}}$ and ARM/SIRM indicates a reduced contribution of SSD grains).

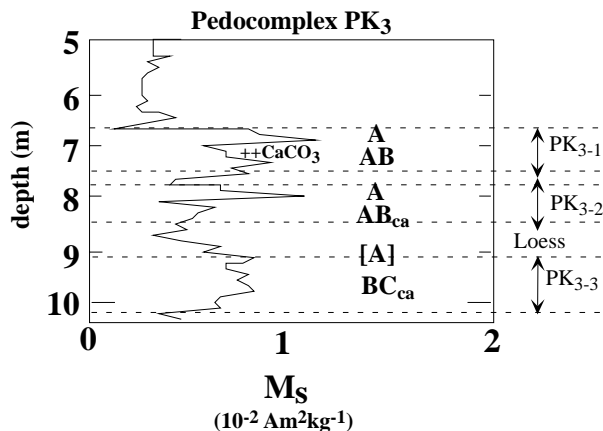


Figure 13: Saturation magnetization M_s variation in pedocomplex PK_3 as a function of depth. A generally higher concentration of magnetic minerals is observed in the A horizons of the paleosols, with the exception of PK_{3-3} .

- **Unit IV**

Susceptibility values in the red-brown A horizon of PK_4 are 5 times higher than in the underlying loess, and display three pronounced peaks, with the maximum near the top: $9.5 \times 10^{-7} \text{ m}^3\text{kg}^{-1}$ (Fig. 12). At a depth of ~ 22.8 m a decrease of susceptibility is observed, as well as a decrease of $\chi_{\text{LF}}/\text{SIRM}$ and of ARM/SIRM and $\chi_{\text{ARM}}/\chi_{\text{LF}}$ in particular, probably in correspondence to the boundary between the upper A horizon and the underlying B_{ca} horizon rich in carbonate nodules. The high $\Delta\chi$ values (up to 15%, see Fig. 1), in the humic horizon, due to the important contribution of SP grains, is accompanied by striking $\chi_{\text{LF}}/\text{SIRM}$ and of ARM/SIRM peaks, indicating that in this particular pedocomplex the production of SP and SD was most pronounced with respect to the others studied pedocomplexes of the Roxolany section.

PK_4 is an important pedocomplex, not only because of its magnetic properties, but also because it represents a sort of magnetic boundary between the upper part of the section (units I to III) and the lower part (unit IV to VI). The evidence is given by the extreme differences observed in the $\chi_{\text{ARM}}/\chi_{\text{LF}}$ parameter, which is rather constant in the upper 20 m, but strongly variable along the lower 28 m. Bioturbation may have a strong influence

during loess depositional processes during sedimentation of the younger part of the sequence.

Loess layer L_4 has noisy signals of ARM/SIRM and $\chi_{\text{ARM}}/\chi_{\text{LF}}$ which are significantly lower than in the younger loess layers (L_1 , L_2 and L_3), indicating a constant but lower concentration of SSD grains. At 26 - 28 m depth a decrease of $(B_0)_c$ accompanied by an increase of $\chi_{\text{LF}}/\text{SIRM}$ may indicate an increasing influence of SP grains, probably due to a relatively warmer period in the cold time interval represented by L_4 .

- **Unit V and VI**

Unit V is characterized by 3 pedocomplexes in its upper part (PK_5 , PK_6 and PK_7). An enhanced susceptibility is observed for PK_5 and PK_7 , whereas the values of PK_6 are similar to the overlying and underlying loesses L_5 and L_6 . The coercive forces also correlate well with lithology, with magnetically softer components predominating in the pedocomplexes and harder ones in the loess L_5 and L_6 , although the values in the loesses are much lower than in the other loess layers (Fig. 12). They return to high values in L_7 as observed in L_3 and L_4 . Three $(B_0)_c$ minima, at approximately 37 m, 38.30 m and at 39.5 m depth were observed (Fig. 12, 14). These occur where ~8 cm thick layers of calcrete nodules were identified, indicating the presence of incipient soils: at 37 m depth, a peak in $\chi_{\text{ARM}}/\chi_{\text{LF}}$ indicates a relative increase of the SSD contribution, as well as at a depth of 38.3 m, although with smaller amplitude (Fig. 14). At these depths, $\chi_{\text{LF}}/\text{SIRM}$ has a clear inverse behaviour, resulting in two minima, indicating a low contribution of SP and/or MD grains. At ~39.7 m the opposite pattern is observed, with low $\chi_{\text{ARM}}/\chi_{\text{LF}}$ and high $\chi_{\text{LF}}/\text{SIRM}$, indicative of relatively more SP minerals. From a magnetic point of view the most developed incipient soil is the one at 37 m depth, because of the highest contribution of SD grains.

In general, the high scatter of ARM/SIRM, $\chi_{\text{LF}}/\text{SIRM}$ and $\chi_{\text{ARM}}/\chi_{\text{LF}}$ in both loesses and pedocomplexes between 31 m and 36 m gives evidence of the complexity of this part of the loess sequence at Roxolany, in which the Matuyama/Brunhes boundary occurs. This may be due to stronger bioturbation and weathering processes during interglacial and glacial periods with respect of the observation made in unit I to III, resulting in the ARM/SIRM, $\chi_{\text{LF}}/\text{SIRM}$ and $\chi_{\text{ARM}}/\chi_{\text{LF}}$ peaks observed at 32 m, 34 m and 36 m depth.

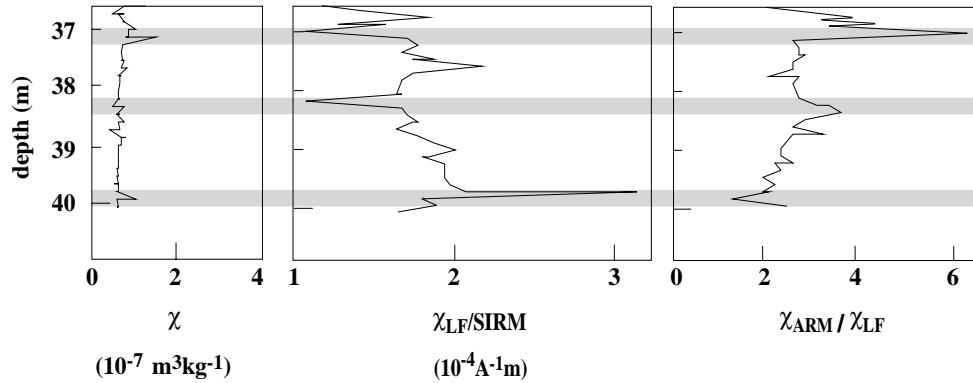


Figure 14: Susceptibility, $\chi_{LF}/SIRM$ and χ_{ARM}/χ_{LF} from 37 m to 40 m depth (loess layer L_7). The anomalies observed in these parameters correspond to horizons in which calcite concretions are concentrated (see text for details).

In the lower part of L_7 , at a depth of 41 m a humic [A] horizon occurs, overlying a BC_{Ca} horizon and indicating the presence of another incipient soil. Magnetic susceptibility is slightly enhanced (between $2 - 3 \times 10^{-7} \text{ m}^3\text{kg}^{-1}$), as well as M_s , χ_{ARM}/χ_{LF} and $ARM/SIRM$, indicating an increase of SP but also SSD grains.

The lowermost pedocomplexes PK_8 and PK_9 are classified as red decalcified (Braunlehm) soils. They are considered to be similar to PK_6 but much more developed (Tsatskin et al., 1998).

In PK_8 susceptibility increases progressively throughout the A horizon reaching a peak at ~ 43.80 m, in correspondence with $(B_o)_c$ minima. $ARM/SIRM$, as well as χ_{ARM}/χ_{LF} , has enhanced values in its upper part suggesting a higher contribution of SSD grains in the upper part of the pedocomplex, while the SP contribution is increased in correspondence with the susceptibility peak (see the $\chi_{LF}/SIRM$ peaks from 43.5 - 44.2 m depth). A similar susceptibility distribution is observed in PK_9 , where the susceptibility peak occurs in the lower part of the A horizon, where also the relative contribution of SP is increased (high $\chi_{LF}/SIRM$ values and low $ARM/SIRM$ values).

2.5 Discussion

According to the paleopedological study of Tsatskin et al. (1998) and in addition to the chronological constraints provided by the Matuyama/Brunhes chron boundary (Fig. 2) the loess/paleosol sequence at Roxolany has been divided into three main parts:

- a) The lowermost loess (L_8), braunlehm soils (PK_8 and PK_9) and incipient soil of the Matuyama chron, older than 780 ka;
- b) the interval around the Matuyama/Brunhes transition, encompassing PK_5 through PK_7 ;
- c) the upper Brunhes chron from the top to approximately 22-22.5 m with PK_1 through PK_4 (Fig.1).

The pedological properties of the pedocomplexes indicate that they formed in different environmental conditions. These paleoclimatic interpretations suffer some uncertainty because of the changes that can occur after burial, and the effects these may have on the reconstruction of the climatic parameters (Catt, 1995). Nevertheless, according to Retallack (1990), there is one parameter, the depth of the calcic horizons, that can be quantitatively linked to mean annual rainfall if the paleosol is not truncated or calcified secondarily. Therefore an attempt to reconstruct the conditions under which the soils originated was performed (Tsatskin et al., 1998; tab.1).

All younger major paleosols in Roxolany have the characteristics of chernosems (i.e. a rather thick humic horizon and signs of bioturbation evidenced by the presence of krotovinas; Scheffer und Schachtschabel, 1998), although to a varying extent. The older pedocomplexes PK_6 , PK_8 and PK_9 (braunlehms) differ from the younger soils by a more intense red coloration associated with rubefication (Gendler et al., 1997; rubefication is actually observed also in PK_4), indicating a warmer and moister climate. Magnetic properties are also different between younger and older paleosols, which have smaller concentrations of magnetic minerals (lower M_s). On the other hand, the relative contribution of the magnetic minerals and their grain sizes is similar in both younger and older paleosols, as observed in the ARM acquisition spectra (Fig. 8). The smaller amount of ferrimagnetic minerals is consistent with the pedological observations which assign braunlehm pedocomplexes to a more wet and warm climate, when the formation of magnetically weak Fe^{3+} oxides was favoured.

units	soil type	supposed environment	mean annual precipitation (mm)	mean annual temperature (°C)	additional environmental factor
I	PK ₁ chernosem calcified	subhumid steppe	475	10	
II	PK ₂₋₁ brown calcified	semiarid steppe (?)	300-400	9-10	lithogenic ?
	PK ₂₋₂ chernosem calcified	subhumid steppe	450-500	10-11	
	PK ₃₋₁ brown strongly decalcified	subhumid/semi-arid steppe	500-550	13-14	lithogenic ?
III	PK ₃₋₂ chernosem decalcified	subhumid prairie	550-600	15-16	
	PK ₃₋₃ chernosem-like	subhumid steppe	450-500	14-15	paleohydro-morphism
IV	PK ₄ chernosem rubefied	warm seasonally dry forest	600-700	16-18	
V	PK ₆ red-brown calcified	warm semiarid chapparral?	700-900	18-20	lithogenic ?
VI	PK ₈ red-brown decalcified (transitional to Braunlehm)	warm subhumid chapparral	800-1000	18-20	
	PK ₉ red decalcified (Braunlehm)	lowland warm forest	800-1000	18-20	floodplain hydromorphism

Table 1: Micromorphological environment reconstruction at Roxolany (from Tsatskin et al., 1998).

The question whether a magnetic investigation can reveal the major differences between the younger (PK₄ and younger) and the older part of the sequence can be answered in a first attempt by observing the susceptibility maxima in the different paleosols. Generally higher values are observed for PK₂ to PK₄, while the older pedocomplexes have distinctly lower values. This is in general agreement with susceptibility records from other loess/paleosol sequences in eastern Europe (Forster et al., 1996, Spassov, 1998) in Central Asia (Forster et al., 1994) and in China (Heller and Liu, 1984; Kukla et al., 1990; An et al., 1990; Maher and Thompson, 1994), indicating the trend of global climate evolution since the M/B polarity reversal.

A more discriminating parameter for the two portions of the sequence, including also the magnetically weak loesses, is the anhysteretic remanent magnetization (ARM), a magnetic signal that reflects the presence of remanence-carrying SSD magnetic minerals. In the upper part of the sequence (upper 20 m) the contribution of SSD grains relative to SP grains remains almost constant, with no difference between loesses and paleosols (χ_{ARM}/χ_{LF} in Fig. 12). While the ARM values in the paleosols are similar in all units, with the exception of PK₄ (see PK₂, PK₃, PK₇, PK₈ and PK₉ in Fig. 9), χ_{ARM}/χ_{LF} values in the loesses of unit IV, V and VI are clearly lower. Mean bulk susceptibility in L₁ and L₂ (7.99

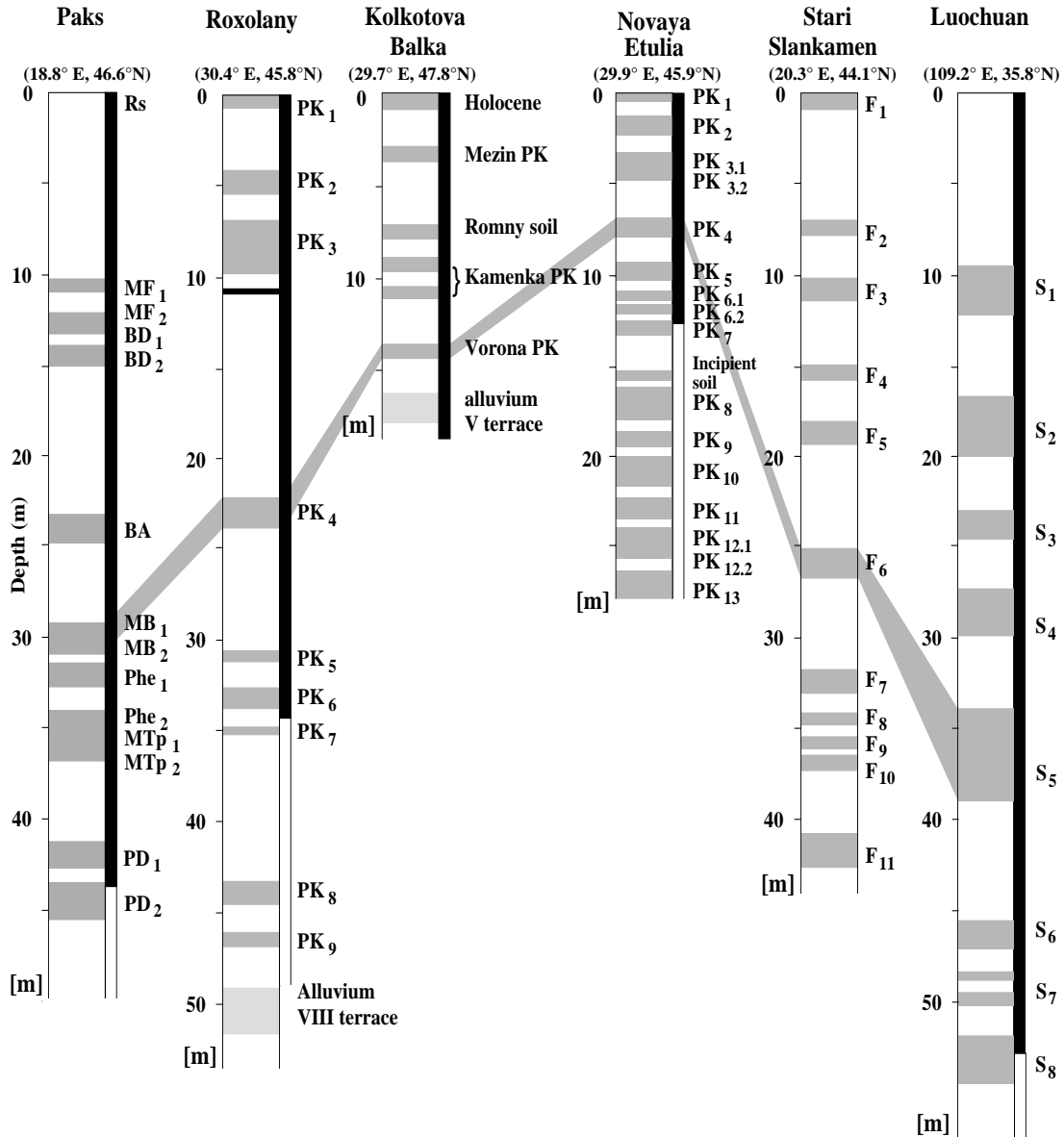


Figure 15: Correlation chart of loess/paleosol sections in the Black Sea area with Central Europe and China. Sections from left to right: Paks and Roxolany, this work; Kolkotova Balka from Virina et al. (1997), stratigraphic nomenclature according to Velichko (1990); Novaya Etuliya from Spassov (1998); Stari Slankamen from Bronger (1976); Luochuan from Heller and Liu (1986). Black and white bars to the right of the sediment profiles indicate Brunhes normal and Matuyama reversed polarity, respectively.

$\times 10^{-8} \text{ m}^3\text{kg}^{-1}$) is almost identical to that in L_4 and L_7 ($7.57 \times 10^{-8} \text{ m}^3\text{kg}^{-1}$), but $\chi_{\text{ARM}}/\chi_{\text{LF}}$ has more than doubled in the younger loesses. Considering the small susceptibility differences, an increased contribution in the older loess strata of coarse MD grains relative to the SSD component is postulated. χ_{ARM} per unit mass in magnetite SD grains ($8 \times 10^{-7} \text{ m}^3\text{kg}^{-1}$, Thompson and Oldfield, 1986) is higher than in MD grains ($1 \times 10^{-7} \text{ m}^3\text{kg}^{-1}$,

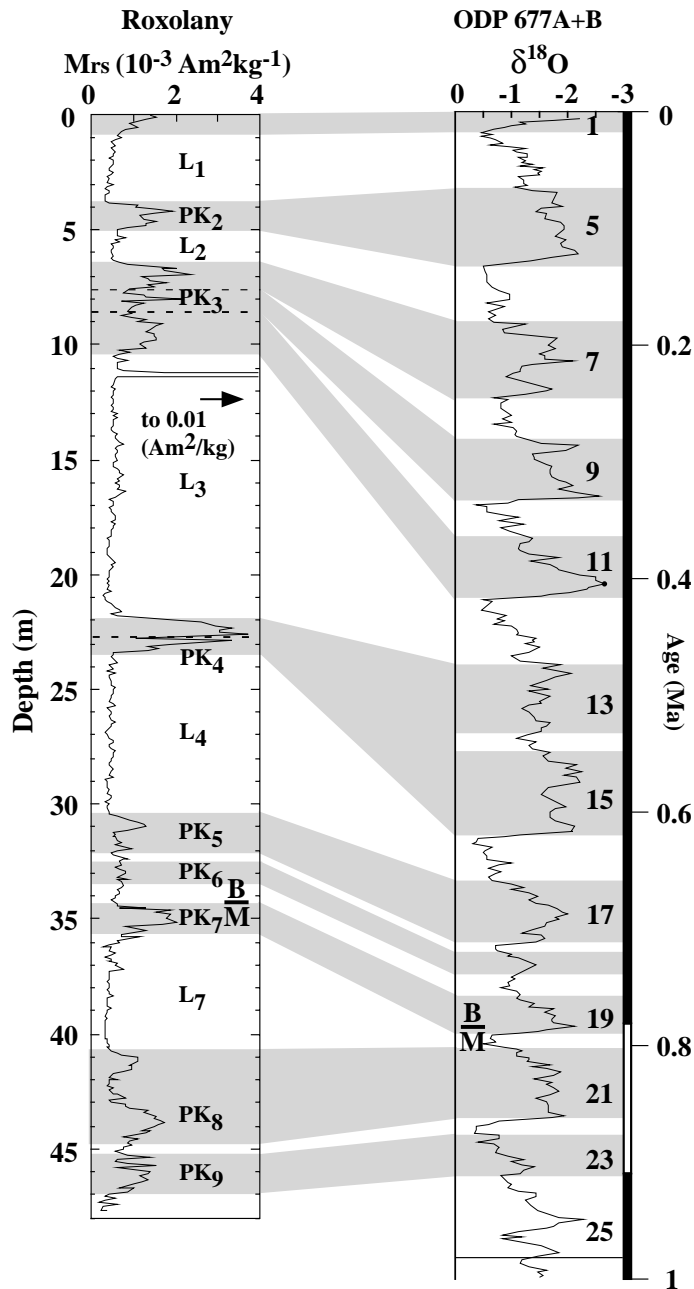


Figure 16: Saturation remanent magnetization as a function of depth at Roxolany compared with the astronomically tuned oxygen isotope record from ODP core 677 (Shackleton et al., 1990) on an absolute timescale. The stratigraphic position of the Matuyama/Brunhes boundary is located near the top of pedocomplex PK₇.

Thompson and Oldfield, 1986), while the susceptibility change is much smaller (~15% smaller in SD magnetite, Thompson and Oldfield, 1986). This observation is in agreement with the grain size coarsening observed in the older loesses (Tsatskin et al., 1998). Wheth-

er this is due to variability in the wind regime, a possible key factor that may be combined with a change in the source material, has still to be clarified. Nevertheless, important changes in the wind regime may imply also a change in the source material.

Using the Matuyama/Brunhes boundary, and considering the outstanding pedologic and magnetic characteristics of PK₄, an attempt was made to correlate the section at Roxolany with other loess sections (Fig. 15) and with the oxygen isotope curve (Fig. 16) (Shackleton et al., 1990). PK₄, the magnetically most strongly developed paleosol, can be correlated on pedological arguments with paleosols in eastern Europe showing similar characteristics, like the Vorona pedocomplex in nearby Tiraspol (Kolkotova Balka, Virina et al., 1997), the paleosol F₆ at Stari Slankamen in the Carpathian basin (Bronger, 1976) (Fig. 15) and the pedocomplex PK₄ in the section at Novaya Etuliya (Spasov, 1998). The idea of a global climatic link between loess evolution in Europe and the Chinese loess plateau (Bronger and Heinkele, 1989) allows a correlation of PK₄ at Roxolany with the most strongly developed paleosol S₅ in the Chinese loess Plateau, and also with oxygen isotope stages 13, 14 and 15 (Fig. 16).

The reason for the strong magnetic enhancement is long exposure to climatic conditions favouring magnetic enhancement rather than magnetic depletion (Han et al., 1996): precipitation-temperature conditions did not reach the magnitudes observed in the older paleosols PK₈ and PK₉ with suggested mean annual precipitation around 1000 mm/yr and mean annual temperatures around 18°-20° C, but are at 600-700 mm/yr and 16°-18°C, respectively (Tsatskin et al., 1998).

Pedocomplex PK₂ is interpreted as an interglacial soil, and is correlated to oxygen stage 5. Magnetic measurements show that during the formation of PK₂₋₁, conditions were more favourable to pedogenic magnetic enhancement (especially due to SP grains) than during formation of the older PK₂₋₂. The latter can be associated with oxygen isotope substage 5e, also in consideration of the similarity of its A horizon and that of PK₁ (Tsatskin et al., 1998).

Since oxygen isotope substage 5e was “warmer” with respect to substages 5a, b, c and d, the unexpected lower magnetic enhancement of PK₂₋₂ may be due to climatic conditions less favourable to magnetic enhancement. A climate with lower seasonal contrast during formation of PK₂₋₂ (semiarid steppe soil, Tsatskin et al., 1998) with respect of that during formation of PK₂₋₁ (subhumid steppe, Tsatskin et al., 1998) may have favoured a weaker magnetic enhancement.

Pedocomplex PK₃, formed by three paleosols, as confirmed also by magnetic analysis (figs. 12,16), can be correlated with oxygen isotope stages 7, 9 and 11. The highest M_s and susceptibility values are observed in PK₃₋₁, decreasing in the underlying PK₃₋₂ and PK₃₋₃. PK₃₋₁ is associated with forest steppe environments either in slightly moister and warmer climate than today with strong dry-wet contrast, or developed on a more clayey substrate (Tsatskin et al., 1998). PK₃₋₂ and PK₃₋₃ are considered closer to grassland chernosem soils well supplied with water. Hence, the lower magnetic enhancement could be related to reducing conditions during soil formation, especially in PK₃₋₃, where M_s in the humic and accumulation horizon are almost equal (Fig. 16).

PK₄, the magnetically strongest paleosol of the outcrop is correlated with three oxygen isotope stages, (interglacials 13 and 15, glacial 14). Stages 13 and 15 are not better expressed than the other interglacials and thus do not explain the strong enhancement of PK₄. Possibly very long exposure to climatic conditions favouring low weathering intensity has provoked the strong magnetic enhancement.

From their study of modern soil, Han et al. (1996) proposed that magnetic destruction takes place beyond the limiting climate conditions with mean annual temperatures of 15°C and/or mean annual precipitations of 1200 mm. The pedological study of Tsatkin et al. (1998) suggested that PK₄ was formed in a warm seasonally dry forest environment (annual mean temperatures between 16° and 18°C, annual mean precipitations between 600 and 700 mm, tab. 1). Hence, the relatively dry climatic conditions under which PK₄ was formed might have been decisive in favouring the magnetic enhancement.

The three pedocomplexes PK₅, PK₆ and PK₇ can be correlated with the oxygen isotope stage 17, the interstadial of the glacial period corresponding to oxygen isotope stage 18 and to stage 19, respectively. The lowermost pedocomplexes PK₈ and PK₉ are correlated with oxygen isotope stages 21 and 23, respectively, belonging to the Matuyama chron. As already mentioned, the less pronounced magnetic enhancement observed in the paleosols below PK₄ is related to warmer and wetter climate that may have favoured magnetic depletion.

The magnetic properties of the loess layers also exhibit remarkable differences, especially when weak pedogenic features are present, or when transition zones from pedocomplexes to loesses and vice versa are approached.

In the loess layer L₁, where susceptibility is constant and gives no sign of pedogenic enhancement, the coercivity minimum and the increase of $\chi_{LF}/SIRM$ (relative increase of

SD magnetic minerals) can be interpreted as a sign of warming and can be correlated with oxygen stage 3. Loess layers L_3 and L_4 are characterized by high sedimentation rates. In L_3 , just below PK_{3-3} , $\chi_{LF}/SIRM$ and $ARM/SIRM$ drop and coercivities increase. This indicates a decrease of SP grains but also an increase of magnetically harder minerals. Between 11 m and 15 m, the values remain constant as a result of a very cold climate and fast deposition episodes. In the lower half of L_3 a contrasting pattern is observed. This behaviour suggests that in the youngest part of horizon L_3 the magnetic parameters are controlled by hard detrital magnetic minerals, while in the older part the contribution of softer detrital minerals increases. Stronger winds at the beginning of the sedimentation of layer L_3 could explain the lower coercivities through the presence of large MD grains. This observation correlates well with the rewarming observed in the lower part of oxygen isotope stage 12 (Fig. 16).

In L_4 the anomaly in the coercivities and remanence data can also be attributed to a short warming, consistent with the oxygen isotope curve for stage 16. In loess L_7 the calcrete nodules at 37 m, 38.30 m and at 39.5 m depth are clearly reflected in the remanence and coercivity properties with different magnetic grain size characteristics that could witness differences in the climates involved (Fig. 14), indicating that the incipient soil at 37 m formed under warmer conditions than those at 38.30 m and 39.50 m.

A high variability of dust accumulation in the Black Sea area in different cold stages of the Quaternary is indicated by the strongly varying loess thickness (from 1 m to 12 m, with an estimated sedimentation rate varying from 5 to 20 cm/ka. From a magnetic point of view L_1 , L_3 , L_4 and L_7 have similar high coercivities, while L_2 , L_5 , L_6 and L_8 are characterized by a magnetically softer component, probably because of their reduced thickness favouring the influence of pedogenesis of the adjacent pedocomplexes. The low χ_{ARM}/χ_{LF} values measured in L_4 and L_7 , in particular, indicate the presence of a softer component than in L_1 , L_2 and L_3 . This can be attributed to a relative increase of MD grains, which is consistent with the grain coarsening observed in the older loesses (Tsatskin et al., 1998).

2.6 Conclusions

The loess/paleosol sequence at Roxolany consists of six major pedocomplexes and distinct loess layers the latter being identified by the constant low magnitude of their magnetization. Higher concentration of ferromagnetic minerals and clearly higher susceptibilities characterize paleosols.

Determination of the Matuyama/Brunhes boundary at 35 m depth provides the only absolute age assignment. By extrapolation beyond the M/B boundary, using the average sedimentation rate of the upper part of the section (~ 4.5 cm/ka), loess deposition at Roxolany started some 1 Ma ago. The recognition of the M/B boundary permits correlation of the climate variability in the Black Sea area with global climate change during the Quaternary as expressed by the oxygen isotope record from marine sediments. Nearby loess sites, but also more remote sections in Europe and Eastern Asia, can be correlated with the Roxolany loess/paleosol development giving evidence of synchronous terrestrial paleoclimatic changes.

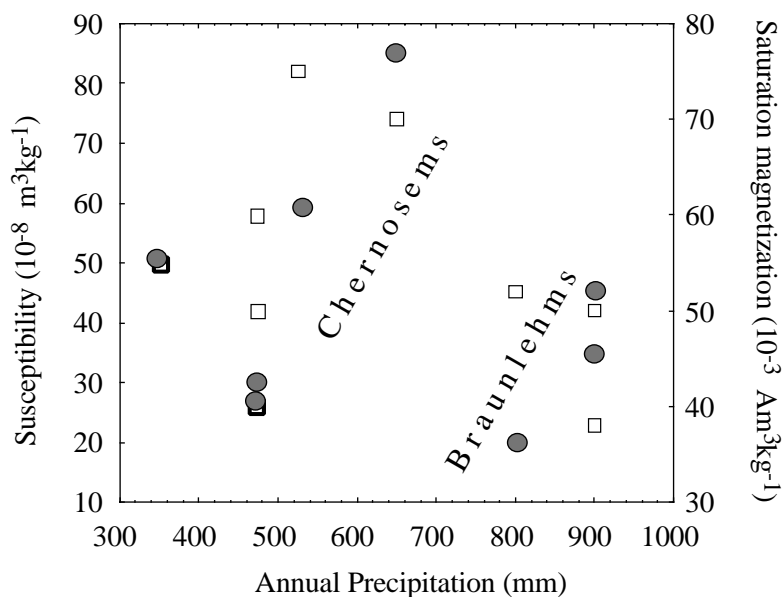


Figure 17: Annual precipitation versus susceptibility (black dots) and saturation magnetization (white squares) for chernosems and braunlehms at Roxolany. Precipitation values from table 1.

Another chronological marker is represented by the tephra layer found at 11.2 m depth, below PK₃. Absolute age determination of this volcanic layer by means of the Ar/Ar method turns out to be very difficult since the micas and amphiboles are contaminated: the biotite is most likely not of juvenile origin and gives an age of about 50 Ma (± 3), which is incompatible with the paleomagnetic age determination. The amphibole is associated to a younger event and may be of juvenile origin, but ages between 730 ka and 1.6 Ma were found, which are also too high. According to the chronologic interpretation of Tsatskin et al. (1998), which is based on the paleomagnetic measurements and correlation with marine oxygen isotope stages, the tephra at Roxolany should have an age between 400 ka and 450 ka, in oxygen isotope stage 12.

The paleopedologic study of Tsatskin et al. (1998) has demonstrated different climatic conditions under which the different paleosols and loess layers formed. A generally warmer and wetter climate characterised the formation of PK₅ to PK₉, with Mediterranean soil properties (braunlehm) as compared to the younger paleosols PK₁-PK₄ which formed mainly in subhumid to subarid steppe environments.

The relationship between annual precipitation (table 1, Tsatskin et al., 1998) and magnetic susceptibility and saturation magnetization has been plotted in Fig. 17. Both parameters seem to increase with increasing annual precipitation in the chernosems, but have lower values in the braunlehms. A simple linear or logarithmic climofunction as postulated for the Chinese loess by Heller et al. (1993) or Maher and Thompson (1994) does not hold if the braunlehms are considered.

Han et al. (1996) in studying modern soils in China found a quasi-logarithmic increase of the magnetic enhancement with annual mean temperature and/or annual mean precipitation. When saturation conditions are reached and exceeded, magnetic depletion starts due to destruction of magnetic minerals under gleying and reducing conditions. Fig. 17 confirms this trend, where quasi-linear climofunction segments may be constructed for the two major soil types. The “dry” chernosems support the “simple” model of Heller et al. (1993) and Maher and Thompson (1994) and follow the trend of Han’s et al. (1996) data, whereas the slope of the climofunction in the “wet” braunlehms appears quite undetermined and enhancement has been replaced at least partly by depletion. The magnetic climofunction in these braunlehms cannot be utilized for precipitation reconstructions unless the degree of destruction of magnetic minerals could be independently recognized.

The strong remanence fluctuations below PK_4 as expressed by the ARM/SIRM, χ_{lf} /SIRM ratios (Fig. 12) may be indicative of the supposed depletion processes.

Magnetic parameter ratios, however, generally reflect the climate variations not only during interglacial periods, where magnetic enhancement and/or depletion overprint the original detrital magnetic signal, but also during cold periods. Incipient soils, horizons of concentration of calcitic concretions and climate variability (change in the wind regime) which are difficult to observe in the field, may be identified magnetically. The magnetic features can be correlated with the marine oxygen isotope variations. The coercivity variations observed in loess layers L_1 , L_3 and L_4 (Fig. 12), for example, are similar to the fluctuations in the oxygen isotope curve during stages 2-3-4, 12 and 16, respectively (Fig. 16), and help to better define the correlation between magnetic properties and oxygen isotope variations.

Chapter 3

MAGNETIC PROPERTIES OF TWO LOESS/ PALEOSOL SECTIONS FROM THE WESTERN (XIA- GAOYUAN, GANSU PROVINCE) AND THE CENTRAL (HOZHUANG, SHAANXI PROVINCE) CHINESE LOESS PLATEAU

3.1 Introduction

The western Chinese loess plateau is delimited in the north by the Tengger and Badain Jaran deserts, in the west by the Qilian Mountains and in the east by the Liupan Mountains (Fig.1). The loess formation was strongly influenced by the cold winter monsoon winds blowing from the northwest through the Hexi Corridor, resulting in high sedimentation rates diminishing progressively to the south (Lei and Sun, 1984). The central loess plateau, extending from the Liupan mountains in the west to the southward directed segment of the Yellow river in the east along the Liuliang mountains, to the northern slopes of the Qinling mountains in the south and the Mu Us in the north, was less affected by the northern cold winds but more by the moister and warmer summer monsoon winds (Ding et al., 1998). This wind action results in different thicknesses of the loess sequences from the western loess plateau (thickness of > 300 m) to the central part (thickness about 150 m), and in different characteristics of the paleosol pedogenesis which is more strongly developed in the central loess plateau. In the moister paleoclimate, pedogenesis prevailed not only during interglacial periods, but to a reduced extent also during glacial times.

Pedogenesis affects the magnetic properties of loess/paleosol sequences and leads to enhanced magnetic susceptibility in the paleosols of the Chinese loess plateau (Heller and Liu, 1982, 1984). Time series of loess susceptibility variations and marine oxygen isotope records are closely correlated (Heller and Liu, 1986). This reconfirms the lithological/magnetic paleoclimate relation and underscores the influence of climatic factors such as temperature and humidity on the magnetism of loess/paleosol sequences. Because of the present day climate gradient across the Chinese loess plateau, two sections - one on the western and the other on the central plateau - have been selected in order to detail the climate influence on the formation of magnetic signals of both loess and paleosols.

The profiles were sampled at Xiagaoyuan (36°32' N 105°01' S, 150 km northeast of Lanzhou, Gansu province, western loess plateau, Fig. 1) and Houzhuang (35°32' N 109°17' E, near the city of Huangling, Shaanxi Province, central loess plateau)(Fig. 1). The present climate is characterized by similar temperature but higher precipitation at Houzhuang than at Xiagaoyuan. The mean annual precipitation and temperature are ~650 mm/yr and 9.4°C, respectively, in Huangling (representative for the climate in

Houzhuang, Liu et al., 1964), whereas the corresponding values amount to ~340 mm/yr (Liu et al., 1964) and 9.5°C (Heinkele, 1990), respectively, in Lanzhou (representative for Xiagaoyuan). Since Xiagaoyuan is situated at ~2000 m altitude, lower mean annual temperatures are to be expected than at Lanzhou (~1500 m altitude).

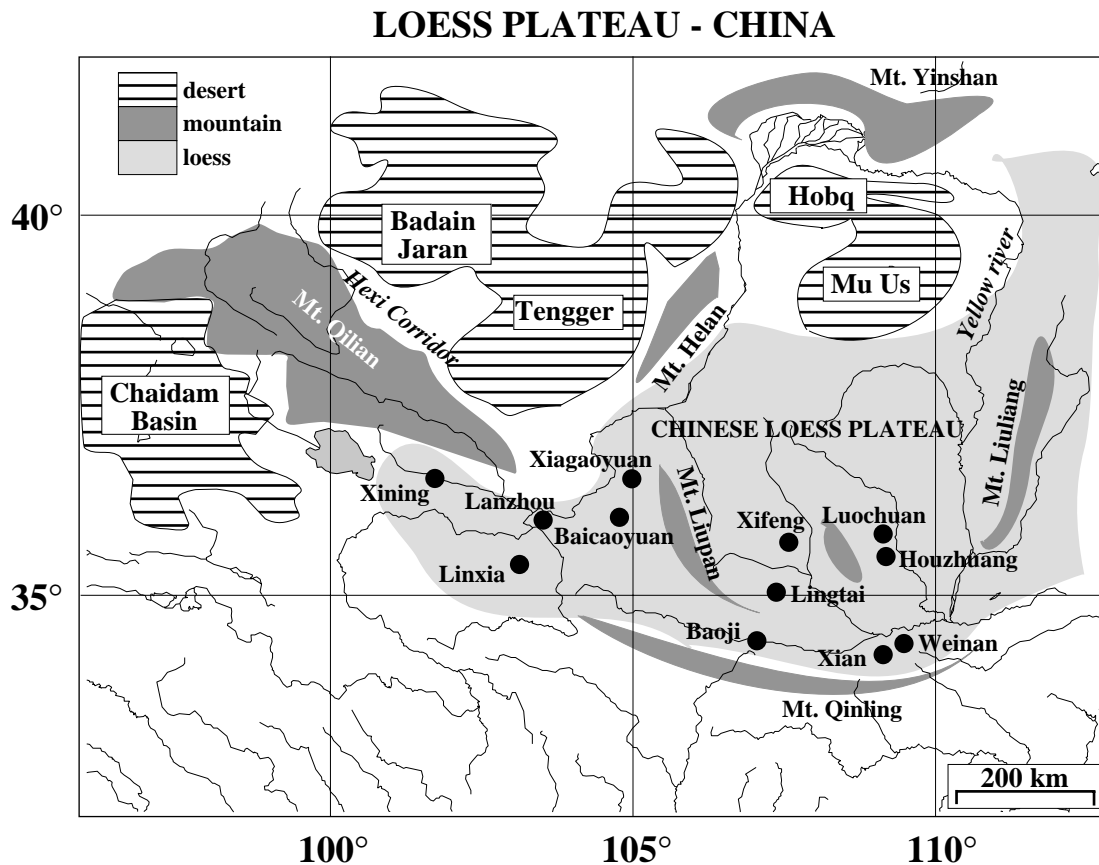


Figure 1: Location of the Chinese loess plateau (modified after Ding et al., 1991)

In both sequences, deep trenches were cut into the hill slopes with the help of local farmers. About 1 m wide stair steps provided access to undisturbed material. Trench 1 at Xiagaoyuan represents the upper 9 m of the loess sequence. Sampling from 7 m down to 23 m depth was continued in a second, partially overlapping trench (Fig. 2). The two sections were a few meters apart on the same slope where no signs of slippage were visible. The sections were correlated observing lithological horizons with beginning pedogenesis and utilizing magnetic susceptibility measurements in the field and in the laboratory. The susceptibility variations in the overlapping portions (shaded in Fig. 2) are very small. An increase in susceptibility was measured in trench 1 from ~7.5 m to ~8.7 m, followed by a

small decrease down to 9 m. A similar pattern is observed from 8 m to 10 m at trench 2.

At Houzhuang the upper trench (from the surface down to 8 m depth) and the lower trench (from 7 to 20 m depth) were sampled from two opposite nearly vertical slopes (~20 m distant from each other).

The boundary between loess layer L_1 and paleosol S_1 was taken as reference for the correlation, where a strong susceptibility increase was observed in both trenches. Samples were taken every 5 cm (every 10 cm from 10 m to 16 m depth at Xiagaoyuan). A total of about 449 samples was taken at Houzhuang and about 450 samples at Xiagaoyuan.

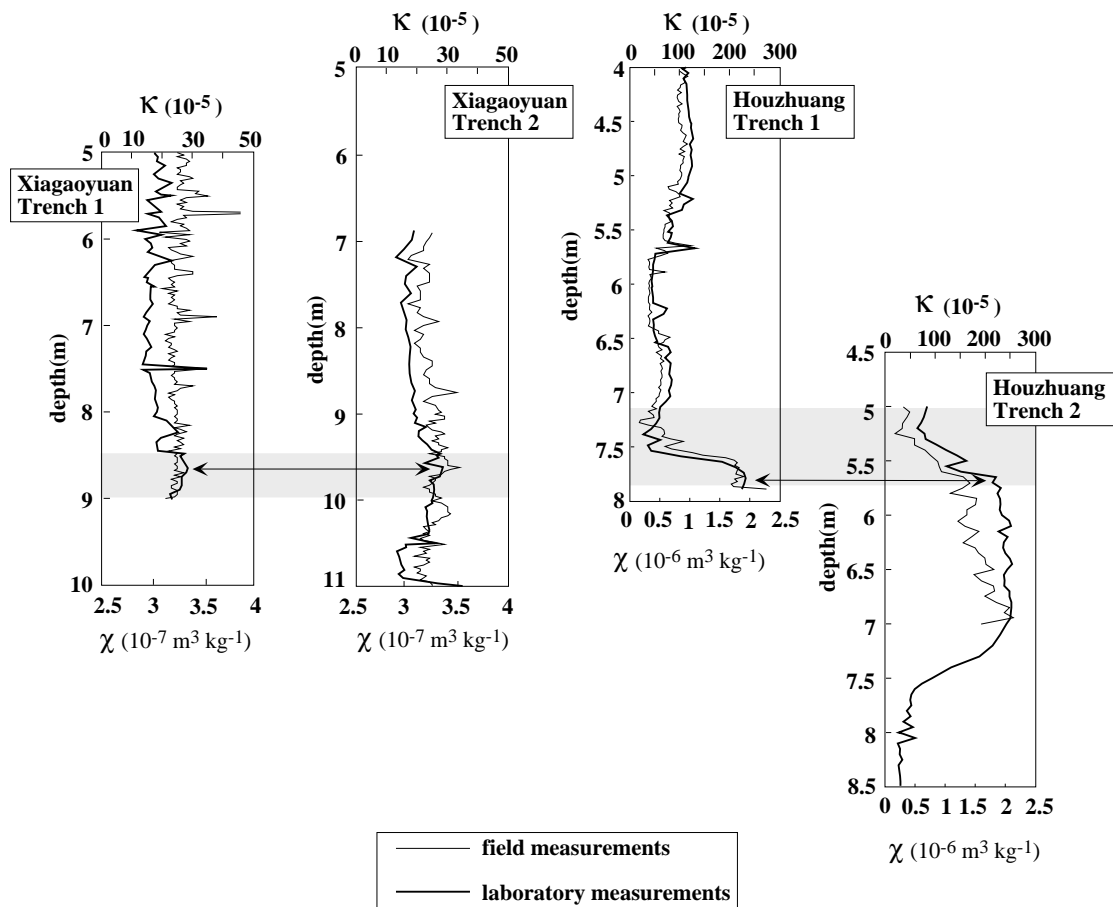


Figure 2: Susceptibility measured in the field (κ) and in the laboratory (χ) as a function of depth for the trenches at Xiagaoyuan and Houzhuang. The shaded intervals correspond to the overlapping part of the trenches. At Houzhuang the increase in susceptibility in paleosol S_1 is used as reference for the correlation. At Xiagaoyuan the correlation was simplified since both trenches are situated on the same slope. The depths in all trenches were initially measured from arbitrary reference points. After correlating the susceptibility profiles, corrected depths are derived as indicated.

The lower part of the composite section at Xiagaoyuan corresponds to the transition

from loess layer L_2 to paleosol S_1 (age ~ 130 ka), whereas the sampling at Houzhuang reaches down to the upper part of L_3 (age ~ 250 ka) (Fig. 3). The boundary L_2 - S_1 is at a depth of ~ 23.30 m in Xiagaoyuan and at a depth of ~ 10 m in Houzhuang (Fig. 3). Hence, the sedimentation rate at Xiagaoyuan is about 25 cm/ka and more than three times higher than that in Houzhuang (~ 7.7 cm/ka). During the last interglacial (marine oxygen isotope stage 5, paleosol S_1) the sedimentation rate at Xiagaoyuan is about 10 cm/ka, almost three times higher than at Houzhuang (~ 3.5 cm/ka). This indicates strong climatic differences also during this period, which is consistent with present day mean temperatures and precipitation differences in the western and central loess plateau.

The high sedimentation rate at Xiagaoyuan provides the possibility of developing a high resolution timescale for susceptibility and median grain size variation during the studied last ~ 70 ka beyond the accuracy of the orbitally tuned glacial/interglacial timescale. Porter and An (1995) identified six Heinrich events (Heinrich, 1988) in the Malan loess, the younger glacial horizon of the Luochuan section. In order to improve the age information needed to establish the correlation between high latitude Northern Hemisphere climate and the Chinese monsoon system, e.g. by identifying Heinrich events as well as Dansgaard-Oeschger cycles (Dansgaard et al., 1993) or Bond cycles (Bond et al., 1992), Chen et al. (1997) measured susceptibility, CaCO_3 content and grain size variation during the last glacial in three sections on the western Chinese loess plateau. Climate variations (interstadial and Heinrich events) observed in those sections correlate well with the observations made in ice and deep sea cores. A similar approach is attempted here using susceptibility and grain size variations during the last glacial cycle at Xiagaoyuan (sedimentation rate of ~ 25 cm/ka).

3.2 Lithological description

The loess/paleosol sequence at Xiagaoyuan, depicted in figure 3, includes a ~ 2 m thick surface soil, an underlying loess layer extending to a depth of ~ 16 m and two pedocomplexes at ~ 17 m (S_1S_1 , nomenclature following Kukla and An, 1989) and ~ 23 m (S_1S_3). The surface soil is a calcareous chernosem, and consists of a 0.6 m thick A_{ca} (humic horizon, a greyish-brown sandy loam, crumbly with roots biofeatures), a 1 m thick AB_{ca} (a heterogeneous sandy loam with abundant krotovinas, showing also spots of

CaCO₃ everywhere) and a BC_{ca} horizon down to 2 m depth (reworked parent material). This recent soil is labelled S₀ in Fig. 3, and represents the Holocene soil. The Holocene soil is preceded by the ~14 m thick loess layer L₁ that formed during the last glacial period (marine oxygen isotope stages 2, 3 and 4). This layer is not homogeneous, but interlayered with several centimeter-thick structures (figs. 3, 4), such as darker layers (from olive yellow to brownish horizons: from 6 m to 6.20 m, at 12 m, 14 m and 15.30 m depth), CaCO₃ patches or concretion layers (at 5 m, 8 m, 12.20 m, 14.10 m and 15.40 m depth) and layers showing pedogenic re-working (at 3.50 m depth) or biological activity (from 9 to 11 m depth). These layers are labeled PL (Pedogenic Layers) in Fig. 4 where a very detailed lithological description is also given.

The lower part of the composite section, from 16.2 m to 23 m, is characterized by the presence of two well developed paleosols interlayered by a loess layer which shows remains of pedogenic activity.

From 16.2 to 17.70 m a paleosol is present which is characterized by a 1.10 m thick A horizon (a yellowish to dark-yellowish-brown silty loam, showing krotovina fillings in the upper part) and a 0.40 m thick BC_{ca} horizon (carbonate accumulations). The loess layer from 17.70 to 21.30 m has at 18.90 m and at 20 m depth krotovinas infillings of up to 10 cm thickness. These two horizons can be considered as remainders of pedogenic activity during a warmer and more humid climate. Another pedocomplex occurs from 21.40 to 23 m depth. In the upper part there is a 60 cm thick AB_{ca} horizon, a yellowish brown loam with krotovinas filled with loess material. The lower boundary of the horizon shows everywhere druses of gypsum and diffuse carbonates. The lower part of the AB_{ca} horizon has a clear boundary to the underlying A₁ horizon, a 50 cm thick yellowish brown clayey loam with weakly blocky aggregates and secondary CaCO₃ mycelia. The lowermost 50 cm are formed by a B_c horizon overlying a B_{ca} horizon, with many krotovina disturbances in the upper part and earthworm holes in the lower part.

At Houzhuang there are no unaltered loess layers as observed in Xiagaoyuan. The upper 2.80 m of the section are characterized by a pedocomplex composed of two soil bodies showing well developed A, B and BC horizons (S₀). The upper 0.40 m are represented by a yellowish-brown silty A_p loam horizon, with a sharp ploughed lower boundary.

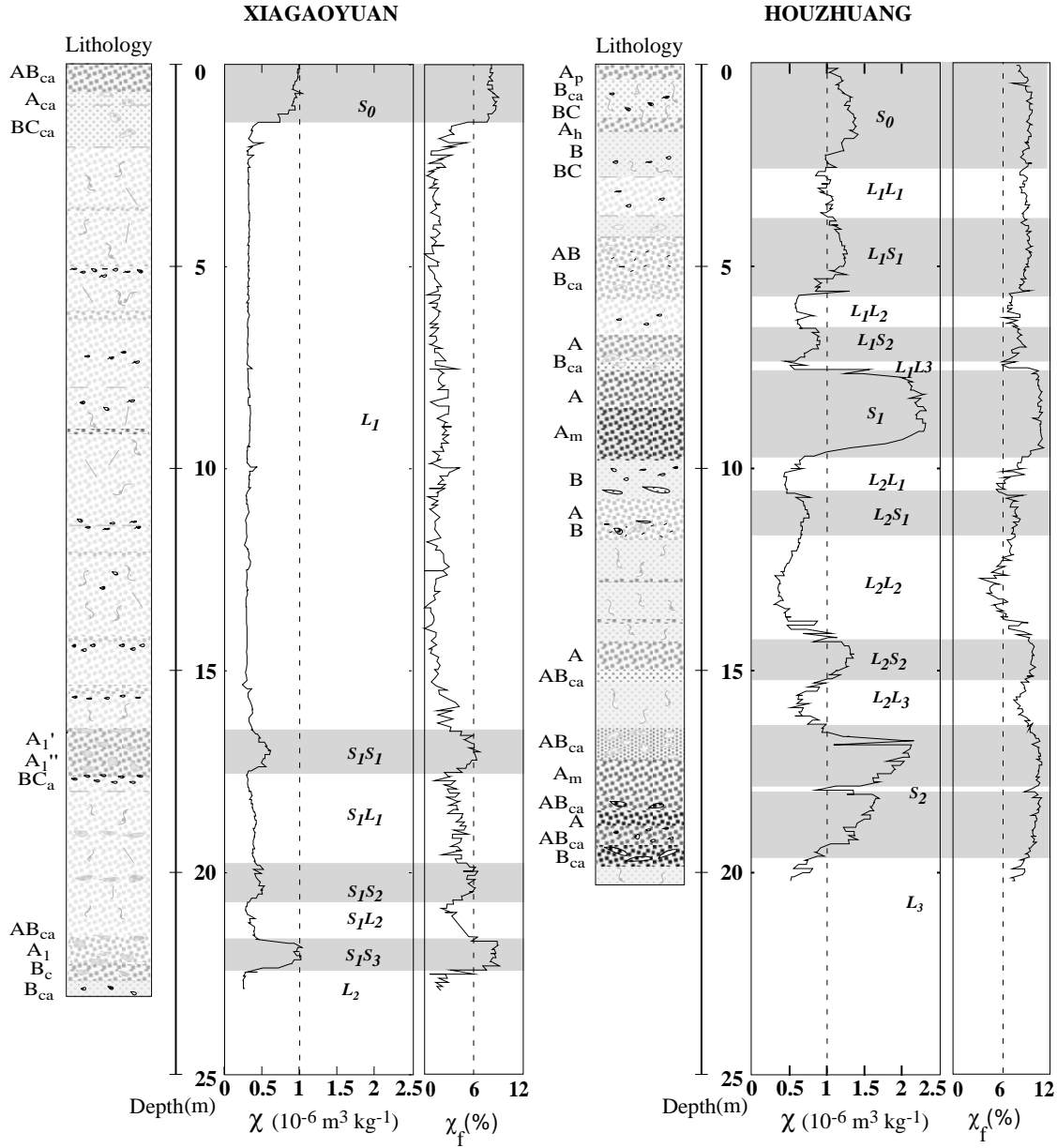


Figure 3: Lithology, specific magnetic low field susceptibility χ and frequency dependent susceptibility χ_f [$\chi_f = 100 \times (\chi_{LF} - \chi_{HF}) / \chi_{HF}$] of the loess sequences at Xiagaoyuan (western loess plateau) and Houzhuang (central loess plateau). The major and incipient paleosols and loesses were identified in the field (pers. comm. A. Tsatskin) following the Soil Survey Staff (1975) and the Russian system (Egorov et al., 1977). S = paleosol, L = loess. Higher sedimentation rates in Xiagaoyuan are characteristic for the western loess plateau, as well as a lower weathering activity with respect to the central loess plateau (Houzhuang), where sedimentation rates are lower (S_1 at a depth of ~8 m and 2 m thick, whereas at Xiagaoyuan it is at a depth of 16 m and 7 m thick) and the susceptibility signal much stronger, also in the loess.

Below A_p , a B_{ca} and BC horizon of 1 m thickness are present, composed of a dark yellowish brown silty loam with abundant $CaCO_3$ patches. This soil body is superimposed on a second one at 1.40 m depth, represented by a 0.30 m thick A_h horizon, a dark brown clay loam, more strongly humified than the upper horizon, but still aggregated and with abundant pseudomycelia. The underlying B and BC horizons are 1.10 m thick, with dark yellowish brown clay.

From 2.80 to 4.30 m depth (L_1L_1) there is a 1 m thick horizon of reworked loess (with rare loess kindel and mycelia) overlying a 50 cm thick heterogeneous loam horizon, with krotovinas filled with reddish, grey yellow mixed material. The next paleosol (L_1S_1) consists of an AB horizon, a clayey loam, with krotovinas (some filled with $CaCO_3$ “vermicular” neoformations, but not found in the ground mass) and a B_{ca} horizon, a loam with $CaCO_3$ pseudomycelia, grading downward into heterogeneous loam. Krotovinas and rounded clayey inclusions (dense, gleyed) are found. This horizon grades downward to a loess horizon: a silt loam, porous with abundant $CaCO_3$ spots (L_1L_2 , from 5.80 to 6.55 m depth).

From 6.55 to 11.70 m depth the sequence is characterized by pedocomplexes which are labeled L_1S_2 from 6.55 m to 7.40 m, L_1L_3 from 7.40 m to 7.60, S_1 down to 9.60 m, L_2L_1 from 9.60 m to 10.60 and L_2S_1 down to 11.70 m depth. L_1S_2 is composed by an A horizon (a heterogeneous yellowish brown loam with abundant biological features, primarily earthworms and krotovinas) and a B_{ca} horizon, a light olive-brown sandy loam enriched with diffuse carbonate. L_1L_3 corresponds to the lower 20 cm of this B_{ca} horizon.

S_1 is a pedocomplex with a 90 cm thick A horizon (dark brown clayey loam) and a 1.10 m thick A_m horizon (dark yellowish brown loam, well aggregated with abundant mycelia, the darkest horizon in the profile). Then follows a 1 m thick decalcified B horizon (L_2L_1). L_2S_1 indicates a paleosol made of an A (brownish silt loam with dense biological turbation and no visible $CaCO_3$ neoformations) and a B horizon (silty loam with abundant mycelia). A thick loess layer (L_2L_2) interlayered with two darker layers which are a few cm thick, extends from 11.70 m to 14.50 m.

L_2S_2 is a 1 m thick paleosol with an A horizon (a brownish silt loam with biological features) and an underlying 30 cm thick AB_{ca} horizon, a loam with dull $CaCO_3$ spots. From 15.20 m to 16 m a reworked loess layer (dark loam, L_2L_3), overlies a 3.30 m thick

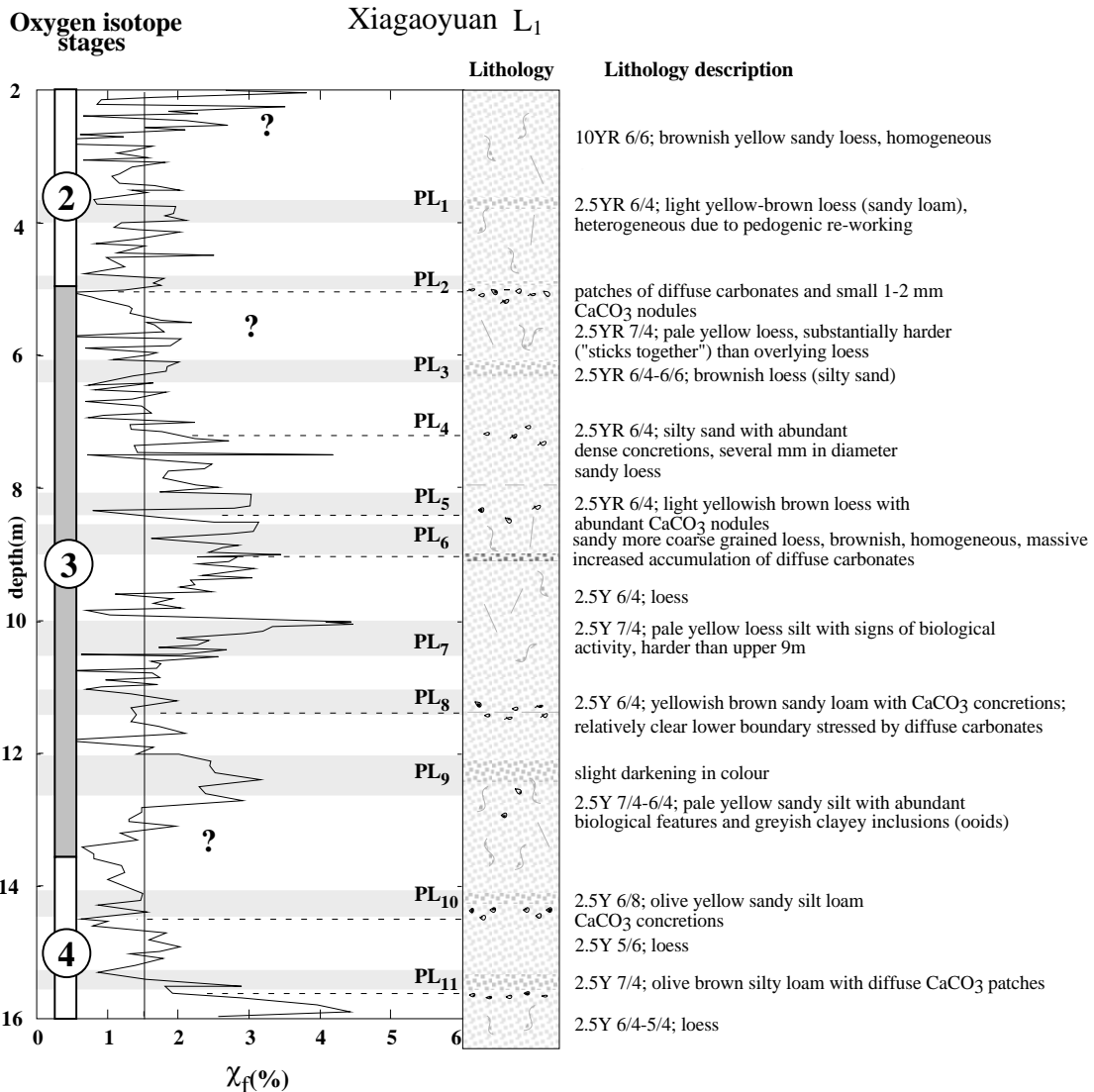


Figure 4: Frequency dependence of magnetic susceptibility χ_f (%) plotted as a function of depth and lithology for the loess layer L₁ (last glacial) at Xiagaoyuan. PL indicates Pedogenic Layers, which are the result of correlation made between susceptibility and lithological observation in the field. The layer L₁ corresponds to the oxygen isotope stages 2, 3 and 4. Lithological description includes Munsell colour numbers.

pedocomplex (S₂).

The latter is characterized by a 80 cm thick AB_{ca} horizon (strong brown loam with abundant krotovinas) and a 1 m thick A_m horizon (dark brown clay loam, strongly aggregated with CaCO₃ elongated efflorescence). The lower 1.50 m of S₂ show a 25 cm thick AB_{ca} horizon (dark yellowish brown loam with loess kindel), a 30 cm thick A horizon (a decalcified strong brown loam), a 50 cm AB_{ca} horizon (with abundant CaCO₃ spots) and

a 45 cm thick B_{ca} horizon (with loess kindel up to 10 cm). The upper 30 cm of the underlying loess horizon L₃ are characterized by large hard carbonate concretions.

3.3 Rock magnetic results

3.3.1 Magnetic susceptibility

Low field susceptibility and lithology correlate well in both sequences (Fig. 3), with high values generally corresponding to paleosols and low values to loess. However, the maximum and also the minimum susceptibility values in Xiagaoyuan and Houzhuang differ considerably, as does the frequency dependence of susceptibility χ_f (F-Factor, Fig. 3), which has in general lower values in loess.

At Xiagaoyuan weak susceptibility is recorded in loess layer L₁, with a minimum value of $0.24 \times 10^{-6} \text{ m}^3\text{kg}^{-1}$ at a depth of 15.40 m and a mean value for L₁ of $0.31 \times 10^{-6} \text{ m}^3\text{kg}^{-1}$. A susceptibility increase is observed in the Holocene soil S₀ (maximum χ of $1 \times 10^{-6} \text{ m}^3\text{kg}^{-1}$) and during the last interglacial, represented by the loess/paleosol sequence between 16 and 23 m: susceptibility is enhanced in the paleosol layers S₁S₁ ($\chi_{\text{max}} = 0.6 \times 10^{-6} \text{ m}^3\text{kg}^{-1}$), S₁S₂ ($\chi_{\text{max}} = 0.5 \times 10^{-6} \text{ m}^3\text{kg}^{-1}$) and S₁S₃ ($\chi_{\text{max}} = 1 \times 10^{-6} \text{ m}^3\text{kg}^{-1}$). The susceptibility minima (χ_{min}) measured in the layers S₁L₁ ($\chi_{\text{min}} = 0.28 \times 10^{-6} \text{ m}^3\text{kg}^{-1}$) and S₁L₂ ($\chi_{\text{min}} = 0.30 \times 10^{-6} \text{ m}^3\text{kg}^{-1}$) are similar to the minimum values measured in L₁ ($0.24 \times 10^{-6} \text{ m}^3\text{kg}^{-1}$). Maximum susceptibility enhancement by a factor 4 was thus observed from the magnetically weakest loess to the strongest paleosol layers.

The highest χ_f values were measured in paleosol S₁S₃ and in the Holocene soil S₀ (mean: 8.7%). S₁S₁ and S₁S₂ have mean values around 6% while the lowest values were measured in the loess layers (mean: 1.7% for L₁ and 3.85% for S₁L₁ and S₁L₂). The low χ_f values measured in Xiagaoyuan in the layers S₁L₁ and S₁L₂ indicate that during the last interglacial the climate varied strongly from warm and wet periods, which led to the formation of the well developed paleosols S₁S₃, S₁S₁ and of the less pronounced S₁S₂, to rather cold and dry periods during which the loess layers S₁L₁ and S₁L₂ formed.

Because of the high sedimentation rate, the sequence at Xiagaoyuan is suitable for detailed analysis of the susceptibility data, in particular during the last glaciation (loess

layer L₁). Figures 3 and 4 show the frequency dependence of susceptibility (χ_f) variation as a function of depth. A general trend towards higher values is observed in the central part of loess layer L₁, with a mean value of 1.90% for the layer interpreted to correspond to oxygen stage 3 (Fig. 4), and a mean value of 1.30% for stages 2 and 4. In the central part of loess layer L₁ (between ~8 and ~13 m) the frequency of the χ_f fluctuations decreases accompanied by higher amplitudes (χ and χ_f) (Fig. 3).

Most of the χ_f peaks can be correlated with field observations of the presence of incipient pedogenic activity, such as the darker layers indicating biological activity or carbonate concretions (Fig. 4). Similar lithological variations have been identified in other loess sequences on the western loess plateau (Li et al., 1992; Chen and Zhang, 1993; Chen et al., 1997). χ_f peaks are found in the sediments corresponding to oxygen isotope stage 3 (from pedogenic layer PL₂ to PL₉). Further variations were found in stage 2 (PL₁) and 4 (PL₁₀ and PL₁₁). Several χ_f peaks (Fig. 4: questionmarks) were found in addition where pedogenic activity was not observed in the field.

The sequence at Houzhuang is characterized by significant pedogenic activity observed in the horizons between soil S₀ and paleosol S₁ (Fig. 3). This is confirmed by a mean susceptibility value from the bottom of layer S₀ to the top of layer S₁) at Houzhuang ($0.94 \times 10^{-6} \text{ m}^3\text{kg}^{-1}$) which is a factor 2.35 higher than that at Xiagaoyuan ($0.40 \times 10^{-6} \text{ m}^3\text{kg}^{-1}$). Susceptibility is enhanced by a factor 5.3 from the magnetically weakest sample ($\chi = 0.43 \times 10^{-6} \text{ m}^3\text{kg}^{-1}$, measured in loess layer L₁L₃) to the strongest sample ($\chi = 2.3 \times 10^{-6} \text{ m}^3\text{kg}^{-1}$, measured in paleosol S₁). χ_f varies generally between 6 and 11%, with the lowest values near 4% at about 12.5 m depth in L₂L₂.

The highest χ (2 to $2.3 \times 10^{-6} \text{ m}^3\text{kg}^{-1}$) and χ_f values (between 11 and 12%) at Houzhuang were measured in the pedocomplexes S₁ and S₂, whereas lower values (χ between 0.29 and $1.1 \times 10^{-6} \text{ m}^3\text{kg}^{-1}$ and χ_f between 4% and 9%) were measured in the weathered loess (L₁L₁, L₁L₂ and L₂L₂) and paleosols formed during interstadial periods (L₁S₁, L₁S₂ and L₂S₁). In the upper 7.50 m of the section (above paleosol S₁) χ is not a strong discriminating factor between loess and paleosol: for example, paleosol L₁S₂ has a weaker susceptibility ($0.70 \times 10^{-6} \text{ m}^3\text{kg}^{-1}$) than loess layer L₁L₁ ($1.00 \times 10^{-6} \text{ m}^3\text{kg}^{-1}$). In the lower part the difference from a magnetic point of view between loess and paleosol is

clearer, although a magnetically weak paleosol is present (L_2S_1 , χ mean: $0.68 \times 10^{-6} \text{ m}^3\text{kg}^{-1}$).

A well defined linear correlation between χ and the difference between low and high frequency susceptibility ($\Delta\chi = \chi_{LF} - \chi_{HF}$) is observed in both sections investigated (Fig. 5), indicating that ferromagnetic grains at the SP/SSD threshold size (at room temperature) contribute to the enhancement of susceptibility. A wider spectrum of susceptibilities is observed at Houzhuang (up to $2.3 \times 10^{-7} \text{ m}^3\text{kg}^{-1}$) with respect to Xiagaoyuan (up to $1.0 \times 10^{-7} \text{ m}^3\text{kg}^{-1}$). Fig. 5 points out the direct relationship between enhancement of susceptibility and increase of the superparamagnetic contribution. At Xiagaoyuan it is possible to recognize distinct groupings for the different horizons, indicating S_0 and S_1S_3 as the most magnetically enhanced and L_1 as the weakest.

The curves have nearly identical slopes and intersect the χ -axis at $2.4\text{-}2.6 \times 10^{-7} \text{ m}^3\text{kg}^{-1}$. This value is thought to represent the background susceptibility χ_B of detrital minerals with frequency independent susceptibility. It is similar to the values measured in other Chinese loess sections (values between 1.4 and $1.9 \times 10^{-7} \text{ m}^3\text{kg}^{-1}$, Forster et al., 1994a). It is represented by the actual data at Xiagaoyuan (for $\Delta\chi \approx 0$, Fig. 5a) whereas χ_B no longer occurs in the actual data at Houzhuang because pedogenic enhancement has overprinted the detrital “background” susceptibility even for the least weathered loess.

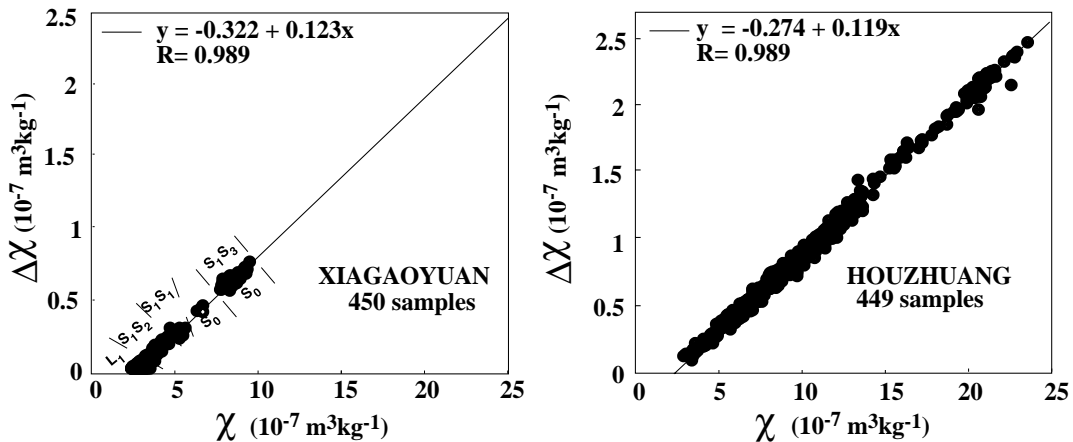


Figure 5: Low field susceptibility χ at low frequency as a function of the difference $\Delta\chi$ with the susceptibility measured at high frequency for the sections at Xiagaoyuan and Houzhuang. In both sections a clear linear correlation is observed.

Susceptibility was measured for four fractionated samples (two loess and two paleosol samples from Xiagaoyuan and Houzhuang) (Fig. 6). A strong grain size dependence is observed in all samples, with susceptibility increasing towards the finer fractions except the pristine loess M23.60 at Xiagaoyuan where susceptibility is nearly constant throughout the grain size fractions.

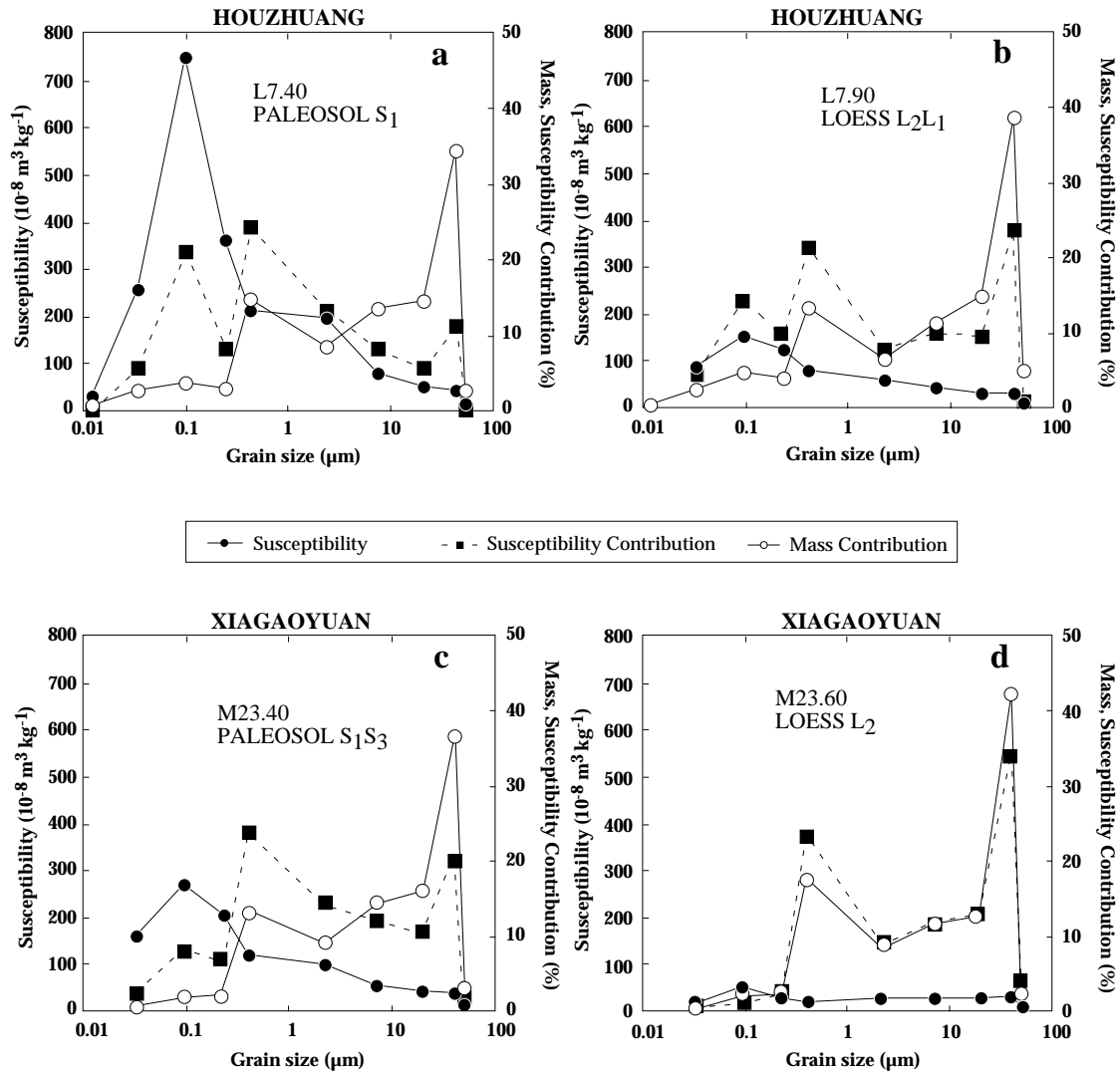


Figure 6: Ten grain size fractions have been obtained by sieving, fractional sedimentation and fractional centrifugation (see also Part I, Chapter 3). Low field susceptibility measured at low frequency (KLY-2: 980 Hz), mass and susceptibility contribution of the grain size fractions for two loess (L7.90 and M23.60) and two paleosol samples (L7.40 and M23.40) from the sections at Houzhuang (a, b) and Xiagaoyuan (c, d).

Susceptibility always peaks in the 0.091-0.228 μm fraction and decreases in the fractions below 0.091 μm , a behaviour which was also observed in the loess section at Paks (Part II, Chapter 1). This decrease is possibly caused by partial clumping of the fin-

est magnetic grains $< 0.091 \mu\text{m}$ onto coarser grains. The susceptibility contribution is highest in the silty fraction ($> 42 \mu\text{m}$) for the loess samples (24% in Houzhuang - sample L7.90 - and 34% in Xiagaoyuan - sample M23.60 -). In these two samples a second mass susceptibility contribution peak is observed in the $0.396 - 2.2 \mu\text{m}$ fraction because of its characteristic large grain size range and resulting large mass contribution (Fig. 6b, c). A sharp drop in the susceptibility contribution below 4.5% is then observed in Xiagaoyuan, because of the largely missing clay fraction in the loess at Xiagaoyuan, while at Houzhuang the value still adds up to ca. 30% in the weathered loess with its significant clay fraction. In the paleosol samples at Xiagaoyuan (M23.40) and at Houzhuang (L7.40) the maximum susceptibility contribution resides in the $0.396 - 2.2 \mu\text{m}$ fraction (around 25%). It decreases clearly in the Xiagaoyuan paleosol (total value = 17.6% for the fractions $< 0.228 \mu\text{m}$), remaining high in Houzhuang (35.8% for the fractions $< 0.228 \mu\text{m}$). The grain-size dependent magnetic measurements demonstrate the important role of the very fine ferromagnetic grains for the susceptibility enhancement. They also shed light on the formation process itself.

The mass distribution in the loess samples is characterized by a slightly higher contribution of silt (39% in L7.90 and 42% in M23.60) than in the paleosol samples (34% for L7.40 and 37% for M23.40). The mass contribution of the grain sizes $< 0.228 \mu\text{m}$ is smaller in the samples from Xiagaoyuan ($\sim 4.4\%$), whereas in Houzhuang the clay component is nearly doubled ($\sim 9.5\%$). This probably results from the general grain size fining from northwest to southeast across the loess plateau but also from generally stronger pedogenesis (Liu, 1964).

For pure and pristine loess (M23.60 at Xiagaoyuan), the susceptibility contribution closely parallels the mass distribution. The original material is equally magnetic throughout the whole grain size spectrum. Mass and susceptibility contributions start diverging with the beginning of pedogenesis. When pedogenesis proceeds, the magnetic contribution of the coarse fraction is reduced relative to the mass contribution because the fine grain size susceptibility contributions become prominent (e.g. L7.40 at Houzhuang, where more than 1/3 of the total susceptibility is concentrated in the mass fraction $< 0.228 \mu\text{m}$ which represents $< 1/10$ of the total mass).

3.3.2 Hysteresis measurements

The hysteresis properties of 564 samples from the sequences at Xiagaoyuan and Houzhuang have been measured using a modernized coercivity spectrometer (Burov et al., 1986) in order to obtain coercive force $(B_0)_c$, coercivity $(B_0)_{cr}$, saturation remanence (M_{rs}) and saturation magnetization (M_s) .

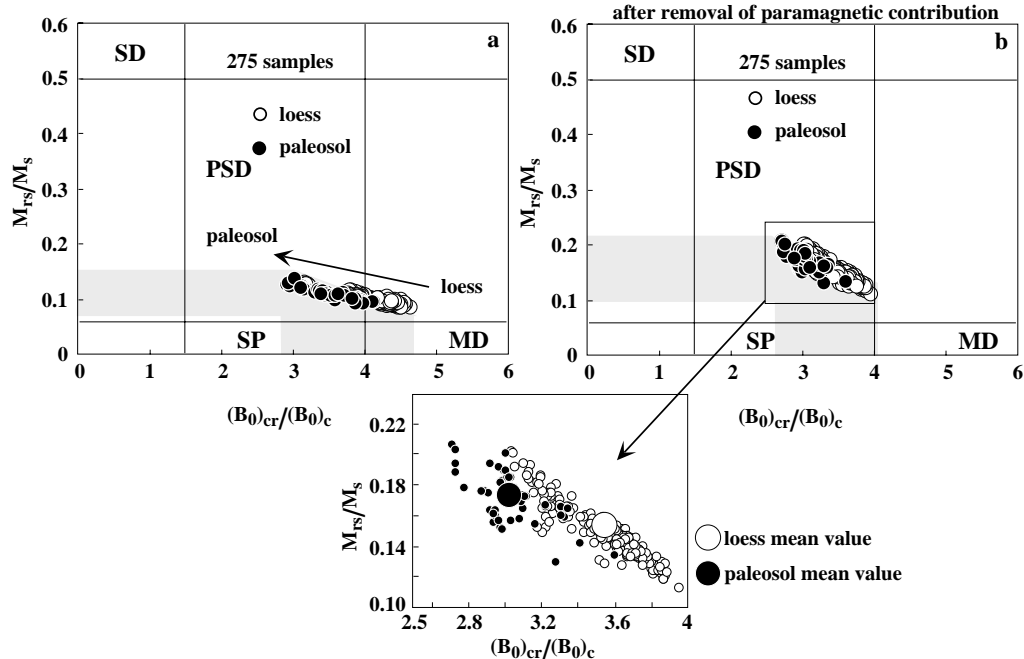
Day plots of hysteresis parameters (Day et al., 1977) give information on the grain size distribution of magnetite minerals (Fig. 7). M_{rs}/M_s is a measure for the relative contribution of MD, PSD, SD and SP magnetites, where lower values are due to the presence of MD grains or/and SP grains, and higher values indicate the presence of stable single domain minerals (Stoner and Wohlfarth, 1948; Bean and Livingston, 1959). The $(B_0)_{cr}/(B_0)_c$ ratio generally decreases to a limiting value of 1 as the SD grain size is approached.

The actual results are affected by the non-ferromagnetic components present in the sediment, especially paramagnetic minerals. The paramagnetic (and diamagnetic) contribution may be corrected for by subtracting the high field magnetization caused by the high field susceptibility χ_h (which results from both the paramagnetic and diamagnetic minerals) from the hysteresis data. The field values chosen for the subtraction have to exceed the ferromagnetic saturation fields, i.e. the field necessary to complete the ferromagnetic loops. A further contribution to χ_h could originate from high coercivity minerals (hematite and/or goethite), but it has been demonstrated that this contribution is negligible (Forster and Heller, 1997).

Figs. 7a and 7c have apparent coercivity ratios ranging from 4.4 to 2.8 at Houzhuang and 4.6 to 2.8 at Xiagaoyuan. The spread is mainly caused by the loess samples, which range from the MD field into the PSD field. At Xiagaoyuan, loess and paleosol samples overlap in the coercivity ratio range between 3 and 4. The magnetization ratio increases linearly with decreasing coercivity ratio. At Houzhuang, where magnetic alteration affects almost all samples, the paleosols behave differently: they have a higher M_{rs}/M_s to $(B_0)_{cr}/(B_0)_c$ gradient than the one observed at Xiagaoyuan, resulting in a slope increase below a $(B_0)_{cr}/(B_0)_c$ ratio value of 3.0.

The above apparent hysteresis behaviour is caused by a significant paramagnetic magnetization contribution to the total induced magnetization at higher fields. Coercive force is also influenced since large paramagnetic magnetization reduces $(B_0)_c$. Hence, the elongated distributions in figs. 7a and 7c indicate that paramagnetism plays an important

XIAGAOUYUAN



HOUZHUANG

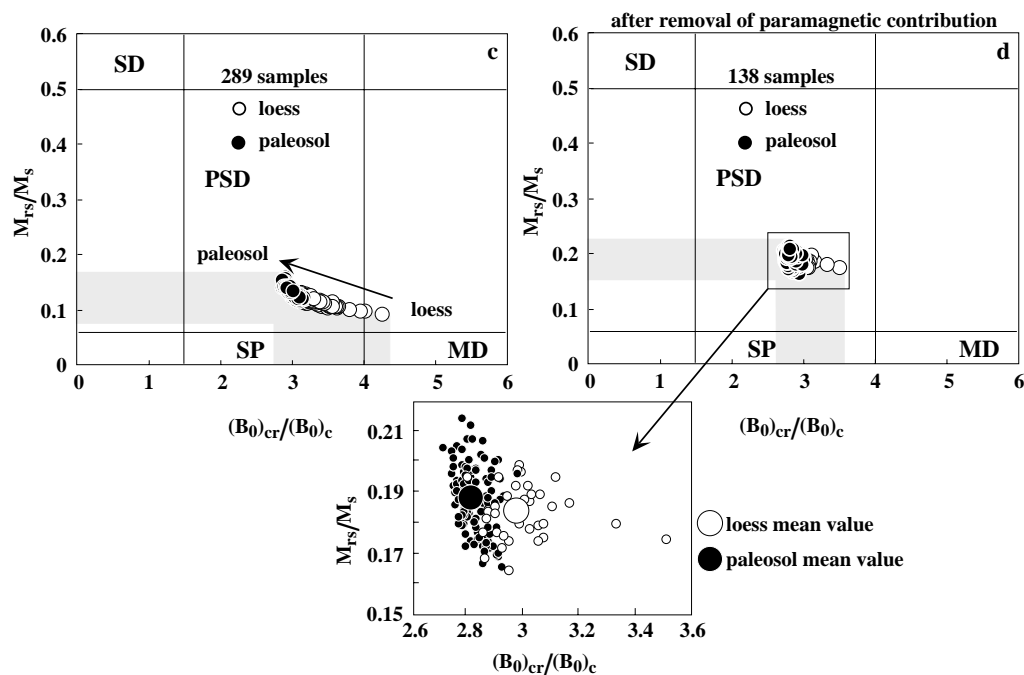


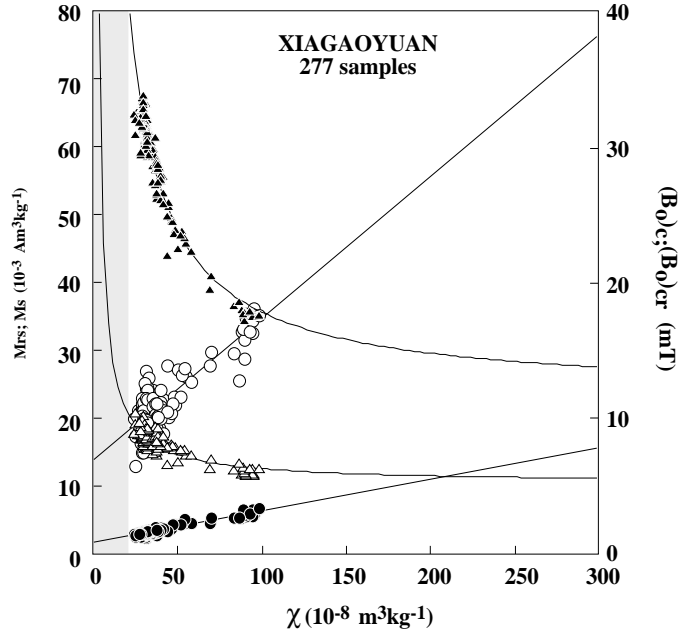
Figure 7: Hysteresis parameters of the sections at Xiagaoyuan and Houzhuang plotted on Day diagrams (Day et al., 1977). Hysteresis parameters were plotted before (a, c) and after (b, d) removal of the paramagnetic mineral contribution. The magnetic properties of the loess samples are shifted towards the centre of the PSD field after subtraction of the paramagnetic signal because of the relatively higher concentration of these minerals (b, d). For both sequences a zoom on the distribution of loess and paleosol samples with their mean value is given, represented by the black (paleosol) and white (loess) big dots (see text for detail).

role in the loess samples whereas ferromagnetism pre-dominates the magnetic properties of the paleosols with their ferromagnetic low field susceptibilities. After correction for the paramagnetic contribution, a generally closer grouping of the samples in the PSD field is observed. At Xiagaoyuan (Fig. 7b) the distribution is still elongated and $(B_0)_{cr}/(B_0)_c$ ranges from 2.6 to 4, while the magnetization ratio spectrum has increased to values between 0.10 and 0.22. The mean $(B_0)_{cr}/(B_0)_c$ and M_{rs}/M_s value for the loess samples are 3.54 ± 0.20 and 0.147 ± 0.016 , respectively whereas a lower $(B_0)_{cr}/(B_0)_c$ value of 3.02 ± 0.19 and higher M_{rs}/M_s value of 0.173 ± 0.016 was measured in the paleosol samples.

The higher elongation ($(B_0)_{cr}/(B_0)_c$ value between 2.7 and 3.9) observed in Xiagaoyuan after paramagnetic correction may indicate a large variability of coarser grain sizes in the loess samples which is obscured in the paleosols by the increasing contribution of finer grained ferromagnetic material. It could also indicate that the loesses in Xiagaoyuan are not “pristine” to the same extent. Especially the loesses S_1L_1 and S_1L_2 , which have layers that indicate the presence of soil forming processes, have higher susceptibilities and frequency dependence values than the glacial loess L_1 .

At Houzhuang the grouping is tighter and nearly all samples fall in a narrow coercivity and magnetization range. The samples with coercivity ratios > 3 belong to the loess layer L_2L_1 and L_2L_2 , which have the lowest low field susceptibility in the studied section. Paleosol mean $(B_0)_{cr}/(B_0)_c$ and M_{rs}/M_s values at Houzhuang are similar to those at Xiagaoyuan, where the $(B_0)_{cr}/(B_0)_c$ value (2.98 ± 0.13) in the loess is slightly higher than in the paleosols (2.81 ± 0.053).

Coercive force $(B_0)_c$, coercivity $(B_0)_{cr}$, saturation magnetization M_s and saturation remanence M_{rs} were plotted against susceptibility χ (Fig. 8). $(B_0)_c$ and $(B_0)_{cr}$ decrease with increasing susceptibility in both sections. Although the susceptibilities in Xiagaoyuan are restricted to generally low values, the fitted $(B_0)_c$ and $(B_0)_{cr}$ curves of both sections trend to nearly identical coercivities at high susceptibility (around 5 mT for $(B_0)_c$ and around 14 mT for $(B_0)_{cr}$). These are considered to represent the typical coercivities of the pedogenic susceptibility enhancing ferromagnetic minerals, and are similar to values from other Chinese (Eyre and Shaw, 1994) and European loess/paleosol sequences (Forster and Heller, 1997). M_{rs} and M_s vary in both sections linearly and again with nearly identical slopes as a function of susceptibility. This was also observed by



Fitted functions for Xiagaoyuan

Fitted functions for Houzhuang

● $M_{rs} = 1.50 \times 10^{-3} + (4.60 \times 10^{-2}) \times \chi$ $R = 0.95$

● $M_{rs} = 2.40 \times 10^{-3} + (4.10 \times 10^{-2}) \times \chi$ $R = 0.97$

○ $M_s = 1.35 \times 10^{-2} + (20.80 \times 10^{-3}) \times \chi$ $R = 0.86$

○ $M_s = 1.27 \times 10^{-2} + (21.90 \times 10^{-3}) \times \chi$ $R = 0.98$

△ $(B_0)_c = 5.4 + 107/\chi$ $R = 0.81$

△ $(B_0)_c = 4.5 + 181/\chi$ $R = 0.98$

▲ $(B_0)_{cr} = 12.0 + 610/\chi$ $R = 0.96$

▲ $(B_0)_{cr} = 12.1 + 642/\chi$ $R = 0.98$

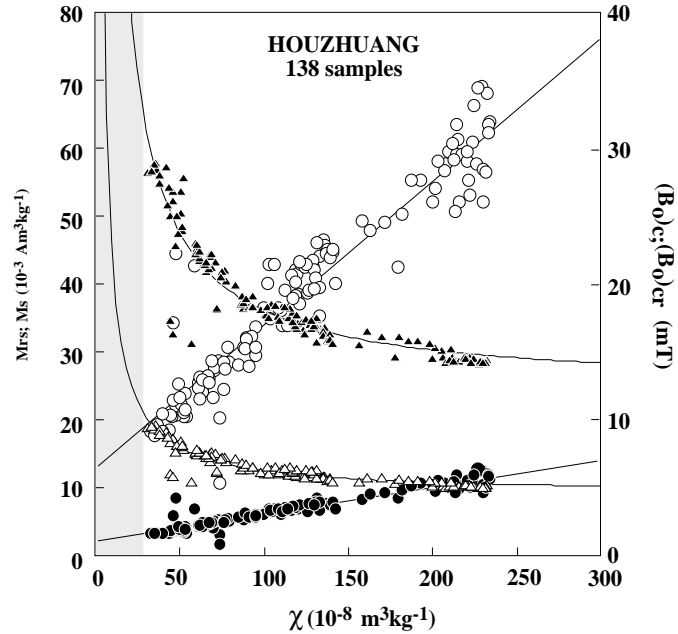


Figure 8: Variation of saturation magnetization M_s , saturation of remanence M_{rs} , coercive force $(B_0)_c$ and coercivity $(B_0)_{cr}$ with low field susceptibility χ . Best fit functions are given for all four parameters at Xiagaoyuan and Houzhuang.

other authors (Eyre and Shaw, 1994; Forster and Heller, 1997; Florindo et al., 1999). It is concluded that the enhancing mineral fraction in all paleosols and weathered loesses is of the same type with respect to mineralogy and grain size distribution regardless of the intensity of pedogenesis.

The latter also seems to determine the quantity of this mineral fraction in a way which we are far from fully understanding.

3.3.3 Temperature dependence of magnetic properties

Further information on the magnetic mineralogy can be obtained by monitoring the temperature dependence of low field susceptibility, remanent magnetization and hysteresis parameters. Hysteresis loops were measured for two samples from the Xiagaoyuan section (paleosol sample M23.40 taken from the paleosol layer S_1S_3 , and loess M23.60 taken from layer L_2) at temperatures between 25 and 700°C using a VSM (Fig. 9). The ferromagnetic magnetization which is saturated at 300 mT decreases progressively with increasing temperature in both samples as does the paramagnetic magnetization. Both samples have a ferromagnetic component up to 500°C. At 600°C and 700°C no hysteresis is recognized, the behaviour becoming dominated by the diamagnetic component (Fig. 9a, b).

Loess sample M23.60 has at room temperature and 300 mT, a saturation magnetization M_s which is about 40% of that of paleosol M23.40 (Fig. 9b). This result is consistent with room temperature hysteresis measurements performed with the coercivity spectrometer (Burov et al., 1986), which indicate that M23.60 has a saturation magnetization M_s which is about 50% of the one of sample M23.40. By using the latter values as reference, the weight of the samples measured with the VSM can be estimated, and hence their magnetizations and specific susceptibilities be calculated. Masses of 94.0 mg for sample M23.40 and 82.2 mg for sample M23.60 were obtained.

M_s and M_{rs} disappear at 600°C, indicating magnetite and/or maghemite as the main carrier(s) of the magnetization (Fig. 9c, d). At room temperature and 100°C, coercive force is higher for the loess sample (16 mT and 14 mT, respectively) than for the paleosol (12 mT and 11 mT). Above 200°C the difference between $(B_0)_c$ measured for M23.40 and M23.60 never exceeds 10% (Fig. 9e) and a change in the slope is observed, with an

increasing slope for the paleosol and a decreasing slope for the loess sample. The slope change appears clearer in the paleosol sample M23.40: a similar observation was made by Argyle and Dunlop (1990) in magnetite samples reduced from hematite (size ~ 540 nm); they interpreted the anomalous decrease of $(B_0)_c$ at 200°C as caused by domain wall pinning due to lattice defects.

HYSTERESIS (25°C - 700°C) XIAGAOYUAN

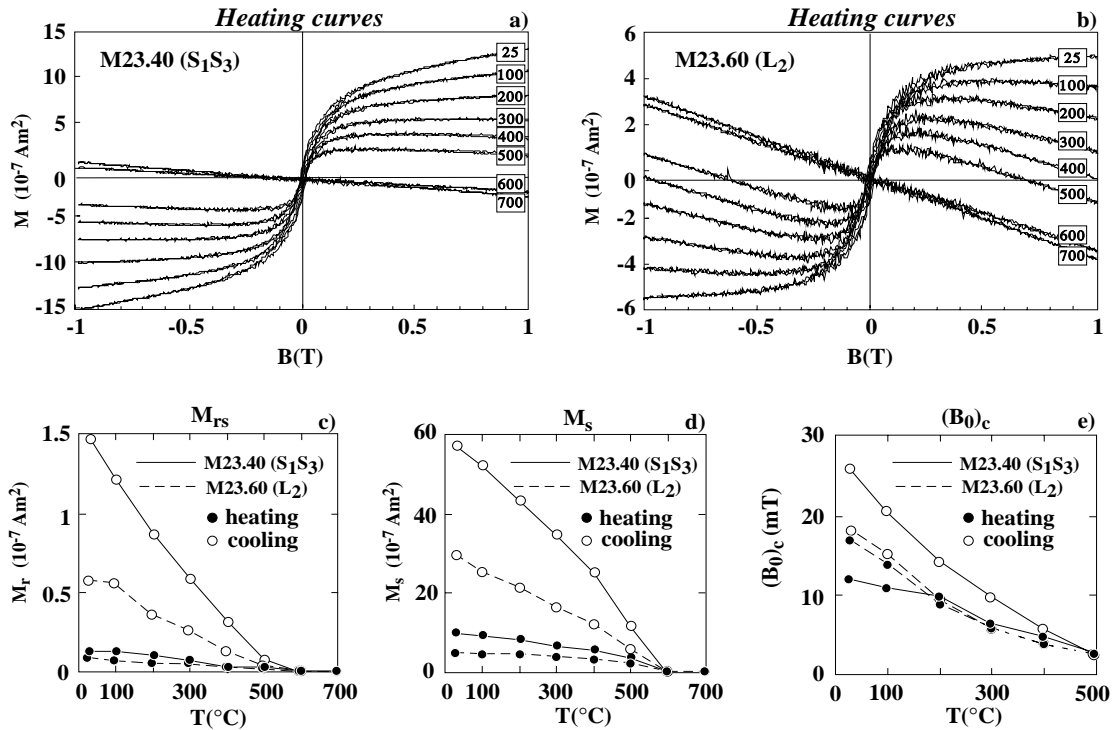


Figure 9: Hysteresis measurements as a function of temperature for unknown but very similar quantities of a paleosol (M23.40) and a loess sample (M23.60) from the loess sequence at Xiagaoyuan (a, b). The measurements were performed in air at eight different temperatures, ranging from 25 to 700°C . Above 500°C the diamagnetic component predominates, indicating magnetite and/or maghemite as the carrier(s) of the ferromagnetic signal. The remanent magnetization M_r , saturation magnetization M_s and coercive force $(B_0)_c$ values obtained after paramagnetic and diamagnetic corrections are plotted as a function of temperature for both samples (c, d, e, respectively). Coercive force was plotted for temperatures $\leq 500^\circ\text{C}$ only.

The large coercivity decrease in the loess sample M23.60 below 200°C could result from domain wall movement and rearrangement in MD magnetite grains (Heider et al., 1988).

The temperature dependence of hysteresis parameters was also measured during cooling from 700°C to room temperature (Fig. 9c, d and e). All parameters, especially

for the paleosol M23.40, show a strong increase below 500°C with respect to the values measured during heating. Chemical processes occurring at high temperatures are responsible for this enhancement, such as formation of new magnetite and/or maghemite minerals, partly harder than the original magnetite.

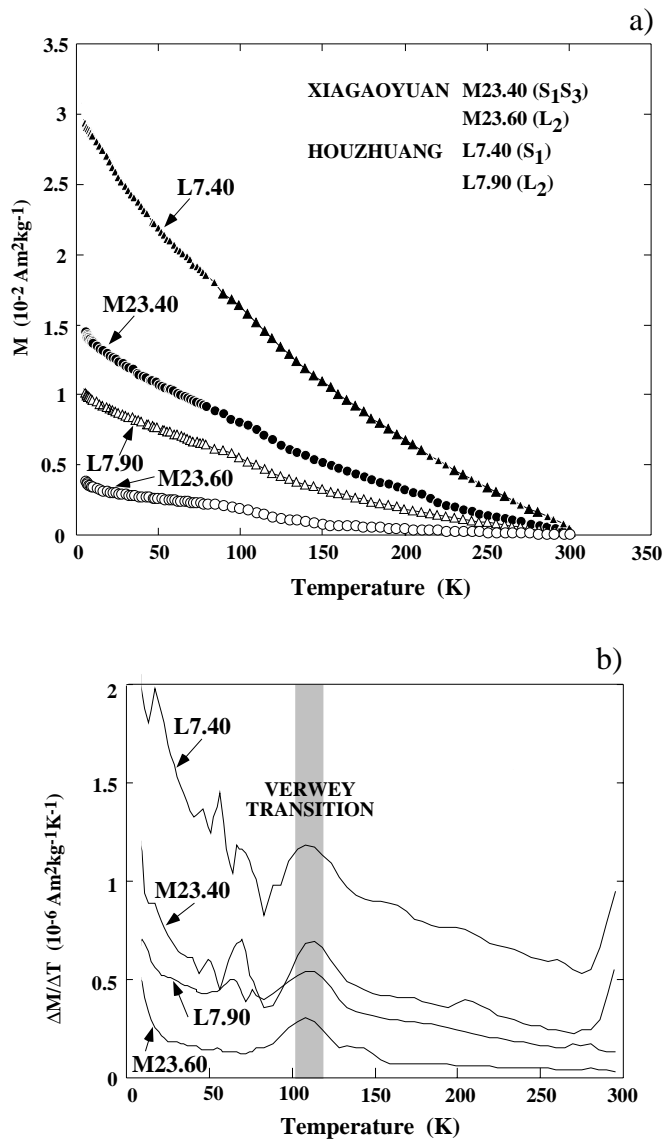


Figure 10: Low temperature TRM(T) experiments performed on two loess and two paleosol samples from Xiagaoyuan and Houzhuang (a) and their derivative curves (b). A significant peak of the gradient in the temperature range between 100 and 120 K indicates the presence of magnetite (Verwey transition).

To determine the diamagnetic contribution, the curves measured at 600°C and 700°C were fitted using a linear function, under the assumption that the diamagnetic and paramagnetic mineralogy does not alter during these temperatures. A diamagnetic susceptibility χ_d of $-0.91 \times 10^{-8} \text{ m}^3\text{kg}^{-1}$ for paleosol M23.40 and of $-1.11 \times 10^{-8} \text{ m}^3\text{kg}^{-1}$ for

loess M23.60 was determined. The paramagnetic susceptibility χ_p at room temperature is slightly higher in the paleosol ($2.17 \times 10^{-8} \text{ m}^3\text{kg}^{-1}$) than in the loess ($1.91 \times 10^{-8} \text{ m}^3\text{kg}^{-1}$), but its relative contribution to the total susceptibility is higher in the loess (5.45%) than in the paleosol (2.0%) The χ_p values are in agreement with those observed for other loess sequences in China (Forster and Heller, 1997), but the small data set is not sufficient to conclude that in general the paramagnetic susceptibility increases with increasing susceptibility.

Low temperature TRM(T) measurements were performed on four samples, two from Xiagaoyuan (paleosol S₁S₃ M23.40 and loess L₂ M23.60) and two from Houzhuang (L7.40 from layer S₁ and L7.90 from layer L₂) in order to determine the carrier of the ferromagnetic signal (Fig. 10a). Both paleosol samples L7.40 and M23.40 exhibit a strong magnetization compared to the loess samples L7.90 and M23.60. The demagnetization curve is slightly concave in all samples. The gradient curves of the TRM(T) curves always show pronounced peaks between 100 K and 120 K, which are taken as evidence of the Verwey transition, being characteristic of magnetite (Fig. 10b). This does not preclude, however, the simultaneous existence of maghemite (Eyre and Shaw, 1994).

The four samples from Xiagaoyuan and Houzhuang were also used for a ZFC experiment from 2.5 up to 300 K (Fig. 11a). The applied field upon heating was 1 mT. The susceptibility values obtained at 300 K are comparable with the results obtained with the Bartington susceptibility bridge, although the measurement technique is different (Table. 1).

sample	Susceptibility ($10^{-6} \text{ m}^3 \text{ kg}^{-1}$)			susceptibility loss (%)
	Bartington	S-600 (ZFC)	Maximum Minimum	
paleosol L7.40	2.10	2.00	3.57 1.31	64
loess L7.90	0.75	0.70	3.40 0.65	81
paleosol M23.40	1.10	1.09	4.25 0.89	80
loess M23.60	0.35	0.35	3.60 0.35	91

Table 1: Susceptibility values at room temperature measured using the susceptometer S-600 and the Bartington susceptibility bridge. The maximum and minimum susceptibility value during the ZFC experiment are given for all samples, as well as the susceptibility loss (%) from 2.5 K to its lowest value (below 100 K) Maximum susceptibility is measured at the lowest temperature, while the lowest values precede the onset of the contribution of the SP grains to the magnetic signal (see Fig. 11).

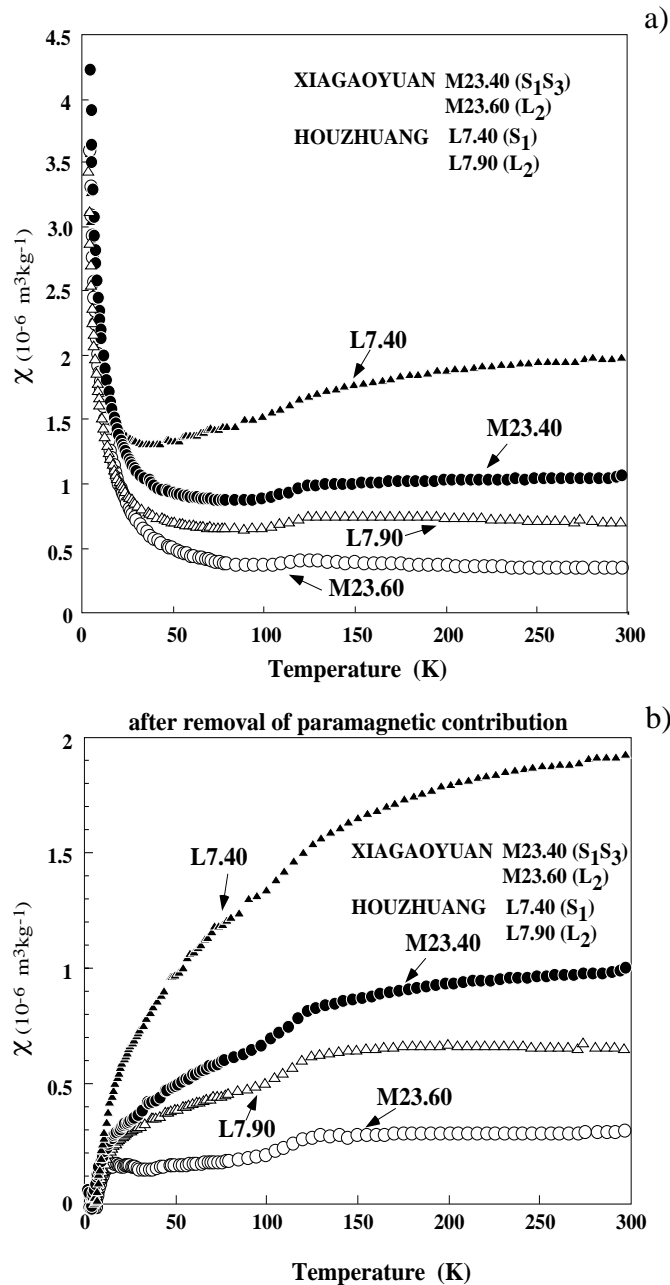


Figure 11: Zero Field Cooling (ZFC) in two loess and two paleosol samples from Xiagaoyuan and Houzhuang. The samples were cooled down to 2.5 K in zero field and heated up to room temperature in a 1 mT DC field (a). The paramagnetic contribution was subtracted assuming its predominance at temperatures below 20 K. The residual curves reflect the distribution of unblocking temperatures of SD grains (b). The paleosol samples L7.40 and M23.40 show the strongest increase in susceptibility up to room temperature, whereas in the loess samples L7.90 and M23.60 the susceptibility increases only slightly at lower temperatures and stays almost constant above 150 K. As in the TRM(T) curves, a kink occurs in all susceptibility curves between 100 K and 120 K giving evidence of the presence of magnetite.

At very low temperature (around 3 K), susceptibility values are rather consistent for samples L7.40, L7.90 and M23.60 (varying from 3.40 to $3.60 \times 10^{-6} \text{ m}^3\text{kg}^{-1}$) (Table 1). Slightly higher values are observed in paleosol M23.40 ($4.25 \times 10^{-6} \text{ m}^3\text{kg}^{-1}$). The signal similarity at this temperature results from the strong contribution of paramagnetic minerals. With increasing temperature a sharp drop in susceptibility is observed, which is attributed to the temperature dependence of paramagnetic susceptibility.

Therefore the linear segment of the $1/\chi$ susceptibility curve in the temperature range between 3.5 and 20 K was fitted with a linear function. The gradient of this line was taken as an estimate of the paramagnetic signal. Using this approach the paramagnetic contribution to the susceptibility at room temperature was calculated. For paleosol sample M23.40, χ_p is $8.03 \times 10^{-8} \text{ m}^3\text{kg}^{-1}$ (7.4% of the total susceptibility χ measured at room temperature: $1.09 \times 10^{-6} \text{ m}^3\text{kg}^{-1}$), for loess sample M23.60 χ_p is $6.14 \times 10^{-8} \text{ m}^3\text{kg}^{-1}$ (17.5% of the total χ measured at room temperature: $0.35 \times 10^{-6} \text{ m}^3\text{kg}^{-1}$). A similar result showing higher paramagnetic contribution in loess samples is observed at Houzhuang. In paleosol L7.40, 3.0% of total susceptibility ($\chi = 2.00 \times 10^{-6} \text{ m}^3\text{kg}^{-1}$) is paramagnetic ($\chi_p = 6.06 \times 10^{-8} \text{ m}^3\text{kg}^{-1}$), while in the loess L7.90 χ_p ($= 5.47 \times 10^{-8} \text{ m}^3\text{kg}^{-1}$) represents 7.8% of total susceptibility ($\chi = 0.70 \times 10^{-6} \text{ m}^3\text{kg}^{-1}$).

A comparison between the results obtained for Xiagaoyuan using the S-600 and the VSM has to be made with caution, because of the high sensitivity of the function used to fit the curve obtained by low-T measurements.

The residual susceptibilities at temperatures between 40 K and 80 K vary from 9% (for M23.60) to 36% (for L7.40) of the initial value. With rising temperature the remaining ferromagnetic signal shows a strong increase in the paleosol samples L7.40 and M23.40 (Fig. 11b) up to room temperature. In the loess samples L7.90 and M23.60, susceptibility increases strongly up to 150 K, and then stays rather constant up to room temperature.

Small kinks at ~ 120 K are clearly present in the susceptibility curve of samples M23.40, M23.60 and M7.90, while this effect is hardly recognizable in the strongly magnetic paleosol sample L7.40. The kinks are again thought to be caused by the Verwey transition of magnetite (see also Fig. 10a and b), but are partially obscured by the strongly enhanced susceptibility in sample L7.40 due to the high concentration of SP

magnetic minerals, which display the kink behaviour only very faintly. They may be subdued to magnetic shape anisotropy or oxidized to maghemite. The first argument is rather unlikely since growth of elongated tiny magnetite crystals has never been observed in nature or laboratory experiments (Taylor and Maher, 1988). Therefore oxidized magnetite is preferred in our interpretation as the mineral source of the superparamagnetic material. The predominant role on the shape of the measured ZFC is played by the SP grains. At very low temperatures (a few Kelvin) all monodomain grains have a stable magnetization (even the finest grains). At this low thermal energy state the anisotropy energy barriers to rotate the magnetization are very high. An assembly of randomly oriented magnetic moments may be assumed. When the temperature rises, thermal energy increases and a statistical alignment along the applied field of the magnetic moments causes a strong increase of the magnetization and thus of susceptibility. For a particle with a given volume, the temperature at which this occurs is the unblocking temperature (Bean and Livingston, 1959). With further increasing temperature the thermal energy becomes larger than the anisotropy energy, so that thermal equilibrium is reached, accompanied by a drop in magnetization and susceptibility. The susceptibility increase observed in the ZFC experiment can thus be attributed to an additive contribution of larger and larger magnetic grains that unblock with rising temperature. The susceptibility peak is reached when these contributions are compensated by the superparamagnetic reduction (loss of magnetization) of the already unblocked grains (Sappey et al., 1997). In the paleosol sample the susceptibility peak is much higher than in the loess samples, indicating a higher concentration of SP grains over the temperature spectrum from 10 to 300 K.

3.4 Discussion

3.4.1 Chronology

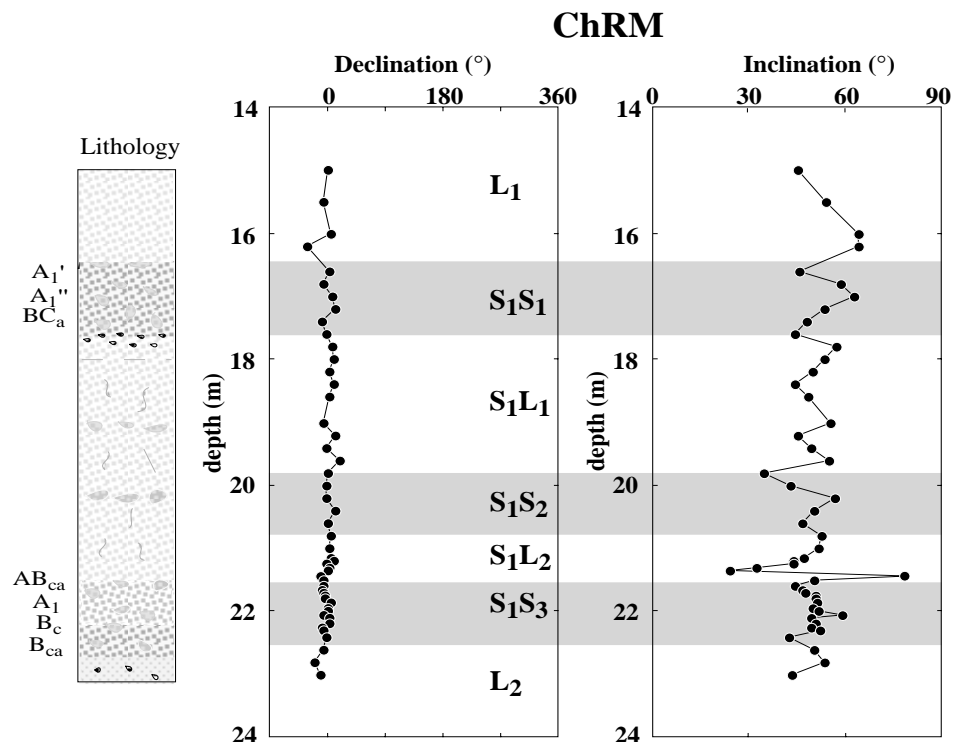


Figure 12: Declination, inclination and lithology at Xiagaoyuan (western Chinese loess plateau), at depths where the Blake geomagnetic polarity event is expected to occur. At Jiuzhoutai and Xining, reversed polarity zones have been reported in paleosol S₁S₃ and loess S₁L₂, respectively (Zhu et al., 1994; Fang et al., 1997).

The magnetic properties of Chinese loess are used in this study to obtain qualitative information on the climate evolution, in particular during the last glacial-interglacial cycle. For this purpose a well defined chronology is necessary. The studied sequences formed during the youngest part of the Brunhes epoch, and the only polarity feature in this epoch that has received any observational support in loess sediments is the Blake event (Smith and Foster, 1969), although the evidence is still controversial. Fang et al. (1997) report a detailed profile obtained from a well at Jiuzhoutai (Lanzhou city, Gansu province). They find a polarity signature consisting of two reversed intervals separated by a short normal polarity interval, the whole pattern spanning 42 cm and representing the time interval 120-115 ka BP. The entire feature falls within paleosol S₁S₃. Zhu et al.

(1994) reported an even more complex pattern from a loess sequence at Xining, ~150 km northwest of Lanzhou: spanning 55 cm (117-112 ka BP), it consists of three reversed polarity intervals separated by two normal polarity zones, and the entire pattern falls in a loess unit, not a paleosol as at Lanzhou. Zhu et al. (1998), in an attempt to identify the Blake event in the central loess plateau, related its preservation to the sedimentary environment. High and continuous sedimentation as well as minor pedogenesis are the ideal conditions for recording such a short polarity episode.

In this work an attempt was made to identify the Blake event at Xiagaoyuan, where the sedimentary environment is similar to that at Jiuzhoutai and Xining. A.F. demagnetization was applied to 56 samples from 15 m to 23 m depth (every 20 cm from 15 m to 21 m depth, and every 5 cm from 21 m to 23 m depth), including the lower (younger) part of layer L₁, layers S₁S₁, S₁L₁, S₁S₂, S₁L₂, S₁S₃ and the upper ~20cm of L₂. The main susceptibility features observed at Jiuzhoutai and Xining are present at Xiagaoyuan (Fig. 3), but no indication of a reversal is found (Fig. 12). This counterindication may be due to complexity in the remanence acquisition process and/or to sedimentological phenomena (such as undetected stratigraphic breaks and/or slumping).

An indirect method used for dating the sequence is to compare the magnetic variations with the oxygen isotope curves ($\delta^{18}\text{O}$) obtained from marine sediments (Heller and Liu, 1986; Kukla et al., 1990). In Fig. 13, the astronomically tuned oxygen isotope record at ODP site 677 for the last ~250 ka and the loess susceptibility variations are correlated to construct a timescale for the sequences at Xiagaoyuan and Houzhuang. The main $\delta^{18}\text{O}$ stages correlate well with the susceptibility variations, with warm isotope periods corresponding always to high susceptibility values (caused by soil forming processes).

In both sequences, the Holocene soil S₀ corresponds to $\delta^{18}\text{O}$ stage 1 (Holocene) that started around 11.5 ka BP (before present) (Johnsen et al., 1992). The lower limit of S₀ is correlated to a major susceptibility drop observed between 1.40 - 1.50 m depth at Xiagaoyuan, and with a susceptibility minimum between 2.60 - 2.70 m depth at Houzhuang.

The $\delta^{18}\text{O}$ variations of stage 5 and the susceptibility variations measured from 15.50 m to 23 m depth at Xiagaoyuan are similar, and the substages 5a, b, c, d, e can be correlated with the layers S₁S₁, S₁L₁, S₁S₂, S₁L₂, S₁S₃, respectively. At Houzhuang such a pat

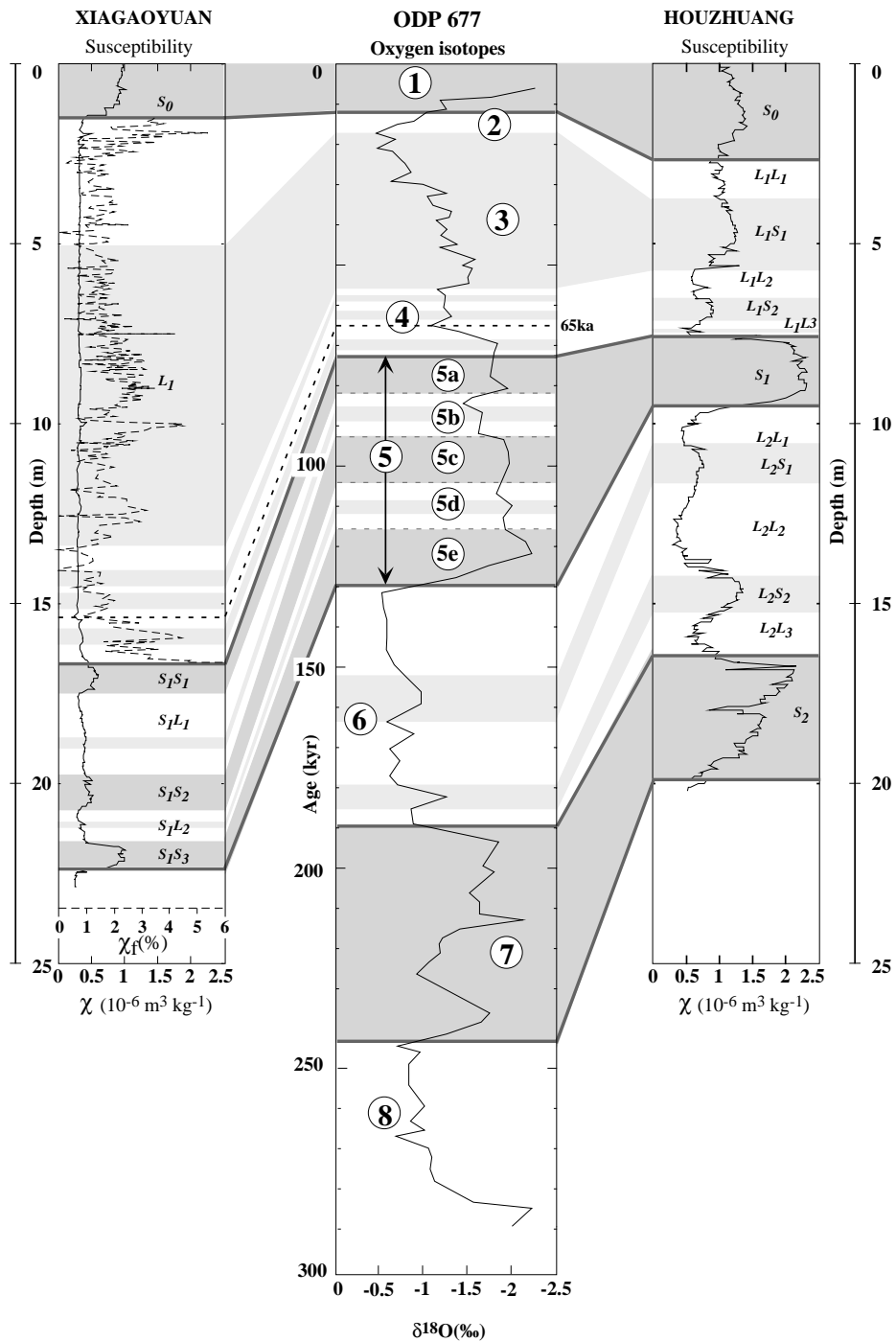


Figure 13: Oxygen isotope record from Ocean Drilling Program (ODP) site 677 (1°12'N, 83°44'W) from Shackleton and Hall (1989) and Shackleton et al. (1990) tuned to an absolute timescale using the insolation curve of Berger (1978) compared with the loess susceptibility profiles at Xiagaoyuan and at Houzhuang. The numbers in the circles represent the oxygen isotope stages. From the correlation between susceptibility and oxygen isotopes (the shading refers to the oxygen isotope stages and substages) a high sedimentation rate for the sequence at Xiagaoyuan is derived (25 cm/ka for the last glacial, which corresponds to the stages 2, 3 and 4, and 6.3 cm/ka for the last interglacial, which corresponds to stage 5), while at Houzhuang the sedimentation rate is lower (7.4 cm/ka for the last glacial and 3.7 cm/ka for the last interglacial).

tern is not observed: the features observed at Xiagaoyuan are here welded in the pedocomplex S_1 .

Pedocomplex S_1 at Houzhuang formed in the same time period as the subdivided layer S_1 at Xiagaoyuan, but under much warmer and wetter conditions. It is not possible to recognize the subunits S_1S_1 , S_1L_1 , S_1S_2 , S_1L_2 and S_1S_3 observed at Xiagaoyuan, which indicate distinct climate changes occurring in this period on the western loess plateau. A major susceptibility drop characterizes the lower limit of pedocomplex S_1 in both sections, as given at the S_1S_3 - L_2 and S_1 - L_2 boundary in Xiagaoyuan and Houzhuang, respectively. At Houzhuang, $\delta^{18}\text{O}$ stage 7 correlates with the susceptibility enhancement measured from 16.40 to 19.60 m depth. An increase of $\delta^{18}\text{O}$ is observed between 220-230 ka B.P. which corresponds to a distinct decrease of susceptibility in the paleosol S_2 . This cooling event has also been observed in other loess/paleosol sequences on the central loess plateau and often results in a clear subdivision of paleosols (An et al., 1990; Heller et al., 1991).

3.4.2 Magnetic profiles

- **Loess/paleosol sequences at Xiagaoyuan and Houzhuang**

The susceptibility variations with depth in the Chinese loess plateau and the good correlation with the oxygen isotope curve indicate that the paleoclimatic and paleoenvironmental changes during the last 130'000 years at Xiagaoyuan and during the last 250'000 years at Houzhuang can be monitored using rock magnetic parameters.

Besides low field susceptibility χ , hysteresis-derived properties, such as saturation magnetization M_s , coercive force $(B_o)_c$, coercivity $(B_o)_{cr}$ and some ratios derived from these parameters such as χ/M_s , χ_{ARM}/χ and $\chi/SIRM$ have been plotted together with the lithology as a function of profile depth in figs. 14 and 15. These figures summarize the information about neoformation of magnetic minerals and their grain size in relation to changes of paleoclimate and environment for the geological time covered by the two sections.

High M_s values characterize the paleosols of both sections: up to $3.6 \times 10^{-2} \text{ Am}^2\text{kg}^{-1}$ for paleosol S_0 and S_1S_3 in Xiagaoyuan and up to $7 \times 10^{-2} \text{ Am}^2\text{kg}^{-1}$ for paleosol S_1 in

XIAGAORYUAN

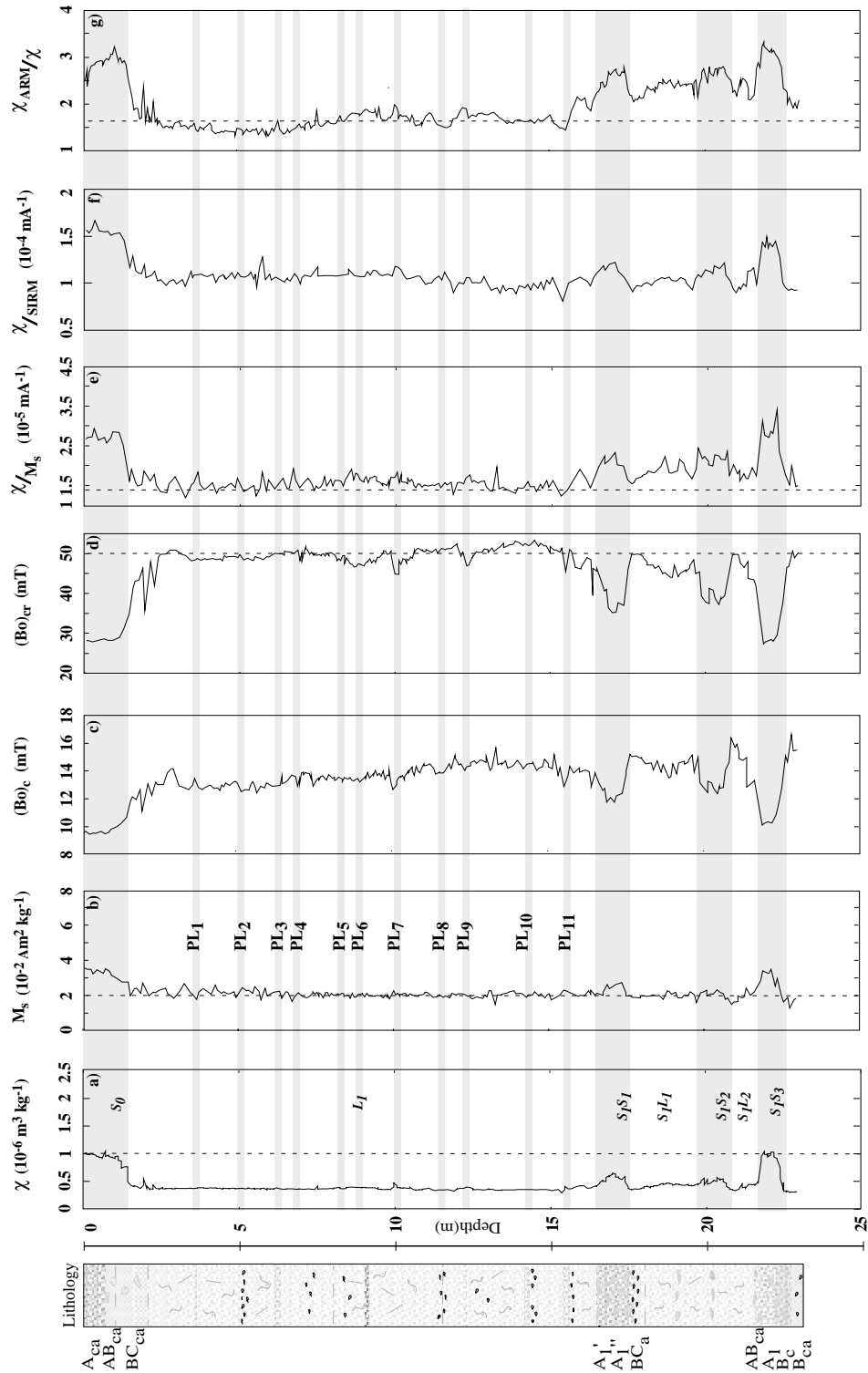


Figure 14: Susceptibility χ (a) saturation magnetization M_s (b), coercive force $(B_0)_c$ (c), coercivity $(B_0)_{cr}$ (d), χ/M_s (e), $\chi/SIRM$ (f) and χ_{ARM}/χ (g) plotted as a function of depth at Xiagaoyuan. Pedogenic layers observed in loess layer L_1 are indicated by PL (Fig. 3) (see text for details).

HOUZHUANG

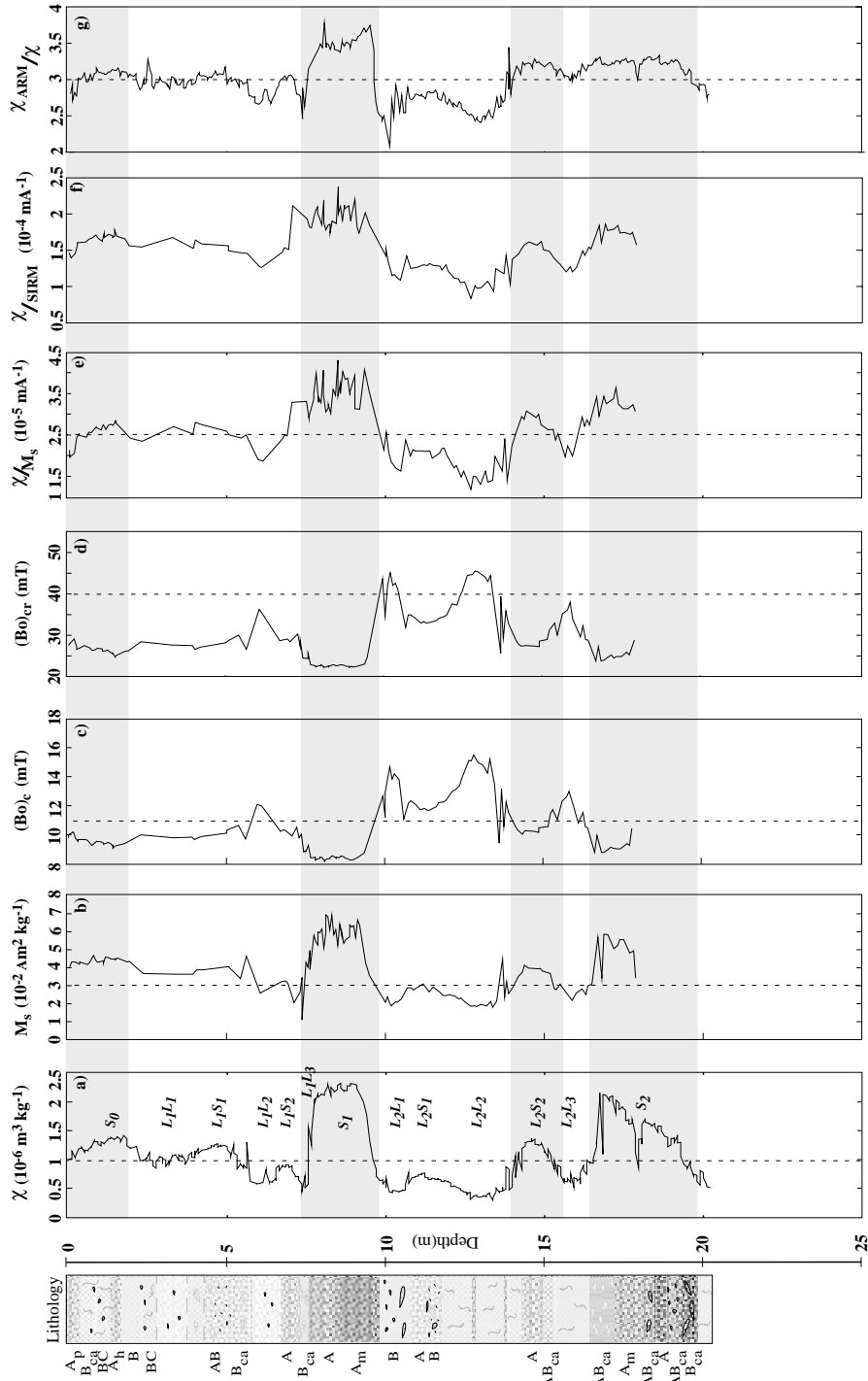


Figure 15: Susceptibility χ (a) saturation magnetization M_s (b), coercive force $(B_0)_c$ (c), coercivity $(B_0)_{cr}$ (d), χ/M_s (e), $\chi/SIRM$ (f) and χ_{ARM}/χ (g) plotted as a function of depth at Houzhuang.

Houzhuang, about twice the maxima at Xiagaoyuan. The higher paleosol M_s results from higher ferromagnetic mineral concentrations as is also suggested by the χ data which, however, are influenced by additional grain size effects.

M_s in paleosols S_2 and S_1 at Houzhuang is much higher than that of the Holocene S_0 whereas similar but much smaller absolute intensities are observed at Xiagaoyuan in S_0 and in S_1S_3 (the highest in this profile). S_1S_3 is the equivalent of the Eemian interglacial substage (oxygen isotope stage 5e).

At Xiagaoyuan, M_s remains low and almost constant around $2 \times 10^{-2} \text{ Am}^2\text{kg}^{-1}$ in the loess L_1 and in the cold periods S_1L_1 and S_1L_2 of the last interglacial indicating a rather constant ferromagnetic mineral influx. The slight absolute M_s increase and apparent higher amplitude noise within the uppermost 7 m is probably caused by recent surface weathering since this part of the section was not dug as deeply as the rest of the profile. At Houzhuang, low ferromagnetic mineral concentrations are seen only in two very short segments of loess L_2 whereas L_1 maintains higher values between 3 and $4 \times 10^{-2} \text{ Am}^2\text{kg}^{-1}$ which are hardly attained at Xiagaoyuan, even by the paleosols.

The ratio χ/M_s offers information about the presence of SP grains because all SP grains contribute to the ratio in contrast to χ_f where the ultrafine grains at the SP/SSD boundary are in control. Again, equally high χ/M_s ratios are observed in the paleosols S_0 and S_1S_3 at Xiagaoyuan as for M_s , and S_1S_2 is now clearly recognized.

Similar wetter and warmer climate seems to have prevailed in the western loess plateau during oxygen isotope stage 5e and the Holocene in some contrast to the SPECMAP isotope data (Imbrie et al., 1984). Lowest ratio values around 1.5 persist in L_1 whereas a small increase is noticed for S_1L_1 and S_1L_2 indicating slightly stronger weathering in these cold intervals. In L_1 , similar small-scale fluctuations are recorded as for χ_f (pedogenic layers in Fig. 4) which support the evidence of short-lived climate warming events during the last glacial. A clear correlation with the pedological and χ_f evidence, however, is not always observed. L_1 seems to be divisible into three subhorizons because a tiny increase of χ/M_s can be recognized from about 7 m to 13 m which may reflect oxygen isotope stage 3. The cold isotope stages 2 and 4 would therefore - and also from the χ_{ARM}/χ evidence (see below) - be represented from 2 m to 7 m, and from 13 m to 16 m, respectively. At Houzhuang, high SP production generally causes high ratios in loess and

extremely strong χ/M_s in the paleosol layers. This behaviour is expected for the generally much more humid and warmer climate of the central loess plateau. In fact, S_1 contains three χ/M_s maxima and appears to be subdivided into subunits which may correspond to the oxygen isotope stages 5a-e.

χ_{ARM}/χ is taken as a measure of SD contribution in ferrimagnetic assemblages (Thompson and Oldfield, 1986) because SD particles readily acquire ARM. Low values of this parameter between 1.4 to 1.7 characterize again the L_1 loess at Xiagaoyuan. They clearly increase in the upper part of S_1 (in both soils and loess layers) and are doubled in paleosols S_0 and S_1S_3 . χ_{ARM}/χ expresses most clearly that alteration and iron mobilization have taken place in Xiagaoyuan also in both cold stages of S_1 . Thus it becomes clear that not only SP but also SD ferrimagnetic material forms during pedogenesis. This is also documented in Houzhuang where χ_{ARM}/χ falls below 2.5 only in the decalcified B horizon of S_1 (at 10 m depth), but is usually around 3 or higher throughout the whole profile. Stronger alteration during pedogenesis seems to favor increased growth of SD material either biotically or abiotically in addition to the formation of SP-sized ferromagnetic particles.

Coercive force $(B_o)_c$ and coercivity $(B_o)_{cr}$ are always low in the pedogenically altered horizons in both profiles. In Xiagaoyuan minimal $(B_o)_c$ of about 10 mT is observed in S_0 and S_1S_3 whereas these minima in Houzhuang are even smaller with about 8 mT in S_1 and S_2 . Likewise the coercivity $(B_o)_{cr}$ has minima of about 27 mT in S_0 and S_1S_3 at Xiagaoyuan and goes down to 22 to 25 mT in S_1 and S_2 at Houzhuang. The frequent layers of low-grade pedogenic activity PL_1 to PL_{11} in L_1 at Xiagaoyuan are sometimes identified by slightly reduced coercive force and coercivity. In general, the low $(B_o)_{cr}$ connected with high χ and χ_{ARM}/χ and only faint indication of the Verwey transition during low temperature experiments (Fig. 10) indicate the predominant role of pedogenically formed oxidized SD magnetite for the remanent magnetization as derived at Roxolany by du Pasquier (1999). This maghemitization may be skin-deep as suggested by van Velzen (1999) or may penetrate the SD grains more thoroughly. The always higher $(B_o)_c$ and $(B_o)_{cr}$ values in the loess at Xiagaoyuan as compared to Houzhuang are taken as further evidence for the mild loess alteration in the more arid climate of the western loess plateau. Constantly high $(B_o)_{cr}$ around 50 mT in the Xia-

gaoyuan loess is consistent with the presence of oxidized detrital magnetite.

- **Last glacial period at Xiagaoyuan**

Median grain size, low field susceptibility and its frequency dependence of all samples collected at Xiagaoyuan were measured, and have been plotted in Fig. 16 on an oxygen isotope matched timescale obtained from the astronomically tuned ODP 677 core (Shackleton et al., 1990). As observed in the oxygen isotope variations from the GRIP Summit ice core (Dansgaard et al., 1993), the late glacial period (Late Weichselian) was characterized by a series of abrupt climate shifts. These variations (Dansgaard-Oeschger cycles = D-O cycles) show a cyclicity characterized by a progressive cooling followed by the launch of the ice armada in the Atlantic during its colder phase (Heinrich events). Such events were followed by a prominent rewarming, thus starting another series of D-O cycles. The series of warming and cooling cycles forms the so-called Bond cycles (Bond et al., 1993) (Fig. 16a).

A detailed correlation between grain size and oxygen isotope variations is not straightforward on the millennial scale (recording of the D-O cycles). A similar trend is observed in both records, with coarser grain sizes corresponding to the upper and lower boundary of the glacial period. The grain size fining the central part of loess layer L₁ (Fig. 16b) corresponds to increased amplitudes of the D-O cycles (between interstadials 17 and 18, Fig. 16a), indicating a general warming. In the lower part of paleosol S₀, a decrease of susceptibility and of its frequency dependence is preceded by a major peak at ~14 ka. These variations are interpreted as evidence of the Younger Dryas (low susceptibility and coarser grain size) preceded by the Bølling interstadial.

A detailed inspection of susceptibility and χ_f shows the presence of two more peaks between 14 and ~15 ka. A correlation of the substages of interstadial 1 (1a, b, c, d, e) with χ_f highs and lows seems to be possible, but while susceptibility amplitude increases with time between ~15 and ~12 ka, oxygen isotope peaks are decreasing in the same time interval (Johnsen et al., 1992).

Interstadial 1 is preceded by an abrupt cooling, the so-called Heinrich event 1 (H1, Fig. 16). Further back in time the correlation between interstadials observed in the GRIP core, χ_f variations and pedogenic layers is not clear, mainly because of the small changes of the two latter parameters. In the GRIP core, between interstadial 2 and 1, a minor oxy-

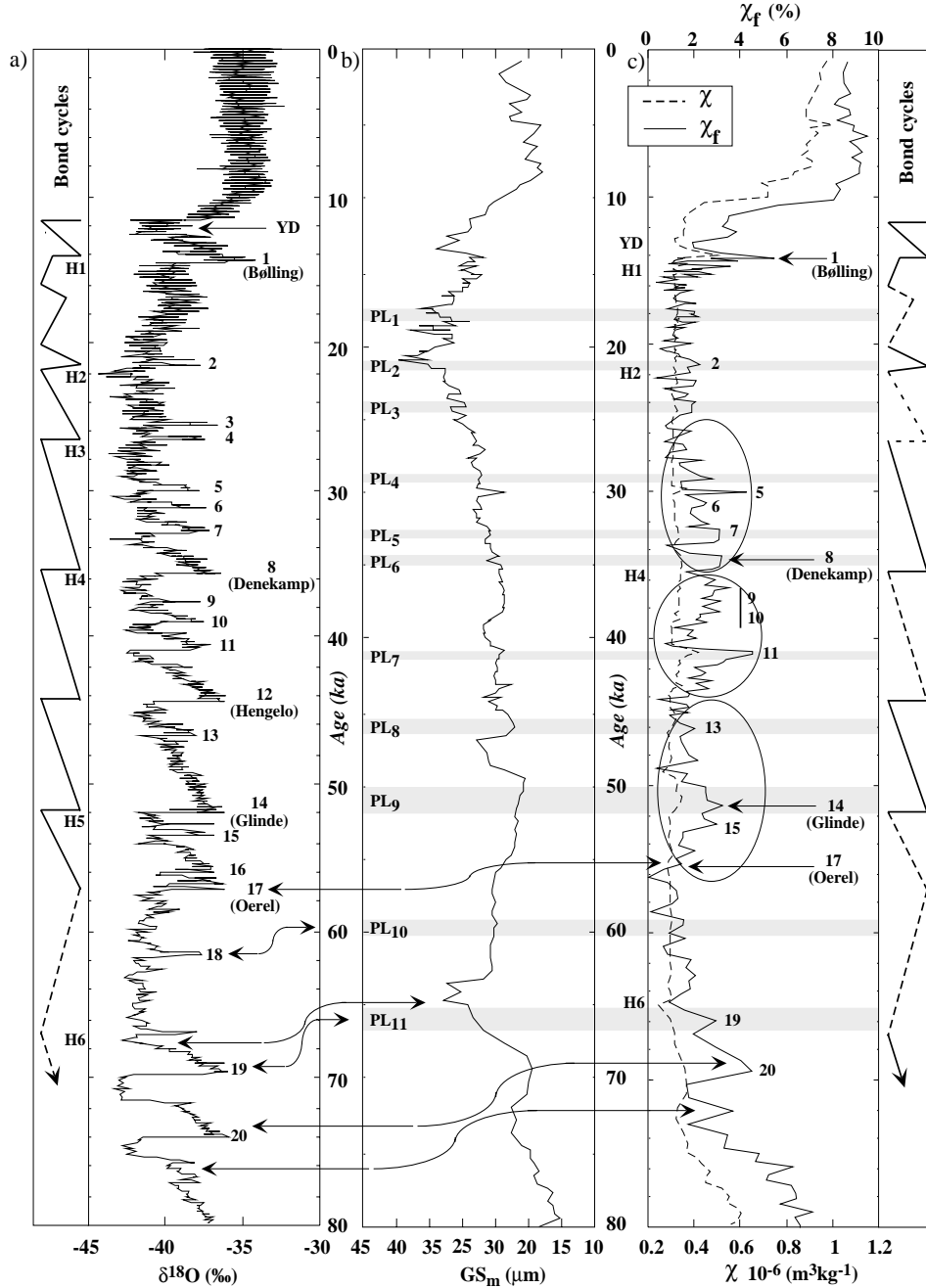


Figure 16: Correlation between median grain size GS_m (b), frequency dependence of susceptibility χ_f (%) and susceptibility χ (c) and oxygen isotope variations $\delta^{18}O$ (‰) (a) as a function of time for the last 80 ka at Xiagaoyuan. The grain size and susceptibility timescale were obtained using the astronomically tuned oxygen isotope curve from ODP 677 (Shackleton et al., 1990). A comparison is made using the oxygen isotope variations measured in the GRIP summit ice core (Daansgard et al., 1993). In Fig. 16a the Heinrich events (H1-H6) and the Bond cycles are presented (Bond et al., 1993). 20 interstadials were identified in the GRIP core (numbers in Fig. 16a; YD: Younger Dryas). Fig. 16c indicates that susceptibility and its frequency variation partly reflect climatic changes in correspondance to the Bond cycle, although they do not always reflect the amplitude of the interstadials. Grain size variations in figure 16b also reflects climate changes, with coarser median grain sizes characteristic for cold periods (such as oxygen isotope stage 2 and 4) and finer for warmer periods (oxygen isotope stage 3, see also Fig. 13).

gen isotope increase is observed, which may have produced pedogenic layer PL₁. Interstadial 2 is correlated with PL₂, where a distinct χ_f oscillation is observed. PL₃ does not match with interstadials 3 or 4 observed in the GRIP core, which are a few millennia older. This discrepancy could be explained by a lack of precision of the orbitally tuned susceptibility and grain size timescale.

The central part of the last glacial, between ~58 and ~30 ka (from interstadials 17 to 5) is characterized by well-expressed D-O cycles. Rather than correlating the individual interstadials with χ_f peaks and pedogenic layers (Fig. 16c), it is more appropriate to refer to the Bond cycles delimited by Heinrich events 3, 4 and 5. The correlation of H5 with grain size, susceptibility and/or carbonate content in the loess deposits results in an age of ~52 ka according to Chen et al. (1997), ~43 according Fang et al. (1999) and of ~50 ka following Porter and An (1995). In fact at ~43 ka a cooling period is observed (just before interstadial 11) which has correlated with H5 (Fang et al., 1999; Thouveny et al., 1994: observed in lake sediments from Europe). We prefer an age for H5 of ~52 ka (Bond et al., 1992, a detailed work on the Dansgaard-Oeschger cycles in sea sediments is provided by Völker, 1999), an age characterized by a strong increase of foraminifer size > 150 μm (not observed at ~43 ka). The χ_f increase in the central part of the last interglacial can be correlated with the Bond cycles (see ellipses in Fig. 16c), although climatic changes on the millennial scale are difficult to recognize in the Xiagaoyuan loess because of the relatively widely spaced sampling and low sedimentation rate, but also because of the observed pedogenic activity.

The lower part of loess layer L₁ is characterized by two pedogenic layers (PL₁₀ and PL₁₁). PL₁₀ appears to be ~2 ka younger than interstadial 18, a difference that may again be attributed to discrepancies of the GRIP and ODP timescale. Similar discrepancies are observed for the interstadial 19 (=PL₁₁), the interstadial 20, and for H6, with apparent ages between 2 and 4 ka older in the GRIP core.

Grain size variations in Xiagaoyuan correlate well with the oxygen isotope variations: coarser grain sizes were deposited during the cold oxygen isotope stages 2 (highest values around 20 ka, the Last Glacial Maximum) and 4 (around 60 ka). In the middle part of the studied section, a grain size decrease is observed, but the signal is not as sensitive as the frequency dependent susceptibility variations. Grain size can be used to confirm the climatic changes that occurred during the last glacial, in terms of changes in the wind

regime, but is not sensitive enough to clearly identify the interstadials observed in the GRIP summit ice core.

3.5 Conclusions

The studied sections could not be subdivided chronostratigraphically by means of polarity features. The Blake event could not be recognized, probably because of a not high enough sedimentation rate or disturbances due to weathering processes. Therefore the chronostratigraphic subdivision of the sequences was constructed by matching the magnetic susceptibility curves with the oxygen isotope record at ODP site 677 (Shackleton and Hall, 1989; Shackleton et al., 1990)(Fig. 13). Our subdivision assigns the surface soil S_0 of both sequences to oxygen isotope stage 1 (Holocene). Stages 2, 3 and 4, corresponding to the last glacial period, correlate well with loess layer L_1 at Xiagaoyuan and with the layers L_1L_1 to L_1L_3 at Houzhuang. Several features, such as the slight re-warming observed during stage 3 with respect to stages 2 and 4, is observed at Xiagaoyuan (pedogenic layers, increased frequency dependence of susceptibility) and more prominently at Houzhuang (paleosol L_1S_1 with clearly enhanced susceptibility and less distinct change in frequency-dependent susceptibility (Fig. 3). Stage 5 corresponds to the pedocomplex S_1 in both sections. At Xiagaoyuan, the susceptibility variations from S_1S_1 to S_1S_3 could be correlated with the substages 5a to 5e, indicating that the major climatic changes occurring during the last interglacial had a global impact on the terrestrial surface. Stage 6 was correlated at Houzhuang with the horizons L_2L_1 to L_2L_3 , and stage 7 with pedocomplex S_2 (Fig. 13).

The loess sequences at Xiagaoyuan and Houzhuang reflect the different climate evolution in the western and in the central Chinese loess plateau, respectively during the last ~130 ka. At Xiagaoyuan the sedimentation rate (~18 cm/ka) is by a factor ~2.4 higher on average than that in Houzhuang (~7.5 cm/ka), indicating that during the last climate cycle strong westerly winds were blowing across the western Chinese loess plateau, transporting huge amounts of dust through the Hexi corridor (Fig. 1). The lower accumulation observed in the central loess plateau is due to the longer distance from the dust source area (Houzhuang is situated about 350 km southwest from Xiagaoyuan) and the presence of the Liupan mountains that act as a barrier for the winds blowing from the northwest.

The Liupan mountains also mark the boundary of regions with different soil forming processes in the studied loess sequences. The section at Xiagaoyuan is formed mainly by unaltered loess. Only three distinct paleosol horizons have been identified macroscopically (S_0 , S_1S_1 and S_1S_3). At Houzhuang strong weathering processes affected the entire section, resulting in several pedocomplexes. The horizons classified as loesses are weathered and not “pristine” as are the loess layers in Xiagaoyuan. The different weathering history is clearly reflected by the susceptibility variations (Fig. 3). Although a similar pattern is observed in both sections with high susceptibility values in the paleosols and lower values in the loesses, the susceptibility values for the loesses at Houzhuang are often similar to those of the paleosols at Xiagaoyuan.

Grain size fractionation is a powerful tool for determining the magnetic grain size responsible of the magnetic enhancement measured in the paleosols. Low field susceptibility has a distinct grain size dependence. In pristine loess the susceptibility contribution follows closely the mass distribution, i.e. all grain size fractions have nearly identical susceptibilities. The bulk magnitude is mainly controlled by magnetic minerals occurring in grain sizes $> 2.2 \mu\text{m}$ (corresponding to the predominance of the silt-sized grain fractions). With increasing pedogenesis the contribution of the finest ferromagnetic minerals increases, reaching $\sim 60\%$ of the total susceptibility for grain sizes $< 2.2 \mu\text{m}$, which is extremely high considering the small mass of these grain size fractions ($\sim 25\%$ of total mass). This observation and the susceptibility increase between 10 K and 300 K observed during ZFC experiments (Fig. 11) support the idea of an *in situ* formation of fine grained ferromagnetic minerals responsible for the susceptibility enhancement observed in the paleosols (Zhou et al., 1990). The model of variable influx and dilution of magnetic material as proposed by Kukla et al. (1988) to explain the strong susceptibility variations between loess and paleosol can now be discounted.

Hysteresis measurements performed at room temperature, as well as temperature-dependent magnetic measurements, prove that the magnetic mineralogy in Xiagaoyuan resembles that in Houzhuang, with nearly identical background susceptibility in both sections ($2.61 \times 10^{-7} \text{ m}^3\text{kg}^{-1}$ at Xiagaoyuan and $2.30 \times 10^{-7} \text{ m}^3\text{kg}^{-1}$ at Houzhuang), and similar relationships between susceptibility and hysteresis parameters. A significant anomaly on the TRM(T) curve around $\sim 100 \text{ K}$ (Fig. 10) results from the presence of pure magnetite, confirmed by the hysteresis measurements performed at temperatures from

25°C to 700°C (with predominant diamagnetism at temperatures above 600°C). The magnetite is partly detrital, but may also be related to the destruction of iron-bearing paramagnetic minerals during pedogenesis. Maghemitization affecting SP-SSD magnetite grains, results in the appearance of a “smeared” Verwey transition during ZFC, although this can not be demonstrated by measurements on the grain size fractions (see also Chapter 1, Part II).

Magnetic properties measured throughout the profiles reflect climate variations. High concentrations of ferromagnetic minerals characterize paleosols, the concentrations in the paleosol S_1 at Houzhuang being almost double that of paleosol S_1S_3 at Xiagaoyuan. The magnetic grain sizes responsible for this enhancement are mainly those in the SP-SSD grain size range. Coarser magnetic grains characterize loesses, especially loess layers L_1L_1 , L_1L_2 and L_2 at Xiagaoyuan ($(B_0)_{cr}$ constantly around 50 mT), in correspondence to the B and BC horizons of the overlying paleosols. The coercivity distribution in L_1 reflects climatic changes indicated by the oxygen isotope curve: The minima are related to the presence of SSD magnetic minerals rather than coarser MD magnetic grains, and were identified between pedogenic layer PL_1 and the Holocene soil, and between pedogenic layer PL_9 and PL_{11} (Fig. 13), in correspondence with oxygen isotope stages 2 and 4, respectively.

The correlation between the frequency dependence of susceptibility and the oxygen isotope curve from the GRIP core underscores that the monsoon regime is controlled by global climate changes occurring during the last interglacial-glacial cycle. The millennial climatic fluctuations recorded in the GRIP ice core are reflected by the susceptibility variations (Fig. 16) during the last glacial period in the western loess plateau. Despite this observation, the presence of pedogenic layers may smooth out the original climate signal seen as abrupt changes from cold to warm in the Greenland ice core data.

Chapter 4

***CLIMATE CHANGES DURING THE LAST GLACIAL/
INTERGLACIAL CYCLE: LINK BETWEEN
SUSCEPTIBILITY, GRAIN SIZE AND ¹⁰BE IN THE
WESTERN (XIAGAOYUAN, GANSU PROVINCE) AND
THE CENTRAL (HOZHUANG, SHAANXI PROV-
INCE) CHINESE LOESS PLATEAU***

4.1 Introduction

The relationship between the Chinese monsoon system and the climate changes in the high latitude northern hemisphere has been highlighted by the strong correlation between susceptibility in Chinese loess and oxygen isotope variations in deep-sea cores (Heller and Liu, 1986; Kukla and An, 1989). The strong link between the oxygen isotope stages and the susceptibility peaks persists during the whole Quaternary. Ding et al. (1992) identify the uplift of the Tibetan plateau as a forcing factor maintaining the Siberian-Mongolian high pressure and Aleutian low pressure system in their present positions, a system responsible for the dust deposition on the Chinese loess plateau.

Three separate paleosols (each associated with a susceptibility increase) with intervening loess layers (each associated with low susceptibility) can be identified, although paleosol S_1S_2 is not visible in the field. These horizons (S_1S_1 , S_1L_1 , S_1S_2 , S_1L_2 and S_1S_3) can be correlated with the oxygen isotope stages 5a, b, c, d and e, respectively (as observed at Xiagaoyuan, chapter 3, Fig. 1).

In the western Chinese loess plateau the Siberian-Mongolian winds blowing during the winter season cause high sedimentation rates which are at least twice those in the central loess plateau. The climate changes for the last ~130 ka can be identified with high resolution. In the central Chinese loess plateau, for example, the climate changes are strongly controlled by the humid summer monsoon, rather than by the cold and dry winter winds. This results in lower sedimentation rates (less than 5 cm/ka for the last interglacial paleosol S_1 , corresponding to oxygen isotope stage 5, and ~13 cm/ka for the glacial loess layer L_1 , corresponding to stages 2, 3 and 4 at Luochuan, Heller and Evans, 1995) and a high pedogenic activity during interglacial but also, on minor extend, during glacial periods.

A few attempts have been made to determine paleoprecipitation quantitatively during the last glacial/interglacial in the Chinese loess plateau using susceptibility alone or combined with ^{10}Be . Heller et al. (1993) used ^{10}Be to discriminate the detrital and the pedogenic component of the susceptibility for the loess/paleosol sequence of Luochuan. The pedogenic component of susceptibility was then used to reconstruct the rainfall, using Holocene precipitation values for calibration. Maher et al. (1994) obtained rainfall values by calculating the difference between the susceptibility in paleosols and the susceptibility value of loess layer L_9 , the least altered and silty loess bed. A logarithmic cli-

mofunction obtained from susceptibility and precipitation measured on 9 modern soils across the Chinese loess plateau was used for calibration. Discrepancies in the results obtained from these two approaches are related to the different model assumptions. Heller et al. (1993) assumed simply that the ^{10}Be atmospheric dust flux F_A is constant and that the detritic ^{10}Be -flux is linearly related to the susceptibility dust flux. The grain size dependence of the ^{10}Be concentration also plays a role. If it is not considered the detrital ^{10}Be -flux during glacials is probably overestimated. In order to shed light on the relationship between susceptibility and ^{10}Be , both parameters and the grain size distribution with their median grain size values (50% percentile) were measured for the beds corresponding to the last interglacial at Xiagaoyuan and Houzhuang.

4.2 Results

4.2.1 ^{10}Be , susceptibility and median grain size variation during the last interglacial cycle

At Houzhuang a total of 24 samples from the paleosol layer S_1 was studied for ^{10}Be concentration, susceptibility and median grain size (Fig. 1). The samples were taken every 10 cm over a distance of 2.5 m resulting in a mean time resolution of $\sim 3'500$ years per sample for paleosol S_1 . The absolute ^{10}Be concentration in the paleosol layer S_1 shows a maximum value of 4.76×10^8 atoms/g (Fig. 1), which is almost identical with the maximum value measured at Luochuan for the same paleosol layer ($\sim 4.7 \times 10^8$ atoms/g, Shen et al., 1992), while Gu et al. (1996) measured a maximum value of $\sim 6.0 \times 10^8$ atoms/g for the paleosol layer S_1 at Weinan. The ^{10}Be concentration in S_1 differs between Weinan, Luochuan (maximum value measured in the lower part of S_1 , and a subsequent decrease upward) and Houzhuang (rather constant values in the central portion of S_1). In Weinan the highest ^{10}Be concentrations are found in a clay rich B horizon of S_1 , decreasing in the overlying A and AC horizon (values between 4 and 5×10^8 atoms/g). At Houzhuang lithologic observation identified the paleosol S_1 as a pedocomplex formed mostly by an A and an A_m horizon, which show a rather constant median

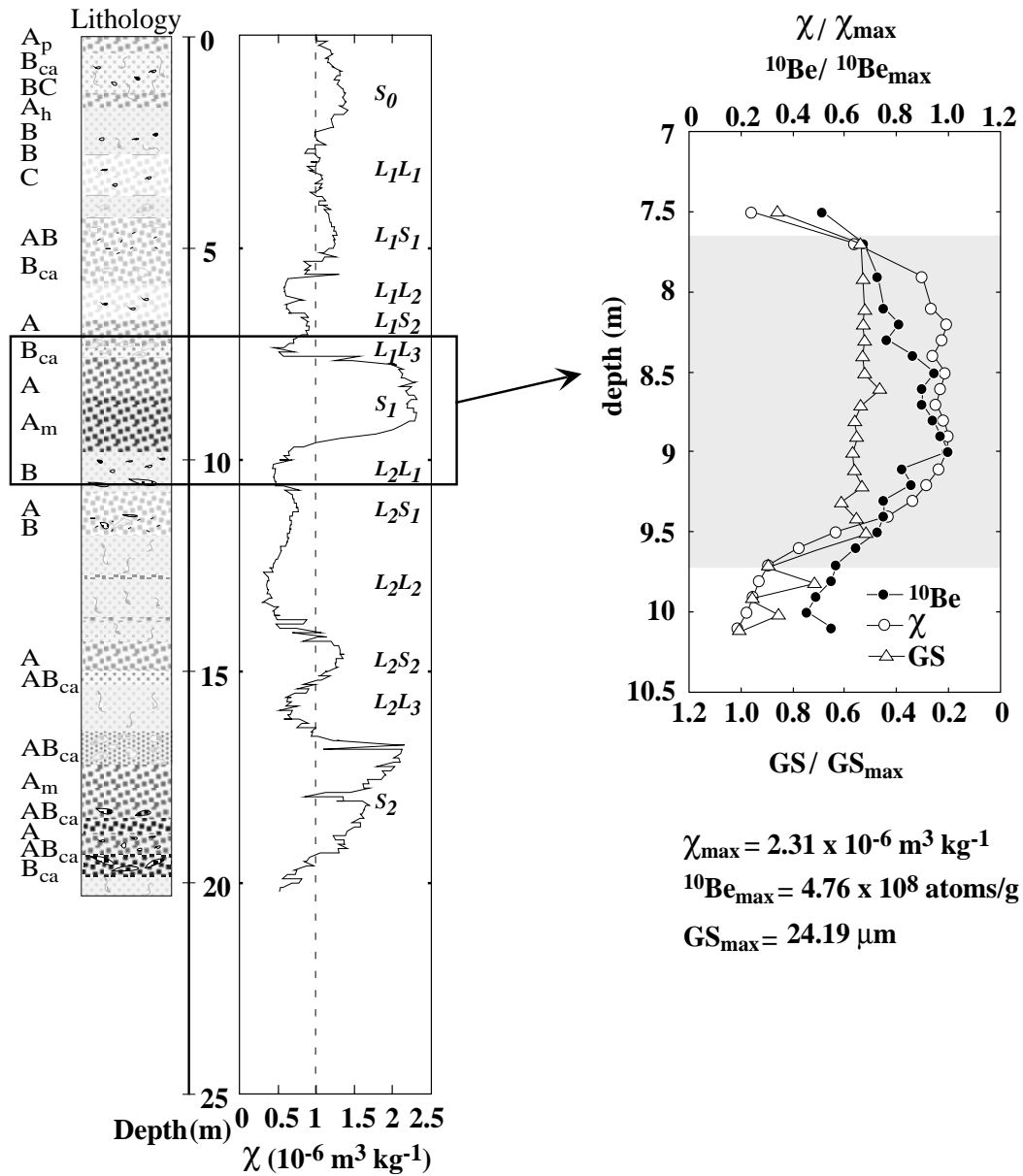


Figure 1: ^{10}Be , susceptibility (χ) and median grain size (GS) variation in the paleosol layer S_1 of the loess/paleosol sequence at Houzhuang (to the left: lithology and susceptibility variations are plotted for the whole section). The ^{10}Be , χ and GS values are normalized using their highest value, defined as $^{10}\text{Be}_{\max}$, χ_{\max} and GS_{\max} . The grain size variations scale is plotted inversely to facilitate comparison between the three parameters.

grain size ($\sim 13 \mu\text{m}$). These characteristics may explain the constant ^{10}Be concentration, similar to that measured at Weinan in the A and AC horizon.

The susceptibility increases by a factor of ~ 5 from loess layer L_2L_1 to paleosol S_1 , while the increase in ^{10}Be concentration is much smaller (factor 2), as observed also

by Beer et al. (1993) in Luochuan. These authors explained this difference as the result of pedogenesis causing an enhancement of susceptibility but not affecting the ^{10}Be concentration.

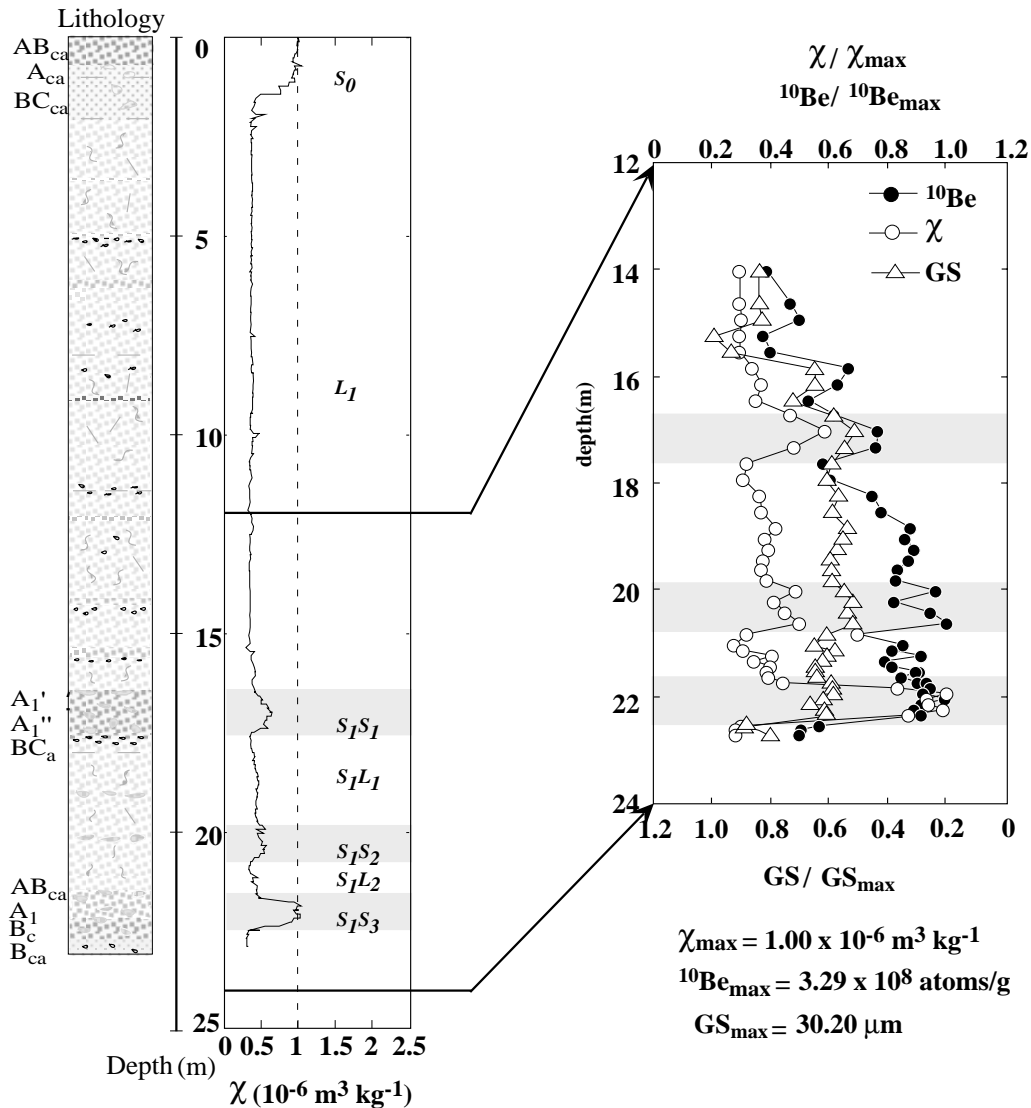


Figure 2: ^{10}Be , susceptibility (χ) and median grain size (GS) variations for the pedocomplex layer S_1 of the loess sequence at Xiagaoyuan (on the left the lithology and susceptibility variation is plotted for the whole section). The ^{10}Be , χ and GS values are normalized using the maximum value $^{10}\text{Be}_{\text{max}}$, χ_{max} and GS_{max} . The grain size variation scale is plotted inversely to facilitate comparison between the three parameters.

At Xiagaoyuan a total of 44 samples was measured, covering a sediment interval of 9 m thickness, which corresponds to a time span of ca. 70 ka (Fig. 2). ^{10}Be was measured at 30 cm intervals from 14 to 19 m (average time resolution of $\sim 2,500$ years), at 20 cm intervals from 19 to 21 m (average time resolution of $\sim 1,500$ years) and every 10 cm

down to 22.70 (mean time resolution of less than 1000 years). A decrease of the ^{10}Be concentration is observed from the bottom to the top of the pedocomplex S_1 . Maximum ^{10}Be concentration was measured in the paleosol layers S_1S_2 and S_1S_3 (peak value of 3.29×10^8 atoms/g at 20.80 m depth), while the minimum values were measured on the boundary between S_1S_1 and the overlying L_1 (1.74×10^8 atoms/g).

Susceptibility and ^{10}Be variations at Xiagaoyuan behave differently than at Houzhuang and Luochuan (Shen et al., 1993): Three separate susceptibility peaks developed during the 5a time period. From the bottom to the top of this pedocomplex, we observe a distinct susceptibility decrease from S_1S_3 (mean value of $0.92 \times 10^{-6} \text{ m}^3\text{kg}^{-1}$) to the overlying layers (40% of the mean value in layer S_1S_3 for S_1L_2 , 49% for S_1S_2 , 40% for S_1L_1 and 55% for S_1S_1). This behaviour is not observed in the ^{10}Be concentration: The mean value for S_1S_3 is 2.99×10^8 atoms/g. In more detail, in the younger horizons the concentration remains constant or decreases only slightly (91% of the S_1S_3 mean value for S_1L_2 , 102% for S_1S_2 , 86% for S_1L_1 and 78% for S_1S_1). The difference between susceptibility and ^{10}Be may be illustrated by the following examples: the susceptibility values measured at 21.00 m and 22.70 m depth are identical ($0.28 \times 10^{-6} \text{ m}^3\text{kg}^{-1}$), while the ^{10}Be concentration changes from 2.79 to 1.63×10^8 atoms/g, respectively. Thus the high degree of similarity observed in Luochuan (Beer et al., 1993) and in Houzhuang between susceptibility and ^{10}Be concentration is not reproduced in Xiagaoyuan, although a similar relative variation of ^{10}Be and susceptibility can be observed in both curves.

4.2.2 Relationship between ^{10}Be concentration, susceptibility and grain size

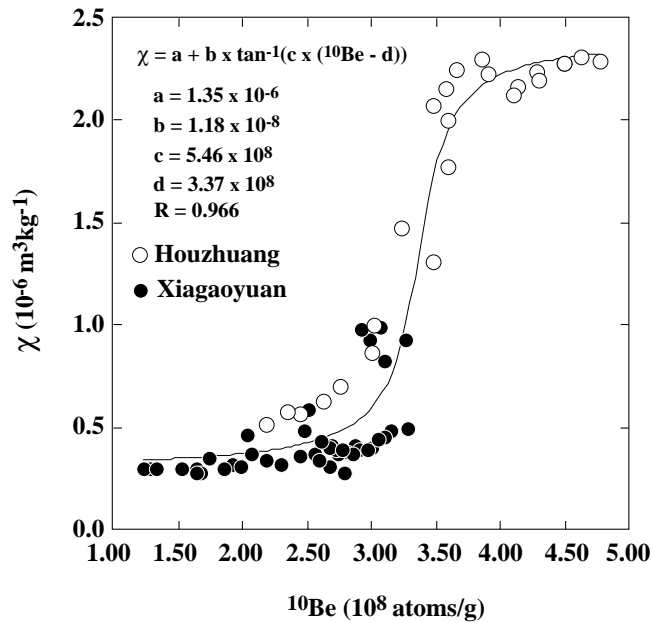


Figure 3: ^{10}Be plotted as a function of susceptibility at Houzhuang and Xiagaoyuan. The low susceptibility values represent mainly loess samples, whereas the high susceptibilities and ^{10}Be concentrations were measured in paleosol S_1 at Houzhuang.

In figure 3 ^{10}Be is plotted as a function of susceptibility, and the best fitting function for this data set is represented by an inverse tangent function, where the constants a and d represent the shift with respect to the origin, b and c the shape of the curve.

The shape of the fitting function is mainly determined by the samples from Houzhuang, which have a broader spectrum of susceptibility, corresponding to the samples collected in paleosol S_1 (values $> 1.0 \times 10^{-6} \text{ m}^3\text{kg}^{-1}$) and in the adjacent loess layers (see also Fig.1) and of the ^{10}Be concentration. At Xiagaoyuan a restricted range of susceptibility values is associated with ^{10}Be concentrations varying from 1.20 to 3.40×10^8 atoms/g. The exceptions are the samples collected in the paleosol S_1S_3 , with ^{10}Be concentrations between 2.8 and 3.40×10^8 atoms/g and susceptibilities values between $(0.75$ and $1.00 \text{ m}^3\text{kg}^{-1})$. Figure 3 also shows that the magnetic enhancement (from ~ 1.00 to $\sim 2.00 \times 10^{-6} \text{ m}^3\text{kg}^{-1}$) is associated with a relatively small increase on ^{10}Be concentration (between ~ 3.00 and $\sim 4.50 \times 10^8$ atoms/g).

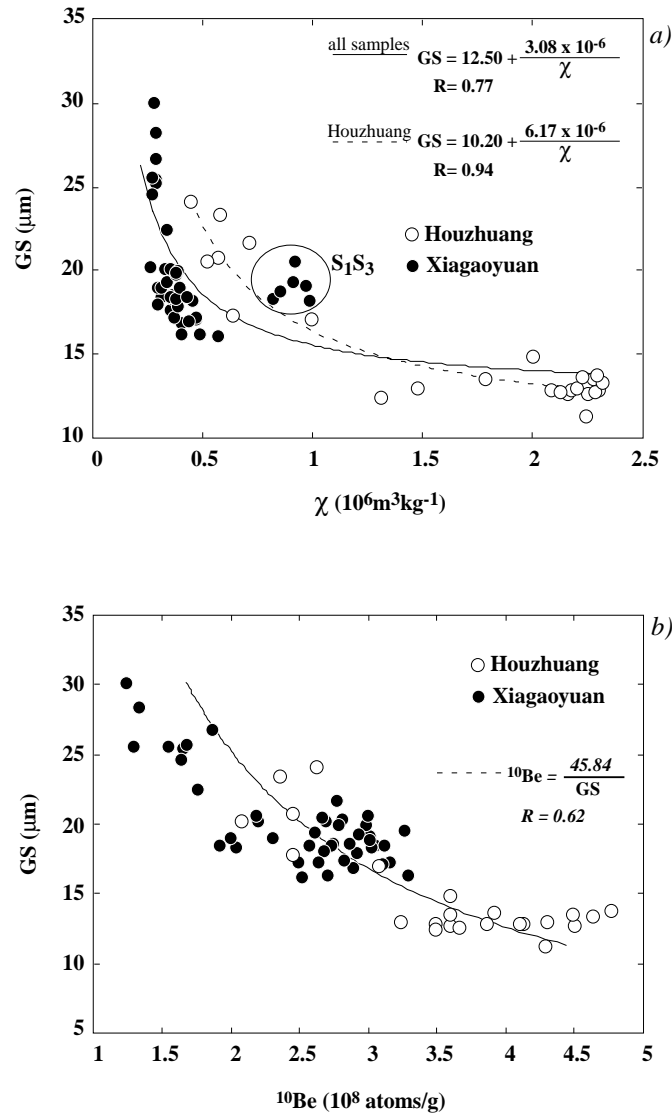


Figure 4: Susceptibility (a) and ^{10}Be (b) plotted as a function of median grain size. Susceptibility and grain size correlate well only if the magnetically strongly enhanced samples are considered (samples from Houzhuang). The relationship between grain volume and surface area controls the ^{10}Be concentration: decreasing GS is associated with increasing ^{10}Be concentration.

The effect of grain size on susceptibility and ^{10}Be concentration is plotted in figure 4. Both best fitting equations are obtained using a $1/x$ function, although the correlation factor in Fig. 4a is relatively low ($R=0.77$). The correlation R observed between the susceptibility of loess samples from Xiagaoyuan and their GS is 0.77, increasing only the samples from Houzhuang are considered (R increases up to 0.94). This may be caused by the larger susceptibility spectrum at Houzhuang than at Xiagaoyuan.

Fig. 4b shows that ^{10}Be decreases with increasing GS. This behaviour can be

explained recalling that for spherical grains the ratio between surface and volume is inversely proportional to the radius.

Having established the relationship between ^{10}Be concentration and GS (which is the median grain size for a bulk sample, obtained from a grain size interval that ranges from 1 to 180 μm), ^{10}Be concentration was measured as a function of grain size fractions using four fractionated samples (Fig. 5). The samples M23.40 from horizon S_1S_3 and M23.60 from horizon L_2 at Xiagaoyuan and L7.40 from horizon S_1 and L7.90 from horizon L_2 at Houzhuang were selected. It is found that ^{10}Be resides mostly in the clay fractions (grain sizes $\leq 2.2 \mu\text{m}$).

All four samples have concentrations $< 2.0 \times 10^8$ atoms/g for the grain size fractions $> 20.00 \mu\text{m}$. The concentrations increase to $5\text{-}8 \times 10^8$ atoms/g for the grain size fractions $\leq 2.2 \mu\text{m}$ (figs. 5a, b). While the maximum concentration for the samples from Xiagaoyuan is measured for the smallest fraction (8.04×10^8 atoms/g), a decrease in both loess and paleosol samples for the grain size fraction $< 0.39 \mu\text{m}$ was observed at Houzhuang. These results affect only partly the percentage variations of the ^{10}Be concentration in the different grain sizes (Fig. 5c,d): the lowest contributions are given by the fractions $> 2.20 \mu\text{m}$, with values varying between 2 and 18% for the loess and paleosol samples. The maximum concentration was found in the $0.39\text{-}2.20 \mu\text{m}$ grain size fractions for all four samples (between 30 and 45%). This is not only due to the presence of very fine grain sizes, but also to its larger grain size spectrum and thus larger mass contribution to the total mass. In the $< 0.39 \mu\text{m}$ grain size fraction the concentration decreases at both sites, with values between 10% and 20%, which is relatively high, considering the small contribution of this fraction to the total mass. In order to explain the decreased ^{10}Be concentration observed for the $< 0.39 \mu\text{m}$ grain size fraction at Houzhuang, the following hypothesis is suggested: The ^{10}Be extraction efficiency for these fractions was higher at Xiagaoyuan ($\sim 86\%$ for M23.40 and $\sim 88\%$ for M23.60) than at Houzhuang ($\sim 79\%$ for both samples). The Xiagaoyuan values are in the range of the efficiency measured by Shen et al. (1992), i.e. 86%.

Under the assumption that the 10% extraction efficiency difference between Xiagaoyuan and Houzhuang is due to “lost” ^{10}Be falling in the $< 0.39 \mu\text{m}$ grain size fraction, the latter should have had a value of 7.50×10^8 atoms/g for the paleosol sample and 3.80

$\times 10^8$ atoms/g for the loess sample, resulting in concentration values for the grain size fraction $< 0.39 \mu\text{m}$ at Houzhuang similar to the concentration in the grain size fraction $0.39\text{-}2.20 \mu\text{m}$.

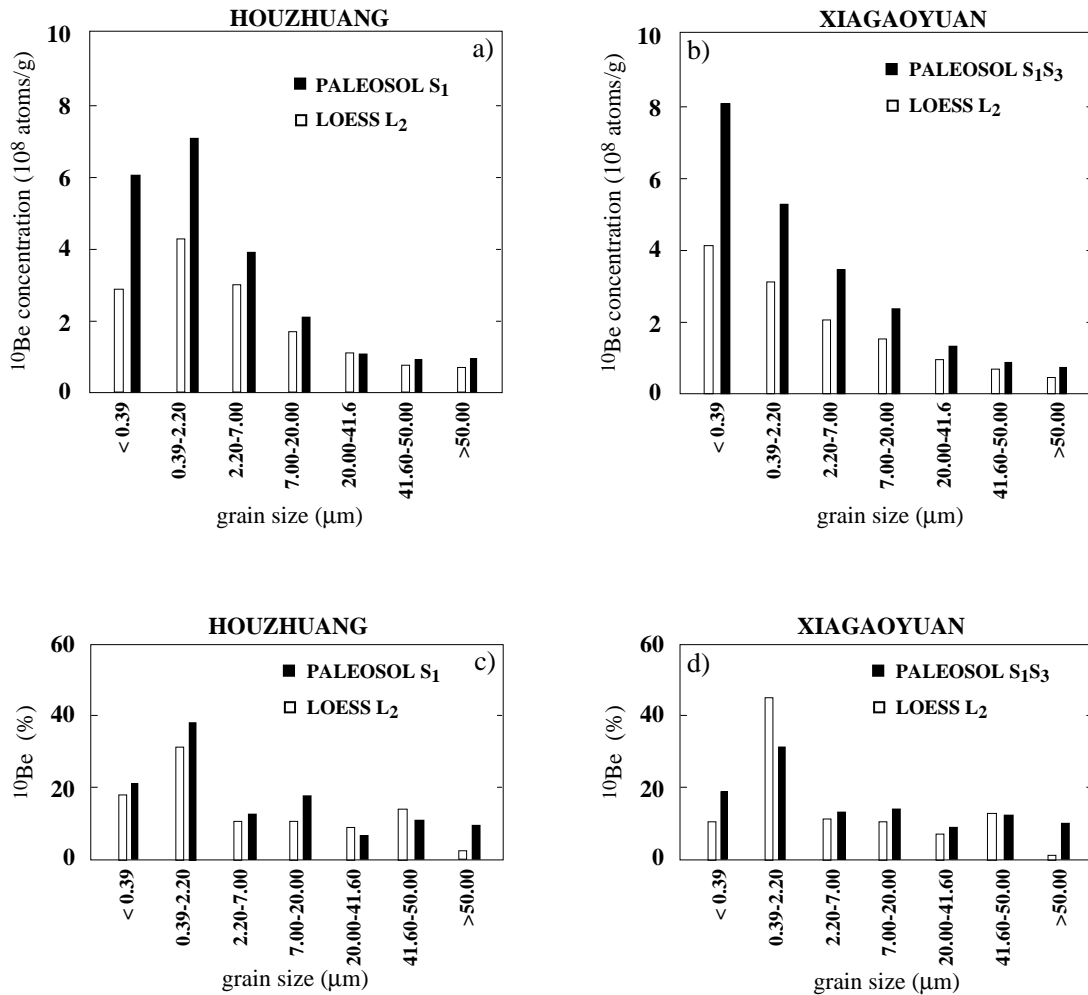


Figure 5: ^{10}Be concentration as a function of grain size at Houzhuang (a) and Xiagaoyuan (b), with higher values in the paleosol samples than in the loess samples. More than half of the total ^{10}Be content is concentrated in the grain size fractions $< 2.2 \mu\text{m}$ for the loess and paleosol samples at Houzhuang (c) and Xiagaoyuan (d) (^{10}Be concentration normalized with the mass of the corresponding grain size fraction). At Houzhuang the concentration decreases anomalously in the $< 0.39 \mu\text{m}$ fraction (a).

Alternatively, the ^{10}Be concentration decrease could be explained by the long residence of the sediment in water during the fractionating procedure. If the sediment containing ^{10}Be is in solution, the relationship between the absorbed and the adsorbed phase

is expressed by $k'_d = [N^{10}\text{Be}/g_{\text{DUST}}]/[N^{10}\text{Be}/g_{\text{WATER}}]$, N being the number of ^{10}Be atoms and g the weight in gram (Baumgartner, 1995). Although adsorption increases by two orders of magnitude in 20 days, with the k'_d value decreasing from 10^7 to 10^5 , those values are still in the range of the particle affinity for ^{10}Be .

4.2.3 ^{10}Be and susceptibility fluxes

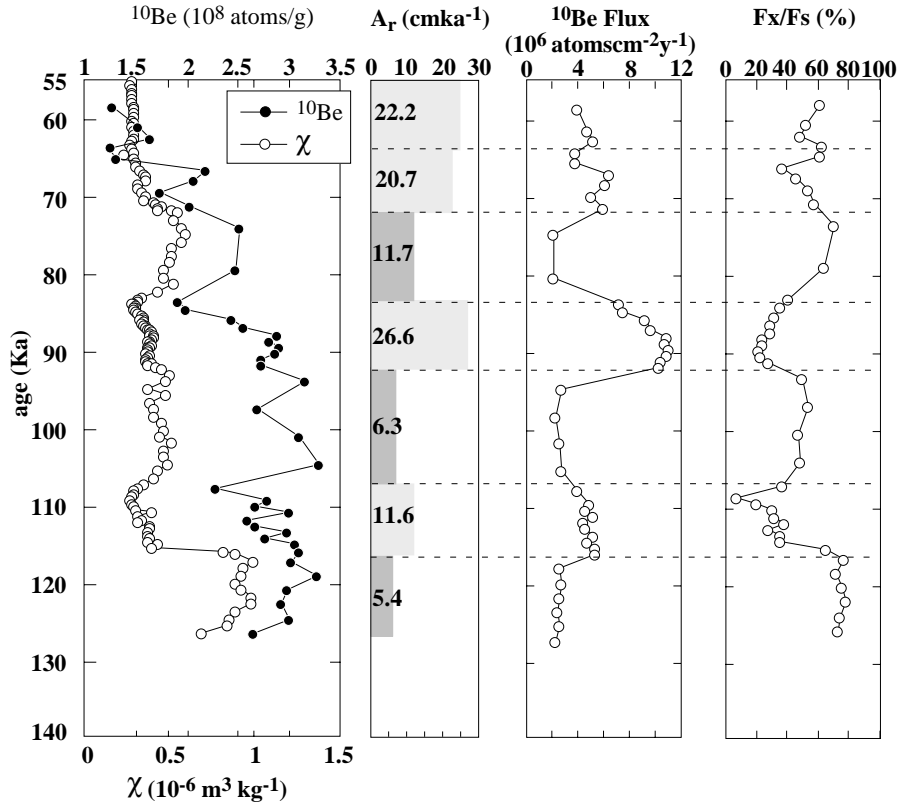
Susceptibility and ^{10}Be curves can be correlated with the astronomically-tuned marine oxygen isotope variations (Beer et al., 1993). Average sedimentation rates and hence ^{10}Be and susceptibility fluxes can be calculated using this procedure.

Susceptibility, and ^{10}Be are plotted in Fig. 6 on an absolute timescale using the astronomically tuned ODP 677 $\delta^{18}\text{O}$ curve (Shackleton et al., 1990; see Fig. 13, chapter 3). Those results were used to calculate mean accumulation rates for the last interglacial horizons at Xiagaoyuan and Houzhuang. A mean accumulation rate of 3.2 cm/ka and a ^{10}Be flux of $\sim 2 \times 10^6$ atoms $\text{cm}^{-2} \text{yr}^{-1}$ was obtained for the paleosol layer S_1 at Houzhuang, values almost identical with those measured at Luochuan (Shen et al., 1992). At Xiagaoyuan the mean accumulation rates in the paleosol layers (5.4 cm/ka for S_1S_3 , 6.3 cm/ka for S_1S_2 and 11.7 cm/ka for S_1S_1) are in general lower than in the inter-layered loess layers between (11.6 cm/ka for S_1L_2 and 26.6 cm/ka for S_1L_1). This results in ^{10}Be fluxes close to $\sim 2 \times 10^6$ atoms $\text{cm}^{-2} \text{yr}^{-1}$ in the paleosol layers. The values are higher in the loess layers with values between ~ 4 and $\sim 5 \times 10^6$ atoms $\text{cm}^{-2} \text{yr}^{-1}$ in S_1L_2 and values up to 11×10^6 atoms $\text{cm}^{-2} \text{yr}^{-1}$ in S_1L_1 .

A mean ^{10}Be concentration of 2.25×10^8 atoms/g for dust (2.7×10^8 atoms/g were measured during a recent dust fall in China, Shen et al., 1992), and a direct local ^{10}Be fallout of 0.84×10^6 atoms $\text{cm}^{-2} \text{yr}^{-1}$ (an averaged value for production rate of 0.57×10^6 atoms $\text{cm}^{-2} \text{yr}^{-1}$ was recently proposed by Masarik and Beer, 1999) are calculated from the slope and intercept of the regression line in Fig. 6b.

Beer et al. (1993) proposed a method to separate detrital from pedogenic susceptibility using ^{10}Be . The idea is that both susceptibility flux (F_S) and ^{10}Be flux (F_B) are composed of two components: the susceptibility flux by a dust flux component (F_D) and a

Xiagaoyuan



a)

b)

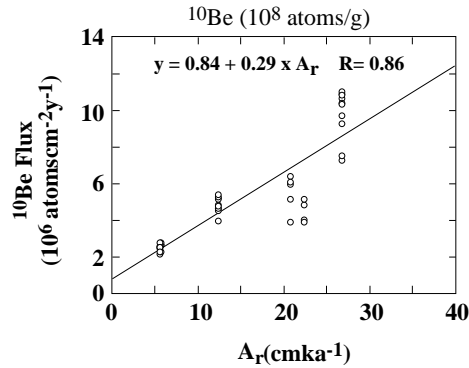


Figure 6: ^{10}Be concentration and susceptibility plotted on a timescale covering the last interglacial period at Xiagaoyuan (a). High sedimentation rates A_r were calculated for the last interglacial (between 5.4 cm/ka and 26.6 cm/ka). ^{10}Be fluxes vary from 2×10^6 atoms $\text{cm}^{-2} \text{y}^{-1}$ to 11×10^6 atoms $\text{cm}^{-2} \text{y}^{-1}$ (b). The correlation between ^{10}Be flux and accumulation rate for the loess and paleosol layers gives a value for the mean ^{10}Be concentration in the dusts and for the direct ^{10}Be fallout (for sedimentation = 0, see text for detail). The ratio pedogenic susceptibility flux (F_χ) to total (F_s), calculated from equation 5 (see text) results in higher values in paleosols than in loess layers.

pedogenic flux component (F_X), and the ^{10}Be flux by an atmospheric component (F_A) and a dust component (F_D),

$$F_B = F_A + F_D \quad (1)$$

$$F_S = F_{D'} + F_X \quad (2)$$

Under the assumption that $F_{D'}$ is proportional to F_D , it is possible to quantify F_X :

$$F_{D'} = \alpha F_D \quad (3)$$

$$F_X = F_S - \alpha(F_B - F_A) \quad (4)$$

$$F_X / F_S = (1 - \alpha(F_B - F_A) / F_S) \quad (5)$$

The most important assumption made in this model is the proportionality of $F_{D'}$ and F_D . The constant α from equation 3 is obtained from the slope of the regression line representing the correlation between F_S and (F_D) (fig. 7). Note that the constant α is only characteristic for a specific loess/paleosol sequence.

Using this method the pedogenic contribution F_X to total susceptibility was calculated (Fig. 6a). F_X is generally higher in the paleosols (~50% in S_1S_2 and ~60% in S_1S_1). The highest values were found for paleosol S_1S_3 (up to 80%). In the loess layers S_1L_1 and S_1L_2 the pedogenic contribution is reduced to values between ~10% and 35%. Deviating results are obtained for the loess samples from the bottom of L_1 with an age between 55 and 70 ka for which a mainly detritic susceptibility is expected. Heller et al. (1993), for example, found at Luochuan an average pedogenic contribution of ~20% for stage 4 (25% for stages 2, 3 and 4 together), while in Xiagaoyuan the mean value is ~50%. The peak values, of ~60%, reached for the loess samples with an age of ~58 ka and ~64 ka coincide with an increase of χ_f (see Fig. 13, chapter 3, Part II). The minima (at ~61 ka and ~65 ka) imply a lower pedogenic susceptibility contribution, considering the dry and cold climate during these time periods.

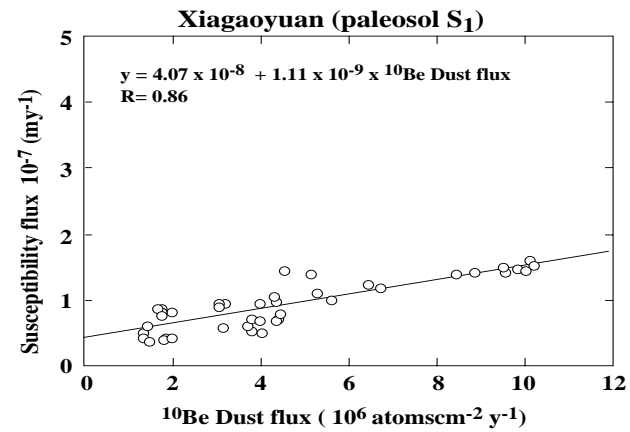
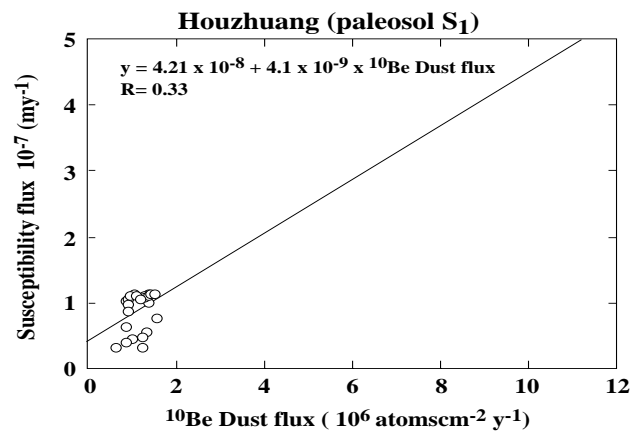
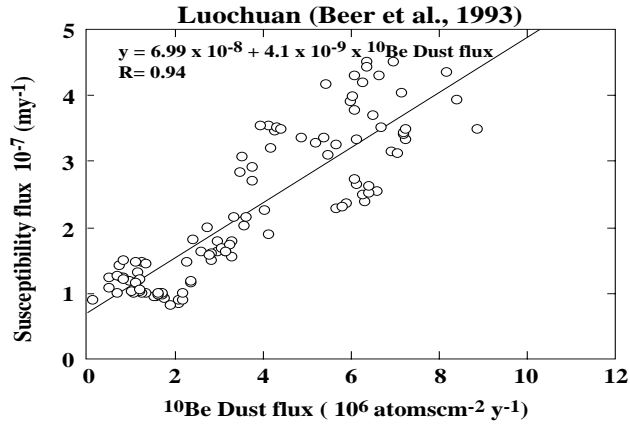


Figure 7: ^{10}Be dust flux plotted as a function of the susceptibility flux for Luochuan (Beer et al., 1993), Houzhuang (paleosol S₁) and Xiagaoyuan (paleosol S₁). The slope obtained by Beer et al. (1993) represent the constant a used to separate the pedogenic from the detrital susceptibility flux (Fig. 7a). For Xiagaoyuan (c) a different a value was obtained. At Houzhuang and Luochuan the α value is the same, although the correlation R in Houzhuang indicates no correlation between ^{10}Be dust flux and susceptibility flux.

4.2.4 The role of grain size

One objective of the present study was to determine the link between ^{10}Be , grain size and magnetic low field susceptibility, the most commonly used magnetic parameter in environmental magnetism.

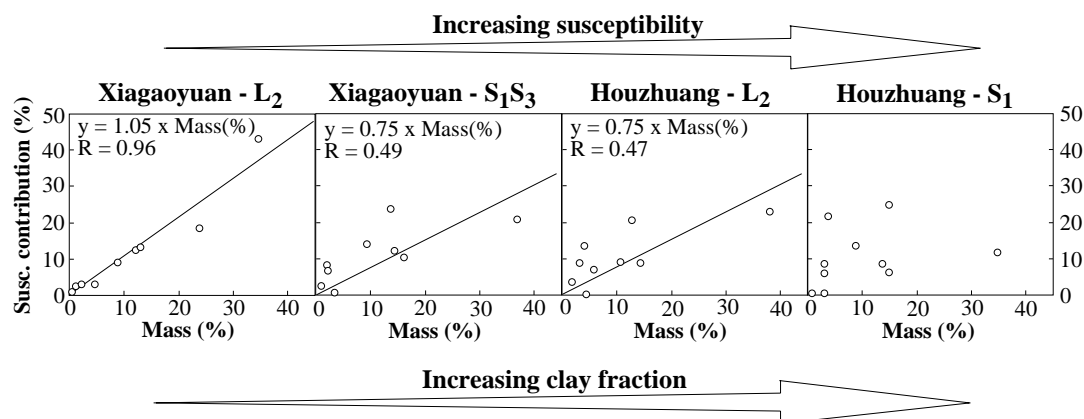


Figure 8: Susceptibility of different grain size fractions as a function of their mass contribution for four different samples at Xiagaoyuan and Houzhuang (data from Fig. 6, p. 155). The correlation factor R decreases with increasing clay fraction and susceptibility, with a value of 0.96 for pristine loess (Xiagaoyuan - L₂) and no correlation at all for strongly weathered paleosol (Houzhuang - S₁).

Susceptibility measurements performed on fractionated samples (Fig. 6, Chapter 3, Part II, p. 155) demonstrate that its relation with grain size strongly depends on the degree of pedogenesis: in loess samples the major susceptibility and mass contribution is due to the coarser grain sizes. With increasing pedogenesis, the mass contribution of the finest grain sizes slightly increases, while their susceptibility contribution rises dramatically. This results in a decrease of the linear correlation factor between mass and susceptibility contributions, and eventually a breakdown of correlation altogether, with increasing pedogenesis (Fig. 8): the best correlation factor was calculated for the most unaltered loess sample ($R=0.96$), with a slope close to 1. Although pedogenesis changing the original magnetic mineralogy cannot be discounted completely, the correlation found for sample L₂ at Xiagaoyuan can be considered as typical for pristine loess.

A detailed analysis of the grain size distribution for the four samples in Fig. 8 was performed using a Mastersizer (Malvern Instrument) for the interval between 0.5 μm and 180 μm (size range of the used lens). All four samples have a bimodal grain size spectrum in which the peak at smaller grain size grows with increasing pedogenesis (Fig. 9).

The increasing clay content results from the destruction of the coarser fractions that are constantly waning with increasing pedogenesis.

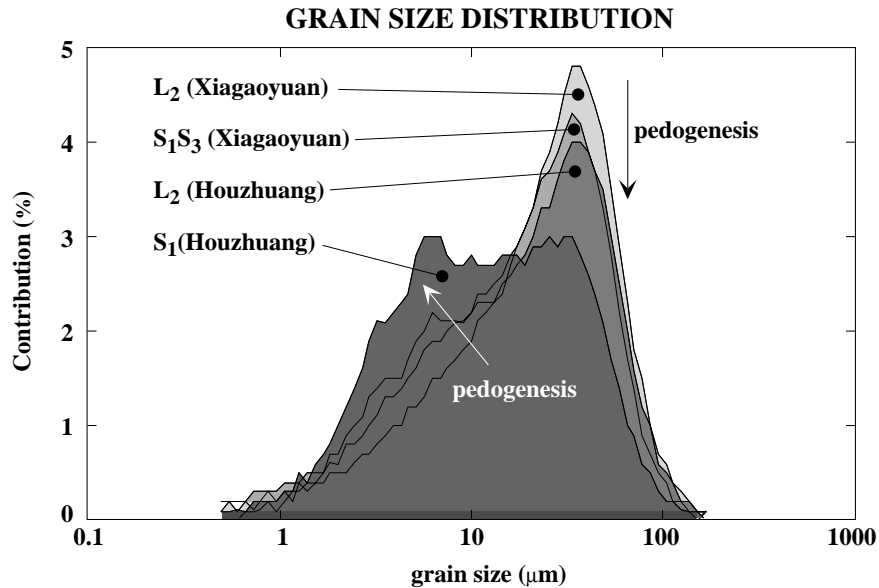
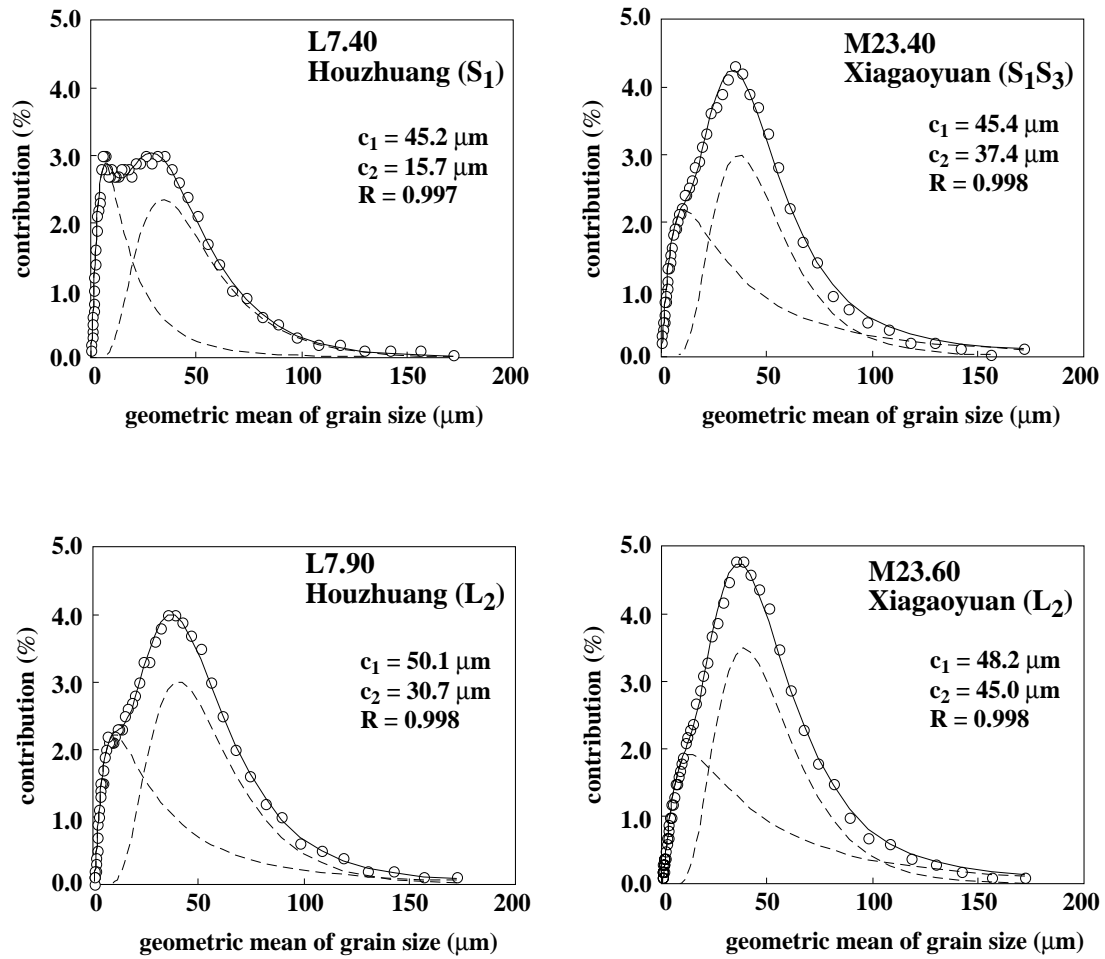


Figure 9: The grain size spectrum of four different samples from Xiagaoyuan and Houzhuang plotted on a logarithmic scale. The increasing degree of pedogenesis results in a larger contribution from the finest fractions at the expense of the coarser grains.

The distributions in Fig. 9 can be described mathematically using 2 log-normal functions, obtained using the Levenberg-Marquardt method; this approach should discriminate between the original grain size distribution and the superimposed distribution originating from pedogenic processes (Fig. 10).

The median grain size for the coarser distribution (expressed by c_1 in Fig.10) is similar in all four samples, with slightly higher values in loess samples (values of 48.2 μm for sample M23.60 and 50.1 μm for sample L7.90) than in the paleosol (45.2 μm in sample L7.40 and 45.4 μm in sample M23.40). A more important variation is observed for the smaller grains (c_2), with values between 45.0 μm for the less altered loess sample M23.60 and 15.7 μm for the most weathered paleosol sample L7.40. where the clay fraction contribution is highest.



$$y(r) = \frac{1}{r} a_1 \exp\left[-b \ln^2 \frac{r}{c_1}\right] + \frac{1}{r} a_2 \exp\left[-b \ln^2 \frac{r}{c_2}\right]$$

Figure 10: Grain size spectra of two loess and two paleosol samples from Houzhuang and Xiagaoyuan plotted as a function of their contribution to the total grain size spectrum. The measurement interval is between 1 μm and 180 μm . The sum of 2 log-normal function were used to fit the measured distributions. Two distinct components were obtained and are represented by the dashed curves. The median grain size is represented by the constants c_1 and c_2 , referring to the distribution “1” and “2”, the amplitude by r , the dispersion by b . R is the correlation factor.

grain size distribution (interval: 0.015 - 40 μm)

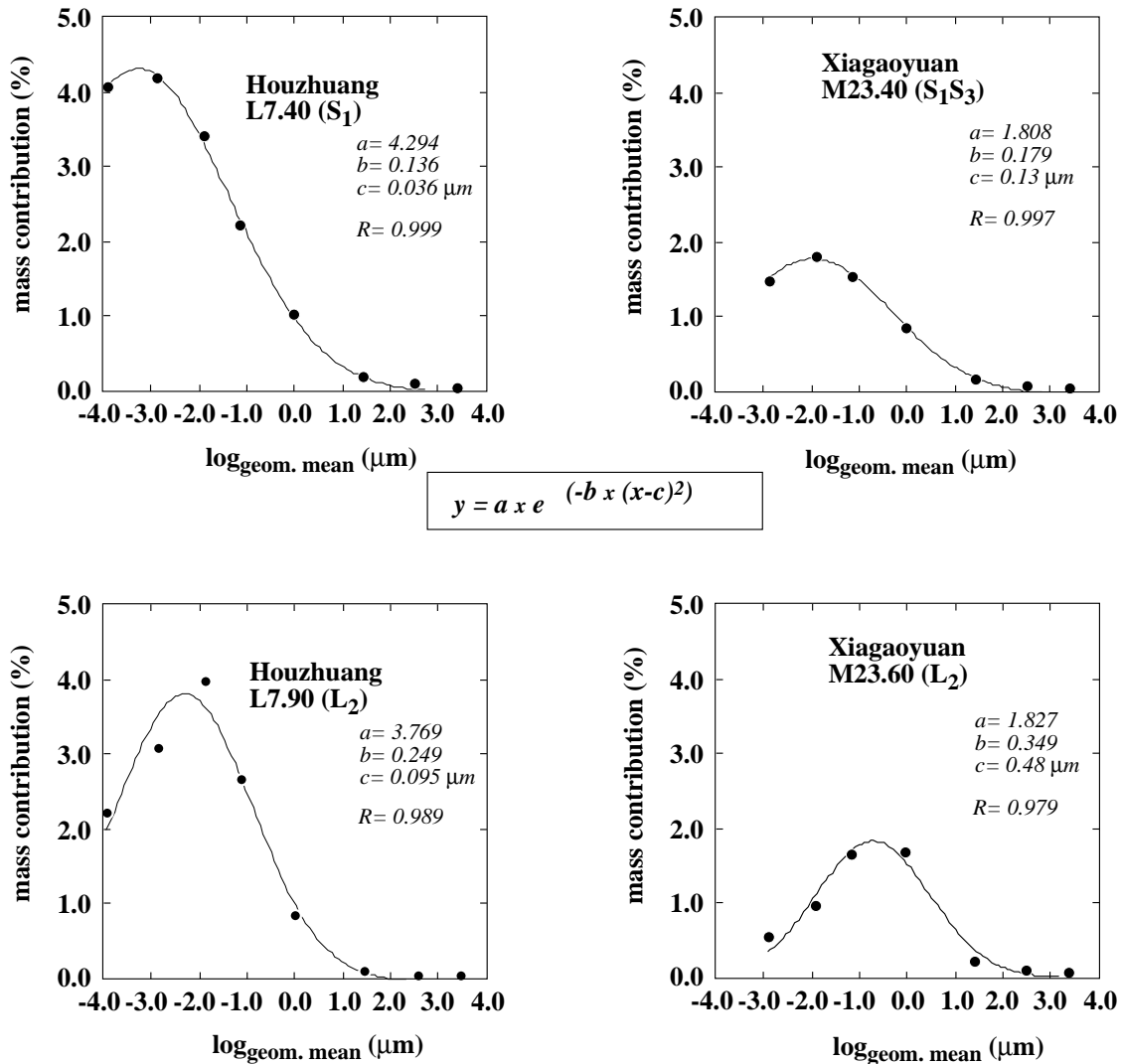


Figure 11: Grain size distribution in four different samples from Houzhuang and Xiagaoyuan. Black dots represent the measured distribution and were fitted using a log-normal function. The constant a represents the amplitude, b the dispersion factor, c the median grain size and R the correlation factor.

A similar procedure was applied to the finer grain size distributions obtained for the same samples using sedimentation and centrifugation (grain size range: 0.015 μm - 42 μm ; Fig. 11). The largest median grain size was obtained for loess sample M23.60 ($\sim 0.48 \mu\text{m}$) and the minimum for paleosol sample L7.40 ($\sim 0.036 \mu\text{m}$). From this calculation, and in consideration of the median grain sizes obtained from figure 10, it clearly appears that a reliable modeling for grain size distribution spectra must consider also grain sizes $< 1 \mu\text{m}$ (which was the lower limit for the calculation made using the distribution in Fig.

9 and 10), responsible for the major ^{10}Be contribution. For this reason the correlation between ^{10}Be concentration and the median grain size in Fig. 4b has a coefficient of only $R = 0.86$, resulting from the varying contribution of the 2 components of the grain size spectrum (Fig. 10) which are not connected directly with a unique median grain size value.

To overcome these difficulties, an empirical relationship between the median grain size obtained from the measurements with the mastersizer (figs. 1, 2 and 4) and those obtained from Fig. 10 (c_1 and c_2 values) was established. The following assumptions were made: 1) the grain size spectra in loess sediments is the result of two components (expressed by the two log-normal functions found in Fig. 10) that have constant median grain sizes, but have variable amplitudes; 2) the grain size spectra of the samples M23.60 and L7.40 are considered typical for unaltered loess and strongly weathered paleosol, respectively.

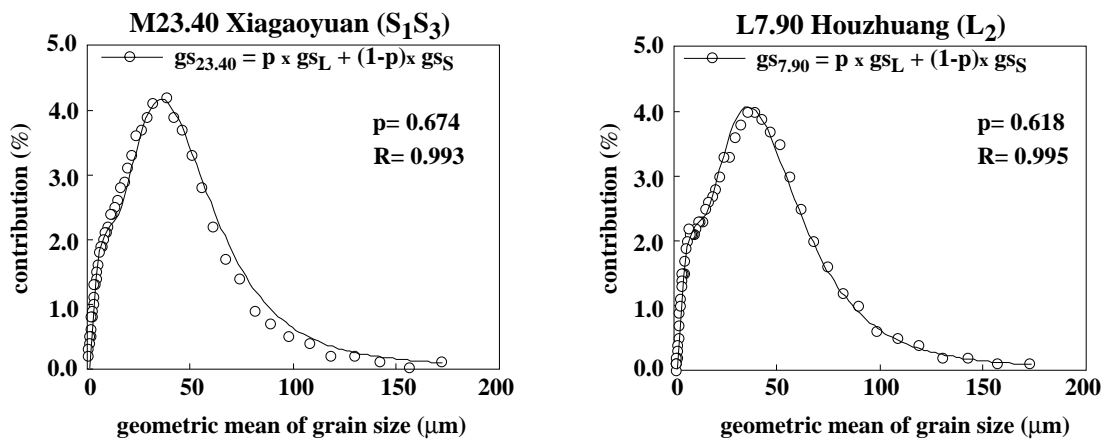


Figure 12: The grain size spectra of paleosol M23.40 and loess L7.90 were fitted using the equation 6 (see text for detail). A similar p value was calculated for both functions, resulting from the contribution of 2 similar distribution (gs_S and gs_L) in both spectra. The geometric mean was calculated for each grain size class and plotted on the x-axis.

The functions $gs_{7.90}$ and $gs_{23.40}$, describing the grain size spectra of samples L7.90 and M23.40, which have intermediate degrees of pedogenesis, were fitted using the following equation:

$$gs_x = p \cdot gs_S + (1 - p) \cdot gs_L \quad (6)$$

where gs_S and gs_L are the log-normal functions obtained by fitting the spectra of

paleosol L7.40 and loess M23.60, respectively, and p is a constant that expresses the contributions of gs_S and gs_L . Using this approach the fitting functions in Fig. 12 were obtained.

The high correlation factor R indicates that the assumption of a bi-modal grain size spectrum originating from two distributions with constant median grain size is reasonable. A relationship between measured median and calculated median grain sizes can thus be established.

It is now possible to establish recursively an empirical relationship between the calculated median grain sizes and the median grain size obtained from the Mastersizer, so that every median grain size can be associated with a value of “ p ” (from equation 6).

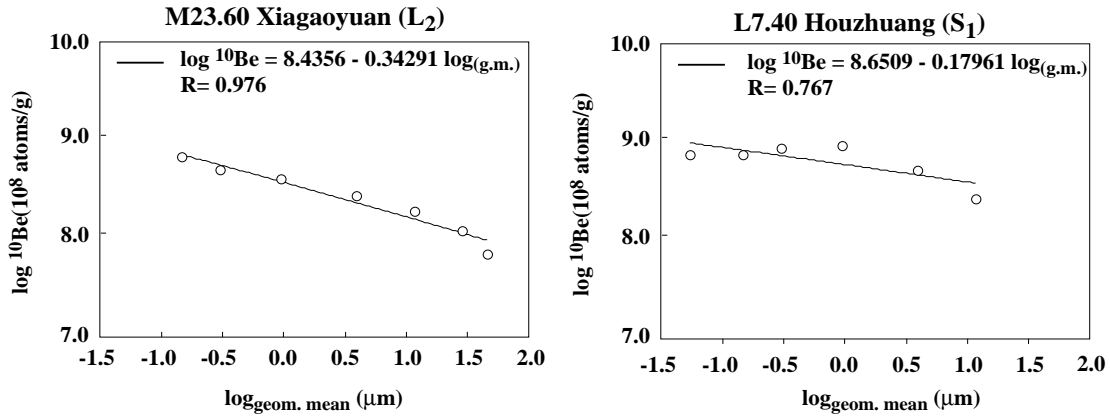


Figure 13: Bilogarithmic ^{10}Be concentration in seven (M23.60) and six (L7.40) grain size fractions (see also Fig. 11). The fitting was calculated from 0.090 to 50 μm for loess sample M23.60, and from 0.030 to 7.0 μm for paleosol L7.40.

By knowing the grain size distribution of a loess sample, it is possible to model the ^{10}Be concentration for a given ^{10}Be dust flux F_D and atmospheric flux F_A . The following relationship can be written

$$^{10}\text{Be}_{TOT} = \int_0^{\infty} pGS_S(r)f_S(r)(dr) + \int_0^{\infty} (1-p)GS_L(r)f_L(r)(dr) \quad (7)$$

where p indicates the relative contributions of gs_S and gs_L . The functions $f_S(r)$ and $f_L(r)$ describe the relationship between ^{10}Be concentration and median grain size, measured in Fig. 6 for the four already discussed samples (Fig. 13).

Sample M23.60 was taken as representative for the ^{10}Be concentration in pristine

loess. A clear linear correlation was found. In paleosol L7.40 the correlation was made considering the grain sizes that belong to the log-normal distribution calculated in Fig. 12.

4.3 Conclusions

The central purpose of the study at Xiagaoyuan and Houzhuang was to obtain information on the ^{10}Be concentration in relation to susceptibility and grain size distributions. The two loess/paleosol sequences incorporate the same source material but developed under different climatic conditions. ^{10}Be concentrations reflect the global climatic changes as does susceptibility (Shen, 1986). At Houzhuang the measured ^{10}Be concentration increases by a factor two in the paleosol S_1 with respect to the overlying and underlying loess layers, resembling the result at Luochuan (Beer et al., 1993). Small local differences of the ^{10}Be concentrations are related to variable development: at Houzhuang, pedocomplex S_1 consists of two superimposed thick A-horizons which have constant median grain size and constant ^{10}Be concentration whereas in Luochuan and Weinan (Gu et al., 1992), the highest ^{10}Be concentrations were found in the clay rich horizon of pedocomplex S_1 . The ^{10}Be concentration as a function of depth in these three sequences is different, but is consistent with the lithological characteristics (e.g. grain size) of pedocomplex S_1 at all w sites.

At Xiagaoyuan, ^{10}Be concentration and susceptibility do not show the high degree of similarity with lithology as observed at Houzhuang. The pedogenic contribution to total susceptibility calculated using the model of Heller et al. (1993) is generally higher in Xiagaoyuan than that obtained by Heller et al. (1993) for Luochuan. On the other hand, ^{10}Be concentration and grain size are closely correlated at both sites, with increasing grain sizes being accompanied by decreasing ^{10}Be concentrations. The correlation functions differ slightly between the two sites.

The paleoprecipitation model of Heller et al. (1993) may be improved in two ways. First, a model should be developed which considers the effect of grain size on the ^{10}Be concentration. This concentration depends strongly on the original grain size of the source material from which the loess derives. Loessification, and more importantly,

weathering and pedogenic processes may change the original grain size distribution. Hence, the measured median grain size in the altered sediments will not correspond to the value at the time of deposition. The distribution will not change essentially during cold periods. At present, for technical reasons we have only median grain size data for the whole sequence at Xiagaoyuan. The very limited number of grain size spectra available for pristine loess samples does not allow to extend the relationship between grain size spectra and ^{10}Be concentration to the whole loess/paleosol sequence at present. Hence reliable modeling including the grain size effect cannot yet be undertaken.

The second approach is based on the theoretical calculation of the atmospheric ^{10}Be flux, F_A . This flux depends directly on the ^{10}Be production rate which is controlled by the time-variable intensity of the earth's magnetic field (Elsasser et al., 1956; McHargue et al., 1995; Frank et al., 1997; Masarik and Beer, 1999), and varies by up to a factor 2 during the last 130 ka (Meynadier et al., 1992). By knowing the paleointensity of the earth's magnetic field for the last ~130 ka, it is possible to calculate the production of cosmogenic radionuclides. The dust component of ^{10}Be flux may then be obtained from the total ^{10}Be concentration simply by subtraction of the geomagnetically corrected atmospheric flux. This remains as a task for the future.

Chapter 5
CONCLUSIONS

- **Dating of loess sediments and paleoclimate**

One essential necessity to study the climatic variations that occurred during the Quaternary is a reliable time framework for the studied sequences. This was attempted by magnetostratigraphic investigations. Standard demagnetization techniques were used to determine the characteristic component of the natural remanent magnetization (NRM) in 3 loess/paleosol sequences (Chapter 1, 2 and 3, part II). The Matuyama/Brunhes (M/B) polarity reversal was identified in Paks (Hungary) and Roxolany (Ukraine). Short duration polarity events, such as the Blake event, could not be detected. Thus a magnetostratigraphic tie point was provided for the sections at Paks and Roxolany, but not in the Chinese sections where only the upper ~25 m of two sections at Xiagaoyuan and Houzhuang were sampled (the M/B boundary in the huge Chinese loess deposits is normally found at depths exceeding 50 m in the central loess plateau and 180 m in the western loess plateau).

The susceptibility variations measured at Roxolany correlate well with those measured at Luochuan (Heller and Liu, 1986) and with the astronomically-tuned oxygen isotope ratios from ODP core 677 (Shackleton et al., 1990) (Chapter 2, part II) opening a second possibility of magnetostratigraphic dating. Quaternary glacial/interglacial climatic changes as documented also by loess susceptibility were driven by processes affecting the entire northern hemisphere. This is confirmed by the observation of the susceptibility variations observed at Paks and in the Chinese sequences at Luochuan (Heller and Liu, 1986) and Xifeng (Liu et al., 1988) and other localities on the Chinese loess Plateau as well as in Central Asia (Forster et al., 1994) and Europe (Forster et al., 1996). Major susceptibility enhancement in these sections is observed in the paleosols that formed during the last ~500 ka (paleosols S_1 to S_5 in Chinese loess; PK_1 to PK_4 at Roxolany; BD, BA and MB at Paks). The magnetic analysis at Roxolany confirmed the micromorphological soil study results, indicating that the first ~300 ka of the Brunhes epoch were characterized by a more humid and warm climate favoring the formation of Mediterranean type soils (braunlehms) rather than chernosems on the Russian plain. By analogy with recent soils in China (Han et al., 1996) the lower susceptibility signals measured in the older paleosols of the Brunhes epoch at Roxolany may result from destruction of ferromagnetic minerals due to a reducing environment. Although it was possible to identify two distinct climofunctions for chernosems and braunlehms, quantitative

paleoprecipitation reconstructions are difficult to establish.

In order to establish a reliable time frame for the sequences at Xiagaoyuan and Houzhuang, where no polarity time markers were identified, the susceptibility correlation with the astronomically-tuned oxygen isotope curve was used as a dating tool. The sampled interval at Xiagaoyuan was assigned an age of ~130 ka, comprising the whole last interglacial/glacial cycle (oxygen isotope stages 5, 4, 3, 2 and 1). At Houzhuang, where the sedimentation rate is reduced, the sampled interval covers a time span covering the last ~250 ka, including also sediments corresponding to oxygen isotope stages 7 and 6. The most detailed correlation was constructed for the sequence at Xiagaoyuan which is characterized by a low degree of weathering (with respect to the one observed at Houzhuang) and a high sedimentation rate. The susceptibility variations from paleosol S_1S_1 to paleosol S_1S_3 match the oxygen isotope substages 5a, b, c, d and e during the last interglacial period (from ~130 ka to ~70 ka B.P.). The frequency dependence of susceptibility measured through loess layer L_1 at Xiagaoyuan (corresponding to the last glacial period) was correlated with the oxygen isotope curve obtained from the GRIP ice core in Greenland. The results permit one to conclude that the short-term climate changes recorded in the ice core are imprinted in the terrestrial loess paleoclimatic record, too. They underscore their global importance, also on a millennial scale (Porter and An, 1995; Chen et al., 1997; Fang et al., 1999).

On the other hand, important regional climatic differences are noticed which control the sedimentary history in loess sediments. The sedimentary environment in the European sections is much more complex than the one on the Chinese loess plateau, where the loess was deposited on a wide peneplain plateau and all the horizons are in superposition and horizontally layered. The section at Paks, for example, presents signs of erosion (“delle”) that complicate cross-correlation with adjacent sites. Although regional climatic differences can affect the magnetic properties, the global climatic signature is not completely overprinted.

- **Magnetic mineralogy**

Several techniques were applied to study the magnetic properties of the loess sequences under consideration. Besides the classic measurements (hysteresis parameters at room temperature on bulk samples), low temperature measurements methods were

used. To improve the potential of these methods, bulk samples were fractionated using sedimentation and centrifugation methods. The advantage of this method, compared with magnetic extraction methods, is the possibility of having a ferromagnetic population with a narrow spectra of grain sizes in each fraction. Possible clumping of individual magnetic grains and the electrostatic forces between clays and magnetic minerals can cause a discrepancy between the theoretical and the actual magnetic grain size fraction distribution. This method was applied to four samples from Paks, and two samples each from Xiagaoyuan and Houzhuang, which cover wide ranges of lithology and susceptibility, from typical pristine loess to strongly weathered paleosols. A strong correlation between magnetic enhancement and growth of the finest magnetic grains (SP and SSD) is observed in all samples. The *in situ* production of fine ferromagnetic minerals during pedogenesis is the origin of the magnetic enhancement. Models that propose the variation of the ferromagnetic component in the source material as the cause for the different magnetic signals in the loess and paleosol layers are discounted.

Low temperature measurements (ZFC, TRM and hysteresis measurements) performed on bulk samples and grain size fractionated material from Paks indicate magnetite/maghemite as the main carrier(s) of the magnetic signal. The presence of the Verwey transition in the coarse grain size fractions is taken as evidence of detrital magnetite. The absence of the transition in the finest fractions may be caused by oxidation of the very fine grained pedogenic magnetite minerals (maghemitization). The relatively high coercivity values of the finest fraction (< 0.228 nm) from a paleosol sample from Paks may be caused by the presence of *in situ* formed fine grained hematite.

ZFC experiments were able to separate the ferromagnetic from the paramagnetic signal. Paleosols and loesses have very similar bulk contents of paramagnetic minerals. Grain size analysis proved that the paramagnetic contribution in the coarser fraction of the paleosols is less important than in the loesses but is larger in the finest fractions. Besides iron hydroxides, which are abundant in Paks but could not be identified magnetically, destruction of iron-bearing paramagnetic minerals during pedogenesis may be considered as the source for the new ferromagnetic minerals formed *in situ*.

The magnetic mineralogy is the same in the central and western Chinese loess plateau, with magnetite/maghemite as the main carrier(s) of the magnetic signals. High temperature hysteresis performed on a paleosol and a loess sample allowed the separation of the diamagnetic, the paramagnetic and the ferromagnetic signal. The diamagnetic signal

is 20% higher in the loess sample, while the absolute paramagnetic contribution (12%) is higher in the paleosol. This result resembles the observations made in Paks, but the absence of grain size dependent hysteresis measurements for the samples collected at Xiagaoyuan and Houzhuang does not allow an analysis of their distribution over the whole grain size spectra.

- **Magnetic profiles**

The enormous potential of susceptibility variations in loess/paleosol sequences for paleoclimatic reconstruction has been already pointed out. Susceptibility is a powerful tool for correlation with other independent climate proxies, but it does not discriminate between magnetic components of different origin in the aeolian sediments. A cross-correlation with other parameters such as the frequency dependence of susceptibility, hysteresis parameters, anhysteretic remanent magnetization, isothermal remanent magnetization, etc. may help identifying type, concentration and size variation of the minerals carrying the magnetic signal, so that finally a paleoenvironmental interpretation can be achieved.

At Roxolany, the magnetic properties throughout the profile were compared with the micromorphological analysis performed by Tsatskin et al. (1998). The main difference between the upper part of the section (from pedocomplexes PK₄ to PK₁) and the lower part (from pedocomplex PK₉ to PK₄) is presented by the high frequency fluctuations of the magnetic properties observed in the lower part of the sequence, not only in the pedocomplexes, but also in the loess layers. This is probably caused by a more humid and warmer climate with increased bioturbation during the earlier period. The difference, expressed mainly by the coercivity and the ratios ARM/SIRM, $\chi_{LF}/SIRM$, χ_{ARM}/χ_{LF} is not seen clearly in the susceptibility and saturation magnetization profile. Only the multi-parameter approach identifies the short term climatic fluctuations affecting the depositional processes and detects features, such as weakly developed pedogenic layers or layers with calcrete concretions which can hardly be recognized in the outcrop. The fluctuations of the magnetic properties in the lower part indicate that during the older cold periods the biological activity was more important than during loess deposition in the upper part of the section. Hence not only interglacials were moister and warmer, but also glacial periods.

A similar approach was taken at Xiagaoyuan and Houzhuang. Important environmental differences between the western and central loess plateau during the last 130 ka have been recognized. At Houzhuang, high concentrations of SP and SD ferrimagnetic minerals were detected not only in the paleosols formed during interglacial periods, but also in the weathered loesses formed during glacial periods, caused by the persistent predominance of the summer monsoon at Houzhuang. At Xiagaoyuan, the high sedimentation rate during the last glacial period and the low degree of weathering permit a higher resolution analysis of the climatic changes. Variations in the magnetic grain size (increased presence of SP and/or SSD magnetic minerals correlate with the pedogenic layers determined lithologically) reflect the short- and long-term climate changes during the last glacial. They occur at more or less the same times - minor age differences may be due to unrecognized sedimentation rate changes - when abrupt paleoclimate events (Heinrich events, Bond cycles) were recorded in the GRIP ice core (Dansgaard et al., 1993).

- **^{10}Be in loess**

The ^{10}Be concentration in loess/paleosol sediments results from two input sources: a detrital flux, which consists of ^{10}Be adsorbed to aeolian dust grains and an atmospheric flux, in which ^{10}Be is adsorbed to aerosol particles. The second source determines the ^{10}Be concentration increase observed in the paleosol layers and is mainly due to precipitation. Beer et al. (1993) and Heller et al. (1993) attempted to correlate ^{10}Be and susceptibility fluxes. They assumed a simple linear relationship between the detrital ^{10}Be flux and the dust component of the susceptibility flux in order to determine the magnitude of the pedogenic susceptibility. Taking the same approach at Xiagaoyuan, it is found in this study that the pedogenic component of paleosol layer S_1S_3 exceeds 80% of the total susceptibility. Unusual results were found for the lowermost part of loess layer L_1 which corresponds to oxygen isotope stage 4. The L_1 pedogenic component in this cold and arid climate site varies between 40% and 60% and is higher than the pedogenic percentage in the same layer at Luochuan where paleoclimate was moister and warmer (Heller et al., 1993). The discrepancy is related to the high variability of the grain sizes in the layers deposited during the last interglacial (finer grain size) and those deposited at the beginning of the last glacial (much coarser). In order to develop a more realistic model that of

Heller et al. (1993, the atmospheric flux may be recalculated taking geomagnetic field variations into account. Such a model may also be superior to correcting the detrital ^{10}Be flux as a function of the original loess grain size distribution.

References

- An, Z. S., Wang, J. and Li, H., Paleomagnetic research of the Luochuan loess section (in Chinese with English abstract), *Geochimica*, 4, 239-249, 1977.
- An, Z. S., Liu, T. S., Lu, Y C., Porter, S. C., Kukla, G., Wu, X. H. and Hua, Y. M., The long-term paleomonsoon variation recorded by the loess-paleosol sequence in central China, *Quat. Int.*, 7/8, 91-95, 1990
- Aragon, R., Sheperd, J. P., Koenitzer, J.W., Buttrey, D. J., Rasmussen, R. J. and Honig, T. M.. Influence of nonstoichiometry on the Verwey transition in $\text{Fe}_{3(1-\delta)}\text{O}_4$. *J. Appl. Phys.*, 57(1), 3221-3222, 1985.
- Argyle, K. S. and Dunlop, D. J., Low-temperature and high-temperature hysteresis of small multidomain magnetites (215-540 nm), *J. Geophys. Res.*, 95, 7069-7083, 1990.
- Backman, J., The age of the first cycle of ice-rafted debris in the North Atlantic Ocean, *Terra Cognita*, 3, 221, 1983.
- Banerjee, S. K., New grain size limits for paleomagnetic stability in hematite, *Nature Phys. Sci.*, 232, 15-16, 1971.
- Banerjee, S. K., Hunt, C. P. and Liu, X. M., Separation of local signals from the regional paleomonsoon record of the Chinese loess Plateau: A rock magnetic approach, *Geophys. Res. Lett.*, 20, 843-846, 1993.
- Bard, E., Hamelin, B., Fairbanks, R. G. and Zindler, A., Calibration of the ^{14}C timescale over the past 30'000 years using mass spectrometric U-Th ages from Barbados corals, *Nature*, 345, 405-410, 1990.
- Baumgartner, S. M., Kosmogene Radioisotope im Pleistozän des Summit-GRIP-Eiskerns - Implikationen für die Klimaforschung, PhD-Thesis, ETH-Zürich, pp. 266, 1995.
- Bean C. P. and Livingston, J. D., Superparamagnetism, *J. App. Phys.*, 30, 120-129, 1959.
- Beer, J., Shen, C., Heller, F., Liu, T., Bonani, G., Dittrich, B., Suter, M. and Kubik, P. W., ^{10}Be and magnetic susceptibility in Chinese loess, *Geophys. Res. Lett.*, 20, 57-60, 1993.
- Bégét, J. E. and Hawking, D., Influence of orbital parameters on Pleistocene loess deposition in central Alaska, *Nature*, 337, 151-153, 1989.
- Berger, A., Long-term variations of caloric insolation resulting from the Earth's orbitals elements. *Quat. Res.*, 9, 139-167, 1978.
- Berger, A., Accuracy and frequency stability of the Earth's orbital elements during the Quaternary, in: A. Berger, J. Imbrie, J. Hays, G. Kukla and B. Saltzman (Eds), *Milankovitch and Climate Part I*, Reidel, Dordrecht, pp. 3-40, 1984.

- Birkeland, P. W., *Soils and Geomorphology*, Oxford University Press, New York, pp. 372, 1984.
- Blinov, A., The dependence of cosmogenic isotope production rate on solar activity and geomagnetic field variations, in: *Secular Solar and Geomagnetic variations in the last 10'000 Years*, (F. R. Stephenson and A. W. Wolfendale, eds.) Kluwer Academic Publishers, pp. 329-340, 1988.
- Bloemendal, J. and De Menocal, P., Evidence for a change in the periodicity of tropical climate cycles at 2.4 Myr from whole-core magnetic susceptibility measurements, *Nature*, 342, 897-900, 1989.
- Bronger, A., Zur quartären Klima- und Landschaftsgeschichte des Karpatenbeckens auf paläopedologischer und bodengeographischer Grundlage. *Kieler Geographische Schriften*, 45, 268 pp., 1976.
- Bronger A. and Heinkele, Th., Micromorphology and genesis of paleosols in the Luochuan loess section, China: Pedostratigraphic and environmental implications, *Geoderma*, 45, 123-143, 1989.
- Bronger A. and Heinkele, Th., Paleosol sequences as witness of Pleistocene climatic history, *Catena Supplements*, 16, 163-186, 1989a.
- Brown, L., Sacks, I. S., Tera, F., Klein, J. and Middleton, R., Beryllium-10 in continental sediments, *Earth Planet. Sci. Lett.*, 55, 370-376, 1981.
- Brown, E. T., The geochemistry of beryllium isotopes: Applications in geochronometry, PhD thesis, Massachusetts Institute of Technology - Woods Hole Oceanographic Institution Joint Program in Oceanography (WHOI Document 90-47), Cambridge and Woods Hole, USA, pp. 273, 1992.
- Brunnacker, K. and Boenigk, W., Über der Stand der paläomagnetischen Untersuchungen im Pliozän und Pleistozän der Bundesrepublik Deutschland, *Eiszeitalter Ggw.*, 27, 1-17, 1976.
- Burbank, D. W. and Li, J., Age and paleoclimatic significance of the loess of Lanzhou, north China, *Nature*, 316, 429-431, 1985.
- Burov, B., Nurgaliev, D. K. and Jasonov, P. G., Paleomagnetic analysis (in Russian), Kazan University Press, 1986.
- Butler, R. F., *Paleomagnetism*, Blackwell Scientific, Cambridge, pp. 319, 1992.
- Butler, R. F. and Banerjee, S., Theoretical single-domain grain size range in magnetite and titanomagnetite, *J. Geophys. Res.*, 80, 4049-4058, 1975.
- Butrym, J. and Maruszack, H., Thermoluminescence chronology of younger and older Loess, In: *Lithology and Stratigraphy of Loess and Paleosoils* (M. Pécsi), Hungarian Academy of Sciences, Budapest, pp. 195-199, 1987.

- Cande, S. C. and Kent, D. V., A new geomagnetic polarity timescale for the late Cretaceous and Cenozoic, *J. Geophys. Res.*, 97, 13917-13951, 1992.
- Cao, J. X. and Ho, C. K., A study of the loess/paleosol sequence and the environmental evolution at Jiuzhoutai, Lanzhou, *Mon. J. Lanzhou University*, 24, 118-122, 1988.
- Carmichael, R. S., *Practical Handbook of Physical Properties of Rocks and Minerals*, Carmichael ed., USA, pp. 358, 1989.
- Catt, J. A., *Palaeopedology manual*. *Quat. Internat.*, 6, 1-95, 1990.
- Catt, J. A., Soils in aeolian sequences as evidence of Quaternary climatic change: Problems and possible solutions, in: *Wind Blown Sediments in the Quaternary Record* (E. Derbyshire), *Quat. proceeding*, 4, John Wiley & Son, Chichester, 59-68, 1995.
- Chen, F. H., and Zhang, W. X., in: *Loess stratigraphy and Quaternary glacial problems in Gansu and Qinghai Provinces*, Science Press, Beijing, 1993.
- Chen, F. H., Bloemendal, J., Wang, J. M., Li, J. J. and Oldfield, F., High-resolution multi-proxy climate record from Chinese loess: evidence for rapid climatic changes over the last 75 kyr, *Palaeogeogr. Palaeoclim. Palaeoec.*, 130, 323-335, 1997.
- Clement, B. M. and Constable, C., Polarity transitions, excursions and paleosecular variation of the Earth's magnetic field, *Rev. geophys. Suppl April*, 433-442, 113-119, 1991.
- Creer, K. M., A.C. demagnetization of unstable Triassic Keuper marls from S. W. England, *Geophys. J. R. Astr. Soc.*, 2, 261-275, 1959.
- Dansgaard, W., Johnsen, S. J., Clausen, H. B., Dahl-Johnsen, Gunderstrup, N., Hammer, C. U., Hvidberg, C., Steffensen, J., Sveinbjörnson, A., Jouze, J. and Bond, G., Evidence for general instability of past climate from a 250 kyr ice core record, *Nature*, 364, 218-220, 1993.
- Day, R., Fuller, M. and Schmidt, V. A., Hysteresis properties of titanomagnetites: grain size and compositional dependence, *Phys. Earth Planet. Inter.*, 116, 53-64, 1999.
- Dekkers, M. J., Some rock magnetic parameters for natural goethite, pyrrhotite and fine grained hematite, PhD Thesis, Univ. Utrecht, pp. 231, 1988.
- deMenocal, P., Ruddiman, W. and Kent, D., Depth of p-DRM acquisition in deep-sea sediment - a case study of the M/B reversal and oxygen isotopic stage 19.1, *Earth. Planet. Sci. Lett.* 99, 1-13, 1990.
- Derbyshire, E., Wang, J., Jin, Z., Billard, A., Egels, Y., Kasser, M., Jones, D. K. C., Muxart, T. and Owen, L., Landslides in the Gansu loess of China, *Catena Suppl.*, 20, 119-145, 1991.

- Derbyshire, E., Meng, X., Wang, J., Zhou, Z. and Li, B., Collapsible loess on the loess plateau of China, In: *Genesis and Properties of Collapsible Soils*, (E. Derbyshire et al., eds.), Kluwer Academic Publishers, 267-293, 1995.
- Ding, Z. L., Liu, t. S., Liu, X. M., Chen, M. Y. and An, Z. S., Thirty-seven climatic cycles in the last 2.5 Ma, *Chin. Sci. Bull.*, 34, 1494-1496, 1990.
- Ding, Z., Rutter, N., Liu, T. S., Evans, M. E. and Wang, Y., Climatic correlation between chinese loess and deep-sea cores: a structural approach, in: *Loess, Environment and Global Change*, edited by T. S. Liu et al., pp. 168-186, Science Press, Beijing, 1991.
- Ding, Z. L., Rutter, N., Han, J. and Liu, T. S., A coupled environmental system formed at about 2.5 Ma in East Asia, *Palaeogeogr. Palaeoclimat. Palaeoecol.*, 94, 223-242, 1992.
- Ding, Z. L., Sun, J. M., Yang, S. L. and Liu, T. S., Preliminary magnetostratigraphy of a thick eolian red clay-loess sequence at Lingtai. the Chinese Loess Plateau, *Geophys. Res. Lett.*, 25, 1225-1228, 1998.
- Dodonov, A. E., Melamed, Y. R. and Nikiforova, K. V. (eds.), *Excursion Guide-Book of the International Symposium on the Neogene-Quaternary Boundary*, IUGS UNESCO IGCP Proj. 41, 182 pp., Nauka, Moscow, 1977.
- Dodonov, A. E., Loess geochronology in Central Asia and Quaternary events, in: 12th Int. Congr. INQUA Progr. with abstracts, Ottawa, pp. 158, 1987.
- Dodonov, A. E., Loess of Central Asia, *Geojournal*, 24(2), 185-194, 1991.
- Donghuai, S., Shaw, J., An, Z. S., Chen, M. Y. and Yue, L. P., Magnetostratigraphy and paleoclimatic interpretation of a continuous 7.2 Ma Late Cenozoic eolian sediments from the Chinese Loess Plateau, *Geophys. Res. Lett.*, 25, 85-88, 1998.
- Dunlop, D. J. and Bina, M-M., The coercive force spectrum of magnetite at high temperatures: Evidence for thermal activation below the blocking temperature, *Geophys. J. Roy. Astron. Soc.*, 51, 121-147, 1977.
- Dunlop, D. J., The rock magnetism of fine particles, *Phys. Earth Planet. Inter.*, 26, 1-26, 1981.
- Dunlop, D. J. and Özdemir, Ö., *Rock Magnetism - Fundamentals and Frontiers*, Cambridge University Press, Melbourne, pp. 573, 1997.
- du Pasquier, J., *Environmental paleomagnetic study of the loess/paleosol sequence from Roxolany (Ukraine)*, Diplom work, ETH-Zürich, unpublished, pp. 62, 1998.
- Dzyaloshinsky, I., A thermodynamic theory of "weak" ferromagnetism of antiferromagnetics, *J. Phys. Chem. Solids*, 4, 241-255, 1958.

- Egorov, V. V., Fridland, V. M., Ivanova, E. N., Rosov, Nosin, V. A., Friev, T. A., Klassifikatsiya i diagnostika pochv SSSR [Classification and diagnostics of the soils of the USSR], Kolos, Moscow, (in russian), 1977.
- Ellwood, B. B., Balsam, W., Burkart, B. Long, G. J. and Buhl, M. L., Anomalous magnetic properties in rocks containing the mineral siderite: Paleomagnetic implications, *J. Geophys. Res.*, 91, 12, 779-790, 1986.
- Elsasser, W., Ney, E. P. and Winckler, J. R., Cosmic-ray intensity and geomagnetism, *Nature*, 178, 1226-1227, 1956.
- Enkin, R. J. and Williams, W., Three-dimensional micromagnetic analysis of stability in fine magnetic grains, *J. Geophys. Res.*, 99, 611-618, 1994.
- Evans, M. E. and Heller, F., Magnetic enhancement and paleoclimate: Study of a loess/paleosol couplet across the loess plateau of China, *Geophys. J. Int.*, 117, 257-264, 1994.
- Eyre, J. K. and Shaw, J., Magnetic enhancement of Chinese loess - the role of $\gamma\text{-Fe}_2\text{O}_3$?, *Geophys. J. Int.*, 117, 265-271, 1994.
- Ewing, J. A., *Magnetic induction in iron and other metals*, The Electrician Publishing Company, 1900.
- Fang, X. M., Li, J. J., Van der Voo, R., Mac Niocaill, C., Dai, X. R., Kemp, R. A., Derbyshire, E., Cao, J. X., Wang, J. M. and Wang, G., A record of the Blake Event during the last interglacial paleosol in the western Loess Plateau of China, *Earth Planet. Sci. Lett.*, 146, 73-82, 1997.
- Fang, X. M., Ono, Y., Fukusawa, H., Pan, B. T., Li, J. J., Guan, D. H., Oi, K., Tsukamoto, S., Torii, M. and Mishima, T., Asian monsoon instability during the past 60'000 years, magnetic susceptibility and pedogenic evidence from the western Chinese Loess Plateau, *Earth Planet. Sci. Lett.*, 168, 219-232, 1999.
- Faustoff, S. S., Bolshakoff, V. A., Virina, E. I. and Demidenko, E. L., Rock magnetic and paleomagnetic methods for studying the Pleistocene (in Russian), *Sci. Tech. Publ. Palaeogeogr. Ser. 3*, pp. 192, URSS Acad. of Sci., Moscow, 1986.
- Fedoroff, N., Contribution à la connaissance de la pedogenèse Quaternaire dans le S-W du Bassin Parisien, *Bull. Assoc. Fr. Etud. Quat.*, 2, 94-105, 1966.
- Fedoroff, N. and Courty, M. A., Morphology and distribution of textural features in arid and semi-arid regions, in: *Micromorphologie des Sols - Soil Micromorphology*, Fedoroff, N., Bresson, L. M. et Courty, M. A., (eds.), AFES, Plaisir, France, 213-219, 1987.
- Fedoroff, N. and Courty, M. A., Indicateurs pedologiques d'aridification, *Bull. Soc. géol. France*, 8(V-1), 43-53, 1989.
- Finkel, R. and Suter, M., AMS in the earth science: technique and applications, *Advances in Analytical Geochemistry*, 1, 1-114, 1993.

- Fitzpatrick, R. W. and Schwertmann, U., Al-substituted goethite - an indicator of pedogenic and other weathering environments in South Africa. *Geoderma*, 27, 335-347, 1982.
- Florindo, F., Zhu, R. X., Guo, B., Yue, L. P., Pan, Y. X. and Speranza, F., Magnetic proxy climate results from the Duanjiapo loess section, southernmost extremity of the Chinese loess plateau, *Journal Geophys. Res.*, 104, 645-659, 1999.
- Forster, T. and Heller, F., Loess deposits from the Tajik depression (Central Asia): Magnetic properties and paleoclimate, *Earth Planet. Sci. Lett.*, 128, 501-512, 1994.
- Forster, T., Evans, M.E. and Heller, F., The frequency dependence of low field susceptibility in loess sediments, *Geophys. J. Intern.*, 118, 636-642, 1994a.
- Forster, T., Heller, F., Evans, M.E. & Havlicek, P., Loess in the Czech Republic: Magnetic properties and paleoclimate. *Studia geophysica et geodetica*, 40, 243-261., 1996.
- Forster, T. and Heller, F., The process of magnetic enhancement in loess sediments from Tajikistan, China and Hungary, *Geophys. Res. Lett.*, 24, 17-20, 1997.
- Frank, M., Schwarz, B., Baumann, S., Kubik, P. W., Suter, M. and Mangini, A., A 200 kyr record of cosmogenic radionuclide production rate and geomagnetic field intensity from ^{10}Be in globally stacked deep-sea sediment, *Earth and Planet. Sci. Lett.*, 149, 121-129, 1997.
- Frechen, M., Horvath, E. and Gabris, G., Geochronology of Middle and Upper Pleistocene loess section in Hungary, *Quat. Res.*, 48, 291-312, 1997.
- Gendler, T. S., Bagin, V. I., Haliulina, E., Heller, F., Hus, J., Hailwood, E. A., Tsatskin, A., Rock magnetic, pedological and Mössbauer study of clay fractions from the loess-paleosol sequence at Roxolany (Ukraine). *Ann. Geophys.* 15 (suppl. I), C101, 1997.
- Goree, W. S. and Fuller, M., Magnetometers using R.F.-driven SQUIDS and their application in rock magnetism and palaeomagnetism, *Rev. Geophys. Space Phys.*, 14, 591-608, 1976.
- Gu, Z. Y., Lal, D., Liu, T. S., Southon, J., Caffee, M. W., Guo, Z. T. and Chen, M. Y., Five million year ^{10}Be record in Chinese loess and red-clay: climate and weathering relationship, *Earth and Planet. Sci. Lett.*, 144, 273-287, 1996.
- Hahn, G., Chronology of the Paks loess exposures, in: *Loess and Periglacial Phenomena*, (M. Pécsi and H. French, eds.), Akadémiai Kiadó, Budapest, pp. 87-101, 1987.
- Han, J. M., Lu, H. Y., Wu, N. Q. and Guo, Z. T., The magnetic susceptibility of modern soils in China and its use for paleoclimatic reconstruction, *Stud. geophys. et geod.*, 40, 262-275, 1996

- Hartl, P. and Tauxe, L., A precursor to the Matuyama/Brunhes transition-field instability as recorded in pelagic sediments, *Earth Planet. Sci. Lett.*, 138, 121-135, 1996.
- Hays, J. D., Imbrie, J. and Shackleton, N. J., Variation in the Earth's orbit: Pacemaker of the ice age, *Science*, 194, 1121-1131, 1976.
- Hedley, I. G., The weak ferromagnetism of goethite (α -FeOOH), *Z. Geophys.*, 37, 409-420, 1971.
- Heider, F., Halgedahl, S. L. and Dunlop, D. J., Temperature dependence of magnetic domains in magnetite crystals, *Science*, 236, 1287-1290, 1988.
- Heinkele, T., *Bodengeographische und paleopedologische Untersuchungen im zentralen Loess Plateau von China - ein Beitrag zur Quartären Klima- und Landschaftsgeschichte*, Schriftenreihe Inst. Pflanzenernährung und Bodenkunde d. Universität Kiel, 9, pp. 120, 1990.
- Heinrich, H., Origin and consequences of cyclic ice rafting in the Northeast Atlantic-ocean during the past 130'000 years, *Quat. Res.*, 29, 142-152, 1988.
- Heller, F. and Evans, M.E., Loess magnetism, *Rev. Geophys.*, 33, 211-240, 1995.
- Heller, F. and Liu, T. S., Magnetostratigraphical dating of loess deposits in China, *Nature*, 300, 431-433, 1982.
- Heller, F. and Liu, T. S., Magnetism of chinese loess deposits, *Geophys. J. R. Astron. Soc.*, 77, 125-141, 1984.
- Heller, F. and Liu, T. S., Paleoclimatic and sedimentary history from magnetic susceptibility of loess in China, *Geophys. Res. Lett.*, 13, 1169-1172, 1986.
- Heller, F., Liu, X. M., Liu, T. S. and Xu, T. C., Magnetic susceptibility of loess in China, *Earth Planet. Sci. Lett.*, 103, 301-310, 1991.
- Heller, F., Shen, C., Beer, J., Liu, X. M., Liu, T. S., Bronger, A., Suter, M. and Bonani, G., Quantitative estimates of pedogenic ferromagnetic mineral formation in Chinese loess and palaeoclimatic implications, *Earth and Planet. Sci. Lett.*, 114, 385-390, 1993.
- Heller, F., Sartori, M., Hus, J., Geeraerts, R., Hailwood, E., Montgomery, P., Gendler, T., Bagin, V., Virina, E. and Tsatskin, A., Paleoenvironmental change documented by magnetic investigations at Roxolany, A loess type section near Odessa (Ukraine), *Geol. Carpathica*, 47, 208-209, 1996.
- Hofmann, H. J., Beer, J., Bonani, G., Von Gunten, H. R., Raman, S., Suter, M., Walker, R. L., Wölfli, W. and Zimmermann, D., ^{10}Be : Half-life and AMS-standards, *Nucl. Instr. Meth. Phys. Res.*, 29, 32-36, 1987.

- Hohl, R., *Die Entwicklungsgeschichte der Erde*, VEB F.A. Brockhaus Verlag, Leipzig, pp. 703, 1980.
- Hus, J. J. and Geeraerts, R., Paleomagnetic and rock magnetic investigation of Late Pleistocene loess deposits in Belgium, *Phys. Earth Planet. Inter.*, 44, 21-40, 1986.
- Hus, J. and Han, J., The contribution of loess magnetism in China to the retrieval of past global changes - some problems, *Phys. Earth Planet. Inter.*, 70, 154-168, 1992.
- Imbrie, J., Hays, J.D., Martinson, D.G., McIntyre, A., Mix, A.C., Morley, J.J., Pisias, N.G., Prell, W.L. and Shackleton, N.J., The orbital theory of Pleistocene climate: Support from a revised chronology of the marine ^{18}O record, in: *Milankovitch and Climate, Part I* (Berger, A.L. et al., eds.), Reidel, Boston, 169-305, 1984.
- Imbrie, J. and Imbrie, J., Modelling the climatic response to orbital variations, *Science*, 207, 943-953, 1980.
- Ivy Ochs, S., The dating of rock surfaces using in situ produced ^{10}Be , ^{26}Al and ^{36}Cl , with examples from Antarctica and the Swiss Alps, PhD-Thesis, ETH-Zürich, pp. 196, 1996.
- Ochs, M. and Ivi-Ochs, S., The chemical behaviour of Be, Al, Fe, Ca and Mg during AMS target preparation from terrestrial silicates modeled with chemical speciation calculation, *Nucl. Instr. Meth. Phys. Res. B*, 123, 135-240, 1997.
- Jacobs, J. A., *Reversals of the Earth's Magnetic field*, Cambridge University Press, pp. 346, 1994.
- Jenny, H., *The Soil Resource, Origin and Behaviour*, Springer Verlag, New York, pp. 377, 1980.
- Johnson, D. L., Keller, E. A. and Rockwell, T. K., Dynamic pedogenesis: new views on some key soil concepts, and a model for interpreting Quaternary soil, *Quat. Res.*, 33, 306-319, 1990.
- Johnsen, S. J., Clausen, H. B., Dansgaard, W., Fuhrer, K., Gundestrup, N. and Steffensen, J. P., Irregular glacial interstadials recorded in a new Greenland ice core, *Nature*, 359, 311-313, 1992
- Juvigné, E., Horvath, E. and Gabris, G., La Téphra de Bag: une retombée volcanique à large dispersion dans le loess Pléistocène d'Europe centrale, *Eiszeiten u. Gegenwart*, 41, 107-118, 1991.
- Kirchenheimer, F., Heidelberg und der Löss, 'Ruperto Carola' Z. Verein. Freunde Student. Univ. Heidelberg XXXI Jahr., 46, 3-7, 1969.
- Kirschwink, J. L., The least-squares line and plane and the analysis of paleomagnetic data, *Geophys. J. R. Astron. Soc.*, 62, 699-718, 1980.

- Kletetschka, G. and Banerjee, S. K., Magnetic stratigraphy of Chinese loess as a record of natural fires, *Geophys. Res. Lett.*, 22, 1341-1343, 1995.
- Kocí, A., Geomagnetic field at the time of reversals, *Veröff. Zentralinst. Physik Erde Potsdam*, 62, 87-92, 1990.
- Kukla, G., Pleistocene Land-Sea correlations 1.Europe., *Earth Sci. Rev.*, 13, 307-374, 1977.
- Kukla, G. J., Loess Stratigraphy of Central Europe. In: *After the Australopithecines*, (K. W. Butzer and G. L. Isaac eds.), pp. 99-188, Mouton, The Hague, 1975.
- Kukla, G. J., Heller, F., Liu, X. M., Xu, T. C., Liu, T. S. and An, Z. S., Pleistocene climate in China dated by magnetic susceptibility, *Geology*, 16, 811-814, 1988.
- Kukla, G. J. and An, Z. S., Loess stratigraphy in Central China, *Palaeogeogr. Palaeoclimatol. Palaeoecol.*, 72, 203-225, 1989.
- Kukla, G. J., An, Z. S., Melice, J. L., Gavin, J. and Xiao, J. L., Magnetic susceptibility record of Chinese Loess, *Trans. R. Soc. Edinburgh: Earth Sci.*, 81, 263-288, 1990
- Lal, D. and Peters, B., Cosmic ray produced radioactivity on the Earth, In: *Handbuch der Physik*, 46, 551-612, 1967.
- Larionov, A. K., Research methods of soils structure (in Russian), 1971.
- Lautridou, J. P., Lithostratigraphie et chronostratigraphie des loess de Haute Normandie, *Acta geol. Acad. Scient. Hungar.*, 22(1-4), 125-132, 1979.
- Lazarenko, A. A., The Loess of Central Asia, in: *Late Quaternary Environments of the Soviet Union*, (A. A. Velichko ed.), pp. 125-131, University of Minnesota Press, Minneapolis, 1984.
- Lei X. and Sun W., Loess in China and its stratigraphic Sequences, in: *The Recent Research of Loess in China* (Sasajima, S. and Wang, Y. eds.), Kyoto Institute of Natural History, pp. 32-41, 1984.
- Li, J. J., Zhu, J. J., Kang, J. C., Chen, F. H., Fang, X. M., Mu, D. F., Cao, J. X., Tang, L. Y., Zhang, Y. T. and Pan, B. T., The comparison of Lanzhou loess profile with Vostok ice core in Antarctic over the last glaciation cycle, *Sci. China, Ser. B.*, 35, 476-487, 1992.
- Liu, T. S. and Chang, T. H., The "Huangtu" (loess) of China, *Rep. VI. Int. Congr. Quat. Warsaw* 1961, 4, 503-524, 1964.
- Liu, T. S., Cheng, M. and Li, X., A satellite images study on the dust storm at Beijing on April 17-21, 1980, in: *Quaternary Geology and Environment of China*, 49-52, China Press, Beijing, 1982.
- Liu, T. S., et al., *Loess and the Environment*, 251 pp., China Ocean Press Beijing, 1985.

- Liu, X. M., Liu, T. S., Xu, T. C., Liu, C. and Cheng, M. Y., A preliminary study on magnetostratigraphy of a loess profile in Xifeng area, Gansu Province. In: *Aspects of Loess Research* (Liu, T. S. ed.), pp. 164-174, China Ocean Press, Beijing, 1987.
- Liu, X. M., Liu, T. S., Xu, T. C., Liu, C. and Cheng, M. Y., The primary study on magnetostratigraphy of a loess profile in Xifeng area, Gansu Province, *Geophys. J. R. Astron. Soc.*, 92, 345-348, 1988.
- Liu, X. M., Liu, T. S., Shaw, J., Heller, F., Xu, T. C. and Yuan, B. Y., Paleomagnetic and paleoclimatic studies of Chinese loess, in: *Loess, Environment and Global Change*, (Liu, T. S. et al., eds.), pp. 61-81, Science Press, Beijing, 1991.
- Liu, X. M., Shaw, J., Liu, T. S., Heller, F. and Yuan, B. Y., Magnetic mineralogy of Chinese loess and its significance, *Geophys. J. Int.*, 108, 301-308, 1992.
- Liu, X. M., Bloemendal, J., Rolph, T., Shaw, J., Liu, T. S. and Heller, F., Quantitative estimates of paleoprecipitation at Xifeng in the loess plateau of China, *Palaeogeogr. Palaeoclim. Palaeoec.*, 113, 243-248, 1995.
- Lowrie, W., *Fundamentals of Geophysics*, Cambridge University Press, pp. 354, 1997.
- Lozek, V., *Quartärmollusken der Tschechoslowakei*, *Rozpr. Ustred. ustavu. Geol.*, 31, pp. 374, 1964.
- Lyell, C., On the delta and alluvial deposits of the Mississippi River, and other points of the geology of North America, observed in the years 1845, 1846, *Am. J. Sci.*, 3, 267-269, 1847.
- MacFadden, B. J., Siles, O., Zeitler, P., Johnson, N. M. and Campbell Jr., K. E., Magnetic polarity stratigraphy of the middle Pleistocene (Ensenadan) Tarjia formation of southern Bolivia, *Quat. Res.*, 19, 172-187, 1983.
- Maher, B. A. and Taylor, R. M., Formation of ultrafine-grained magnetite in soils, *Nature*, 366, 368-370, 1988.
- Maher, B. A. and Thompson, R., Mineral magnetic record of the Chinese loess and paleosols, *Geology*, 19, 3-6, 1991.
- Maher, B. A. and Thompson, R., Palaeoclimatic significance of the mineral magnetic record of the Chinese loess and paleosols, *Quat. Res.*, 37, 155-170, 1992.
- Maher, B. A., Thompson, R. and Zhou, L. P., Spatial and temporal reconstructions of changes in the Asian palaeomonsoon: A new mineral magnetic approach, *Earth Planet. Sci. Lett.*, 125, 461-471, 1994.
- Márton, P., Paleomagnetism of the Paks brickyard exposures, *Acta Geologica Academiae Scientiarum Hungaricae*, 22, 443-449, 1979.

Maruszczak, H. and Nawrocki, J., Stratigraphic-paleogeographic interpretation of the results of magnetic susceptibility investigations of loesses at Nieledeu (SE Poland), *Ann. Univ. Mariae Curie-Sklodowska, Lublin-Polonia*, XLVI, 10, 173-185, 1991.

Masarik, J. and Reedy, R. C., Terrestrial cosmogenic-nuclide production systematics calculated from numerical simulations, *Earth Planet. Sci. Lett.*, 136, 381-395, 1995.

Masarik, J. and Beer, J., Simulation of particle fluxes and cosmogenic nuclide production in the Earth's atmosphere, *J. Geophys. Res.*, 104, 12'099-12'111, 1999.

McDougall, I., Brown, F. H., Cerling, T. E. and Hillhouse, J. W., A reappraisal of the geomagnetic polarity timescale to 4 Ma using data from the Turkana basin, east Africa, *Geophys. Res. Lett.*, 19, 2349-2352, 1992.

McHargue, L. R. and Damon, P. E., The global Beryllium 10 cycle, *Rev. Geophys.*, 29/2, 141-158, 1991.

McHargue, L. R., Damon, P. E. and Douglas, J. D., Enhanced cosmic-ray production of ^{10}Be coincident with the Mono Lake and Laschamp geomagnetic excursion, *Geophys. Res. Lett.*, 22, 659-662, 1995.

Meszaros, E., *Atmospheric Chemistry*, Elsevier, New York, pp. 201, 1981.

Meynadier, L., Valet, J. -P., Weeks, R., Shackleton, N. J. and Hagee, V. L., Relative geomagnetic intensity of the field during the last 140 ka, *Earth Planet. Sci. Lett.*, 114, 39, 1992.

Milankovitch, M. M., *Kanon der Erdestrahlung*, Belgrad, Königl. Serb. Akad. (English: Canon of Insolation and the Ice Age Problem. Transl. by Isr. Prog. Sci. Transl. for the US Dep. Comm., Nat. Sci. Found.), 1941.

Moller, P. and Wagener, K., Dating soil layers by ^{10}Be , in: *Proceedings of the Symposium on Radioactive Dating and Methods of Low-Level Counting*, International Atomic Energy Agency, Vienna, 177-188, 1967.

Mottana, A., Crespi, R. and Ligorio, G., *Der grosse BVL Mineralienführer*, BLV Verlag, pp. 612, 1982.

Nabel, P., The Brunhes Matuyama boundary in Pleistocene sediments of Buenos Aires province, Argentina, *Quat. Int.*, 17, 79-85, 1993.

Nawrocki, J., Wójcik, A. and Bogucki, A., The magnetic susceptibility record in the Polish and western Ukrainian loess-paleosol sequences conditioned by paleoclimate. *Boreas*, 25, 161-169, Oslo, 1996.

Néel, L., Théorie du traînage magnétique des ferromagnétiques en grains fins avec application aux terres cuites, *Ann. Géophys.*, 5, 99-136, 1949.

- O'Brien, K., Secular variations in the production of cosmogenic isotopes in the Earth's atmosphere, *J. Geophys. Res.*, 84, 423-431, 1979.
- Oches, E. A. and Banerjee, S. K., Rock-magnetic proxies of climate change from loess-paleosol sediments of the Czech Republic, *Studia geophysica et geodetica*, 40, 287-300, 1996.
- Ödzemir, Ö. and Banerjee, S. K. High temperature stability of maghemite. *Geophys. Res. Lett*, II, 161-164, 1984.
- Ödzemir, Ö. and York, D., Ar/Ar laser dating of a single grain of magnetite. *Tectonophys.*, 184, 21-33, 1990.
- Ödzemir, Ö. and Dunlop D. J., Chemical remanent magnetization during γ -FeOOH phase transformation, *J. Geophys. Res.*, 98, 4191-4198, 1993.
- O'Reilly, W., *Rock and Mineral Magnetism*, Blackie & Son Ltd, Glasgow, pp. 220, 1984.
- Osipov, V. I. and Sokolov, V. N., Factors and mechanism of loess collapsibility, In: *Genesis and Properties of Collapsible Soils*, (E. Derbyshire et al., eds.), Kluwer Academic Publishers, 49-63, 1995.
- Pavich, M. J., Brown, L., Valette-Silver, N., Klein, J. and Middleton, R., ^{10}Be distribution in soils from Merced River terraces, California, *Geochim. Cosmochim. Acta*, 50, 1727-1735, 1986.
- Pécsi, M., Lithostratigraphic subdivision of the loess profiles at Paks, *Acta Geologica Academiae Scientiarum Hungaricae*, 22, 409-419, 1979.
- Pécsi, M., Chronostratigraphy of Hungarian loesses and the underlying subareal formation, in: *Loess and the Quaternary*, edited by M. Pécsi, pp. 33-49, Akadémiai Kiadó, Budapest, 1985.
- Pécsi, M., The loess-paleosol and related subareal sequence in Hungary, *GeoJournal*, 15, 151-162, 1987.
- Pécsi, M., Loess is not just an accumulation of dust, *Quat. Internat.*, 7/8, 1-21, 1990.
- Pécsi, M., Loess of the last glaciations, In: *Atlas of Paleoclimates and Paleoenvironments of the Northern Hemisphere* (B. Frenzel, M. Pécsi and A. A. Velichko, eds.), Geographical Research Institute Hungarian Academy of Science, Budapest, 110-119, 1992.
- Pécsi, M., Schweitzer, F., Balogh, J., Balogh, M., Havas, J. and Heller, F., A new loess-paleosol lithostratigraphical sequence at Paks (Hungary), *LoessinForm*, 3, 63-78, 1995.

Pen'kov, A. V. and Gamov, L. N., Paleomagnetic datums in Pliocene-Quaternary strata of southern Tajikistan, in: *Abstracts-book of the International Symposium on the Neogene-Quaternary boundary*, edited by K. V. Nikiforova and A. E. Dodonov, IUGS UNESCO IGCP Proj. 41, pp. 46-47, Nauka, Moscow, 1977.

Pierron-Darbonne, A., Rapport de stage 3ème année. C.E.A., Centre d'Etudes de Saclay-L'Orme des Mérisiers, Laboratoire de Magnétisme à Basse Température, pp. 56, 1995.

Pillans, B. and Wright, I., 500'000-year paleomagnetic record from New Zealand loess, *Quat. Res.*, 33, 178-187, 1990.

Porter, S. C. and An, Z. S., Correlation between climate events in the North-Atlantic and China during the last glaciation, *Nature*, 375, 305-308, 1995.

Pye, K., *Aeolian Dust and Dust Deposits*, Academic, San Diego, California, pp. 334, 1987.

Reinders, J. and Hambach, U., A geomagnetic event recorded in loess deposits of the Tönchesberg (Germany): identification of the Blake magnetic polarity episode, *Geophys. J. Int.*, 122, 407-418, 1995.

Retallack, G. J., *Soils of the Past; An Introduction to Paleopedology*, Unwin and Hyman, New York, pp. 500, 1990.

Retallack, G. J., The environmental factor approach to the interpretation of paleosols, In: *Factors of Soil Formation: a Fiftieth Anniversary Retrospective*, edited by R. Amundson, J. Harden and M. Singer, *Soil Sci. Soc. Am. Publ.*, 33, 31-64, 1994.

Richthofen, F. von, On the mode of origin of the loess, *Geol. Mag.*, 9, 293-305, 1882.

Rolph, T. C., Shaw, J., Derbyshire, E. and Wang, J. T., A detailed geomagnetic record from Chinese loess, *Phys. Earth Planet. Inter.*, 56, 151-164, 1989.

Rousseau, D.-D. and Puisségur J.-J., A 350'000-year climatic record from the loess sequence of Achenheim, Alsace, France, *Boreas*, 19, 203-216, 1990.

Ruhe, R. V., Geomorphic surface and the nature of soil, *Soil Sci.*, 82, 441-445, 1956.

Ruhe, R. V. and Olson, C. G., Soil welding, *Soil Sci.*, 130, 132-139, 1980.

Ruocco, M., A 3 Ma paleomagnetic record of coastal continental deposits in Argentina, *Palaeogeogr., Palaeoclimatol., Palaeoecol.*, 72, 105-113, 1989.

Russel, R. J., Origin of loess - a reply, *Am J. Sci.*, 242, 447-450, 1844.

Rutter, N., Ding, Z. L., Evans, M. E. and Wang, Y. C., Magnetostratigraphy of the Baoji loess-paleosol section in the north-central China loess plateau, *Quat. Int.*, 7/8, 97-102, 1990.

Sappey, R., Vincent, E., Hadacek, N., Chaput, F, Boilot, J.P., Zins, D., Nonmonotonic field dependence of the zero-field cooled magnetisation peak in some system of magnetic nanoparticles. *Phys. Rev. B*, 56: 14'551-14'559, 1997.

Scheffer, F. and Schachtschabel, P., *Lehrbuch der Bodenkunde*. 14 Aufl., Enke Verlag, Stuttgart, pp. 494, 1998.

Shackleton, N.J. and Opdyke, N. D., Oxygen isotope and paleomagnetic stratigraphy of Pacific core V28-239, Late Pliocene to Latest Pleistocene, *Mem. geol. Soc. Am.*, 145, 449-464, 1976.

Shackleton, N. J., Backman, J, Zimmermann, H, Kent, D. V., Hall, M. A., Roberts, D. G., Schneiter, D., Baldauf, J. G., Desrairies, A., Homrighausen, R., Huddleston, P., Keene, J. B., Kaltenback, A. J., Krumsiek, K. A. D., Morton, A. C., Murray, J. W. and Westberg-Smith, J., Oxygen isotope calibration of the onset of ice-rafting and history of glaciation in the North Atlantic region, *Nature*, 307, 620-623, 1984.

Shackleton, N. J., and Hall, M. A., Stable isotope history of the Pleistocene at ODP site 677, *Proc. Ocean Drill. Program Sci. Results*, 111, 295-316, 1989.

Shackleton, N.J., Berger, A. and Peltier, W.R., An alternative astronomical calibration of the Lower Pleistocene timescale based on ODP Site 677. *Transaction of the Royal Society of Edinburgh: Earth Sciences*, 81, pp. 251-261, 1990.

Schroeder, D., Zur Geschichte des Mineralnamens "Goethit". *Z. Pflanzenernähr. Bodenkd.*, 151, 137-139, 1988.

Schwertmann, U. and Taylor, R. M., Iron Oxides, In: *Minerals in Soil Environments* (Dixon, J. B., Weed, S. B. eds.), SSSA Series, Madison, Wisconsin, USA, pp. 380-438, 1989.

Smalley, I. J., Possible formation mechanism for the modal coarse-silt quartz particles in loess deposits. *Quat. Int.*, 7/8, pp. 23-27, 1991.

Sharma, P. V., Theoretical study of magnetic attraction due to rock bodies and experimental investigation of the stability of rock magnetism, PhD-Thesis, ETH-Zurich, 89-120, 1966.

Shen, C. D, Beryllium-10 in Chinese loess, PhD-Thesis, Univ. Bern, pp. 60, 1986.

Shen, C. D., Beer, J., Liu, T. S., Oeschger, H., Bonani, G., Suter, M. and Wölfli, W., ^{10}Be in Chinese loess, *Earth Planet. Sci. Lett.*, 109, 169, 1992.

Shen, D H., Shaw, J., An, Z. S., Chen, M. Y. and Yue, L. P., Magnetostratigraphy and paleoclimatic interpretation of a continuous 7.2 Ma Late Cenozoic eolian sediments from the Chinese Loess Plateau, *Geophys. Res. Lett.*, 25, 85-88, 1998.

Simpson, J. A., *Ann. Rev. Nucl. Part. Sci.*, 33, 1983.

- Smith, J. D. and Foster, J. H., Geomagnetic reversal in Brunhes normal polarity epoch, *Science*, 163, 565, 1969.
- Soffel, H. C., *Paläomagnetismus und Archäomagnetismus*, Springer-Verlag, pp. 276, 1991.
- Soil Survey Staff. Soil Taxonomy. A basic system of soil classification for making and interpreting soil surveys. USDA Agriculture Handbook 436. US Government Printing Office, Washington, D.C., 1975.
- Spassov, S., *Umweltmagnetismus und Löss: Das Profil von Novaya Etuliya, Moldavien*, Diplomarbeit, ETH-Zürich, unpublished, pp. 61, 1998.
- Spell, T. L. and McDougall, I., Revision to the age of Brunhes-Matuyama boundary and the Pleistocene geomagnetic polarity timescale. *Geophys. Res. Lett.*, 19, 1181-1184, 1992.
- Stacey, F. D. and Banerjee, S. K., *The Physical Principles of Rock Magnetism, Developments in Solid Earth Geophysics*, 5, Elsevier Scientific Publishing Company, New York, pp. 195, 1974.
- Stoner, E. C. and Wohlfarth, E. P., A mechanism of magnetic hysteresis in heterogeneous alloys, *Phil. Trans. Roy. Soc. London*, A240, 559-642, 1948.
- Sugiura, N., Field dependence of blocking temperature of single-domain magnetite. *Earth Planet. Sci. Lett.*, 46: 438-442, 1980.
- Sun, D. H. and Wu, X. H., Preliminary study of Quaternary tectono-climatic cycles in China. *Quat. Sci. Rev.*, 5, 497-501, 1985.
- Sun, D. H., Shaw, J., An, Z. S., Chen, M. Y. and Yue, L. P., Magnetostratigraphy and paleoclimatic interpretation of a continuous 7.2 Ma Late Cenozoic eolian sediments from the Chinese Loess Plateau, *Geophys. Res. Lett.*, 25, 85-88, 1998.
- Synal, H-A., Bonani, G., Döbeli, M., Ender, R. M., Gartenmann, P., Kubik, P. W., Schnabel, Ch. and Suter, M., Status report of the PSI/ETH AMS facility, *Nucl. Instr. Meth. Phys. Res.*, 123 B, 62-68, 1997.
- Taylor, K. C., Lamory, G. W., Doyle, G. A., Alley, R. B., Grootes, P. M., Mayewski, P. A., White, J. W. C., and Barlow, L. K., The " flickering switch" of Late Pleistocene climate change, *Nature*, 361, 432-436, 1993.
- Tauxe, L., Herbert, T., Shackleton, N. J. and Kok, Y. S., Astronomical calibration of the Matuyama-Brunhes boundary: Consequences for magnetic remanence acquisition in marine carbonate and the Asian loess sequences, *Earth Planet. Sci. Lett.*, 140, 133-146, 1996.
- Thellier, R., Sur l' aimantation des terres cuites et ses applications géophysiques, *Ann. Inst. Physique du Globe, Univ. Paris*, 16, 157-302, 1938.

- Thompson, R. and Oldfield, F., *Environmental Magnetism*, Allen & Unwin Ltd., London, pp. 227, 1986.
- Torii, M., Yue, L. P., Hayashida, A., Maenaka, K., Yokoama, T. and Sasajima, S., Natural remanent magnetisation of loess-paleosol deposits in Luochuan area, In: *The Recent Research of Roess in China*, edited by Sasajima, S. and Wang, Y., Kyoto Institute of Natural History, pp. 32-41, 1984.
- Tsatskin, A., Heller, F., Hailwood, E. A., Gendler, T. S., Hus, J., Montgomery, P., Sartori, M. and Virina, E. I., Pedosedimentary division, rock magnetism and chronology of the loess/paleosol sequence at Roxolany (Ukraine), *Palaeogeogr. Palaeoclim. Palaeoec.*, 143, 111-133, 1998.
- Tretyak, A.N. & Volog, Z.E., *Paleomagnitnaya stratigrafiya pliotsen-chetvertichnykh osadochnykh tolshch Ukrainy* [Paleomagnetic stratigraphy of Pliocene and Quaternary sediments in the Ukraine]. Kiev, Naukova Dumka, (in Russian), 1976.
- Trubikhin, V.M. & Chepalyga, A.L., *Paleomagnitnaya stratigrafiya Pliotsena i Pleistotsena Moldavii* [Palaeomagnetic stratigraphy of the Pliocene and Pleistocene in Moldavia], in: *Faunal assemblages, biostratigraphy of the Pliocene and Pleistocene of Moldavia* (Kishinev, Shtiintsa ed.), p. 30-31 (in Russian), 1986.
- Van Velzen, A. J. and Zijdeveld, J. D. A., Effects of weathering on single-domain magnetite in Early Pliocene marine marls, *Geoph. J. Int.*, 121, 267-278, 1995.
- paleosol sequences: a correction of rock magnetic parameters, *Studia Geophysica et Geodetica*, 43, 357-375, 1999.
- Velichko, A. A., Relationship of climatic changes in high and low latitudes of the Earth during the Late Pleistocene and Holocene, in: *Paleogeography and loess. Pleistocene Climatic and Environmental Reconstructions* (Pécsi, M., Velichko, A. A., eds.), pp. 9-26, 1987.
- Velichko, A.A., Loess-paleosol formation on the Russian Plain. *Quat. Int.*, 7/8, 103-114, 1990.
- Verosub, K. L., Fine, P., Singer, M. J., Tenpas, J., Pedogenesis and paleoclimate: Interpretation of the magnetic susceptibility record of Chinese loess-paleosol sequences, *Geology*, 21, 1011-1014, 1993.
- Verwey, E. J. M., The crystal structure of $\gamma\text{-Fe}_2\text{O}_3$ and $\gamma\text{-Al}_2\text{O}_3$, *Z. Krist.*, 91, 65-69, 1935.
- Virina, E. I., Udartzev, V. P., Faustoff, S. S. and Chernova, L. M., Palaeomagnetic stratigraphy of loess sediments of the Precaucasus region. In: *Abstracts, VII Allunion Conference on the Quaternary: Methods of Research, Stratigraphy and Ecology*, 1, 120-121, Tallin, Estonia, 1990.

Virina, E., Gendler, T.S., Tsatskin, A., Heller, F., Hus, J. and Hailwood, E.A., Magnetism of loess-paleosol sequences along the climatic gradient from the centre to the south west of the Russian plain. *Ann. Geophys.*, 15 (Suppl. I), C106, 1997.

Virlet-d' Aoust, P. H., Observations sur un terrain d' origine météorique ou de transport aérien qui existe au Mexique, et sur le Phénomène des trombees de poussière auquel il doit principalement son origine. *Geol. Soc. Fr. Bull.*, 2nd ser., 16, 417-431, 1857.

Voigt, H. H., *Abriss der Astronomie*, Bibliograph. Inst., Zürich, pp. 534, 1980.

Voelker, A.H.L., Zur Deutung der Dansgaard-Oeschger Ereignisse in ultra-hochauflösenden Sedimentprofilen aus dem Europäischen Nordmeer, Dissertation, Institut für Geowissenschaften Bericht 9, Kiel, 1999.

Vogt, S., Herzog, G. F. and Reedy, R. C., Cosmogenic nuclides in extra-terrestrial materials, *Rev. Geophys.*, 28, 253-275, 1990.

Wang, Y. Y., Ishida, S. and Zhao, J. P., The variation of the Quaternary paleoclimate as reflected by the sporo-pollens in the loess of China, In: *The Recent Research of loess in China* (Sasajima, S. and Wang, Y., eds.), pp. 170-184. Kyoto Institute of Natural History, 1984.

Wang, Y., Lin, Z., Lei, X. and Wang, S., Fabric and other physico-mechanical properties of loess in Shaanxi Province, China, *Catena Suppl.*, 9, 1-10, 1987.

Wang, F. B. and Li, B. Y., The lower boundary of the Quaternary in the Himalaya region in China. In: *Quaternary Geology and Environment of China* (Liu T.S., ed.), China Ocean Press, Beijing, pp. 18-26, 1985.

Wang, Y., Evans, M. E., Rutter, N. and Ding, Z., Magnetic susceptibility of Chinese loess and its bearing on paleoclimate, *Geophys. Res. Lett.*, 17, 2449-2451, 1990.

Weiss, P., L' hypothèse du champ moléculaire et la propriété ferromagnétique. *J. Phys.*, 6, 661-690, 1907.

Westgate, J. A., Stemper, B. A. and Péwé, T. L., A 3 m.y. record of Pliocene-Pleistocene loess in interior Alaska, *Geology*, 18, 858-861, 1990.

Wilding, L. P. and Drees, L. R., Spatial variability and pedology, In: *Pedogenesis and Soil Taxonomy I. Concepts and Interactions*, (L. P. Wilding, ed.), Developments in Soil Science IIA, Elsevier, Amsterdam, 29-39, 1984.

Wintle, A. and Packman, S., Thermoluminescence ages for three sections in Hungary, *Quat. Sci. Rev.*, 7, 315-320, 1988.

Yaalon, D. H., Conceptual models in pedogenesis: Can soil-forming functions be solved?, *Geoderma*, 14, 189-205, 1975.

- Young, J. A. and Silker, W. B., Aerosol deposition velocities on the Pacific and Atlantic Oceans calculated from ^7Be measurements, *Earth Planet. Sci. Lett.*, 50, 92-104, 1980.
- Zhang, Z., Zhang, Z. and Wang, Y., *Loess deposits in China*, Geological Publishing House, Beijing, China, pp. 202, 1991.
- Zhao, W. L. and Morgan, W. J., Uplift of Tibetan Plateau, *Tectonics*, 4, 359-369, 1985.
- Zheng, H. B., An, Z. S. and Shaw, J., New contributions to Chinese Plio-Pleistocene magnetostratigraphy, *Phys. Earth Planet Inter.*, 70, 146-153, 1992.
- Zhou, L. P., Oldfield, F., Wintle, A. G., Robinson, S. G. and Wang, J. T., Partly pedogenic origin of magnetic variations in Chinese loess, *Nature*, 346, 737-739, 1990.
- Zhu, R. X., Zhou, L. P., Laj, C., Mazaud, A. and Ding, Z. L., The Blake geomagnetic polarity episode recorded in Chinese loess, *Geophys. Res. Lett.*, 21, 697-700, 1994.
- Zhu, R. X., Coe, R. S., Guo, B., Anderson, R. and Zhao, X. X., Inconsistent paleomagnetic recording of the Blake event in Chinese loess related to sedimentary environment, *Geophys. J. Int.*, 134, 867-875, 1998.
- Zöller, L. and Wagner, G. A., Thermoluminescence dating of loess - recent developments, *Quat. Int.*, 7/8, 119-128, 1990.
- Zöller, L., Conard, N.J. and Hahn, J., Thermoluminescence dating of Middle Palaeolithic open air sites in the Middle Rhine valley/Germany, *Naturwiss.*, 78, 408-410, 1991.

Curriculum Vitae

June 12, 1968 Born in Locarno, Ticino, Switzerland
Nationality Swiss
Originary from Bosco-Gurin, Ticino, Switzerland

Education

1983 - 1987 Liceo, Collegio Papio, Ascona.
1987 - 1993 Eidgenössische Technische Hochschule (ETH), Zürich.
1993 Diplom in Natural Sciences (Geophysics)
Diplomwork at the Institute of Geophysics, ETH - Hönggerberg.
Title: “*Anisotropy of the magnetic susceptibility of Permian red-beds and their reduction spots in the Alpes Maritimes (France)*”.
Referees: Prof. Dr. Friedrich Heller, Prof. Dr. William Lowrie.
1994 -2000 Doctoral Studies, Institute of Geophysics, ETH-Hönggerberg.
Title: “*The Quaternary climate in loess sediments: Evidence from rock and mineral magnetic and geochemical analysis*”.
Referees: Prof. Dr. Friedrich Heller, Prof. Dr. William Lowrie
Dr. Jürg Beer, Prof. Dr. Michael E Evans.

Acknowledgements

Many people have contributed to the final success of my thesis. I would like to express my sincere thanks to all of them.

Special thanks go to

-*Prof. Dr. F. Heller* for the motivation and the support during measuring and writing and for having been much more than a *Doktorvater*, especially during fieldwork.

-*Prof. Dr. W. Lowrie* for having accepted me as a member of the MAG group, and for the support during the last difficult part of my thesis,

-*Prof. Dr. J. Beer* for introducing me into the fascinating and complex world of cosmogenic isotopes,

-*Prof. Dr. Ted Evans* for the very nice time in China, for the motivation and for your help as a loess specialist,

-*Dr. Ann Hirt* for the help, the numerous suggestions during my thesis and for the many enriching discussions,

-*Tatonka Geyer* für die vielen schönen Zeiten, die wir zusammen hatten und haben werden....

-*Prof. Dr. Suter, Prof. Dr. Bonani, Dr. Peter Kubik* for their help and assistance during the measurements at the AMS,

-*Dr. Sasha Tsatskin* for the numerous suggestions on pedologic topics, but mainly for being a good friend: toda!!,

-*Prof. Dr. Chen Haihong*, who made me discover that China is not only Huang-tu,

-*Caroline Stengel, Silvia Bollhalder, Eva Meili, Dr. Gerhard Wagner, Dr. Susan Ivy-Ochs, Dr. Irka Hajdas* always being prepared to help me during ^{10}Be extraction and measurement,

-*Dr. M. Borkovec, Dr. P. Weidler, Prof. Dr. R. Kretschmar*, for their numerous suggestions during the work at the Institute of Terrestrial Ecology, and particular thanks to *Kurt Barmettler*,

-*Prof. Dr. C. Laj, Dr. C. Kissel, Dr. A. Mazaud*, pour l'hospitalité et l'aide pendant mes plusieurs séjours à Gif,

-*Prof. Dr. Hammann, Dr. Eric Vincent*, pour m'avoir permis d'utiliser le susceptometre et pour les conseils sûr le magnétisme à basse temperature,

-*Prof. Dr. Pécsi and colleagues, Prof. Dr. J. Hus, Dr. Geeraerts, Dr. Gendler, Dr. Virina, Dr. Trubykhin, Dr. Chepaliga, Dr. Han Jiamao* and all the students making the field work in eastern Europe and China a pleasure and a success,

-*Ramon Egli, Simo Spassov, Pavel Sroubek, Jacques du Pasquier and Prof. Dr. Danis Nourgaliev, Dr. Pavel Jassonov and Dr. Shamil Ibragimov from Kazan* for their help and suggestions during grain size analysis and hysteresis measurements,

-*The whole Magnetic Group* for acting like a survival kit during the "cold periods",

-*Juanjo y Daniel* por su simpatia y amistad. Un saludo particular a *Marife*,

-*Genitori, Sanzia, Mimma*, per avermi sostenuto finanziariamente durante l'interminabile 1999,

-*Palpôl ...*,

Annette,

für deine Liebe und "Gelduld" ...